Thesis Submitted for the Degree of
Doctor of Philosophy

INTERFACIAL ELECTROACTIVE ASSEMBLIES: FROM MOLECULAR ELECTRONICS TO BIOLOGICAL APPLICATIONS

Author: Colm Mallon B.Sc.

Supervisors: Dr. Tia E. Keyes and Prof. Robert J. Forster

Dublin City University
School of Chemical Sciences
January 2009

I hereby certify that this material, which I now submit for assessment on the programme of study leading to the award of Doctor of Philosophy is entirely my own work, that I have exercised reasonable care to ensure that the work is original, and does not to the best of my knowledge breach any law of copyright, and has not been taken from the work of others save and to the extent that such work has been cited and acknowledged within the text of my work.

Signed: ________________________ ID No.: _____

Candidate

Date: ___________

Acknowledgements

Sincere thanks are due to my supervisors Dr. Tia Keyes and Prof. Robert Forster. Their enthusiasm for a challenge is infectious and their skill and guidance over the course of this study was critical.

IRCSET provided much appreciated funding over the last three years, also thanks to Prof. Niamh Moran and Ciaran De Chaumont from the RCSI for their help with the protein assay. Also, thanks to all those who provided compounds for this work, especially Yann. Thanks also to the technical staff at DCU, who are never short of being excellent.

Thanks are also due to all those in our group, past and present, who had to put up with me, there are too many to mention, but especially Eoin, Elena, Andrea, Bincy, Claudio and Emmet. Outside of collage, a big thank you to John.

After that, champagne for my real friends and real pain for my sham friends.

Contents

Interfacial electroactive assemblies:
From molecular electronics to biological applications

Colm Mallon

Abstract

Spontaneously adsorbed monolayers of di-6^A, 6^B-deoxy-6-(4-pyridylmethyl)amino-γ-cyclodextrin (γ-CD-$(py)_2$) were formed on platinum electrodes. AC voltammetry showed significantly lower capacitance values for electrodes exposed to γ-CD-$(py)_2$ solutions overnight compared to bare electrode values. Co-adsorption of 1-nonanethiol in the presence of a 10-fold excess of cavity guest 1-adamantylamine created layers which exhibited greater blocking ability to the solution phase probe $[Fe(CN)_6]^{4-}$. Complete blocking was achieved by insertion of a high-affinity guest 1-adamantylamine into the cavity. Raman spectra of the γ-CD-$(py)_2$/1-nonanethiol layer exhibited features associated with both pyridine-functionalised CD and alkane moieties. Significantly, co-adsorption of 1-nonanethiol dramatically effected the ability of the γ-CD-$(py)_2$ layer to complex the electroactive, high affinity guest, $[Co(biptpy)_2]^{2+}$. A redox response for the $Co^{2/3+}$ couple was not observed at the pure γ-CD-$(py)_2$ layer, but the molecular recognition properties were turned on by co-adsorbing the alkanethiol molecules with the CD layer. The binding of $[Co(biptpy)_2]^{2+}$ to co-adsorbed monolayers depends on the bulk concentration of guest and was modelled by the Langmuir isotherm, yielding a free energy of adsorption, ΔG_{ads}, of -29 kJ.mol^{-1} for the Co^{2+} state and a limiting surface coverage 1.49 ± 0.25 x 10^{-11} mol.cm^{-2}. The rate of electron transfer from the cobalt metal center to the electrode surface was found to be of the order of 1 x 10^5 s^{-1} by high speed chronoamperometry.

Molecular junctions incorporating monolayers of γ-CD-$(py)_2$, co-adsorbed with 1-nonanethiol have been formed by bringing macroscopic platinum and mercury electrodes together. The mercury electrode was either modified with an alkanethiol layer for bi-layer junction formation, or remained unmodified for monolayer junction formation. The junctions were characterised by determining the effect of junction thickness on the magnitude of the tunnelling current through alkanethiol layers. A tunnelling co-efficient, β, of 0.88 ± 0.01 per carbon atom was determined for these alkanethiol bilayer junctions. Significantly, for bilayer junctions incorporating CD layers, the tunnelling current depends markedly on the nature of the CD guest. Junctions where nonconjugated guests, such as 1-adamantylamine, were included in the CD showed an order of magnitude lower current than junctions incorporating the conjugated guest C_{60}. Moreover, monolayer junctions of CD backfilled with 1-nonanethiol exhibited potential-dependent currents in the presence of CD guest molecule $[Co(biptpy)_2]^{2+}$ but not for $[Co(tpy)_2]^{2+}$, which is structurally analogous but cannot associate with CD. The effect of electrode displacement on these potential dependent currents indicated a redox cycling or electron hopping mechanism of electron transport.

Fibrinogen has been adsorbed at planar and 820 nm nano-cavity gold surfaces. AC voltammetry showed that the capacitance values of electrodes exposed to fibrinogen solutions overnight were lower, by 30 ± 5 μF.cm^{-2}, than those seen at bare gold electrodes. AFM of the protein at the planar surfaces showed a fibrous network of adsorbed protein. Oregon Green labelled fibrinogen layers were imaged using fluorescence microscopy at both the planar and nano-cavity surfaces. The effect of electrode potential on the fibrinogen layer was investigated. It was found that the protein desorbed at a potential of -1.2 V. The rate of this desorption process was investigated by capacitance studies, which showed a two stage desorption process from the planar surface, where $k_1 = 0.400 \pm 0.065$ s^{-1} and $k_2 = 0.011 \pm 0.001$ s^{-1}. The desorbed protein was collected in solution and UV-visible spectroscopy studies showed that 6.3 x 10^{-13} mol.cm^{-2} of protein is desorbed. SDS-PAGE gel electrophoresis studies showed that the desorbed protein was fragmented by the adsorption-desorption process. Selective modification of the nano-cavity arrays resulted in localisation of the protein predominately inside the nano-cavities. The desorption of the dye labelled protein was investigated using fluorescence microscopy at both the planar and nano-cavity surfaces. The diffusion of the protein out of the confocal laser volume was seen to be slower at the nano-cavity surfaces, compared to the planar surface, indicating that the exit of the protein from the cavities is a rate limiting step. An increase in the fluorescence signal was observed at the nano-cavity surface and an enhancement factor of 500 is estimated.

Glossary of Acronyms

Acronym	–	**Explanation**
A	–	Area
ACN	–	Acetonitrile
AFM	–	Atomic force microscopy
C	–	Concentration
CD	–	Cyclodextrin
γ-CD-(py)$_2$	–	di-6^A,6^B$-$deoxy$-$6$-$(4$-$pyridyl$-$methyl)amino $\gamma-$cyclodextrin
C$_{dl}$	–	Double layer capacitance
$[Co(biptpy)_2]^{2+}$	–	Cobalt bisdiphenylterpyridine
$[Co(tpy)_2]^{2+}$	–	Cobalt terpyridine
CV	–	Cyclic voltammetry
D	–	Diffusion co-efficient
DMF	–	N,N-dimethylformamide
DNA	–	Deoxyribonucleic acid
E$^{0'}$	–	Standard potential of a half reaction
EIS	–	Electrochemical impedance spectroscopy
F	–	Faraday constant
h	–	Planck constant
$\hbar$	–	h/2π
i	–	Current
i-d	–	Current-distance
i-V	–	Current-voltage
J	–	Flux
k^0	–	Standard electron transfer rate constant
K$_{ass}$	–	Association constant
M-I-M	–	Metal insulator metal
n	–	Number of electrons
OCP	–	Open circuit potential
PBS	–	Phosphate buffered saline
PZC	–	Potential of zero charge
Q	–	Charge
R	–	Gas constant
r	–	Radius
SAM	–	Self assembled monolayer

SECM – Scanning electrochemical microscopy
SEM – Scanning electron microscopy
SERS – Surface enhanced Raman spectroscopy
SPR – Surface plasmon resonance
STM – Scanning tunnelling microscopy
T – Temperature
$TBABF_4$ – Tetrabutylammonium tetrafluoroborate
THF – Tetrahydrofuran
Z – Impedance
α – transfer co-efficient
β – Tunnelling co-efficient
Γ – Surface coverage
ΔE – Magnitude of potential step
ΔE_p – Peak separation
ΔG_{ads} – Free energy of adsorption
δ – Diffusion layer thickness
ϵ – dielectric constant
ε_0 – Vacuum permittivity
η – Overpotential
θ – Fractional surface coverage
λ – Wavelength
υ – Scan rate

Publications and presentations

Mallon, C.T., Forster, R.J., McNally, A., Campagnoli, E., Pikramenou, Z., Keyes, T.E., 'Surface-Immobilized Pyridine-Functionalized γ-Cyclodextrin: Alkanethiol Co-adsorption-Induced Reorientation', *Langmuir*, (2007), **23**, 6997.

Mallon, C.T., McNally, A., Keyes, T.E., Forster, R.J., 'Mercury-Platinum Tunneling Junctions Incorporating Supramolecular Host-Guest Assemblies', *Journal of the American Chemical Society*, (2008), **130**, 10002.

234th American Chemical Society National Meeting and Exposition, August 19-23, 2007, Boston, MA. *Oral presentation*: 'Hg-Pt tunneling junctions using cyclodextrins complexes as electron mediators.'

5th Spring Meeting of the International Society of Electrochemistry, May 1-4, 2007, Dublin, Ireland. *Poster presentation*: 'Surface immobilised cyclodextrins: Molecular recognition at interfaces.'

4th ECHEMS Meeting, June 25-28, 2008, Brest, France. *Poster presentation*: 'Molecular junctions incorporating supramolecular host-guest chemistry.'

Chapter 1

Literature survey

1.1 Introduction

The study of electrodes modified with molecular layers is important in many domains of science and there are many motivations for creating modified electrodes. These include the creation of practical devices, such as sensors,[1,2] but also the creation of systems capable of testing theory.[3,4] Self-assembly techniques can be used to aid in the formation of molecular layers, leading to the possibility of mimicking the behavior of biological interfaces.[5] Molecular layers assembled at electrodes have also been suggested for the fabrication of nano-devices, some of which have already been successfully created,[6] that could replace the solid-state transistor.[7] This is an attractive prospect for those facing the 'silicon wall'. This thesis focuses on three aspects of electrode modification.

Cyclodextrin (CD) monolayers are convenient and promising platforms for applications such as molecular wire construction and sensing.[2,8,9] This is because of the extensive host-guest chemistry exhibited by cyclodextrins,[10] which is crucial for the development of molecular recognition platforms. The development of CD monolayers as functional surfaces depends on several key issues, such as the CD monolayer's structural, electrochemical and spectroscopic properties.

The use of metal-monolayer-metal junctions is of fundamental interest for many reasons. The ability of molecules to transmit electrons (efficiently or not) or to display negative differential resistance may allow them to replace modern day components, such as transistors or resisters.[7,11,12] Large synthetic effort is needed to create suitable devices, but host-guest supramolecular chemistry could provide a synthetically simpler route to these compounds. A strategic objective of this approach is the demonstration of non-covalent interactions in a molecular junction.

The adsorption of proteins at interfaces is an important area of investigation which has implications for several fields, such as medicine (biological implants and surgical equipment) or the food industry (fouling of equipment).[13,14] However, while much work has gone into probing the adsorption kinetics of proteins at interfaces, the desorption kinetics remain relatively unexplored. The release of a large amount of adsorbed protein into solution by electrochemical means is attractive as this would provide greater control over molecular location. This may also be a useful decontamination procedure.

The thesis is divided into several sections. Chapter 1 is a survey of the relevant literature. The concepts of electrode modification are introduced along with examples of CD monolayers. Metal-monolayer-metal junctions are reviewed and some theory on electron tunnelling is presented. The modification of surfaces with proteins is surveyed and the creation of nano-structured surfaces is briefly summarised. Finally, the theory behind the major techniques used in the course of this work is described.

Chapter 2 outlines the methods and procedures for both preparing and cleaning the various substrates used in the course of this work. In particular, the procedures for fabricating electrodes, micro-electrodes and nano-cavity arrays are described. The origin of all the non-commercially available compounds that are used in this work is described.

Chapter 3 deals with the modification of electrodes with cyclodextrins (CDs). The co-adsorption of alkanethiol molecules with CDs is presented and the influence of this process on the binding of a redox active cavity guest is explored. The thermodynamics of this binding are investigated and the rate of the electron transfer from the guest to the electrode is estimated.

Chapter 4 describes the creation of mercury-platinum tunnelling junctions. These novel junctions are characterised using alkanethiol monolayers, but the use of CD monolayers in the junction, and the influence of the cavity guest, is also presented. A redox active junction incorporating a CD monolayer with a transition metal complex is described.

Chapter 5 presents a study of fibrinogen adsorption at gold electrodes. The layers are characterised using techniques such as fluorescence microscopy and atomic force microscopy. An adsorption model that takes into account the spreading of the protein over time is presented. The influence of electrochemical potential on the layer is probed and the desorption kinetics are investigated.

Finally, Chapter 6 outlines the use of nano-cavity arrays as substrates for fibrinogen adsorption. The selective modification of the cavities is described and the localisation of the protein inside the cavity is demonstrated. The effect of potential on the fluorescence signal from a dye-labelled protein is described and the fluorescence enhancement factor is estimated.

1.2 Electrode Modification

1.2.1 The Double Layer structure

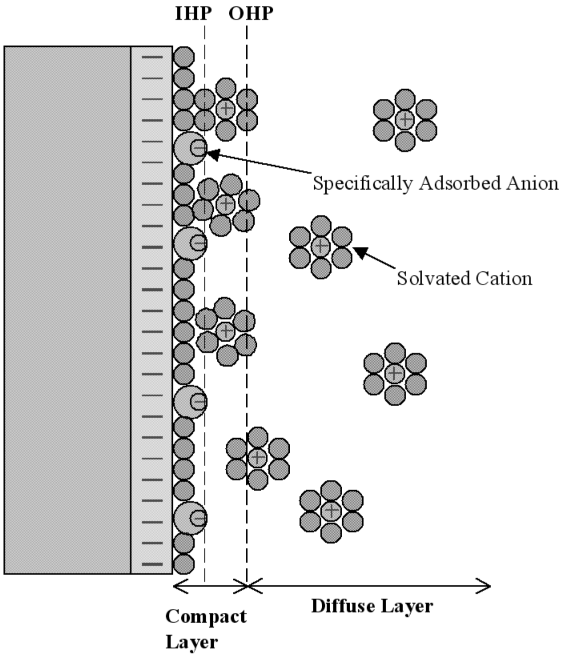

Fig. 1.1: Representation of the double layer structure showing the inner Helmholtz plane (IHP), outer Helmholtz plane (OHP) and the diffuse layer. Adapted from Farrell.[15]

As the modification of electrodes occurs at the electrode-solution interface it is necessary to describe the characteristics of this interface to determine the effects that modification has on it's structure. Electrodes are normally efficient conductors (i.e. they do not support electric fields within their bulk) and excess charge resides at the electrode surface only.[16] The electro-neutrality principle demands that this charge is balanced by ions in the solution. Helmholtz proposed that this counter charge is also located at the interface. This creates two "sheets" of charge separated by the interface; a situation analogous to that of a capacitor. The capacitance across the interface can therefore be modelled by Equation 1.1:

$$C = \frac{(\epsilon\varepsilon_0)}{d} \tag{1.1}$$

where ϵ is the dielectric constant of the insulating medium, ε_0 is the vacuum permittivity and d is the distance between the separated charges. This equation predicts that the capacitance is a constant but experimental data indicate that both potential and electrolyte concentration influence the interfacial capacitance. Further models have considered the distance separating the charges, d, in Equation 1.1, as a function of these parameters.

The deviation from the behavior observed for a pure capacitor arises as the charge on the solution side of the interface occupies a finite and variable thickness. In dilute electrolytic solutions this thickness may be large, but is counterbalanced by thermal processes that act to randomise the ions. This suggests that the charge in the solution phase is greatest at the interface, where the electrostatic forces are greatest, but progressively less charge is observed further from the electrode. Gouy and Chapman proposed that the region adjacent to the electrode is composed of a tightly bound inner layer and a more loosely bound diffuse outer layer.[16] The inner layer can be divided into the inner Helmholtz plane comprising of specifically adsorbed ions and solvent molecules and the outer Helmholtz layer containing solvated ions. The diffuse layer is considered to start beyond the outer Helmholtz plane and extends into the bulk solution, to a distance that depends on the electrolytic concentration (approximately 1 nm for electrolyte concentrations of 0.1 M[16]). This dependence arises from the compression of the layer at higher electrolytic concentrations. However, the diffuse layer is also influenced by the electrode potential. The electrostatic forces become greater as the electrode charge increases, leading to a more compact diffuse layer. Figure 1.1 shows a representation of the double layer as described showing the inner and outer Helmholtz planes within the compact inner layer and the diffuse layer.

The theory proposed by Gouy and Chapman predicted a capacitance minimum at the potential of zero charge (PZC) of the electrode and this is in agreement with experimental observations. However, this model predicts that the capacitance rises continuously as the electrode potential is moved away from the PZC and this is not observed experimentally. This led to a further refinement of the double layer model, proposed by Stern, which takes into account the finite size of ions. The capacitance rises when the potential is moved away from the PZC, but then levels due to the restriction of the finite size of the ions. Stern's model divides the capacitance into two components; the capacitance of the diffuse layer, C_D, and the capacitance of the tightly bound ions (i.e. the inner and outer Helmholtz layers), C_H. The overall capacitance C_{dl} is the sum of these components. Near the PZC C_{dl} is dominated by C_D and a minimum is observed. However, C_H dominates at potentials far from the PZC, and is approximately independent of potential, which causes a levelling of the capacitance in this region. This region, where the capacitance is independent of the potential of the electrode, is sometimes referred to as the Helmholtz region.

1.2.2 Alkanethiol layers on electrodes

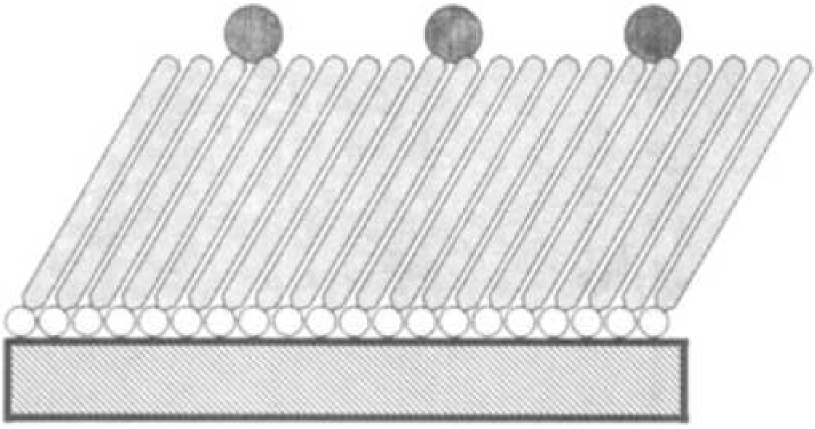

Fig. 1.2: Self-assembled monolayer of alkanethiols on an metal surface with attached redox centers. Adapted from Finklea et al.[4]

Alkanethiols have been used as electrode modifiers for more than two decades.[17] It is generally agreed that the molecule is chemisorbed through the sulfur atom with the loss of the hydrogen[18] although some experimental[19] and theoretical[20] evidence suggests otherwise. Lateral interactions, such as van de Waals forces, can be established between alkanethiols leading to the formation of well ordered blocking films. The sulphur-gold bond energy[5] is approximately 100 kJ.mol^{-1}, and the additional energy gained by lateral interactions is up to 4 kJ.mol^{-1} per methylene group.[21] Figure 1.2 shows a highly ordered alkanethiol layer adsorbed on a metal substrate. One of the most compelling motivations for using alkanethiols is that they self-assembled on metals commonly used as electrodes e.g. gold, silver and platinum. This allows the electrochemistry of the self-assembled monolayer (SAM) to be easily studied and several applications have been developed for both unsubstituted and substituted alkanethiols such as corrosion inhibition,[22] selective recognition of ions,[1] the experimental basis of current electron transfer theory[3,4] or microelectrode array assembly.[23]

The interaction of alkanethiols with other adsorbed molecules has been recognised as an important area for several years. Chidsey and co-workers used unsubstituted alkanethiols to dilute ferrocene terminated alkanethiols so that the ferrocene head groups do not interact.[3] It has been reported that the co-adsorption process also influences the orientation of the ferrocene head group.[24] Furthermore, co-adsorption of alkanethiol molecules with other adsorbates such as DNA and viologen has been shown to result in re-orientation of the initial adsorbate in several studies. Yokoyama[25] and co-workers have used alkanethiol co-adsorption to orientate DNA, so that it stands perpendicular to the metal surface and Vilker and co-workers[26] have performed similar experiments using viologen. The viologen adsorbs with the pyridine rings parallel to the electrode surface, but when co-adsorbed with alkanethiols orientates perpendicular to the surface, as determined using surface enhanced Raman spectroscopy.

An advantage of alkanethiol layers is their ability to form almost defect free layers on metals (especially mercury,[27] but also gold[28] and platinum[29]). By varying the length scale of the alkanethiol the thickness of the layer can be controlled and this is an advantage when investigating the distance dependence of electron tunnelling. Majda and co-workers have investigated the influence of various alkanethiol monolayers on mercury and have found an exponential decrease in the current with monolayer thickness.[30] Similar results have been obtained for attached redox centers such as ferrocene.[4,31] Alkanethiol type layers have also found extensive use in the field of protein adsorption, where the ability to change the polarity of a surface is beneficial.[32]

1.2.3 Monolayers using pyridine surface linkers

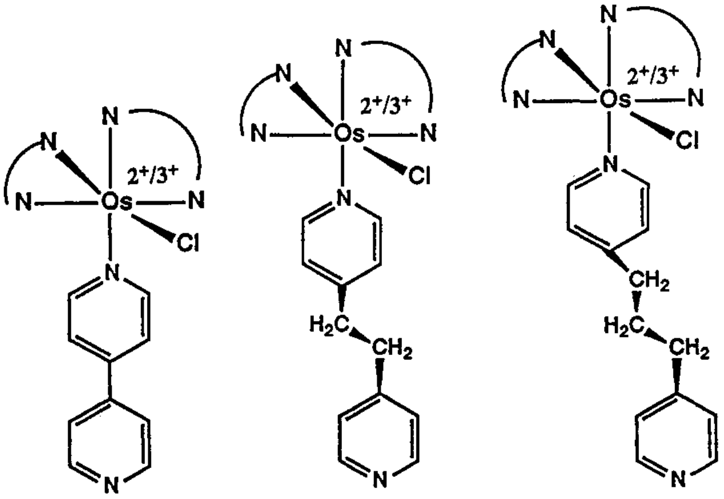

Fig. 1.3: Structure of Osmium complexes used in Forster's and Faulkner's study on electron transfer dynamics. Adapted from reference 33.

It has long been known that pyridine is capable of adsorbing on several metal surfaces.[33] The interaction with the metal surface is normally through the nitrogen atom, but the planar ring can also interact. In 1974 the phenomenon of surface enhanced Raman spectroscopy was reported for pyridine adsorbed on roughened silver.[34] However, platinum is also a common substrate for pyridine adsorption and has advantages over other substrates, e.g. wide potential window in non-aqueous solvents.[35] Ruthenium or osmium complexes with high redox potentials functionalised with pyridine moieties can be easily studied. For example, Forster and Faulkner have used pyridine linkers to immobilise osmium complexes (structures seen in Figure 1.3) on microelectrodes to probe the effect of solvent, temperature and potential on the electron transfer dynamics.[36,37] The electrochemistry of the adsorbed layers was found to be almost ideal. The electron transfer was reported to be a through space event, which was strongly dependent on solvent. The influence of pH on this electron transfer was also investigated and it was found that protonation reduced the rate of electron transfer, possibly by increasing the distance from the redox center to the electrode.[38]

More recently, Qbpy (2,2':4,4":4'4"- quarterpyridyl) has been explored as a surface binding group on platinum.[39,40] Monolayers of both osmium and ruthenium complexes with Qbpy ligands have been shown to exhibit near-ideal electrochemistry. The adsorption dynamics have been probed and were found to follow the Frumkin isotherm and a time dependent surface orientation was suggested by changes in the Raman spectra and electron transfer rates. Other Raman studies have suggested that pyridine adsorbed at platinum electrodes can undergo potential induced reorientation.[41] This body of work shows that pyridine is a useful surface binding group, especially on platinum electrodes and that it can re-orientate in response to certain conditions such as potential or adsorption time.

1.3 Cyclodextrins in supramolecular chemistry

1.3.1 Introduction to cyclodextrins

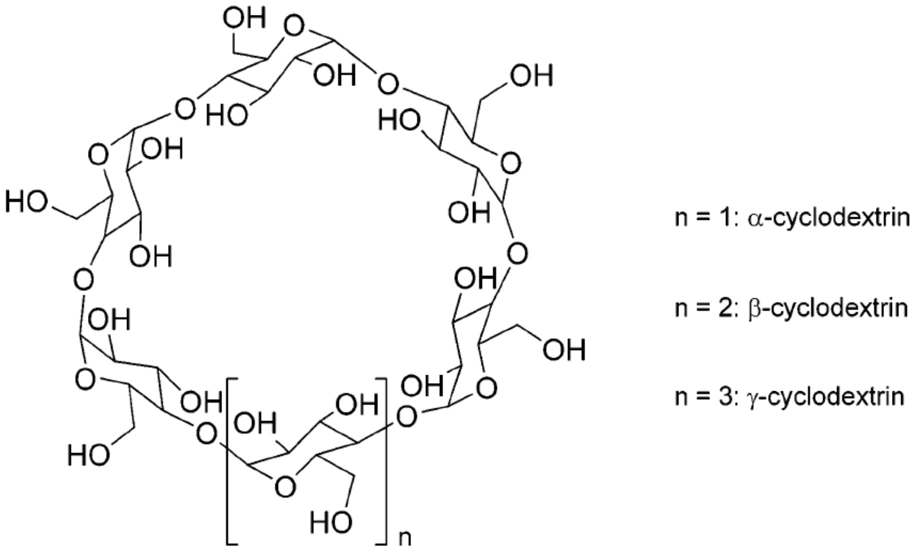

Fig. 1.4: Molecular structure of β-CD. Adapted from reference 51.

Cyclodextrins (CDs) are a family of compounds containing three major, and several rare, cyclic oligosaccharides.[42] The three major CDs are α-CD, β-CD and γ-CD, which are comprised of six, seven and eight glucopyranose units respectively. The structure of β-CD is shown in Figure 1.4. These units are linked together via glycosidic oxygen bridges and together they give the CD a torus-like structure with a cavity of varying size depending on the number of glucopyranose units. These oxygen bridges make the interior of the cavity hydrophobic while the presence of hydroxyl groups at the cavity openings make the exterior of the molecules hydrophillic. The cavity openings are not identical; the wider opening (primary face) has hydroxyl groups from the C-2 and C-3 of the sugar while the smaller opening (secondary face) is populated by hydroxyl groups from the C-6.

The three major CDs have different cavity dimensions as a consequence of greater or lesser numbers of glucopyranose units. The cavity opening at the primary face is 5.7, 7.8 and 9.5 $\AA$ in diameter for α-CD, β-CD and γ-CD respectively, whereas the height of each CD is approximately identical at 7.8 $\AA$.

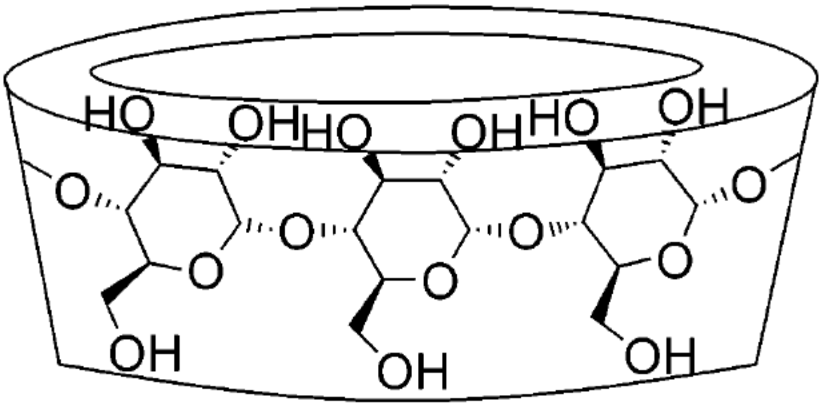

Fig. 1.5: Glucopyranose units that make up the structure of the CD cavity. Adapted from reference 51.

Cyclodextrins have long been shown to form inclusion complexes with organic molecules and have found several applications in commercially important fields such as drug delivery,[43] analytical chemistry[44] and mediation of chemical reactions.[45] As a consequence of this there has been significant efforts made to develop modification procedures for CDs.[46]

By far the most useful and studied aspect of cyclodextrins is their ability to form inclusion complexes with guest molecules (G). This dynamic process is subject to an equilibrium constant which describes the following reaction in solution:

$$CD_{sol} + G_{sol} = CD - G_{sol} \tag{1.2}$$

The association (or formation) constant, K_{ass} can be written as:

$$K_{ass} = \frac{[CD - G]_{sol}}{[CD]_{sol} . [G]_{sol}} \tag{1.3}$$

The binding forces involved in complex formation are thought to include hydrophilic (or van de Waals) interactions between the guest and the CD cavity, hydrogen bonding between the hydroxyl groups of the cyclodextrin and polar moieties of the guest, release of high energy water molecules from the CD cavity and release of ring strain energy in the CD. The exact nature of the driving force for complexation is often difficult to determine as several of these effects can be present in any given system.[47] Clearly, polarity of the guest and solvent system are critical in complexation, as is the size of the guest. In general only molecules less polar than water can include and the size of the cavity and guest must match to create a fully included complex, although complexes can be formed without complete encapsulation of the guest. Much work has been devoted to the determination of the association constants of the three common CDs with various organic guests.[48, 10, 49] The binding strength is variable, but for suitable compounds the free energy of complexation can be of the order of -28 kJ.mol^{-1}.

1.3.2 Cyclodextrins as supramolecular hosts

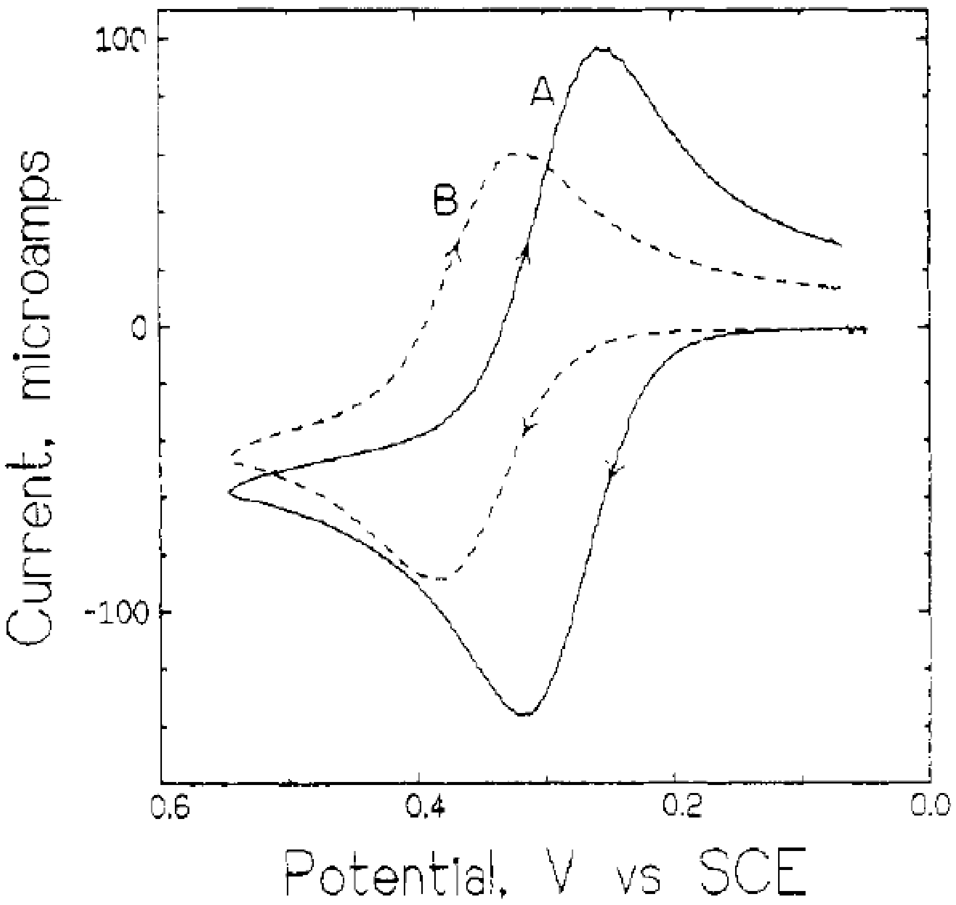

Fig. 1.6: Voltammetric response of ferrocenecarboxylic acid in the absence (A) and presence of β-CD (B). Adapted from Osa et al.[50]

The ability to form inclusion complexes with guest molecules makes cyclodextrins attractive building blocks in supramolecular systems and this aspect of CD chemistry is treated in several reviews.[9, 52, 53, 54, 8] Several groups have shown that metal complexes can include in CD cavities[54] and ferrocene is by far the most commonly studied guest in this category. The CD can associate with a metal complex in several ways but the most common association is where the CD acts as a second sphere ligand by non-covalently binding one of the first sphere ligands of the metal center.

The effect of changing the redox properties of the guest either to facilitate or impede inclusion is of particular interest. In 1985 Osa and co-workers re-

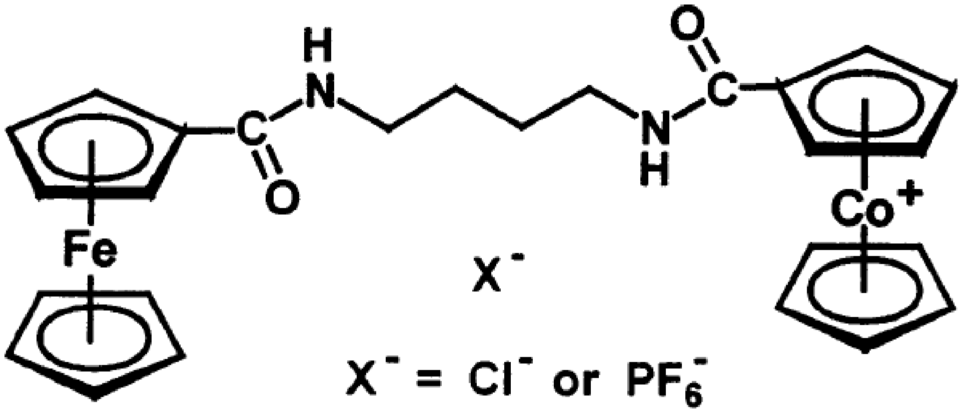

Fig. 1.7: Structure of one of the organometallic complexes studied by Kaifer[51] having two binding sites for cyclodextrins. The binding can be controlled by changing the redox state of the metals. Adapted from Kaifer et al.[51]

ported on the inclusion of ferrocenecarboxylic acid in β-CD.[50] A positive shift in peak potential was observed for ferrocene in the presence of the cyclodextrin (see Figure 1.6), while the suppression of the peak currents was attributed to a slower diffusion constant for the included molecule. The positive shift indicates that the compound is harder to oxidise, which is attributable to the stable CD-ferrocene interaction. The inclusion constant was calculated as 2200 M^{-1} for this system using cyclic voltammetry. No evidence was found to suggest that the oxidised form of the ferrocene could form inclusion complexes, based on theoretical simulations. The variation of the peak current with scan rate suggested that the ferrocene dissociates from the CD before electron transfer occurs. This was reflected in a reduction of peak current for the oxidation of ferrocene at high scan rates, which suggests the presence of a rate determining chemical step. Significantly, as the ferrocene carboxylic acid is de-protonated throughout the study, the work demonstrates the possibility of including charged guests provided the charge is located away from the binding moiety. Similar results are described for interaction of viologens and cobaltocenium with CD cavities.[53]

Kaifer and co-workers have synthesized a molecule with two binding sites, both of which are electrochemically addressable[51] (see Figure 1.7). Positive shifts are observed in the CVs for each site, when in the neutral state, in the presence of β-CD in solution. This again indicates that the ferrocene or cobaltocenium can include in the CD cavity when in the neutral state. Changing the redox states of each metal center can therefore promote or inhibit inclusion at that center. However, the mechanism of oxidising an included guest is not clear.

1.4 Monolayers incorporating cyclodextrins

1.4.1 α/β-CD monolayers

A key objective of electrode modification is the incorporation of host-guest interactions into monolayers.[55] This is due to the potential of such layers as supramolecular systems or sensors. Calixarenes are oligophenols linked in a cyclic array by methylene bridges and they show sensitivity to a variety of ions.[56] These molecules were incorporated into polymeric membranes to create ion selective electrodes in the late 1980s.[57] The parallel development of self-assembly techniques led to the creation of self-assembling molecules based on calixarenes for molecular recognition purposes. Reinhoudt reported a resorcin[4]arene monolayer using alkanethiol linkers to a gold surface in 1994.[58] The resorcin[4]arene contained four surface binding sulphur atoms and monolayer formation at elevated temperatures was required to create ordered layers.

This early work on calixarene SAMs was soon followed by the development of CD based SAMs. Due to their stability, low cost and molecular recognition properties, a large body of work has been reported on immobilised CDs at interfaces. Osa and co-workers published a series of papers[59,60] which dealt mainly with α-CD bound covalently to graphite electrodes which were used to modify the chemistry of included guests, e.g. the chlorination of toluene via the formation of a toluene-CD complex at the interface.[59] However, the cyclodextrins were bound to the electrode surface via a synthetic procedure, i.e. there were no surface active groups on the CD.

Langmuir-Blodgett techniques were used to create cyclodextrin monolayers at the air-water interface by Odashima and co-workers.[61] These layers were found to be permeable channels into which appropriately sized analytes could pass, as determined by horizontal touch cyclic voltammetry.

Monolayers incorporating cyclodextrins were first described by Kaifer and co-workers in 1995 in a now seminal publication.[62] Kaifer described the synthesis of a β-CD completely thiolated at the secondary face and its adsorption onto gold electrodes. Reductive desorption experiments indicated that the surface coverage of this molecule was approximately 64-75% of that expected for a close packed hexagonal monolayer and so sealed or "backfilled" the defects on the surface with a short chain alkanethiol. To avoid sealing the cavity openings with the alkanethiol a known cavity guest (ferrocene) was present in the sealing solution to block alkanethiol adsorption at these sites. Capacitance and blocking experiments revealed that the backfilled layer had a greater defect density (attributable to the CD cavities) than a pure alkanethiol layer, demonstrating the success of the backfilling process. Co-adsorption of alkanethiols has also been used to seal defects in CD monolayers by several other groups.[63, 64] These layers were then used to detect ferrocene in aqueous solutions up to concentrations of 60 μM. The peak currents scaled linearly with scan rate, which is consistent with a surface bound redox signal and the surface coverage was found to vary with the bulk concentration of ferrocene according to the Langmuir isotherm. This isotherm revealed saturation surface coverage of 2.5 x 10^{-11} mol.cm^{-1} and an adsorption co-efficient, β, of 3.9 x 10^{4} M^{-1}.

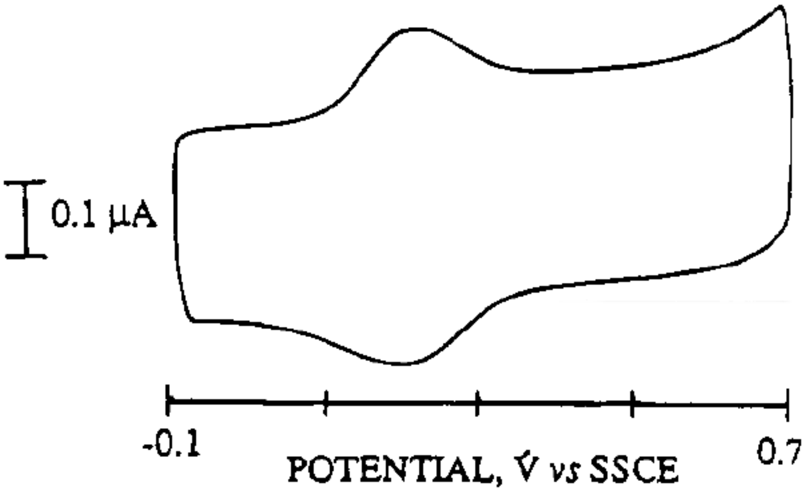

Fig. 1.8: Cyclic voltammogram of 5 μM ferrocene in water with 0.2 M Na_2SO_4 as the supporting electrolyte at Kaifers backfilled electrode. Adapted from Kaifer et al.[62]

Monolayers incorporating CDs are capable of forming inclusion complexes with suitable guests that are in solution. Equation 1.2 therefore becomes:

$$CD_{surface} + G_{sol} = CD - G_{surface} \tag{1.4}$$

and the K_{ass} becomes:

$$K_{ass} = \frac{[CD - G]_{surface}}{[CD]_{surface} \cdot [G]_{sol}} \tag{1.5}$$

The adsorption co-efficient found from the Langmuir isotherm can be related to the free energy of adsorption, ΔG_{ads}, which in turn can be related to the equilibrium constant of the adsorption, K_{eq} (or K_{ass});

$$-RTln\beta = \Delta G_{ads} = -RTlnK_{ass} \tag{1.6}$$

The adsorption co-efficient, β, can therefore be compared to the equilibrium constants determined in solution for the same systems. Kaifer found that the interfacial binding constant was higher by an order of magnitude than the solution phase value for ferrocene inclusion. This result is unexpected as the immobilisation of the CD reduces it's mobility and the reasons behind this phenomenon are still unclear. However, it has been observed in several other CD monolayer studies described below.

Kaifer's report was followed by a large body of work from different research groups on monolayers incorporating either α or β-CDs. Weisser and co-workers reported several thiolated β-CDs in a series of publications. The film characteristics were investigated using Fourier transform infrared (FTIR) spectroscopy, time-of-flight mass spectrometry, contact angle measurements, plasmon surface polariton (PSP) spectroscopy, and cyclic voltammetry.[66] The kinetics of adsorption were investigated and found to follow the Elovich kinetic isotherm for the chemisorption step.[65] Finally, the inclusion of guest molecules into the layers was described and backfilling experiments were also used to seal defective areas in the films.[67] Perhaps the most interesting aspect of this work was

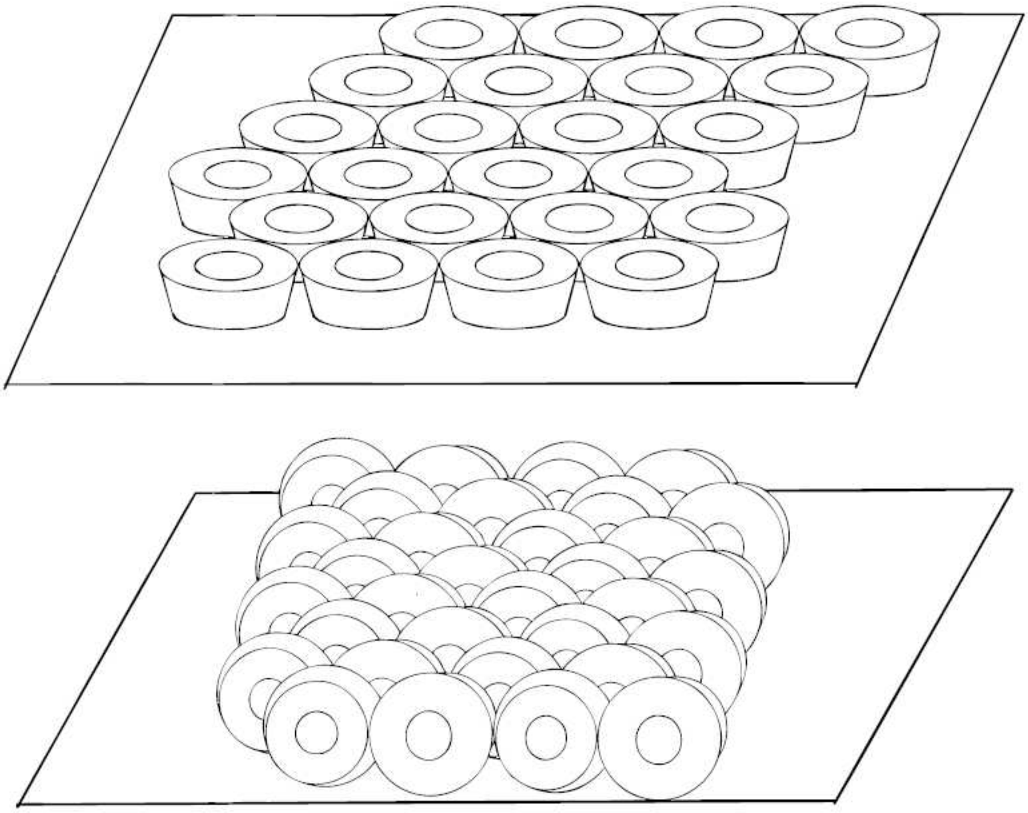

Fig. 1.9: Models for packing of CDs in molecular films; hexagonal close packed (top) and brick packed (bottom). Adapted from Weisser et al.[65]

the consideration of different CD orientations in the layers such as hexagonal close packed or "brick packed" models (see Figure 1.9). It was suggested that the brick packed conformation was due to H-bonding between CD molecules in the monolayer.

Kitano and co-workers have investigated several CD derivatives immobilised on metal surfaces from 1995 onwards.[69, 70, 71] Some of the early work used Raman spectroscopy to monitor the inclusion of guest molecules and this is treated in section 1.4.3. Several publications[72, 73, 68] deal with the selective inclusion (either regio or stereo) of guests such as methyl red and phthalic acid ester derivatives at gold surfaces modified with a thiolated α-CD and hydroquinone as an electroactive probe (see Figure 1.10). Comparisons between K_{ass} for both the free and surface bound systems were made in each case but no general trend was found. While massive increases of up to five orders of magnitude

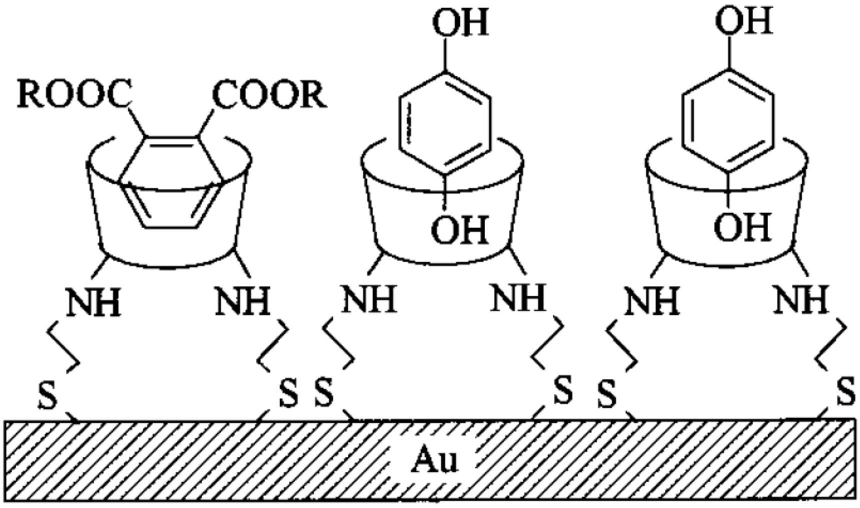

Fig. 1.10: Model of hydroquinone and phthalic ester acid inclusion in cyclodextrin assembly on gold. Adapted from Kitano et al.[68]

were observed in K_{ass} for some of the surface bound systems compared to free systems,[72] decreases were also noted.[73] Kitano has made attempts to rationalise these observations by determining the entropy (ΔS) and enthalpy (ΔH) components of the driving force for inclusion (ΔG) by studying the temperature dependence of K_{ass}. It was found that the entropic contribution to the driving force for complexation was much greater than in solution.[68] The reason for this surprising conclusion was not clear.

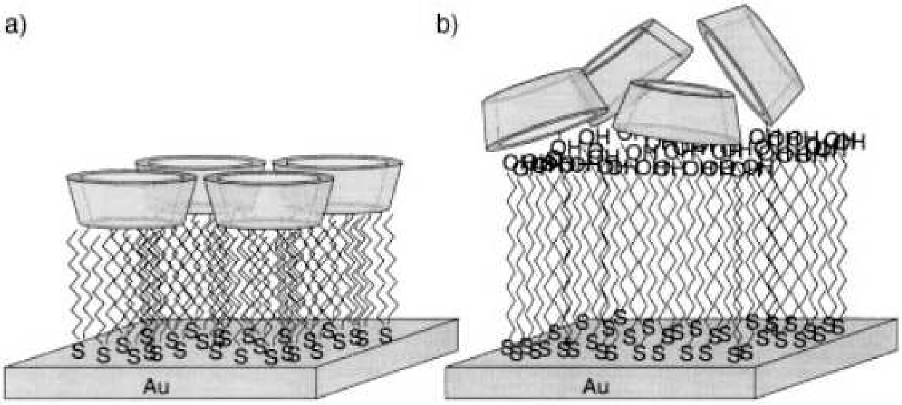

Fig. 1.11: Layer architecture of the SAMs studied by Reinhoudt; (a) Space under CD filled by multiple attachment points and (b) space under CD filled by co-adsorption of alkanethiols. Adapted from Reinhoudt et al.[74]

Reinhoudt and Huskens and co-workers have developed strategies for the creation of ordered, tightly packed monolayers of CDs on gold which are investigated using a variety of techniques such as electrochemistry, wettability studies, X-ray photoelectron spectroscopy, (XPS), time-of-flight secondary ion mass spectrometry, (TOF-SIMS), and atomic force microscopy (AFM). Dialkyl sulfides were used as surface linkers and found to be more effectively adsorbed compared to thiol linkers.[75] AFM images show ordered structures for these β-CD layers on gold and inclusion of 1-anilinonaphtalene-8-sulfonic acid was measured using surface plasmon resonance (SPR) and electrochemical impedance spectroscopy (EIS). The inclusion was modelled using the Langmuir isotherm, yielding a K_{ass} of 2×10^6 M^{-1}. Significantly, methylation at the primary face of the CD decreases the order in the AFM images. This has been attributed to the breaking of intermolecular H-bonds between CDs in the layer.[76]

Reinhoudt and Huskens also investigated two different models for filling the space below the CD cavity in the layer.[74] These models are summarised by (a) using multiple dialkyl sulfides as attachment points for the CD which would fill this space (Figure 1.11 (a)) or (b) co-adsorption of alkanethiols with CDs mono-founctionalised with alkanethiol linkers (Figure 1.11 (b)). AFM revealed that the co-adsorption method did not yield domains in the layer and both methods could be used to detect small organic molecules. However, the more flexible CD (i.e. method b) displayed higher association constants for steroids than the rigid CD (method a).

Much work has also been dedicated to the formation of so called "molecular printboards" by Reinhoudt's group which are used to bind adamantyl or ferrocene functionalised dendrimers.[77,78] Molecular printboards are defined as surfaces modified by CD molecules as described above which can bind guest molecules ("ink"). The surfaces can be modified with CDs in a controlled manner to make a pattern where CD guests can then dock. The position of multivalent guests[79] such as dendrimers and polymers[80] can be controlled and have been imaged using SECM,[81] AFM[82] and STM.[83] Attachment of proteins to the CD monolayers has also been reported.[84,85,86] One of the interesting conclusions of this work is that the ferrocene dendrimers do not associate with the layers after oxidation of the ferrocene to ferrocenium, as evidenced by SPR combined with CV.[87] This is consistent with the work of Osa and co-workers for the solution phase CD-ferrocene interaction previously described.[50]

Galla and co-workers were also among the first groups to study CD monolayers and their work concentrated on di-sulfide containing β-CDs on gold.[88,89] The di-electric constant of the layers was determined as 20-25 and capacitance values stabilised at 9 μF.cm^{-2}. Electrochemical impedance spectroscopy (EIS) was used to determine fractional surface coverages of greater than 99% and inclusion of guests such as 1-adamantylamino-hydrochloride. However, the amount of cavities occupied by the guests was less than 10% of the available sites in the monolayer despite the high fractional coverage.

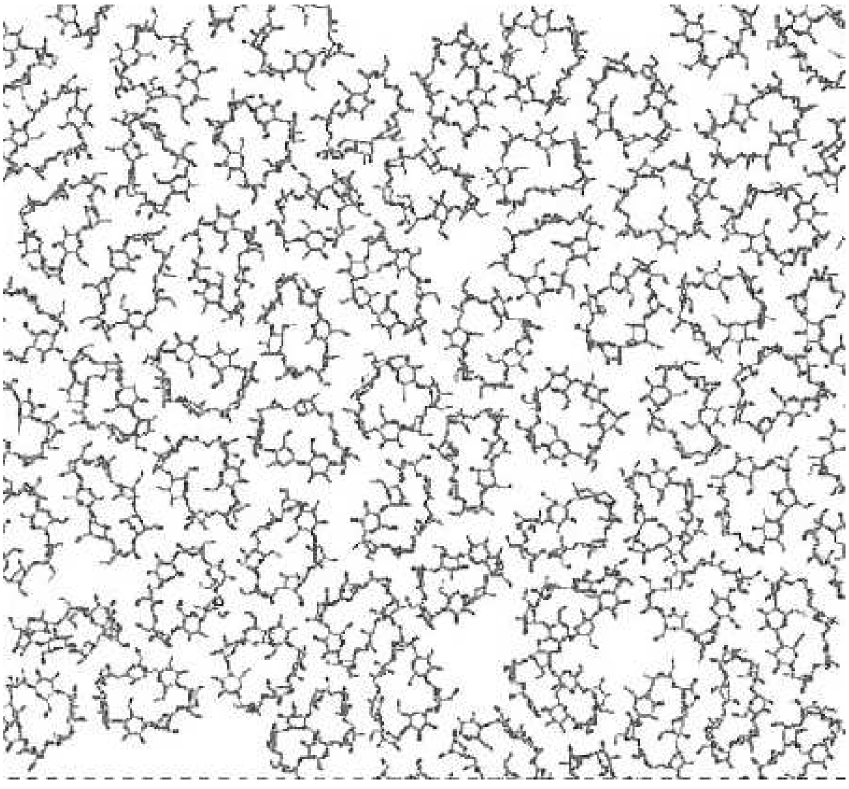

Fig. 1.12: Snapshot (view from the top) of the CD monolayer generated via the random planting algorithm. Adapted from Knoll et al.[90]

Several other CD-monolayer studies have been reported including a computational study of random planting (i.e. random adsorption) of CD derivatives on gold via short and long chain alkanethiol linkers.[90] One weakness in this study was the assumption that the CD cavity orientates parallel to the metal surface at all times but the resulting simulations suggested a layer packed as in Figure 1.12. An interesting conclusion of this work was the suggestion that CDs with long surface binding chains may from a bi-layer type structure.

CDs immobilized onto various surfaces have also been used as sensors by several groups.[91,92,93,94,95] Park and co-workers have described backfilled layers of thiolated α and β CDs on gold which have been used as sensors for molecules such as benzoquinone and glucose.[96,97] A wide variety of surface techniques have been used to investigate CD layers. Quartz crystal microbalance has been employed to study CD layers on gold by Willner.[98] Scanning electrochemical microscopy was used by Bollo and co-workers to investigate the conducting/insulating properties of β-CD monolayers on gold electrodes.[99]

1.4.2 γ-CD monolayers

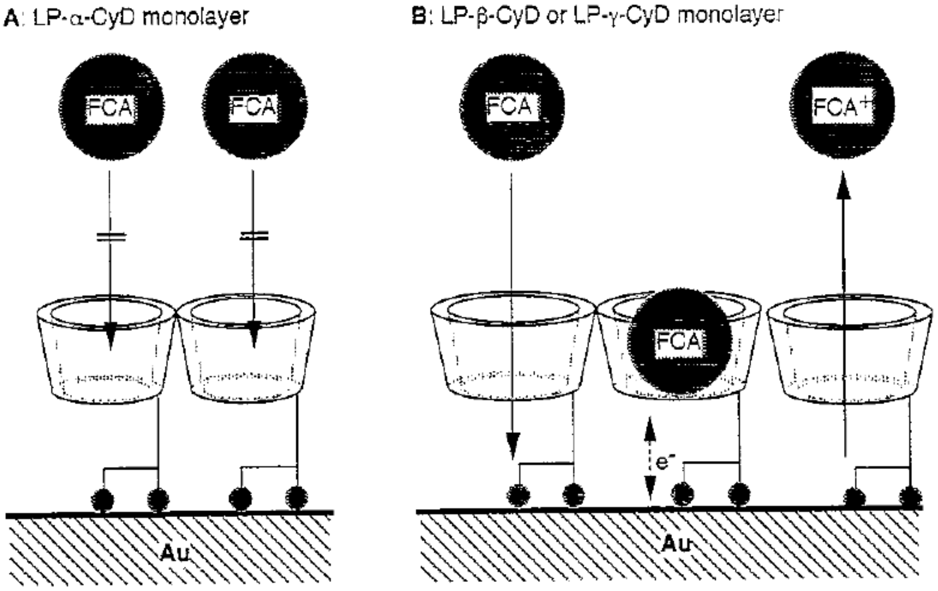

Fig. 1.13: Proposed illustrations for the action of $\alpha/\beta/\gamma$-CD cavities in the LP-CD monolayers in the presence of electrochemically active guest FCA showing the size exclusion properties of the cavities. Adapted from Suzuki et al.[100]

γ-CDs have generally not been studied as widely as α or β-CD. The earliest report of a γ-CD monolayer appeared in 1998 in a contribution by Suzuli and co-workers.[100] This report followed a study of β-CD monolayers by the same group[93] and compared the response of α/β and γ-CDs tethered to a gold surface by a lipoyl group to a solution phase probe, ferrocenecarboxylic acid (FCA). The α-CD layers were shown to inhibit the access of the probe to the electrode surface while the higher order CDs blocked to a lesser extent (see Figure 1.13) presumably due to their larger cavity size. Suzuki followed this work with a study on the positional isomers of a di-substituted γ-CD derivative on gold.[101] Reductive desorption experiments revealed that the surface coverage was lowest for the 6^A, 6^B-isomer at 60% and highest for the 6^A, 6^E-isomer. However, the blocking effects exhibited by the layers towards the solution phase probe $[\mathrm{Fe(CN)_6}]^{4-}$ was highest for the 6^A, 6^B-isomer and the supposed defect free layer comprised of the 6^A, 6^E-isomer displayed only moderate blocking properties. Differences in the response of the layers to FCA in solution suggested differences in cavity orientation between the isomers with the 6^A, 6^E-isomer showing the greatest potential for inclusion. These results clearly show that the differences between layers composed of isomers is significant although no definite trend can be inferred from the data.

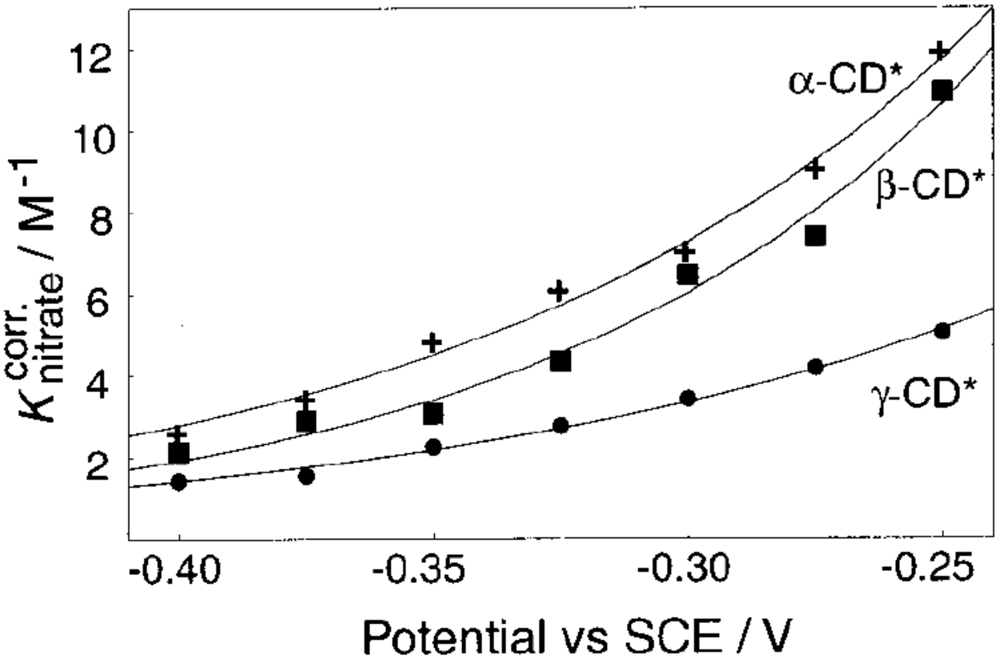

Fig. 1.14: Potential dependence of the nitrate inclusion constant K$_{nitrate}$ for $\alpha/\beta/\gamma$-CD-modified Hg electrodes. The PZC of the modified electrodes was estimated at -0.65V. Adapted from Majda et al.[102]

Majda has created monolayers of permethylated thiolated α/β and γ-CDs on mercury drop electrodes.[102] Inclusion of anions such as NO_3^- and Cl^- was interpreted from an increase in the interfacial capacitance as determined by AC voltammetry. Larger, more hydrophillic ions such as F^- and SO_4^{2-} did not effect the capacitance. However, the inclusion was shown to be almost purely electrostatic in origin, with K$_{ass}$ at the PZC of 0.17 M^{-1} for NO_3^- inclusion at γ-CD layers (see Figure 1.14). This work did reveal the possibility of creating well packed γ-CD monolayers as the surface coverage was determined as 6.8 x 10^{-11} mol.cm^{-2} which is within 5% of the coverage determined at the air-water interface under lateral pressure of 4 mN.m^{-1}. Addition of 1-adamantanol reduces the capacitance observed and has been interpreted as competitive inclusion with the anions. Finally, attempts were made to extend this work to gold electrodes for the β-CD derivative. Reductive desorption revealed lower surface coverage compared to the Hg surface, presumably due to the reduction in lateral mobility experienced by the adsorbates on solid electrodes.

Huskens and co-workers have also extended their work to γ-CD layers.[76] γ-CD was modified with long chain dialkylsulfides and adsorbed at gold electrodes. AFM measurements revealed that these layers were less ordered than β-CD layers. However, parallel lines were observed in the AFM images which can be tentatively attributed to rows of unresolved adsorbates.

1.4.3 Raman studies of CD monolayers

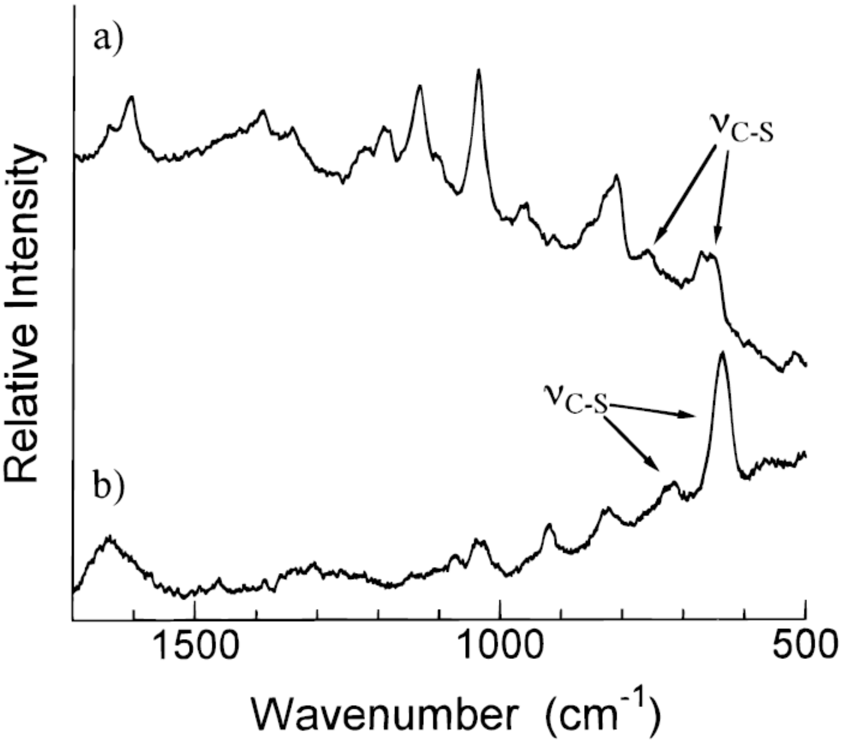

Fig. 1.15: Solid (a) and surface immobilised on colloid silver (b) Raman spectra of thiolated α-CD. Adapted from Kitano et al.[103]

Raman spectroscopy is an attractive technique for the study of monolayers due to the orientational information that can be obtained. Kitano and co-workers have used resonance Raman and SERS in studies of cyclodextrin monolayers. A thiolated β-CD monolayer on silver colloid was described in 1995 and detection of methyl orange (MO) included in the CD cavity by SERRS was suggested.[69] The free CD-MO system showed a decrease in the intensity of characteristic C=C signals and increases in N=N stretches of MO. This pattern was reproduced for the CD SAM in contact with MO which suggests that the MO is complexed in the surface bound CD cavity. In 1997 Kitano reported a thiolated α-CD bound to silver colloid in which solution phase CD-guest and SAM CD-guest interactions were probed using Raman spectroscopy.[103] Figure 1.15 shows the spectra obtained for the solution phase and immobilised CD on silver showing a shift in the C-S stretch in the 600-750 cm^{-1} region. Also the characteristic S-H stretch at approximately 2580 cm^{-1} disappeared upon surface adsorption (not shown). A large increase in K_{ass} was found for the SAM systems, which was determined from the relative intensities of the N=N Raman signal, for the inclusion of *p*- or *o*-methyl red conjugates.

Hill and co-workers also used a thiolated β-CD adsorbed on silver slides to detect aromatics in the gas phase using SERS.[104] The kinetics of adsorption were also investigated by monitoring the intensity of the C-S stretch during the adsorption process. Competitive inclusion of methyl orange with aromatics such as toluene and ethylbenzene in the gas phase was detected by SERS. These results show that Raman spectroscopy can be used to characterise both the CD layers and CD inclusion events.

1.5 Metal-insulator-metal junctions

1.5.1 Theoretical treatment of tunnelling

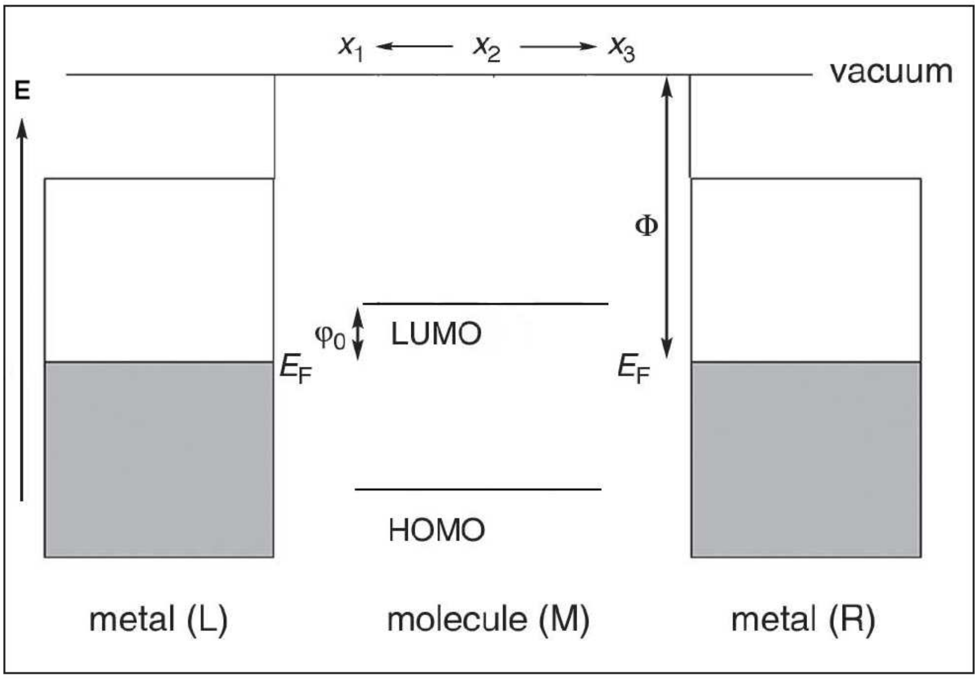

Fig. 1.16: Schematic plot of a M-I-M junction. If the molecule is to have the dominant influence on tunnelling the molecule electrode gaps (points X_1 and X_3) must be significantly smaller than the length of the molecule (distance X_2). The barrier height is clearly reduced by the presence of the LUMO states compared to vacuum. E_F is the fermi energy of the metal, Φ is the metal workfunction and φ_0 is the barrier height when a molecule spans the junction. Adapted from Lindsay.[105]

Conventional one-dimensional electron tunnelling can be modelled as transmission of an electron through a potential step barrier of height V_0 and length d. The electron impinging on the barrier can be described with energy of $E = (\hbar^2 k^2)/2m$, where $\hbar$ is Plank's constant divided by 2π, k is the related to the wavelength of the wavefunction ($k = 2\pi/\lambda$) and m is the mass of an electron. The energy of the electron in the barrier region becomes $V_0 - E = (\hbar^2 \kappa^2)/2m$, where κ is a decay constant and upon passing through the barrier reverts to the initial values although now the amplitude of the wavefunction is changed. The transmission probability through the barrier can be approximated as e$^{-\beta d}$, with the tunnelling co-efficient β equal to the 2κ, or:

$$\beta = 2\sqrt{\frac{2m(V_0 - E)}{\hbar^2}} \tag{1.7}$$

Tunnelling in a vacuum gap between metals is normally described as classical tunnelling and displays a β value of approximately 2.3 $\mathring{A}$. Equation 1.7 predicts that tunnelling depends on the mass of the particle and the height of the energy barrier.

Applying this theory to M-I-M junctions causes some changes to the conventional picture. Firstly, the incident electrons are now at the fermi level, E$_f$, at zero bias voltage. Secondly, the barrier height is lowered as the LUMO of the molecule is in general much lower than the intrinsic vacuum value (see Figure 1.16). Therefore, the barrier becomes E$_{LUMO}$ - E$_f$ at zero bias (or φ_0). Superexchange tunnelling is the term often used to describe the tunnelling mechanisms where the interaction of the electron with the LUMO states of the insulating molecule increases the tunnelling rate. Coherent tunnelling is tunnelling that preserves the phase of electron and is effective over distances of only 25 $\mathring{A}$ but incoherent or diffusive tunnelling can be responsible for tunnelling between greater distances and is responsible for several electron transport events in biological systems such as DNA. Incoherent tunnelling can be thought of as a series of coherent steps between sites on the molecule where the electron remains long enough to disturb its phase.

Applying these considerations to the classical vacuum model of tunnelling means that Equation 1.7 becomes

$$\beta = 2\sqrt{\frac{2m(E_{LUMO} - E_f)}{\hbar^2}} \tag{1.8}$$

The effective mass of an electron m^* is also used instead of m by some groups, to account for the transmission of the electron through the LUMO of the molecules as opposed to through a vacuum. Applying a potential bias across the junction shifts the energies of the electrons away from the Fermi level and so the following relationship is obtained for β:

$$\beta = 2\sqrt{\frac{2m^*(E_{LUMO} - E_f - V/2)}{\hbar^2}} \tag{1.9}$$

This equation predicts that when the bias voltage is equal to twice the barrier height β goes to zero and resonant tunnelling occurs. As the HOMO-LUMO gaps in non-conjugated molecules is of the order of 5-10 eV resonant tunnelling is not often obtained under conventional conditions although the inclusion of redox molecules within junctions offer the possibility of easily accessible states.

Coherent and incoherent tunnelling do not depend on temperature and both show exponential distance dependence. However, other current transport mechanisms can also be present, such as electron hopping. This exhibits temperature dependence and varies with distance as d^{-1}. Electron hopping is accompanied by nuclear motion and can be thought of as a series of electron transfer steps between relatively stable sites.

1.5.2 Molecular junctions

In recent years much attention has been focused on systems which can probe the electronic properties of molecules. The motivation for this research is the creation of electrical components from individual molecules.[7] While many molecules could be envisioned as resisters, those that can display negative differential resistance have attracted much attention, with some success.[106, 107] The possibility of creating a molecular wire has also been explored and research in this area is dominated by some examples of wires[108, 109] and a great deal of fundamental research into the intrinsic nature of electric transport in molecules. Typically, these molecular wire systems are created from donor-bridge-acceptor systems (where the bridge is the molecular 'wire'). Donor-bridge-acceptor systems have been extensively studied in solution,[110] but any potential electrical component would require the development of interfacial donor-acceptor systems. This has led to an interest in the behavior of metal-molecule-metal junctions.

The development of solid state metal-molecule(s)-metal systems has been greatly aided by advances in nanotechnology and scanning probe microscopies. Currently, there are two main methods of determining a molecule's conductivity. In the first of these a scanning probe technique (such as STM or C-AFM) is used in conjunction with a SAM. This scanning probe method facilitates the investigation of a small number of molecules or even a single molecule. The second method involves the close approach of two metals with a mono/bi-layer sandwiched between them. This approach differs from the first in that the number of molecules investigated is much larger (up to 10^{12}) and will be denoted as metal-insulator-metal (M-I-M) junctions. Only studied carried out at room temperature will be reviewed, to allow easy comparison to subsequent results presented in Chapter 4.

Several groups have used STM and conducting atomic force microscopy (C-AFM) to determine molecular conductivity/resistance.[111, 112] Typically, a monolayer of the molecule under investigation is created on an atomically flat substrate, which also acts as one end of the electrical "contact". The STM tip is then used as the other contact by touching the other end of the molecule.

Significant uncertainty about the nature and site of tip contact (with the notable exception of alkanedithiols) has lead to use of C-AFM which allows the amount of force applied to the molecules to be simultaneously measured.[113, 114] The key finding of this work is that the current for all of these systems follows a through-bond tunnelling mechanism, despite the uncertainty regarding the STM tip contact. This conclusion is based on the observation that the tunnelling current, i, can be related to the length of the molecule, (d), by $i \approx exp(-\beta d)$ where β is the tunnelling co-efficient of the molecule. Values of β are generally accepted as $\simeq 1\mathring{A}^{-1}$ for non-conjugated molecules and somewhat lower for conjugated molecules although some variation can be expected due to different methods of contacting the molecules and variation in the amount of through-space tunnelling for each system. An excellent comparison of results from various groups has been provided in a review by Frisbie et al.[115] Single molecule conductivity of hexanedithiol has been determined by, among others, Tao et al. as 10 MΩ by statistical analysis using STM,[116] although it must be stressed that there is wide variation in single molecule conductance values reported.[12, 11]

The investigation of redox molecules by these STM/C-AFM techniques can yield potentially more interesting results due to the presence of accessible redox states in the junction. This can lead to rectification behavior which is a major goal of molecular level electronics.[118, 119] Although research in this field is still in the early stages, Tao reported in 1996 a 10-fold increase in tunnelling current through an Fe-porphyrin complex when the bias voltage was in resonance with the LUMO of the complex.[117] Figure 1.17 shows that the apparent height of the Fe-porphyrin molecules increases as the substrate bias approaches the redox potential of the Fe^{III-II} couple, indicating that the redox properties of the molecule enhance conductivity when in resonance with the applied voltage. Recently, Ulstrup and co-workers have used STM to probe the potential dependent tunnelling of cobalt and osmium complexes[120] and a wire with a built in viologen unit.[121] The cobalt and osmium complexes showed peaks in the tunnelling current-potential scans near the $\mathrm{E}^{0'}$ of the metal complexes, which indicated resonance tunnelling as in Tao's experiment. However, while the tunnelling current increased when near the viologen $\mathrm{E}^{0'}$, a peak was not observed. This was attributed to conformational fluctuations.

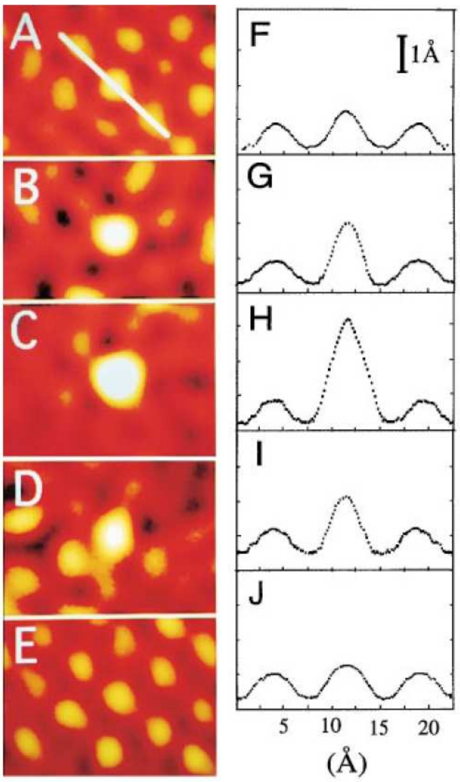

Fig. 1.17: STM image of an Fe-porphyrin molecule (E^0 = -0.48) embedded in an ordered array of porphyrin molecules when the substrate was held at -0.15 (A), -0.30 (B), -0.42 (C), -0.55 (D), and -0.65 V (E), respectively. (F)(J) are the corresponding plots of the apparent height cross sections along the white line indicated in (A). Adapted from Tao.[117]

Similar experiments[122] have also carried out by other groups,[123] yielding complementary results. The major conclusions from this body of work is that assisted electron tunnelling is possible when localized redox levels are close enough to the Fermi levels of the contact electrodes.

1.5.3 M-I-M junctions

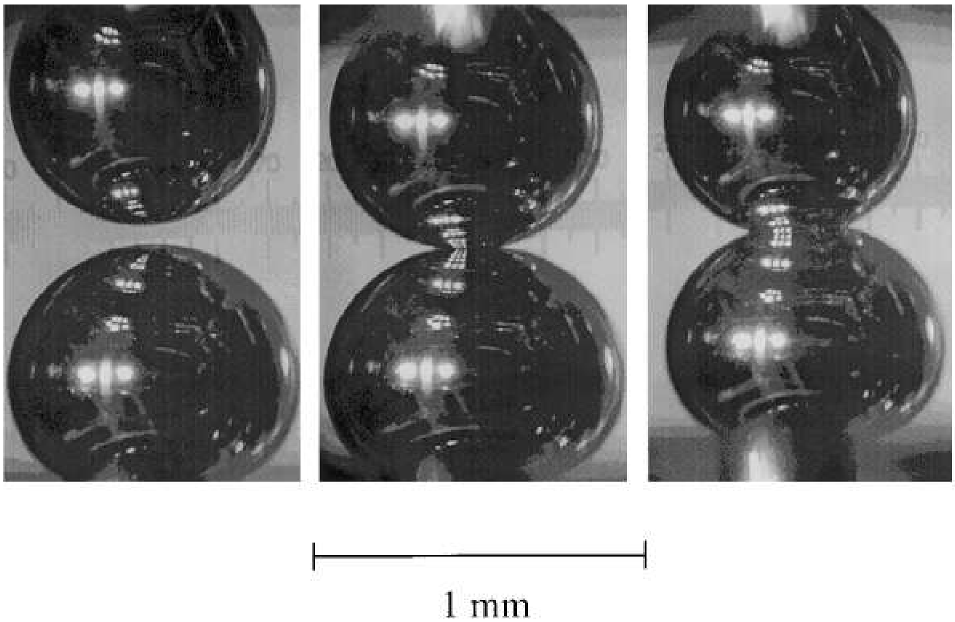

Fig. 1.18: Photograph of the close approach of two Hg drops in alkanethiol solution used to form the Hg-bilayer-Hg junction by Slowinski et al.[124]

Metal-insulator-metal (M-I-M) junctions offer an alternative approach to scanning probe methods for the determination of electronic properties of molecular layers. Despite the lack of advanced instrumentation, the use of macroscopic metal-insulator-metal junctions was pioneered by Mann and Kuhn in 1971.[129] Langmuir-Blodgett films of $CH_3(CH_2)_nCOOH$ were formed on metal plates to form the first contact and the second contact was formed by evaporating a metal film on top of the layer. The natural log of the current was seen to be linear with distance and the tunnelling co-efficient was determined as 1.49 $\mathring{A}^{-1}$. This evaporation technique is still followed by several groups[130, 131, 132] although a large degree of uncertainty exists over the nature of the evaporated second contact. It is generally believed that the evaporated metal damages the organic layer even when cooling techniques are employed.[133]

In 1999 Slowinski, Majda and co-workers reported the first example of Hg-Hg based junctions.[124] These junctions were formed by contacting two mercury drops (see Figure 1.18) in an alkanethiol solution and measuring the current through the bilayer. It was found that the current decreased exponen-

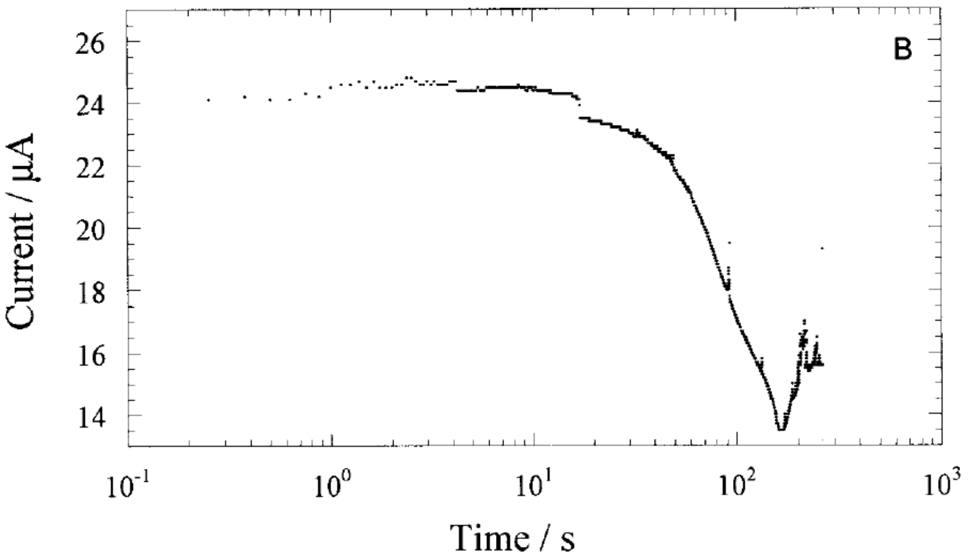

Fig. 1.19: Current-time behavior of a Hg-C_{10}-C_{10}-Hg bilayer at a bias voltage of 1.5 V. Adapted from Slowinski et al.[125]

tially with thickness of the layer and a value of 0.89 per CH_2 was determined. Current-voltage (i-V) curves were also obtained but showed deviations from the theoretical model proposed by Simmons.[134] This work was followed by a series of papers by Slowinski and co-workers on the structure and stability of the junction,[125] improvements to the Simmons model for i-V curves,[135] differences between monolayer and bilayer junctions,[136] the use of dithiols in the junctions[137] and the resistivity of the layers trapped between the junctions.[138]

One of the most interesting conclusions of this work is that bilayers are more conducting than similar thickness monolayers.[136] This demonstrates the importance of chemical contacts to the overall conductivity and a similar point was noted by Frisbie et al. for other methods in their excellent review of current junction fabrication methods.[139] Another interesting point to be noted from Slowinski's work is the presence of peaks in the current-time transients for the Hg-Hg junctions (see Figure 1.19).[125] The decrease in the current was attributed to a progressive disordering of the layer, e.g. all trans bonds changing over time to gauche configurations. Slowinski has favorably compared his single molecule resistivity data to that seen in the literature[135] but as noted above, there is a large fluctuation in these reported values.

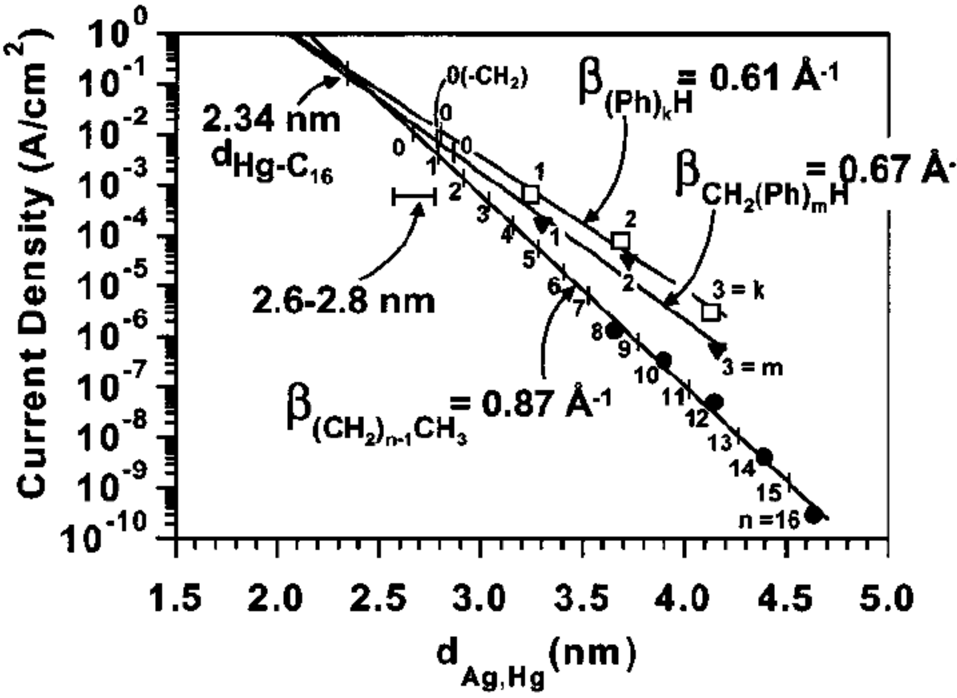

Fig. 1.20: Dependence of tunnelling current on distance for various monolayers determined by Rampi and co-workers.[126]

Rampi, Whitesides and co-workers have also pioneered the use of Hg in M-I-M junctions. In 1998 they first reported the use of two Hg drops in a micro-syringe filled with alkanethiol solution.[140] It was found that the two drops did not coalesce and could therefore be used as a two electrode M-I-M junction. The capacitance of the junction was found to depend on the inverse of the junction thickness, determined by the length of the alkanethiol. This work was extended to a novel M-I-M system in which a Hg drop is lowered onto a metal plate to form a Hg-I-M junction.[141] The metals studied were gold, silver and copper and the focus of this study was the investigation of the break-down voltage of the junctions. The electron transport properties of the Hg-I-Ag junction were reported later and it was found that the current decayed exponentially with junction thickness with a decay parameter of 0.87 $\mathring{A}^{-1}$ for alkanethiols and 0.61 $\mathring{A}^{-1}$ for oligophenylene thiols (see Figure 1.20).[126] This data indicated the importance of conjugation to electron transport. The current-voltage characteristics were also modelled using a modified version of Simmon's theory. The various types of junction created were reviewed in

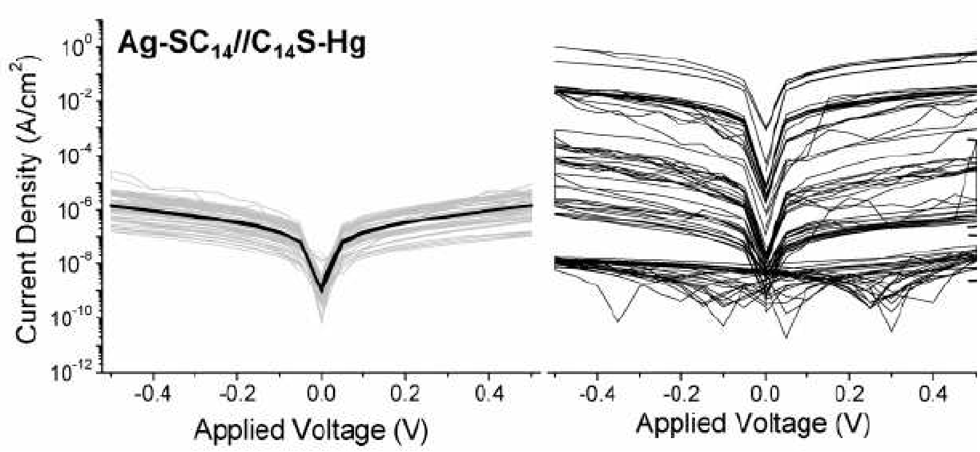

Fig. 1.21: i-V curves for C_{14} bilayer with template stripped silver substrates(left) and e-beam evaporated silver substrates (right). Adapted from Rampi et al.[127]

2002.[142]

The effect of roughness of the film was recently investigated,[127] where two methods for preparing silver substrates were compared, i.e., e-beam evaporation onto Si wafers and template stripping (TS). Template stripping involves depositing silver onto atomically flat substrates and then pulling off the substrate to reveal an atomically flat silver surface. The i-V curves obtained using these curves were highly reproducible (see Figure 1.21). In contrast, the evaporated surfaces, which were approximately five times rougher than the TS surfaces, showed a large variation in the i-V curves collected (see Figure 1.21). The evaporated substrates were also the least stable during the collection of i-V curves and frequent shorts were observed. Despite these limitations, all of Rampi and co-workers work described above was obtained using evaporated substrates, which demonstrates that while roughness definitely has an influence on reproducibility, meaningful results can still be obtained from junction measurements on rougher substrates.

Rampi and co-workers have extended their work to redox active monolayers in M-I-M junctions. Two methods of including redox molecules in junctions have been explored. Typically in the first method an alkanethiol monolayer with an attached redox center is formed on one of the mercury drops. This method has been used to create junctions incorporating ruthenium centers,[128] polycyclic

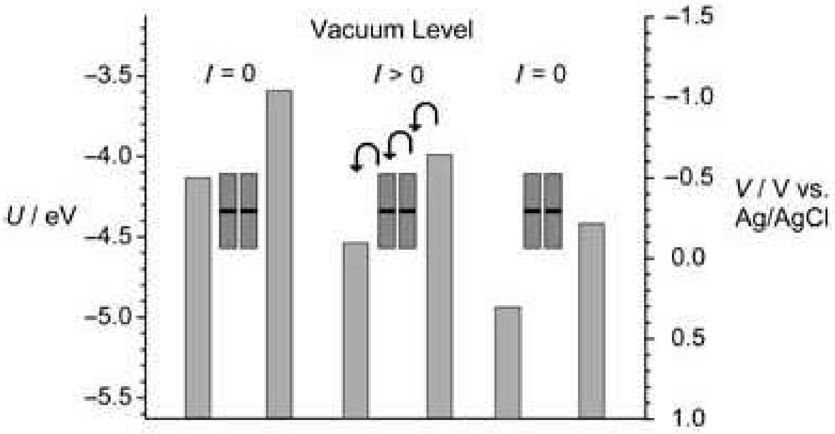

Fig. 1.22: Relationship between the electrochemical potential of a redox couple and the position of the Fermi energy of the mercury electrodes. Adapted from Rampi et al.[128]

aromatic hydrocarbons[118] and cyanoquino-based compounds.[143] The major conclusions from this work are that the bound redox molecules mediate electrons through the junction depending on the potentials of the metal contacts. Figure 1.22 shows the energy levels of the metal contacts being brought in and out of resonance with the redox levels of the trapped molecule. In the case of the ruthenium monolayers it was found that redox centers were needed on both metal electrodes and the distance between the two redox layers was assumed to be on the order of nanometers. Electron hopping was the proposed mechanism for the conductivity between the redox centers. Figure 1.23 shows a schematic of the system studied. The ruthenium moieties at the Hg anode are oxidised to Ru^{3+}. A electron is then transferred to this Ru^{3+} center by electron hopping from the monolayer at the cathode, which leaves the cathodic monolayer in the Ru^{3+} state. Transfer of an electron from the cathode then reduces the Ru^{3+} center. Overall, an electron is transferred from the cathode to the anode via the two ruthenium monolayers.

The second type of redox junction was based on the electrostatic attraction of $[Ru(NH_3)_6]^{2+}$ in between the Hg drops by use of a standard alkanethiol with a deprotonated carboxyl terminating group.[144] The current was seen to increase when the potential of the contacts lay on either side of the redox potential of the trapped ruthenium complex. The mechanism proposed for

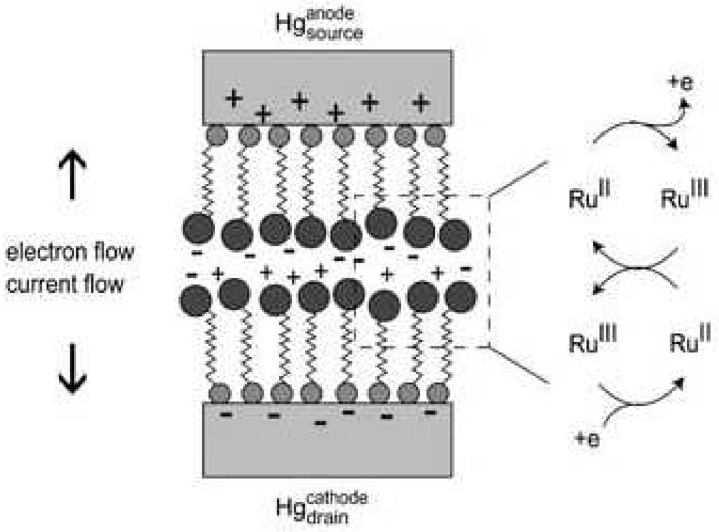

Fig. 1.23: Schematic diagram of the proposed mechanism of charge transport through the Hg-SAM//SAM-Hg junction with bound redox centers. Adapted from Rampi et al.[128]

the increase in current was redox cycling of the $[Ru(NH_3)_6]^{3+}$ between the "source" and "drain" electrodes. However, this mechanism depends critically on the distance between the electrodes and no estimation of this distance was made. It is also unclear how alkanethiol layers which are used routinely as blocking layers can efficiently conduct electrons through these systems. The chain length of the alkanethiol layer used in this study was 11, which would be expected to significantly slow the kinetics of the $Ru(NH_3)_6{}^{3/2+}$ couple and hence the measured current.

Other groups have also used mercury as a "soft" contact for one of the metals in M-I-M junctions. McCreery and co-workers have covalently bonded molecules to a graphitic carbon surface and used a variety of metals, including mercury to form the top contact.[145, 146] Cahen and co-workers have used semiconductors (such as SiO_2) and mercury as the contacts for junctions.[147, 148, 149] However, much of this work has been devoted to determining the influence the Schottky barrier on the tunnelling characteristics. The impedance of classical Hg-Hg tunnelling junctions has been extensively investigated by Wang and co-workers.[150] In conclusion, this body of work demonstrates that M-I-M junctions can be used to probe electron tunnelling events for a variety of systems.

Simple alkanethiol layers can be used to gain information on the fundamental nature of electron tunnelling, but more complex systems incorporating redox moieties have also been explored. These systems are attractive for the creation of molecular devices that can display negative differential resistance properties. The major advantage of these M-I-M junctions is the ease with which they can be fabrication in comparison to scanning probe techniques.

1.6 Interfacial protein adsorption

1.6.1 Protein structure

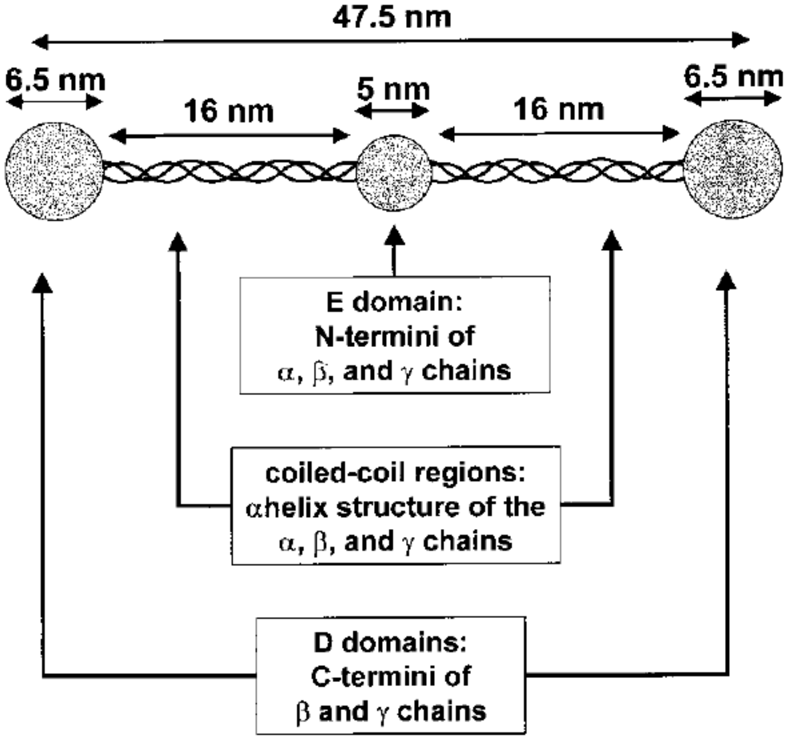

Fig. 1.24: Schematic of the fibrinogen tri-centric structure. Adapted from reference 150.

Proteins are polypeptide chains composed of 20 common amino acids which are linked together by peptide bonds. This peptide bond assembly is often called the protein backbone and it is from this that the side chains of the amino acids extend. The primary structure of proteins is the sequence of these amino acids. However, the protein coils and folds itself into a secondary structure, which is due to the variations in the nature of the amino acid side chains. Some of the side chains, such as alanine and phenylalanine are hydrophobic while others, such as tyrosine and cysteine, are hydrophilic. Others such as lysine and arginine are charged. One of the earliest observations about protein structure was that the more hydrophobic side chains are embedded in the protein core, while the polar and charged ends reside at the protein exterior, where they interact with the solvent.[151] Di-sulfide bridges can be formed in proteins from two cysteine residues under oxidative conditions and these can aid in stabilising the secondary and tertiary structure.

Fibrinogen is a plasma protein that is found in all mammals. It has a molecular weight of approximately 340 kD and is composed of three non-identical disulfide linked chains, which are denoted α, β and γ respectively. These chains have molecular weights of 63.5 kDa, 56 kDa and 47 kDa respectively. The primary structures of these chains have been determined,[152] and it has been suggested[153] that fibrinogen forms a tri-centric structure with two identical domains, denoted D, each side of a third domain denoted E, from two α, β and γ chains. This structure can be seen in Figure 1.24.

Biologically, fibrinogen is involved in blood coagulation and is important in the processes of both haemostasis and thrombosis.[154] It is synthesised in the liver and is present in blood at a concentration of approximately 3 mg/mL. Thrombin converts fibrinogen to an insoluble form known as fibrin, which blocks damaged portions of blood vessels. The mechanism for this process is complex, but its importance for medical reasons has made fibrinogen a much studied protein.[155, 156]

1.6.2 General characteristics of protein layers

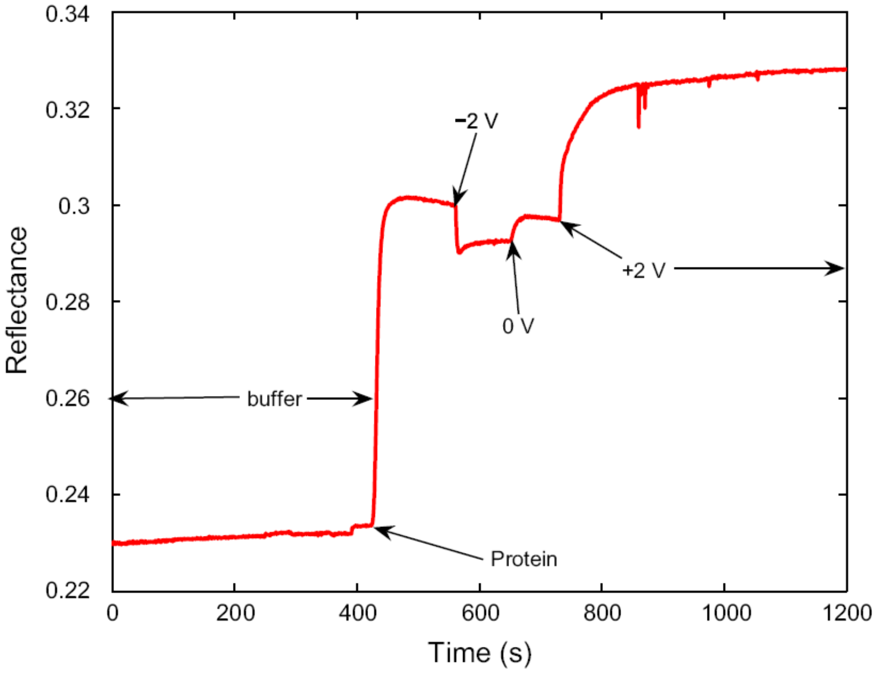

Fig. 1.25: Sensorgram of the reflected signal, constructed from SPR measurements, as a function of time for buffer with added protein, at various applied voltages. Adapted from Martin et al.[157]

Protein adsorption is a common phenomenon and has implications for areas as diverse as biocompatibility of clinical implants, sterilization of surgical instruments and fouling of equipment in the food processing industry.[13, 161] Due to the ease of protein adsorption at surfaces, much work has been carried out in these areas for several decades and many reviews of protein adsorption exist.[162, 163, 14] It is generally accepted that proteins strongly adsorb at solid surfaces for several reasons. Their large size gives them multiple attachment points, thus rendering spontaneous desorption unlikely, as the detachment of all points simultaneously is rare. Fibrinogen has been reported to have approximately 700 attachment points on silica.[13]

Proteins in solution normally carry a charge and, as previously discussed, it typically resides on the exterior of the surface. Several groups have shown that there is a link between the protein adsorption and protein or electrode charge.[157, 164, 165, 166] The potential applied to an electrode was found to greatly influence the speed and amount of soybean peroxidase adsorption onto a gold

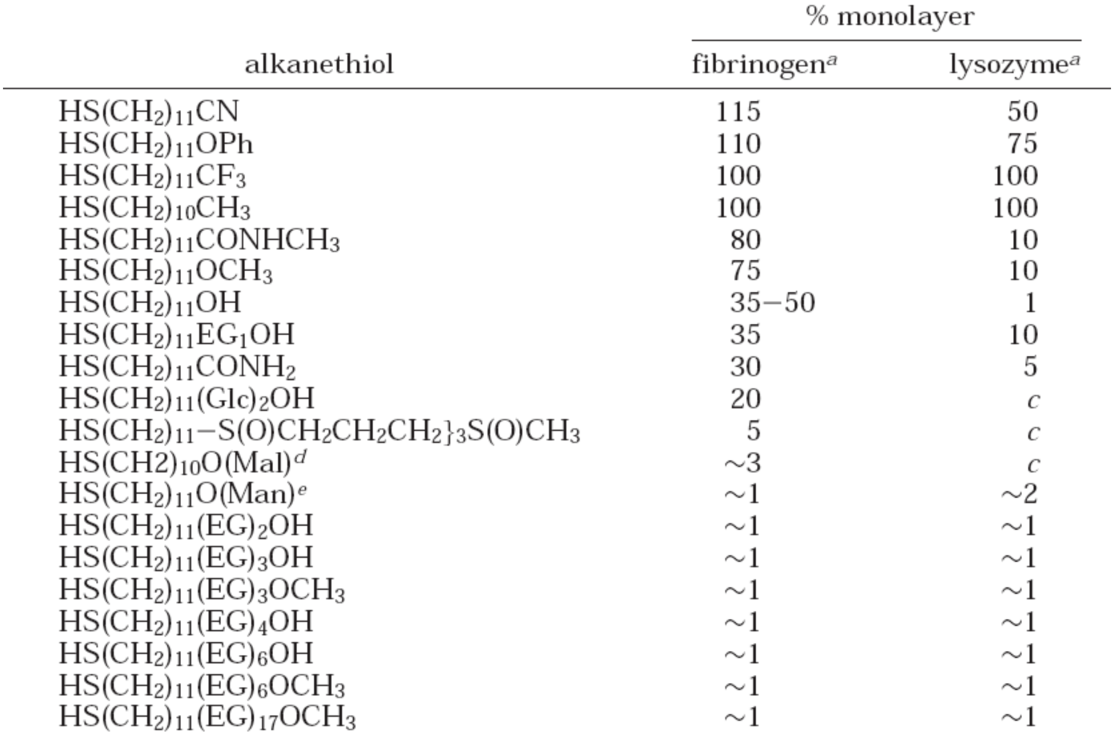

	% monolayer	
alkanethiol	fibrinogen[a]	lysozyme[a]
$HS(CH_2)_{11}CN$	115	50
$HS(CH_2)_{11}OPh$	110	75
$HS(CH_2)_{11}CF_3$	100	100
$HS(CH_2)_{10}CH_3$	100	100
$HS(CH_2)_{11}CONHCH_3$	80	10
$HS(CH_2)_{11}OCH_3$	75	10
$HS(CH_2)_{11}OH$	35−50	1
$HS(CH_2)_{11}EG_1OH$	35	10
$HS(CH_2)_{11}CONH_2$	30	5
$HS(CH_2)_{11}(Glc)_2OH$	20	*c*
$HS(CH_2)_{11}-S(O)CH_2CH_2CH_2\}_3S(O)CH_3$	5	*c*
$HS(CH2)_{10}O(Mal)^d$	~3	*c*
$HS(CH_2)_{11}O(Man)^e$	~1	~2
$HS(CH_2)_{11}(EG)_2OH$	~1	~1
$HS(CH_2)_{11}(EG)_3OH$	~1	~1
$HS(CH_2)_{11}(EG)_3OCH_3$	~1	~1
$HS(CH_2)_{11}(EG)_4OH$	~1	~1
$HS(CH_2)_{11}(EG)_6OH$	~1	~1
$HS(CH_2)_{11}(EG)_6OCH_3$	~1	~1
$HS(CH_2)_{11}(EG)_{17}OCH_3$	~1	~1

Fig. 1.26: Percentage of fibrinogen or lysozyme that adsorb at gold surfaces modified with various SAMs. Adapted from Whitesides et al.[158].

substrate.[157] This protein, which is negatively charged, adsorbed fastest when positive potentials were applied to the substrate and showed some desorption when negative potentials were applied as seen in Figure 1.25. However, the study showed that the removal of all the adsorbed protein was difficult. It was also proposed that fibrinogen adsorbs from PBS onto gold at an optimum rate at the potential of zero charge,[164] although the reasons for this, as fibrinogen is negatively charged in PBS buffer, were not elucidated.

The effect of adsorption on the structure of the protein has received much attention but remains unclear.[13, 14] What is clear is that adsorbed proteins usually unfold or denature at a bare surface due to its attraction to the surface. This process is not typically reversible, although some exceptional cases are dealt with later. However, the pre-modification of the substrate with SAMs can lead to a protecting film that proteins can adsorb onto, normally without the degradation of the protein to the same extent. This concept was suggested first in 1991,[167] and since then much work has gone into tailoring the surface

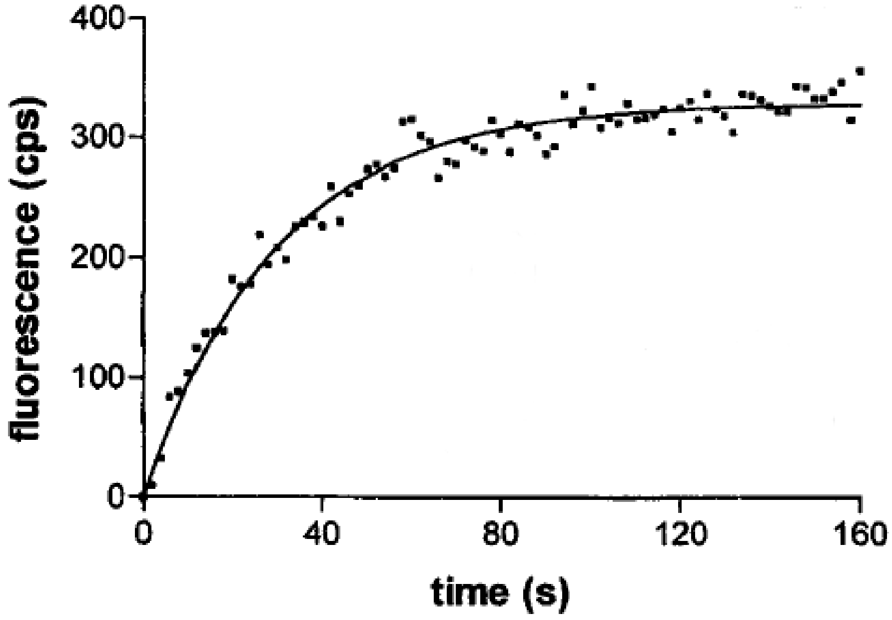

Fig. 1.27: Adsorption kinetics of fibrinogen on a quartz surface, as determined using total internal reflectance fluorescence spectroscopy, fit to a single exponential Langmuir type kinetic model. Adapted from Sanders et al.[159]

layer to protect the protein structure[168, 169, 161] or to resist adsorption.[32] In the latter case, SAMs terminating in ethylene glycol moieties are among the most common and effective.[158]

The kinetics of protein adsorption have been extensively explored in the literature but no clear mechanistic trend has emerged. Many groups have used Langmuir kinetics to describe protein adsorption,[13] but this model neglects adsorbate-adsorbate repulsions, mass transfer to the surface and assumes monolayer formation. Protein adsorption is likely to be more complicated,[13, 158] as it has been seen that proteins are charged and have both polar and non-polar moieties. The adsorption of multilayers of proteins has also been demonstrated.[13] Despite these issues, the adsorption kinetics of fibrinogen have been reported in many studies and the most common model adapted is the Langmuir kinetic model[13, 168, 170] and Figure 1.27 shows a fit using this model obtained from total internal reflectance fluorescence spectroscopy. This study minimised the contributions from mass transfer by agitating the solution and the authors claimed that this simplifies the resulting kinetics. Surface plasmon resonance (SPR) is

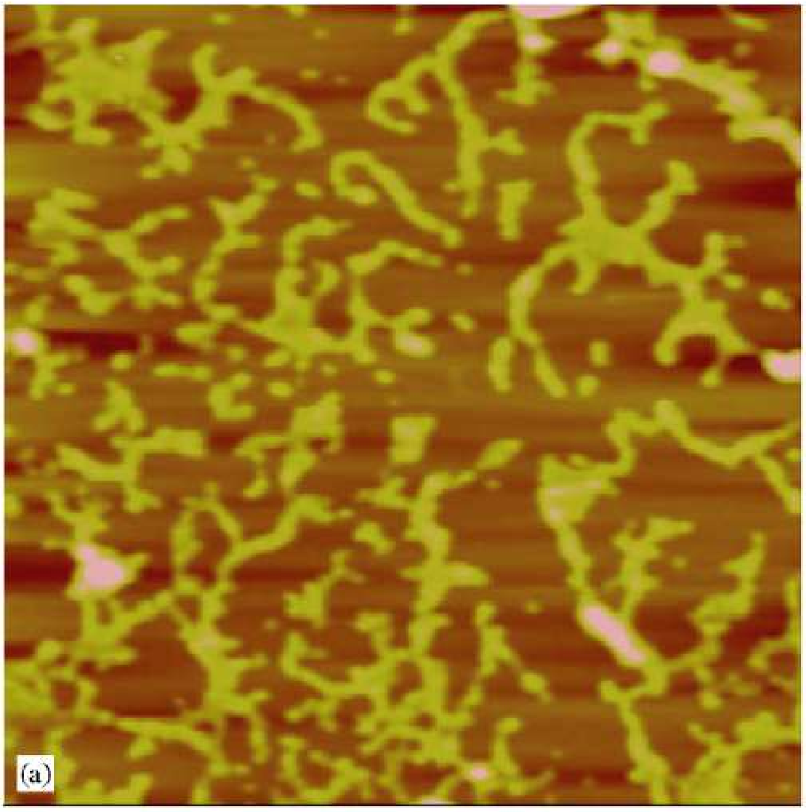

Fig. 1.28: AFM image of fibrinogen adsorbed on a gold surface. The image dimensions are 2 by 2 μm. Adapted from Fang et al.[160]

an attractive technique for these studies and was first used to determine fibrinogen adsorption kinetics in 1995.[168] This study found a linear dependence of the kinetic rate with concentration, suggesting first order kinetics. Several studies have utilised more complex models[171, 172] which incorporate many more variables, but the dominance in the literature of Langmuir models to describe protein adsorption is perhaps due to its simplicity.

Atomic force microscopy (AFM) has been used extensively to characterise bio-molecular layers.[173] Fibrinogen layers were first studied in the early 1990s and the trinodular conformation was soon observed.[174, 175] Several groups have studied fibrinogen on various substrates since then.[153, 176, 177, 170, 178] Two examples of this work are given in Figures 1.28 and 1.29. Figure 1.28 shows a fibrinogen layer adsorbed onto a gold substrate and the figure shows that the fibrinogen adsorbed in streaks on the gold surface, forming a mesh-like network. This was attributed to the interaction of hydrophillic chains at the

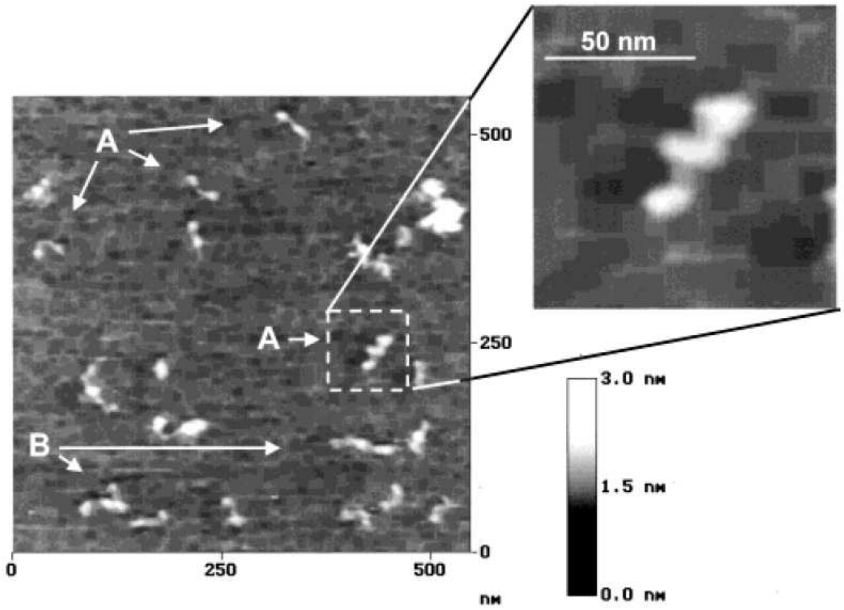

Fig. 1.29: AFM image of fibrinogen adsorbed on titanium surface, where A denotes isolated molecules and B aggregates of the protein. Adapted from Miles et al.[153]

ends of the fibrinogen molecule, i.e. beyond that of the D domains seen in Figure 1.24. These chains interact with each other rather than the surface and so a network can form. This would imply that protein-protein interaction at the surface is a factor in the adsorption kinetics. The resolution and surface coverage in this figure is too low to image single fibrinogen molecules but Figure 1.29 shows fibrinogen adsorbed from dilute solutions onto titanium. This is an important substrate for protein adsorption due to the dominance of titanium as medical implants. This figure shows what the authors claim are single fibrinogen molecules (denoted A) and clusters of fibrinogen molecules (denoted B). The molecule inside the dotted area has been enlarged to show more clearly three globular domains, which is a good match for the proposed structure of fibrinogen. These AFM studies show the importance of substrate polarity on the structure of protein layers.

1.6.3 Desorption of proteins from surfaces

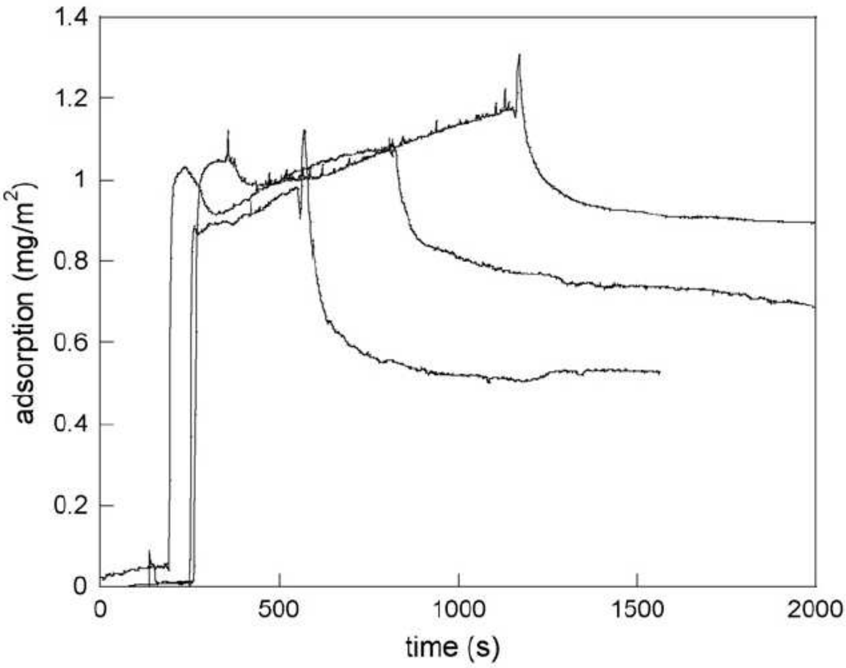

Fig. 1.30: Desorption of lysozyme from silica into blank buffer after different adsorption times determined using SPR. Adapted from Norde et al.[179]

It has been previously discussed that protein adsorption is normally irreversible, i.e. protein desorption into blank buffer is not a spontaneous process, although a fraction of weakly bound protein may desorb. This is due to the high Gibbs energy of adsorption characteristic of proteins, reported to be up to -500 kJ.mol^{-1} for a 100 kD protein.[182] However, while getting proteins to desorb spontaneously is difficult, if not impossible, there are several ways to desorb proteins by manipulating the system under study. Proteins can be desorbed, at least partially, by changing the solvent polarity, the temperature or pH.[183, 181] Exposure to a solution of sodium dodecyl sulfate removes almost all albumin protein from polymer surfaces.[184] Norde and co-workers have studied the effect of spreading of the protein on various surfaces and the subsequent effect that this process has on desorption.[179] It is found that once the protein adsorbs, if the surface concentration is low, it can spread and becomes more tightly bound, making it harder to desorb into blank buffer solutions (see Figure 1.30). Similar conclusions were also reached by other studies.[185] In a relatively rare example, Norde and co-workers found that albumin released

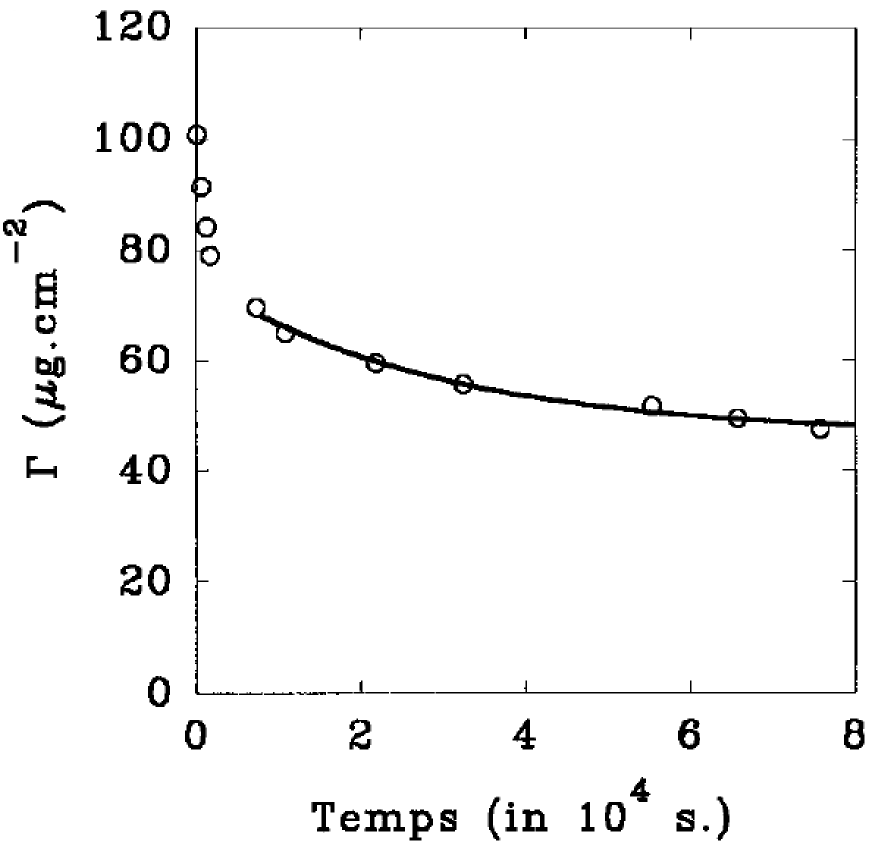

Fig. 1.31: Desorption kinetics of immmunoglobulins from titanium particles measured by radiolabelling of the protein. The solid line is a single exponential fit excluding the first four points. Adapted from Ball et al.[180]

from a silica surface did not show any damage to the secondary structure, as determined using circular dichroism.[186] It was suggested that the key to this reversibility was the surface affinity for polar groups. It appears that hydrophilic surfaces do not degrade the proteins to the same extent as hydrophobic ones. Any exchange into buffer is also more likely when the layers are adsorbed onto hydrophilic surfaces. Therefore, protein adsorption is more irreversible and destructive on hydrophobic surfaces. Fibrinogen has been shown to be more strongly bound at hydrophobic graphite substrates compared to more hydrophillic substrates such as mica.[177,178]

The kinetics of protein desorption has only been investigated in a few studies. MacRitchie found that proteins desorbed from layers formed at the air water interface followed diffusion based kinetics, i.e., followed a $t^{1/2}$ dependence.[13]

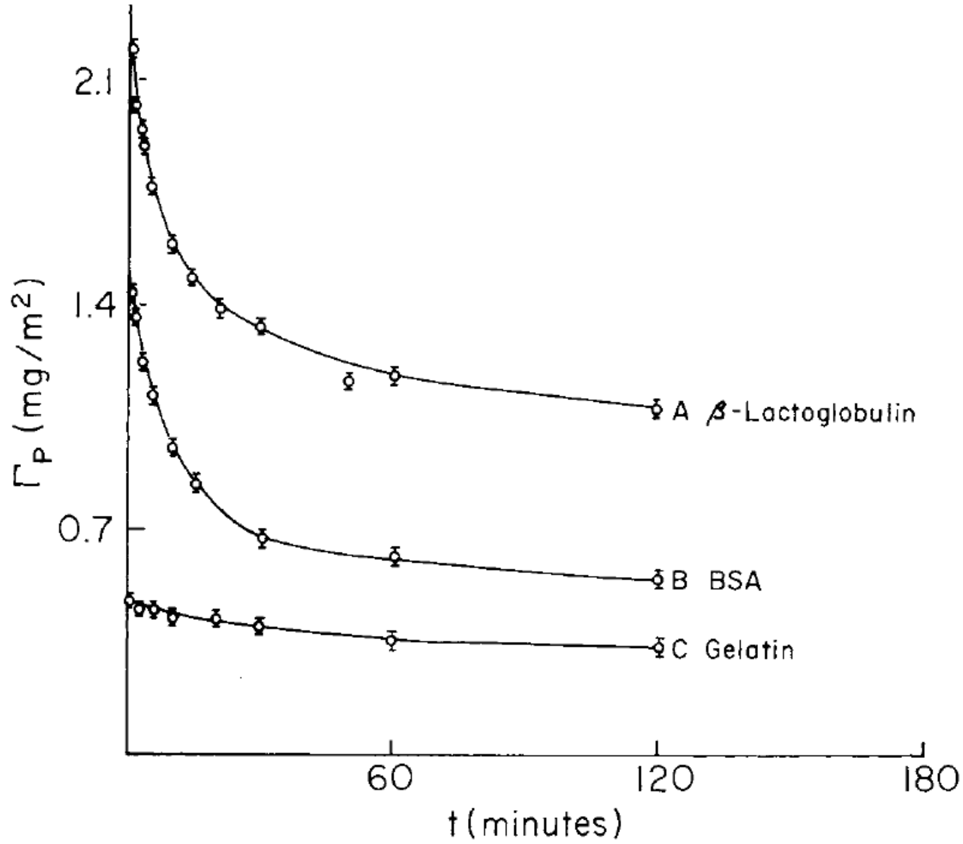

Fig. 1.32: Desorption kinetics of three proteins (β-lactoglobulin, albumin and gelatin) from alumina particles. The desorption was achieved by a change in the buffer pH. Adapted from Sarkar et al.[181]

Norde and co-workers investigated desorption of lysozyme from silica using SPR.[179] Figure 1.30 shows that the time spent adsorbing the protein influences the amount of protein that can be desorbed into blank buffer, as previously discussed. It should be noted that silica is a hydrophillic surface, which would allow some protein to desorb into buffer as discussed above.

Ball and co-workers have also investigated the desorption kinetics of immunoglobulins adsorbed at titanium particles into blank and protein containing buffer using radiolabelled protein.[180] In the protein containing buffer an exchange mechanism dominated, but the desorption into blank buffer had an exponential time dependence, as seen in Figure 1.31. However, the authors did not fit the first four points with this exponential. It can also be seen that a significant amount of protein still resides on the titanium after approximately three hours. Figure 1.32 shows the desorption kinetics of three proteins (β-lactoglobulin, albumin and gelatin) from alumina particles, achieved by modifying the pH of the buffer solution. This figure shows that this method is sufficient for the desorption of most of the β-lactoglobulin and albumin, but the gelatin desorption is slow. These kinetic traces were fit using first order kinetics, but two linear branches were observed in the semi-log plots. This suggests that the desorption process has a fast initial step, followed by a slower step, although the authors did not attribute any physical explanation for this observation. In summary, the desorption kinetics appear to be influenced by the diffusion of protein away from the interface and the amount of protein at the surface.

The effect of electrochemical potential on protein layers has only recently been addressed. It has been shown that charged proteins can be adsorbed or desorbed depending on the electrode potential applied[157] (see Figure 1.25). Recently, SPR has been used to determine the effect of electrode potential on proteins covalently bound to alkanethiol SAMs.[187] This study found that reductive desorption of the SAMs also removed the protein. The application of electrochemical potential to desorb proteins may provide an easy method for decontamination of surfaces.

1.7 Nano-porous assemblies

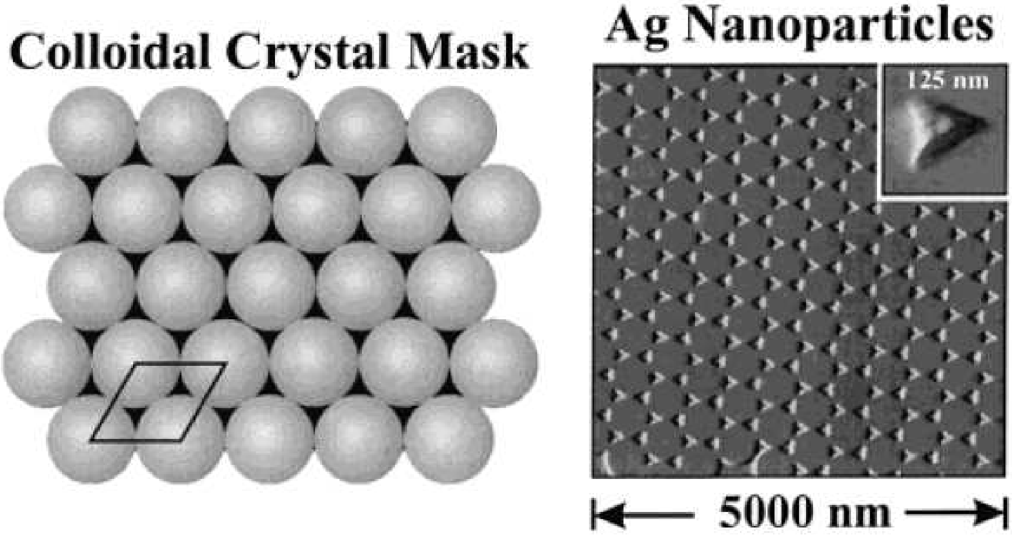

Fig. 1.33: Schematic of polystyrene spheres and the triangular nano-particles that are formed from thermal evaporation deposition through this template. Adapted from Van Duyne et al.[188]

The fabrication of surfaces with features approaching dimensions of a few nanometers is currently a popular area in surface science.[189, 190, 191] Nano-porous assemblies are among the most interesting of these surfaces due to the unconventional optical properties they can display, when the pore diameters are comparable to the wavelength of the visible light.[192, 193, 194] These assemblies can be created in several ways. Lithography techniques[195, 196] (such as photo-lithography or ion beam lithography) are effective, but expensive, routes to these surfaces. Recently, the use of what is known as nano-sphere lithography[190, 197] has become popular for the creation of patterned surfaces. Typically, spheres of polystyrene or silica are assembled on a surface and the voids between the spaces are filled, or partly filled, with the desired material. Different structures can then be formed depending on the method and completeness of the filling process, such as the nano-cavity arrays formed by Bartlett, which are discussed below, and the triangular nano-particle arrays formed by Van Duyne[188] (seen in Figure 1.33).

In the creation of nano-cavity arrays there are many methods to fill the voids between the spheres. The space can be filled with a chemical precursor to the material and subsequent conversion of the precursor via some chemical process.[198] Another popular method is evaporation of metal through the template.[197] Many different nano-scale surfaces features can be created using nanosphere lithography.[188, 197]

A highly convenient method for the filling of the void space between the spheres is electrochemical deposition. This method has been popularised by Bartlett[199] and others.[194] Regardless of the filling methods the next step is the removal of the spheres to leave a nano-porous assembly with pore dimensions determined by the diameter of the spheres used.

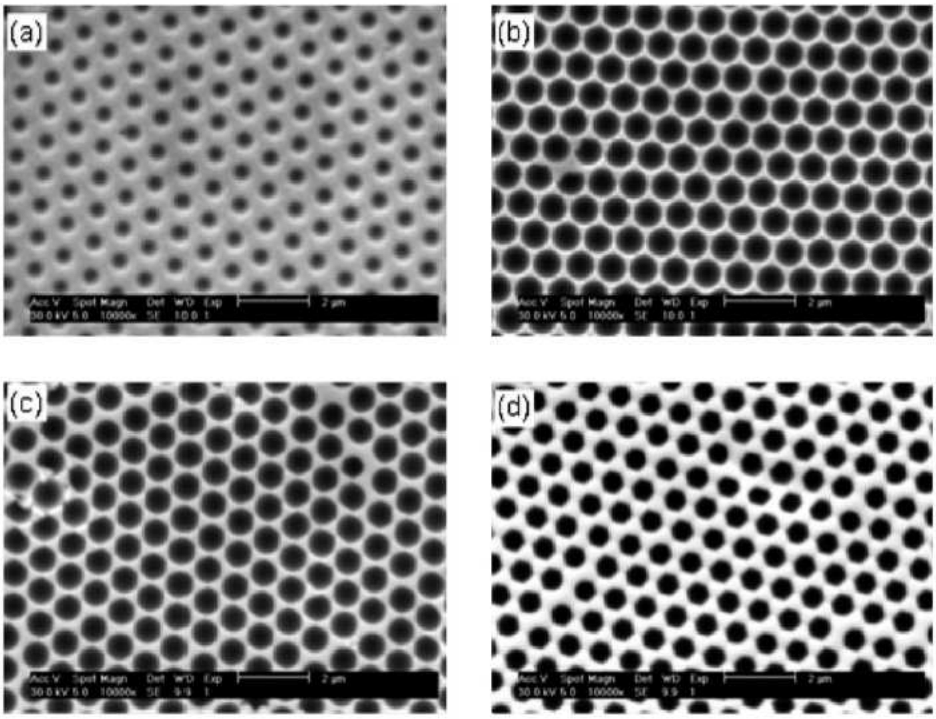

Fig. 1.34: SEM images of nano-cavity arrays having cavity diameter (D) of 900 nm and film thicknesses of: (a) 0.25 D; (b) 0.45 D; (c) 0.7 D; and (d) 0.9 D. Adapted from Bartlett et al.[200]

Many different materials such as carbon,[198] silica,[203] polymers[194] or metals such as platinum[204] or cobalt[205] have been used to create nano-porous assemblies. Gold has also been a popular choice of material to create these arrays, due to its stability and optical properties. Bartlett[199, 206, 207, 201, 200] and others[208, 209, 210] have created gold nano-porous assemblies. Scanning electron microscopy (SEM) was used to investigate the resulting structures,[200] an

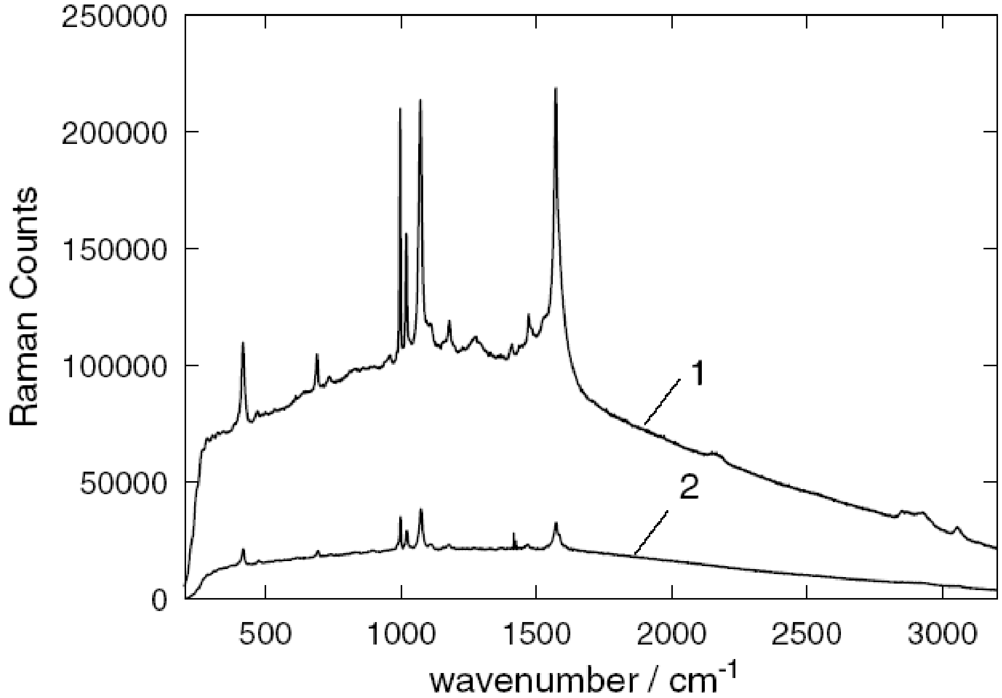

Fig. 1.35: Raman spectra of benzene thiol adsorbed on: (1) a nano-cavity structured gold surface and (2) electrochemically roughened gold surface. Adapted from Bartlett et al.[201]

example of which can be seen in Figure 1.34. This figure shows nano-cavity layers of various thickness, which are formed by passing varying amount of charge during the deposition stage.

These substrates are interesting as they can provide locally trapped surface plasmons,[190] which result in large enhancements in spectroscopic signals such as Raman. Bartlett has investigated the SERS spectrum of benzenethiol adsorbed at the nano-cavity substrates.[201] Figure 1.35 compares the spectrum obtained at a 600 nm nano-cavity array of 150 nm thickness to that obtained at a roughened gold electrode. The enhancement reported for this example is 3 x 10^7 compared to an enhancement at the electrochemically roughened surface of 2 x 10^5. However, two factors that can influence the enhancement observed are the cavity size and the layer thickness. These properties have been investigated for a benzenethiol layer adsorbed at nano-cavity arrays of various sizes and layer thicknesses[202] and the results are summarised in Figure

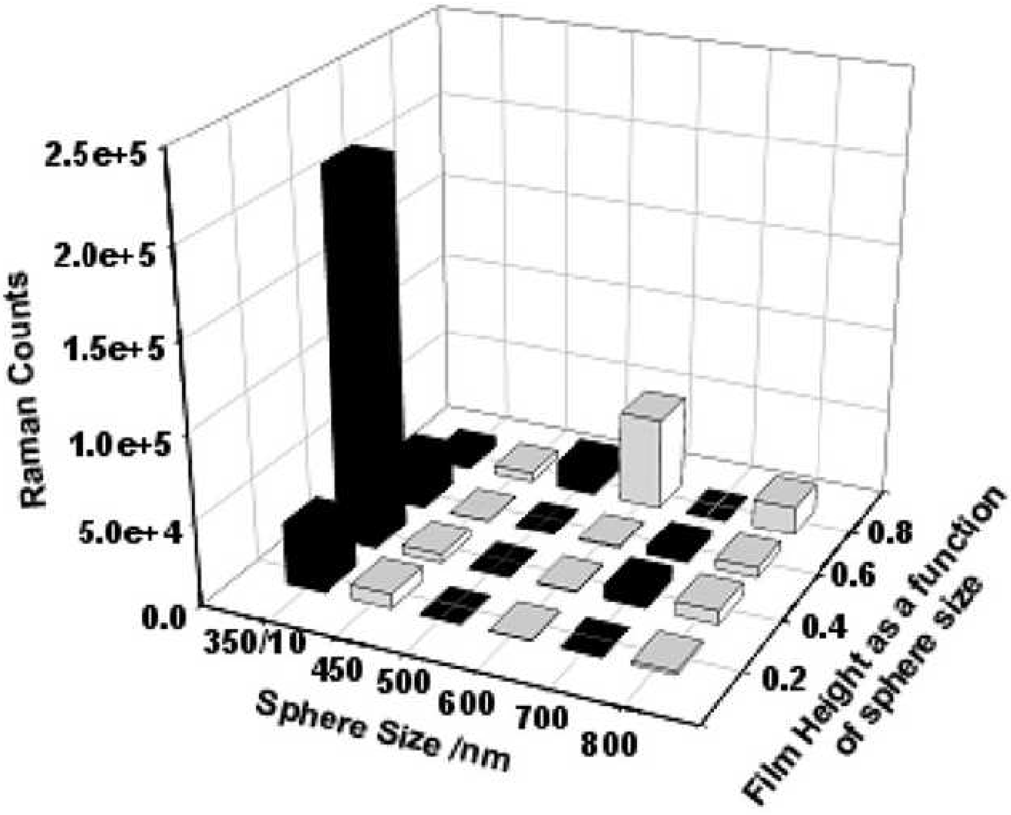

Fig. 1.36: Peak intensity of the 1571 cm^{-1} band in the SERS spectrum of adsorbed benzene thiol as a function of the sphere diameter, d, and fractional film thickness. Adapted from Bartlett et al.[202]

1.36. The enhancement is greatest when the cavity size is either 350 or 600 nm and when the thickness is approximately 300 and 500 nm respectively. These differences are rationalised by the variation of the surface plasmon with both cavity size and layer thickness. Much theoretical work has gone into defining these plasmons.[211, 207, 212, 192] The most recent interpretation[211] shows that the plasmons are localised at the bottom of the cavity for thin layers but as the thickness increases the plasmon enhancement is greatest in the middle of the cavity. This would appear to correlate with Figure 1.36, as the benzene thiol molecules are adsorbed at the cavity walls.

It has been demonstrated relatively recently that fluorescence signals can also be enhanced using surface plasmons localised on surfaces.[213, 214, 215, 216] Much of this work has focused on nano-particles[214, 216] but some studies have also appeared on the fluorescence enhancement exhibited by arrays of nano-holes of 100 nm diameter.[217, 215] However, these holes are produced by focused ion beam milling and the light is transferred through the substrate from underneath. Spherical cavities have not yet been investigated for these effects.

1.8 Techniques

1.8.1 Methods based on impedance

Introduction to methods based on impedance

At the interface between an electrode and a solution there is a build up of ions on the solution side of the interface that balance the charge of the electrode according to the electroneutrality principle (see Figure 1.1). This excess of separated charge at the interface can be related to that of a capacitor as described earlier and is generally called the double layer. The layer thickness depends on the concentration of the solution with more concentrated solutions having more compressed layers. The capacitance of the layer depends principally on the capacitance of the inner adsorbed layer of ions. Thus, the adsorption of compounds onto the electrode surface will change the capacitance as these ions are displaced by the adsorbing compounds. This can be described theoretically by Equation 1.1. An adsorbed layer changes the capacitance in two ways. Firstly, the dielectric constant adjacent to the surface changes depending on the type of adsorption e.g. a layer of organic molecules in aqueous solutions will reduce the dielectric constant. Secondly, the adsorbed layer will increase the distance between the bulk solution (including the interfacial double layer region) and the electrode. The capacitance is therefore expected to decrease for an adsorbed layer of organic molecules of low polarity in solutions with high dielectric constants. Impedance measurements such as AC voltammetry can be used to determine this capacitance and therefore are useful techniques to study modified electrodes. Impedance and, by extension, capacitance can be studied as a function of applied potential, time or frequency of excitation signal.

Basic principles of impedance

Typically, impedance measurements apply a small amplitude sinusoidal excitation voltage signal to a system and monitor the current response. This low amplitude excitation signal, $\Delta E sin(\omega t)$, gives rise to a current response,

$\Delta I sin(\omega t + \phi)$. ϕ is the phase shift of the response signal with respect to the excitation signal. For a pure capacitor the signal is sifted by $-\pi/2$ at low frequencies. The impedance of the system can found by:

$$Z(\omega) = \frac{\Delta E(\omega)}{\Delta I(\omega)} \tag{1.10}$$

This ratio is a complex quantity with a magnitude and a phase shift which depends on the frequency of the excitation signal. Measurement of the impedance of a system as a function of frequency is often called electrochemical impedance spectroscopy (EIS).

The cartesian co-ordinates of impedance can be given by:

$$Z(\omega) = Z_r(\omega) - jZ_j(\omega) \tag{1.11}$$

where Z_r is the real part of the impedance (often called Z') and Z_j is the imaginary part (often called Z") where $j = \sqrt{-1}$. The real part of the impedance can be related to the solution resistance while the imaginary part can be related to the capacitance of the double layer. The phase angle can be used to calculate the magnitude of both by:

$$Z' = |Z| cos\phi \tag{1.12}$$

and

$$Z'' = |Z| sin\phi \tag{1.13}$$

A plot of Z' verses Z" for data obtained by EIS is called a Nyquist plot. The disadvantage of this plot is that the frequency dimension of the data is lost. Knowing that at high frequencies the imaginary part goes to zero, the interception of the line with the x-axis gives a measure of the solution resistance, as at this point the impedance is equal to the real part i.e. $Z = Z'$ and $\phi = 0$. This can be clearly seen in a Bode plot, which plots $log(Z)$ and ϕ against $log(\omega)$.

The double layer capacitance of the system is related to Z'' by the following equation:

$$C_{dl} = \frac{1}{-\omega Z''} \tag{1.14}$$

For a range of frequencies a plot of Z'' verses $\frac{1}{-\omega}$ yields an average value for C_{dl}. This value can be used in conjunction with the solution resistance R_s to calculate the RC constant of the electrode, a measure of the speed at which the double layer charges, an important value when performing short timescale electrochemical experiments.

If the frequency of the excitation is fixed, the impedance of a system can be found as a function of time or applied potential. Capacitance data as a function of these two variables can reveal information such as the potential of zero charge (the potential at which there is no excess of ions at the electrode interface commonly denoted as PZC) when used in conjunction with varying applied potential and adsorption dynamics when monitored as a function of time. This latter application is useful in the study of non-electroactive layers such as cyclodextrin or protein layers.

1.8.2 Cyclic Voltammetry

Introduction to cyclic voltammetry

Cyclic voltammetry is an electrochemical technique that scans a potential region by means of varying the potential applied at a working electrode and recording the current produced. This highly versatile technique can rapidly reveal thermodynamic and kinetic information about redox systems in solution and on an electrode surface. As electron transfer steps are not purely thermodynamical processes the current response is often dominated by kinetics. When the kinetics of the system are fast (reversible systems) the Nernst equation (Equation 1.15) can describe the current response but with slower kinetics (irreversible systems) the current is dominated by the rate of electron transfer and it is necessary to interpret the response in terms of an electron transfer theory such as Butler-Volmer or Marcus theory. Diffusion of the electro-active species also influences the signal, although this parameter is removed upon surface confinement of the redox species.

$$E = E^{0'} + \frac{RT}{nF} ln \frac{C_O}{C_R} \tag{1.15}$$

Normal cyclic voltammetry (CV) is performed using a stationary working electrode, for example glassy carbon or mercury, in a quiet solution. The potential of this working electrode is scanned with respect to a reference electrode, for example the Ag/AgCl (sat. KCl) electrode, using a potentiostat. Finally, an auxiliary electrode, normally platinum wire, is used to conduct the current with respect to the working electrode. This stops reference electrode degradation due to high currents passing through it. Ohmic drop effects (the sum of the current and resistance between working and counter electrodes) can also be minimised by placing this auxiliary electrode near the working electrode. The waveform applied to the working electrode during the course of a CV experiment is shown in Figure 1.37.

The current response from such a scan is called a voltammogram, and is represented as a plot of current versus potential.

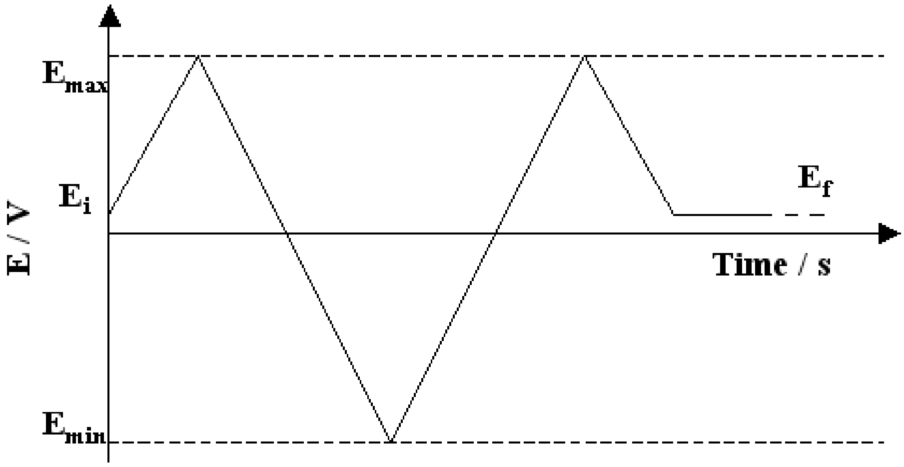

Fig. 1.37: Potential profile during a CV experiment. Adapted from reference 15.

CV of solution phase species

Figure 1.38 shows a CV of a fully reversible species in solution and the corresponding peak currents and potentials. The potential is normally swept linearly from a potential at which no faradic reaction takes place. As the potential reaches the redox potential of the species under investigation it reaches a point where the solute in question can be reduced or oxidised. Thus an increase in current is observed. The sharp response is a result of the logarithmic characteristic of the Nernst equation. As the electrode only reacts with a very small film of solute at the electrode surface a concentration gradient soon arises which draws un-reacted species into the depleted layer. However, as this layer grows the flux of un-reacted species to the electrode surface falls which results in a decrease in peak current and the current decays. Steady-state behavior can be seen at microelectrodes as the diffusion to these small electrodes is extremely efficient. The potential is switched at a value beyond the redox potential and the solute is oxidised or reduced as in the first scan. The scan rate (υ) can vary, typically from 50 mVs^{-1} to 100 Vs^{-1}, and varying the scan rate can give information about the redox system while the peak to peak separation can also yield kinetic information according to the Nicholson method for solution phase species.[218] Underpinning these faradic currents are non-faradic or capacitive currents generated by the double layer charging in

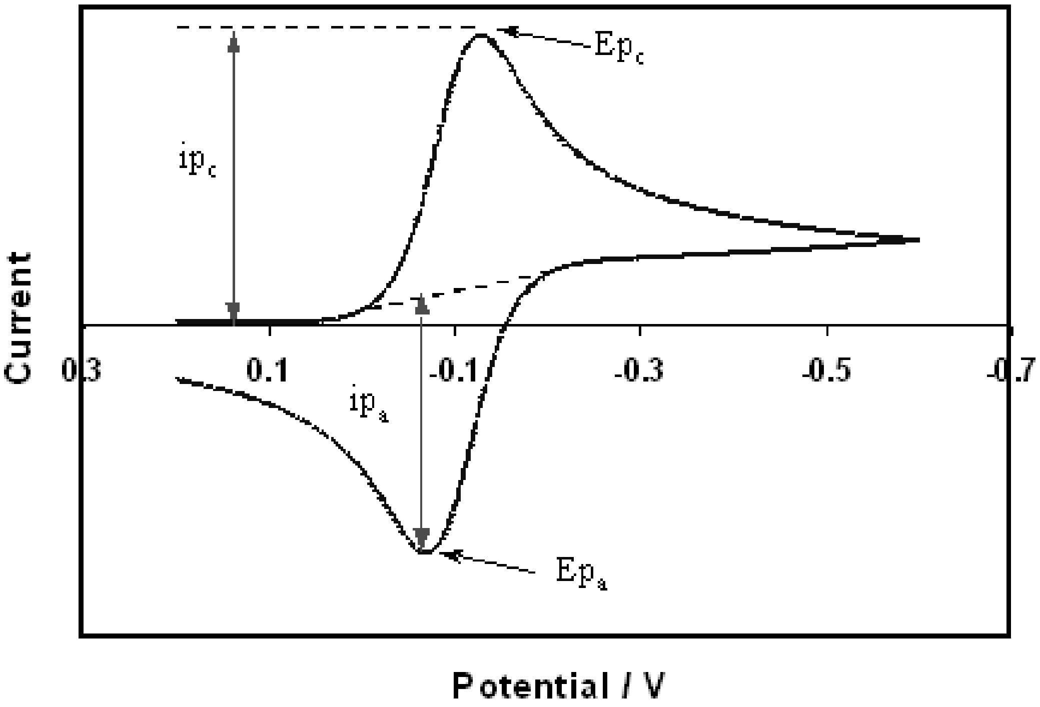

Fig. 1.38: Cyclic voltammogram of a reversible species in solution. Adapted from reference 15.

response to the change of potential applied to the working electrode.

Under reversible conditions the Randles-Sevçik equation applies, which relates scan rate to peak current (i_p) as:

$$i_p = (2.69 \times 10^5) n^{3/2} A D^{1/2} \upsilon^{1/2} C, \tag{1.16}$$

where n is the number of electrons transferred, A is the area of the electrode, D is the diffusion coefficient and C is the concentration of the redox species. The peak potentials are not related to the scan rate for a reversible system but can be altered by the effects of ohmic (or iR) drop. This potential is related to the resistance (R) of the electrochemical cell and the current (i) passing through the cell by Ohm's law. The overall result is a potential that acts to weaken the applied potential by an amount iR. When working with low currents and highly conducting solutions this effect is minimised. If ohmic effects and slow electron transfer rates are absent and under semi-infinite diffusion conditions, the following relationships apply: $\Delta E_p = \frac{0.059}{n}$ volts at 25^{0}C, and $\frac{i_{pa}}{i_{pc}} = 1$ where ΔE_p is the difference in anodic and cathodic peak potentials and i_{pa} and i_{pc} are the anodic and cathodic peak heights respectively.

CV of surface adsorbed species

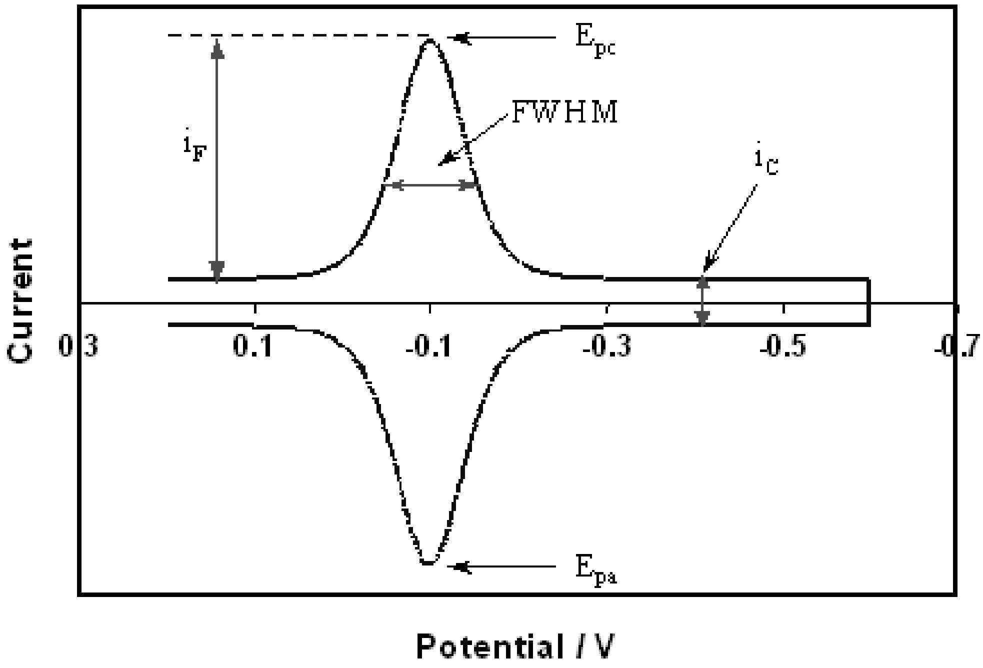

Fig. 1.39: Cyclic voltammogram of a surface bound species displaying fully reversible behavior. Adapted from reference 15.

Species adsorbed onto an electrode surface exhibit a different voltammetric response to those in solution as the species no longer needs to diffuse to the electrode. The resulting shape of the voltammogram can be seen in Figure 1.39 for a finite diffusion layer with fast heterogeneous electron transfer. The peak current can be related to the surface coverage (Γ) by the following equation:

$$i_p = \frac{n^2F^2}{4RT}\upsilon A\Gamma \tag{1.17}$$

where F is the Faraday constant, T is the absolute temperature and R is the gas constant. Thus the peak current varies linearly with scan rate for an adsorbed species, as opposed to varying linearly with the square root of scan rate according to Equation 1.16 for a diffusive species. The surface coverage can also be determined by measuring the Faradaic charge, Q, which is passed using slow scan rates, according to the following equation:

$$\Gamma = \frac{Q}{nFA} \tag{1.18}$$

Under Nernstian conditions the following relationships hold for the cyclic voltammetry of surface confined species assuming that lateral interactions of the adsorbates are not effecting the surface coverage:

$$FWHM = 3.53\frac{RT}{nF} = \frac{90.6}{n}mV \tag{1.19}$$

(where $FWHM$ is the full width at half maximum of the peak of the cathodic or anodic wave) and $E_{pa} = E_{pc}$.

Non-ideal voltammetry can arise for several reasons. A change in orientation between the oxidised and reduced forms can affect the peak splitting while non-uniformity of the adsorbed layer can result in peak broadening, as the local environment of individual molecules may differ. Slow electron transfer rates can also cause deviations from ideal behavior as these systems are not at equilibrium.

1.8.3 Chronoamperometry

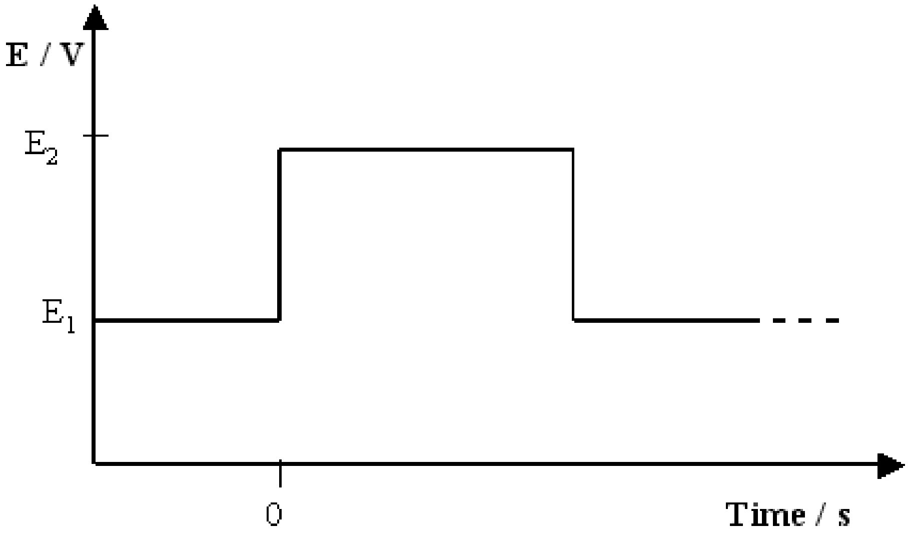

Fig. 1.40: Potential waveform for chronoamperometry showing initial and final potentials with respect to time (E_1 and E_2 respectively). Adapted from reference 15.

Chronoamperometry is a potential step technique in which the potential is changed rapidly from an initial potential (E_1) to a final potential (E_2) with respect to time. The waveform for this signal is shown in Figure 1.40. The application of such a step to a working electrode induces a non-faradic current transient which follows Equation 1.20;

$$i_{(t)} = (\frac{\Delta E}{R})exp(\frac{-t}{RC}) \tag{1.20}$$

where R is the cell resistance, C is the double layer capacitance and ΔE is the step width. If a the formal potential of an adsorbed redox species lies between E_1 and E_2 then faradic current transients which follow Equation 1.21 can also be observed;

$$i_{(t)} = kQexp(-kt) \tag{1.21}$$

where k is the rate constant of electron transfer and Q is the amount of charge passed at the electrode interface. This transient cannot be observed at macro-sized electrodes as the RC charging constant is too long. However, the use of micro and ultramicro-electrodes allows the observation of the second transient, due to the small capacitance exhibited by these electrodes.

1.8.4 Fluorescence spectroscopy

Introduction

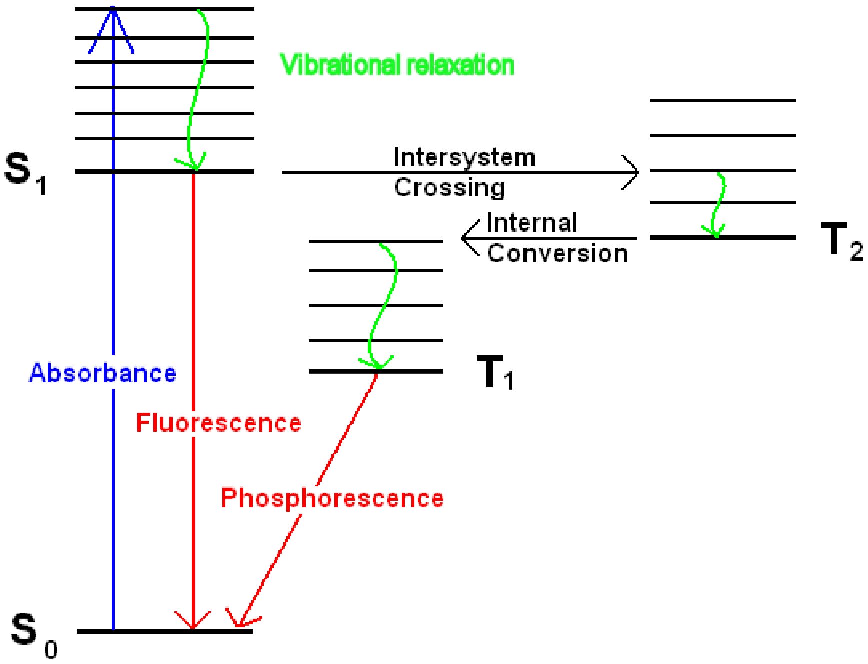

Fig. 1.41: Jablonski diagram showing the energy levels involved in absorbance, fluorescence and phosphorescence processes.

Luminescence is the emission of light from molecules which have been promoted to an excited state by, for example, light absorption. Light absorption processes are ultra-fast (approximately 10^{-15} seconds),[219] and the molecule can then relax to the lowest vibrational level of the excited state, by collisions with solvent molecules (collisional deactivation) and this process occurs in approximately 10^{-12} seconds. Thereafter, the molecule can relax to the ground state by emission of light and the timescale for this process is of the order of 10^{-8} seconds. The wavelength of the light emitted is longer than that absorbed due to the excited state relaxation to the lowest vibrational level. This is commonly known as Stokes shift. These processes can be represented on a Jablonski diagram (Figure 1.41).

Figure 1.41 shows the processes which can occur between the absorption and emission of light. The absorbance of light is represented as a blue arrow and at ambient temperatures occurs principally from the lowest vibrational energy level of the ground electronic state (S_0). The absorbance of light typically results in the population of one of the higher vibrational levels of either S_1 or S_2. Collisional deactivation relaxes the molecule to the lowest vibrational level of S_1 from which fluorescence can occur. The fluorescence spectrum is broad as the molecules can relax to excited vibration levels of the ground state.

The diagram also shows that the excited and ground states can interconvert due to internal conversion and intersystem crossing. Internal conversion involves the deactivation of an electronic excited state by crossover to a high vibrational level in a lower electronic level of the same spin. It is an isoenergetic process and it typically followed by collisional deactivation. Intersystem crossing is similar to internal conversion, but occurs with a change of spin state. In Figure 1.41, the excited single state, S_1, undergoes intersystem crossing to reach an excited triple state, T_2. This triplet state can relax to the lowest vibrational level of T_1 by a combination of internal conversion and collisional deactivation. Conversion of T_1 to S_0 is a radiative process known as phosphorescence. However, as this conversion is forbidden the rate constant for phosphorescence is several orders of magnitude lower than that of fluorescence.

Confocal fluorescence microscopy

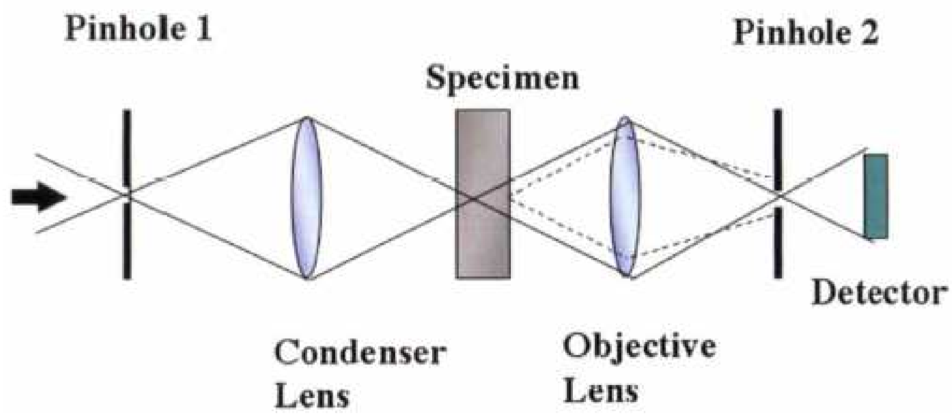

Fig. 1.42: Scheme illustrating the principles of confocal microscopy. Adapted from reference 217.

Fluorescence microscopy has modest levels of resolution when compared to scanning probe or scanning electron techniques because of optical diffraction limits. However, the continued interest in fluorescence microscopy is due to the ability to analyse biostructures in hydrated conditions. The advent of fluorescent labelling has provided much information on the relationship between structure and function in living systems.[220, 221] When combined with confocal microscopy, spacial information is achievable. In a confocal system, light from the excitation source is passed through a pinhole before it reaches the condenser lens (Figure 1.42). This lens focuses the light on a specific point of the sample. However, fluorescence is still observed from around this spot (i.e. above and below) and the whole fluorescence signal is collected at the objective lens. The key to the confocal arrangement is the placement of a second pinhole between the detector and the objective lens, such that only the light from the focal point reaches the detector. Fluorescence from around the focal point is blocked by the pinhole as seen in Figure 1.42. In practice, only one lens can be used as condenser and objective and a single pinhole is sufficient. Fluorescence microscopes of this sort can provide resolution of the order of 200 nm, under favorable conditions.

1.8.5 Raman spectroscopy

Introduction and instrumentation

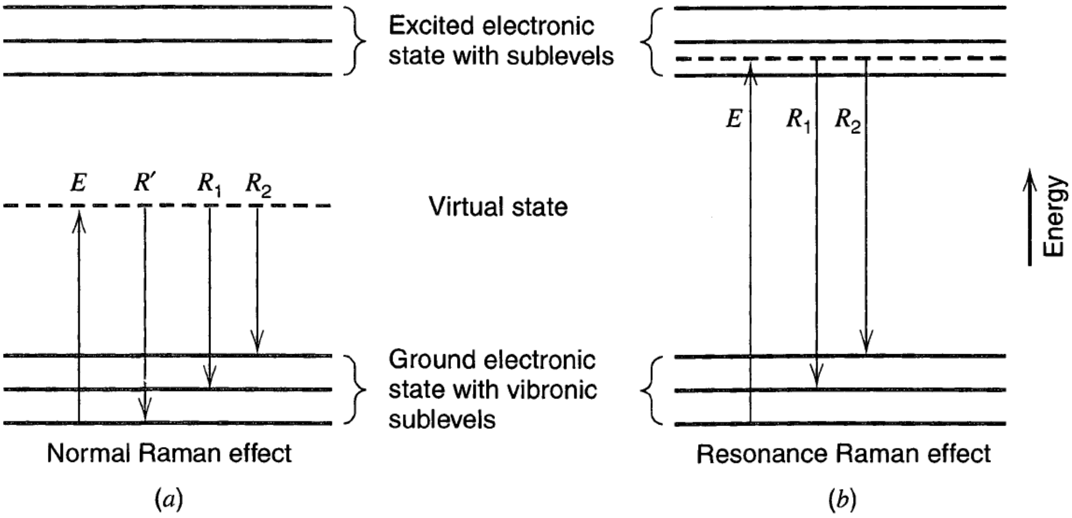

Fig. 1.43: Schematic of Raman, a, and resonance Raman, b, effects. Molecules are excited (E) to a virtual state and relax, R, by scattering light. Rayleigh scattering (R') involves no change in energy, while Raman scattering (R_1 or R_2) results in light shifted in energy by amounts equal to the vibrational levels of the molecule. Resonance Raman involves excitation near an electronic transition. Adapted from reference 16.

Raman spectroscopy is a widely used technique which is based on the inelastic scattering of light. Incident light may be scattered from a substrate in two possible ways; Rayleigh or Raman scattering. Rayleigh scattering is an elastic process and the wavelength of the light is preserved. Raman scattering, however, is inelastic and scattered photons may lie at shorter (Stokes) or longer (Anti-Stokes) wavelengths than the incident radiation. The difference in energy between the incident and scattered light is equivalent to the vibrational quanta of the molecules which scatter the light. Raman spectroscopy provides information complementary to that of IR spectroscopy. A crucial advantage over IR is the insensitivity of Raman to water but it suffers from an inherent insensitivity; on average one in every 10^6 photons undergoes Raman scatter under normal conditions.

Figure 1.43 shows a schematic to illustrate the mechanism of both the Rayleigh and Raman scatter. Incident light can cause excitation of electrons to a "virtual state."[5] Relaxation from this state results in emission of photons, the energies of which depend on which vibrational state the molecule relaxes to. Rayleigh scatter (R') occurs when there is no change in vibrational states while the Raman scatter (R_1 or R_2) results in light shifted in energy by amounts equal to the vibrational levels of the molecule. The principles lines observed are those less in energy than the Rayleigh line (Stokes lines) and these result from relaxation of the virtual state to higher vibrational levels of the ground state, as seen in Figure 1.43. However, if the transition to the virtual state occurs from high vibrational levels of the ground electronic state, the virtual state can relax to low vibrational levels of the ground state. This results in scattered light higher in energy than the Rayleigh line. These anti-Stokes lines contain identical information to, but are significantly weaker than, Stokes lines at normal temperatures.

As a high intensity monochromatic light source is needed lasers are universally used in Raman spectroscopy. The confocal microscope arrangement (described above) is also often used to gain spacial resolution, although it can be less effective for Raman if strongly scattered species lie above or below the confocal plane. The laser beam is focused on the sample using a microscope of high numerical aperture. Scattered light is directed back along the same optical pathway, filtered for Rayleigh scattering and focused through a pinhole to the CCD detector. Only light from the focus can be passed through the pinhole and this removes out of focus background noise.

Raman spectroscopy applied to electrodes

Raman spectroscopy is an attractive method of investigating molecular films on electrodes for several reasons. The structure of the film can be probed and the potential dependence orientation of molecules can be investigated. However, as the intensity of the Raman scatter is inherently weak it is rarely sufficiently sensitive to detect a molecular monolayer. Two methods of enhancement of signal are frequently used to achieve greater sensitivity: Resonance Raman spectroscopy (RRS) or surface enhanced Raman spectroscopy (SERS). Resonance Raman spectroscopy can be performed when the frequency of the laser overlaps with an electronic transition in the sample.[34] This can be seen in Figure 1.43 (b), where the virtual state lies close to an electronic state. This results in a greater interaction between the light and the molecule and typically leads to an enhancement of 5-7 orders of magnitude to the Raman signal for modes associated with the chromophoric units of the molecule.

SERS occurs at submicroscopically roughened coinage metals such as gold, silver and copper and can enhance the signal by typically a factor of 10^7, but there are reports of factors up to 10^{20}. One contributing factor to the enhancement is the heightened electric field experienced by the molecules, arising from the excitation of the metal surface plasmon by the incident radiation. Another contribution to the SERS enhancement comes from broadening of the molecular orbitals, which is experienced by adsorbed molecules on metal surfaces. This can facilitate resonant enhancement. SERS enhancement easily allows investigations of monolayers adsorbed on such metals with surface plasmon bands at similar energies as the incident radiation. As both silver and gold have surface plasmon bands in the visible region they can easily be used as SERS substrates.

1.8.6 Atomic force microscopy

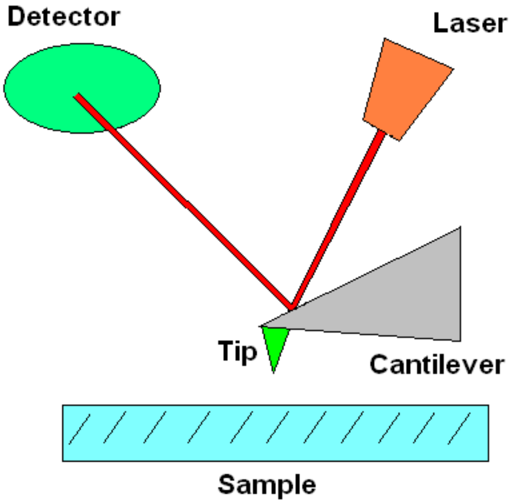

Fig. 1.44: Scheme depicting the principle of AFM. A sharp tip is brought into or near contact with the substrate to be imaged. The tip is scanned in the x-y plane and interacts with the sample, which alters the position of the cantilever. The deflections of the cantilever are measured by a laser.

Atomic force microscopy (AFM) is an extremely powerful technique, capable of atomic resolution, that was developed in the mid 1980s by Binning and co-workers.[222, 223] The technique grew out of the pioneering work of these scientists on scanning tunnelling microscopy (STM), where it was noticed that a variety of forces act on the scanning probe tip. The imaging of samples using these forces was highly attractive as STM can only image conducting substrates.

The principle of AFM is relatively simple and is represented in Figure 1.44. A sharp tip, which need not be atomically sharp, is scanned across the sample in the x-y plane. The tip can touch the sample (contact mode AFM) or remain 10-100 nm above the surface (non-contact mode AFM). The interaction of the tip with the surface depends on several forces, both attractive and repulsive, such as van der Waals forces, electrostatic forces and magnetic forces. These forces act over both long and short ranges, which gives rise to non-contact and contact modes of AFM respectively. The interaction of the tip with the sample causes displacement of the cantilever. The magnitude of the displacement depends on the spring constant of the cantilever and the strength of the tip-sample interactive forces. Typically, the cantilever deflection is measured by focusing a laser on the back of the cantilever and monitoring the amount of beam deviation, although other methods exist. This allows the quantification of the force at the tip-sample interface.

Several modes of operation can be employed in AFM. Constant force imaging mode, (CFI), keeps the cantilever at a constant deflection by means of a feedback circuit. The tip height is adjusted to maintain this deflection, which renders a topographical image. Variable deflection imaging (VDI) simply monitors the cantilever deflection as it is scanned across a surface. Tapping mode AFM is achieved by vibrating the cantilever near the surface. The attractive forces cause an augmentation of this vibration, while repulsive forces dampen it. A topographical image can be achieved by maintaining the tip-substrate height such that the frequency of vibration is constant.

1.9 Conclusion

Recent advances in technology have seen an increase in our understanding of interfacial processes.[224] The development of scanning probe[223] and self assembly[17] techniques in the 1980's have widened the possibilities for interfacial modification and study. The critical areas that these interfacial systems have expanded into include sensing,[1] supramolecular chemistry,[5] electron transfer kinetics,[36] molecular junctions[12] and protein adsorption,[13] while patterning of substrates with sub-micron sized features has also attracted much attention.[190]

This thesis describes work on many of above systems and this chapter has presented an introduction to the concepts of electrode modification with molecular layers. The double layer structure has been shown to be of importance in this area and a brief review of models used to describe its behavior is presented. Cyclodextrin layers are described in Chapter 3 and an introduction to CD chemistry, along with a review of CD monolayers has been presented. This review shows that CD layers can be used as molecular recognition platforms for a variety of target molecules and that the binding events can be modified using many techniques, both electrochemical and spectroscopic.

As metal-monolayer-metal junctions are described in Chapter 4, a summary of electron tunnelling has been presented. The literature relating to STM tunnelling junctions and metal-molecule-metal junctions has been reviewed. This work has shown that significant insights regarding electron transport in molecules can be gained by employing these type of macroscopic junctions. Chapter 5 deals with the desorption of protein layers from electrodes. The relevant literature concerning protein layers and the desorption of proteins has been reviewed here and this work has shown that protein desorption is an activated process, which is usually achieved by a change in solvent polarity or pH. Chapter 6 describes the use of nanostructured materials to study protein release. The literature review presented here has shown that these nanostructured materials offer certain attractive advantages, such as enhancing spectroscopic signals, which may make the monitoring of interfacial molecular processes easier. Finally, the theory behind the major techniques used in this work are briefly reviewed.

Chapter 2

Fabrication and characterisation of substrates

2.1 Introduction

The following chapters deal with the immobilisation of molecules on electrode surfaces. Immobilisation on metal surfaces allows both electrochemical and spectroscopic investigation, often simultaneously.[41,16] Immobilising species on surfaces can often simplify the electrochemical signals observed as the species no longer need to diffuse to the surface.[16] From a spectroscopic point of view, immobilisation at carefully designed substrates can lead to dramatic enhancements of signal. This has led to the development of surface enhanced Raman spectroscopy (SERS) as a useful tool to characterise molecular layers.[5,225] It has recently been observed that fluorescence signals can also be surface enhanced[219,215,216] and these two examples of surface spectroscopy have wide applications in the fields of sensors and supramolecular chemistry. The use of metals, such as gold or platinum, as electrodes provides significant opportunities for surface modification. Alkanethiols have been shown to be very strongly adsorbed on gold[226,28] and mercury[27] electrodes, while pyridine binds strongly to platinum surfaces.[227,228]

The use of immobilised layers as sensors or molecular recognition platforms has been a goal of surface modification for many years.[58, 62] This can be achieved by linking the common surface binding moieties, such as thiol or pyridine groups, to molecules, such as cyclodextrins[10] or calixarenes,[56] capable of some selective interaction with target species. The largest of the common cyclodextrins, γ-CD, is also the least explored in previous studies. However, it has advantages over the smaller CDs, as it alone can complex C_{60},[229] while it has approximately similar capability to complex other α and β-CD guests.[48] The synthesis of a γ-CD molecule linked to two pyridine groups, which is used extensively in Chapters 3 and 4, is described in this chapter, along with the origin of the non-commercially available compounds used in the course of this work.

A key advantage of immobilising electrochemically active species is the removal of mass transport as a limiting factor in the study of electron transfer kinetics. The speed of electron transfer across non-covalent interactions, such as those of host-guest complexes, is especially interesting, considering that this process is similar to electron transfer in biological systems such as proteins[230] and the kinetics of a cyclodextrin-metal complex host guest system are investigated in Chapter 3. Chronoamperometry is a convenient method to observe these electron transfer events, but the RC time constants are too long at conventional electrodes to observe rapid electron transfer kinetics. The RC constant is the time needed for the charging of the double layer at the electrode-solution interface, i.e. the non-faradic current transient. At conventional sized electrodes this current obscures the faradic signal, but microelectrodes[231] have short RC time constants. Therefore, the fabrication of microelectrodes and characterisation of the associated RC constants is a key objective for exploring the nature of electron transfer across immobilised host-guest assemblies and is described in this chapter.

Metal substrates that are structurally modified in a regular way on the nanoscale can show interesting plasmonic behavior. One key objective of substrates of this type is the creation of reproducible SERS platforms. SERS is normally observed at roughened electrodes, but much work has gone into creating SERS active substrates through regular structural modification.[189, 190] Nano-sphere lithography is a useful and cost effective method for the creation of these patterned surfaces.[202] However, it is now becoming evident that fluorescent signals are also enhanced by substrates modified with arrays of sub-micron features.[215] The use of nano-cavity arrays for fluorescent enhancement represents a fresh approach to monitoring molecular layers of fluorescent molecules and is described in Chapter 6. The creation and characterisation of these nano-cavity substrates is critical for the development of these studies and is described in this chapter.

2.2 Experimental

Cyclic voltammetry was performed in a conventional three electrode setup with a platinum mesh as the counter electrode and an Ag/AgCl saturated in KCl reference electrode using a CHI 660 electrochemical workstation. Platinum or gold electrodes were used as working electrodes. All solutions were deoxygenated with Argon prior to use and a blanket of Argon was maintained over the solutions during experimentation.

Impedance spectroscopy was performed using conventional three electrode cell as described above on a BAS-Zahner IM6 impedance measurement unit. An excitation signal of 5 mV was applied to the electrodes and the frequency of this signal was varied between 2000 and 5000 Hz. The DC potential was fixed at 0.3 V (the OCP for this system).

Scanning electron microscopy was carried out using a Hitachi S-3000N scanning electron microscope. Atomic force images were obtained using a Nano-scope III (Digital Instruments) and silicon tapping mode tips (Veeco Probes HMX-10).

2.3 Results and Discussion

2.3.1 Synthesis of γ-CD-py$_2$

Di-6^A, 6^B-deoxy-p-toluenesulphonyl-γ-cyclodextrin, γ-CD-(OTs)$_2$ (0.58 mmols), and 4-(aminomethyl) pyridine (36.4 mmols) were reacted in DMF (10 mL) at 90 ^{0}C for 6 hours. The reaction mixture was poured into acetone (300 mL) and filtered. The precipitate was dissolved in hot water, which was evaporated to approximately 2 mL. This was added to 50 mL of acetone and the resulting precipitate was filtered and dried in a vacuum oven overnight. Product yield was 78% (0.45 mmols, 700 mg). The product was identified by comparing the H-NMR to previous batches of the same compound.

Bis-biphenyl-2,2':6',2''-terpyridine Cobalt (II) ([Co(biptpy)$_2$]$^{2+}$) and terpyridine cobalt (II) ([Co(tpy)$_2$]$^{2+}$) were kindly provided by the School of Chemical Sciences at the University of Birmingham, Edgbaston, Birmingham, B152TT, U.K. The full synthetic procedures and characterisation of the samples, including UV-visible and Raman spectroscopy and electrochemical characterisation, have been previously reported.[232]

2.3.2 Electrode fabrication and cleaning

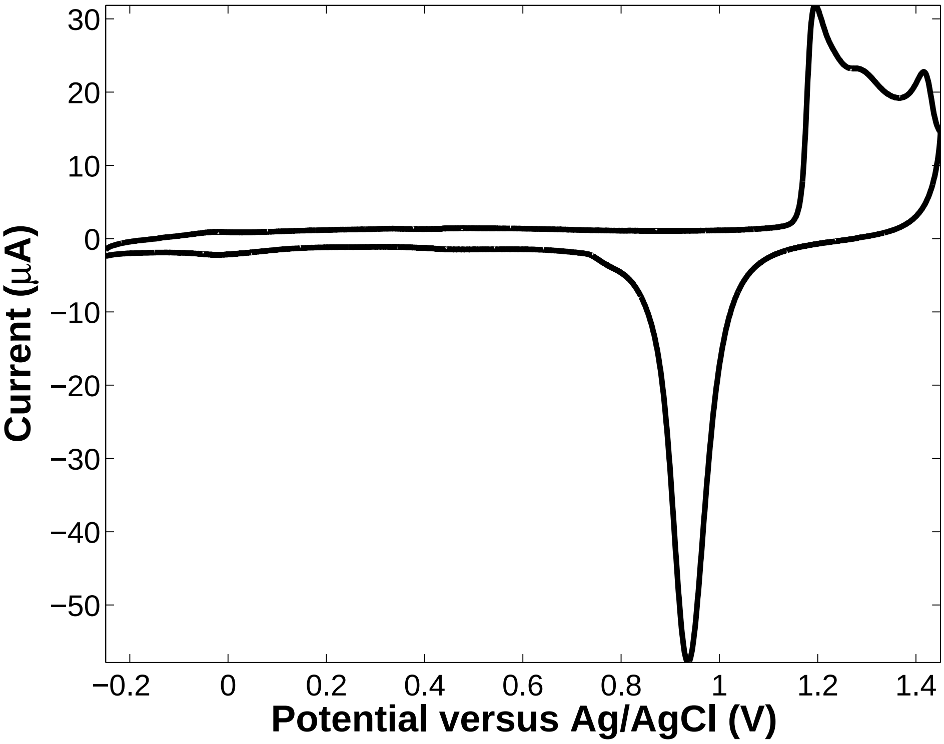

Fig. 2.1: Cyclic voltammogram of a 2 mm diameter gold bead electrode in 0.5 M H_2SO_4. The scan rate is 0.5 V.s^{-1}. The reference electrode was separated from the solution by a salt bridge filled with 0.5 M H_2SO_4 to prevent contamination of the working electrode with chloride ions. The tenth scan is presented.

Both gold disks and beads were prepared from gold wire (99.99 %) obtained from Goodfellow Metals, Cambridge, UK. The gold wire is heated in a butane flame until it forms a bead, typically of diameter 1-2 mm. Platinum electrodes were obtained commercially (CH Instruments) or prepared from platinum wire (99.99 %) obtained from Goodfellow Metals, Cambridge, UK. The platinum wire is cut into approximately 3 cm lengths and soldered to another longer, but inexpensive, connecting wire, which is typically made of copper. This wire is inserted into a glass tube and one end is heated in a butane flame to seal the platinum or gold wire in the glass. This end is then polished with sandpaper to reveal a metal disk. The diameter of the wire used determines the diameter of the disk (both 500 μm and 25 μm were used in the work described in

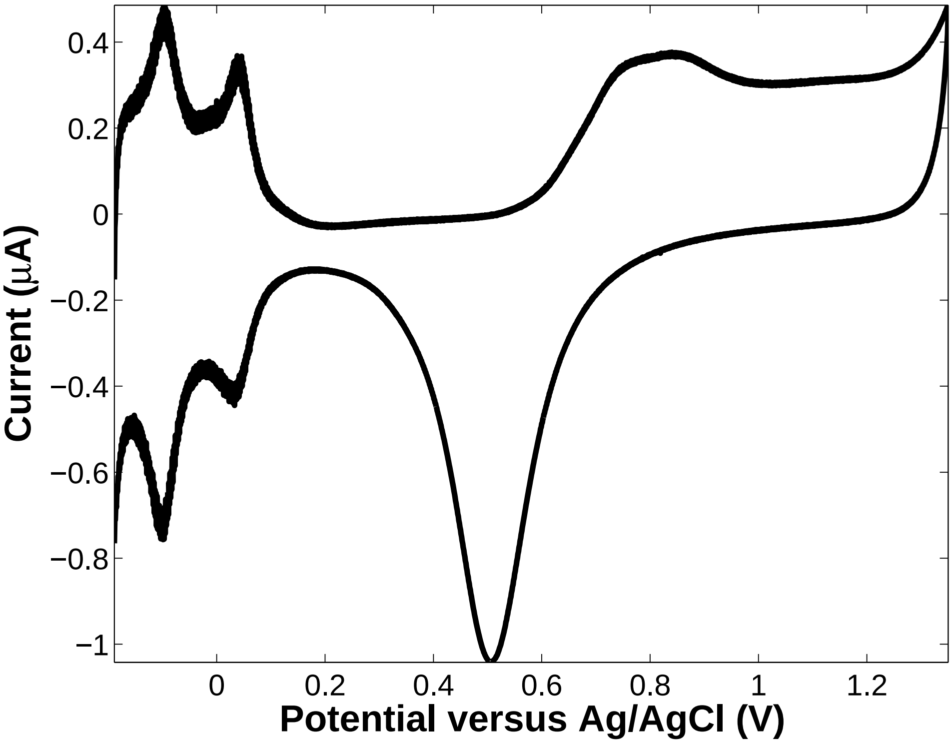

Fig. 2.2: Cyclic voltammogram of a platinum electrode (radius = 250 μm) in 0.5 M H_2SO_4. The scan rate is 0.5 V.s^{-1}. The reference electrode was separated from the solution by a salt bridge filled with 0.5 M H_2SO_4 to prevent contamination of the working electrode with chloride ions. The tenth scan is presented.

Chapter 3). The other end of the electrode is sealed by a plastic cap, through which passes the connecting copper wire. The electrodes are then subjected to successive hand polishing with alumina particles (Buehler, USA) of decreasing size (12.5 μm, 5 μm, 1 μm, 0.3 μm and 0.05 μm) on a felt polishing pad with sonication in water for five minutes between each size.

This polishing procedure is followed by a further electrochemical cleaning step in 0.5 M H_2SO_4. Gold electrodes were scanned between -0.25 V and 1.45 V until stable voltammograms were obtained. The resulting scan can be seen in Figure 2.1, which shows the gold oxide formation at approximately 1.2 V and the subsequent oxide reduction at 0.9 V. Platinum electrodes were scanned between -0.25V and 1.45 and then between -0.2 V and 1.35 V until stable voltammograms were obtained. Figure 2.2 shows a typical voltammogram for this step. The platinum oxidation can be seen at approximately 0.8 V and the oxide reduction is seen at 0.5 V. Hydrogen adsorption and desorption is observed between 0.1 to -0.1 V at two specific sites, resulting in two peaks. An amperometric measurement was then performed at 0.3 V for 30 s to remove adsorbed hydrogen atoms from the platinum surface. The real surface area of the electrode was then found by intergrading the oxide reduction peak where the charge per cm^2 is 390 μC for gold and 420 μC for platinum.[233] The hydrogen reduction peaks can also be used in the case of platinum and the charge per unit area is 210 $\mu C.cm^{-2}$ in this case.[233] The difference between the area determined using the two methods is typically 3%.

The reference electrode was separated from the solution by a salt bridge filled with 0.5 M H_2SO_4 to prevent contamination of the working electrode with chloride ions. Molecular layers were then formed on these substrates.

2.3.3 Microelectrode fabrication and characterisation

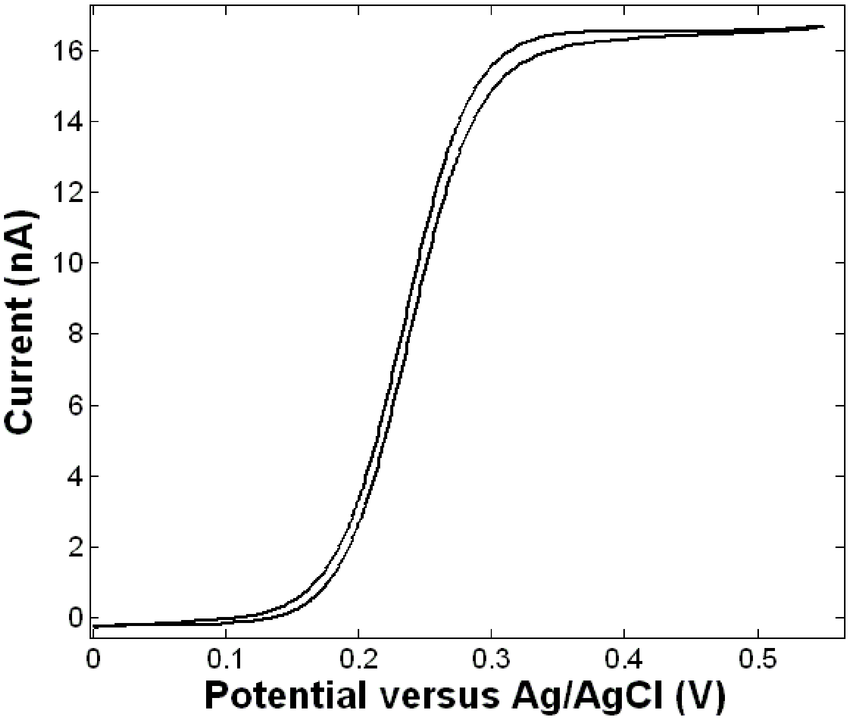

Fig. 2.3: Cyclic voltammogram of a 25 μm platinum electrode in 4.8 mM ferrocene methanol in 0.1 M KCl. The scan rate is 0.0025 V.s^{-1} and the third scan is presented.

As described in the last section, electrodes were prepared from sealing platinum wire (99.99%) of various sizes in soft glass by heating the glass in a butane flame. Micro-electrodes were prepared using 25 μm diameter wire following the previously described procedure. An important factor for electrodes is the surface roughness.[16] This is defined as the ratio of the real and geometric areas of the electrode and is normally desired to be low (i.e. under 2). The real surface area is determined using acid voltammetry and can be reduced by polishing the electrode with small particle size alumina. Cyclic voltammetry in 0.5 M H_2SO_4 can be used to monitor the surface roughness and therefore the progression of the polishing. The geometric area can be obtained by using a solution phase probe of known concentration and diffusion co-efficient and monitoring the peak current. Solution phase probes are only normally affected by the geometric area of the electrode and for macro-electrodes the relationship

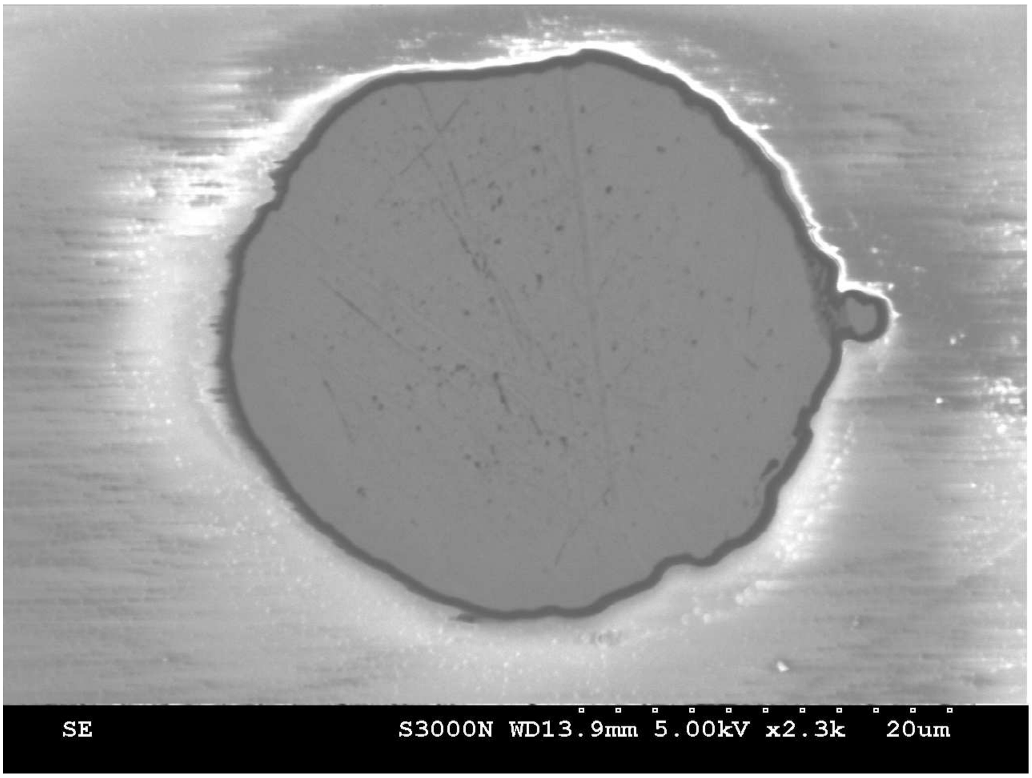

Fig. 2.4: Scanning electron micrograph of a 25 μm platinum micro-electrode, polished with 0.05 μm alumina.

is expressed by the Randles-Sevçik equation which was described in Chapter 1.

The steady state current, i_{ss} seen at micro-electrodes in the presence of solution phase species at slow scan rates can be used to determine the effective electrode radius (r) by Equation 2.1:

$$i_{ss} = 4nFDCr \tag{2.1}$$

where F is Faraday's constant, n is the number of electrons transferred and D and C are the diffusion co-efficient and concentration of the electro-active species respectively. This equation assumes a disk shaped geometry for the electrode.

Figure 2.3 shows the steady state current observed at a 25 μm platinum elec-

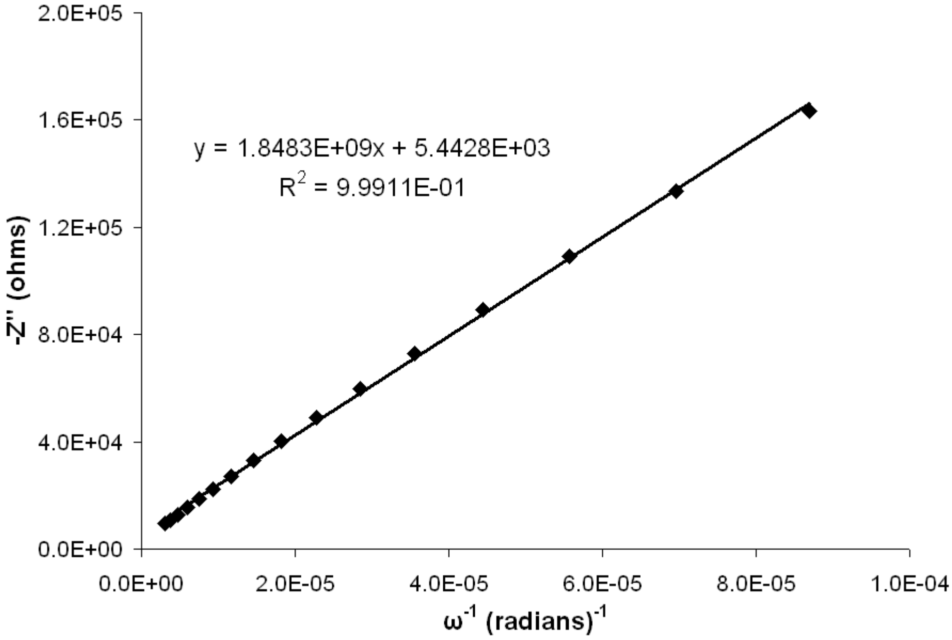

Fig. 2.5: Plot of the inverse of the frequency of excitation signal in radians against the imaginary part of the impedance, Z”, for a 25 μm diameter platinum electrode in 90:10 H_2O: ACN with 0.18 M Na_2SO_4 as the supporting electrolyte. The DC potential applied was 0.3 V versus Ag/AgCl.

trode in 4.8 mM ferrecene methanol (diffusion co-efficient = 6.7 x 10^{-6} $cm^2.s^{-1}$ in aqueous solution). A steady state current of 16.5 nA can be observed which corresponds to a radius of 13.2 μm, which compares favorably with the manufacturer's specifications (25 μm diameter). Scanning electron microscopy (SEM) can be used to investigate the geometry of the electrode and to ensure that the electrode is well sealed in the glass. Figure 2.4 shows a SEM image of the same electrode as that used in the steady state experiment described above. This figure shows that the platinum electrode is well sealed in the glass, is approximately disk shaped and that the electrode diameter is approximately 27 μm, which is in close agreement with the electrochemical determination from the steady state current. This figure shows that the electrode has various surface defects such as scratches although the surface roughness of the electrode was determined as 1.5 by the use of the hydrogen reduction peaks.

The RC constant is an important parameter of micro-electrodes as it determines the time after which meaningful data can be obtained in kinetic studies

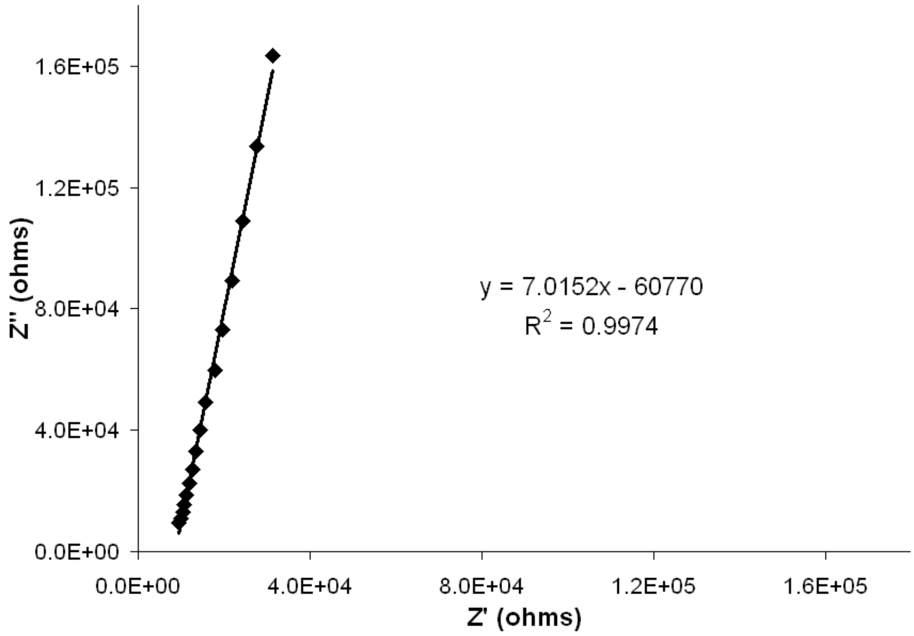

Fig. 2.6: Nyquist plot of a 25 μm diameter platinum electrode in 90:10 H_2O: ACN with 0.18 M Na_2SO_4 as the supporting electrolyte. The DC potential applied was 0.3 V versus Ag/AgCl.

such as chronoamperometry. This parameter was investigated for the 25 μm platinum electrodes by impedance spectroscopy. The imaginary component of the impedance signal is related to the double layer capacitance, C_{dl}, according to Equation 2.2[16]:

$$Z'' = \frac{1}{-\omega C_{dl}} \tag{2.2}$$

where ω is the frequency of the excitation signal in radians. Figure 2.5 shows a plot of the inverse of frequency or excitation signal against Z" for a 25 μm diameter platinum electrode in 90:10 H_2O: ACN with 0.18 M Na_2SO_4 as the supporting electrolyte. This solvent system was chosen as it is the same system used to probe the rate of electron transfer from a cobalt complex ($[Co(biptpy)_2]^{2+}$) to the electrode in Chapter 3 and the determination of the RC constant of the electrodes should be carried out in an identical system for comparison.

The plot shown in Figure 2.5 linear, as predicted by Equation 2.2, and the capacitance can be found from the inverse of the slope of the best fit line. This value can be calculated as 5.3 x 10^{-10} F and is an average capacitance for the frequency range investigated. The imaginary component of the impedance becomes negligible at high frequencies. Therefore, a plot of the real versus imaginary parts of the impedance where the excitation signal is varied should show an x-intercept correlating to the resistance of the cell. Such a plot is shown in Figure 2.6 for a 25 μm diameter platinum electrode in 90:10 H_2O: ACN with 0.18 M Na_2SO_4 as the supporting electrolyte. This plot, also called a Nyquist plot, reveals an x-intercept of 8662 Ω. As the RC constant is the multiple of the cell resistance and double layer capacitance, the RC constant for the 25 μm platinum electrode can be calculated as 4.5 μs under these conditions. This value is typical for this size of electrode in aqueous solutions.

2.3.4 Preparation of nano-cavity gold films

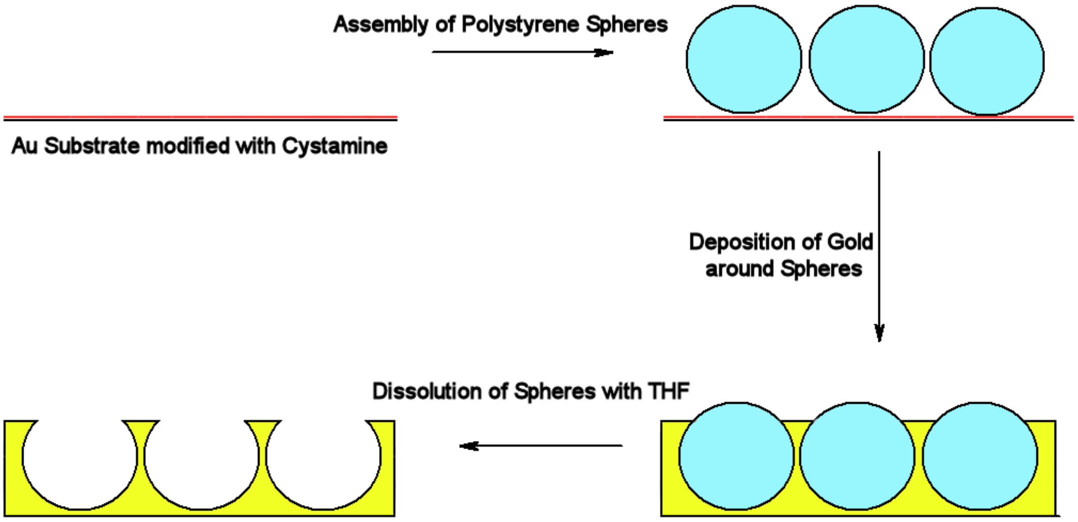

Fig. 2.7: Schematic showing the stepwise creation of nano-cavity arrays. The gold surface is first modified with a cystamine monolayer, represented by the red line. The close packed layer of polystyrene spheres is then formed on the gold surface. Electrochemical deposition of gold around the spheres is then carried out. Finally, the spheres are dissolved in THF to leave nano-cavity arrays.

Nano-cavity gold films have been produced by electrochemical deposition through a polystyrene self-assembled template on gold coated silicon wafers, following the general procedures laid out by Bartlett[202, 206, 207, 212] and others.[208] The overall scheme is portrayed in Figure 2.7. The polystyrene sphere template was formed by first adsorbing a layer of cystamine onto the gold substrates from a milli-molar solution of cystamine overnight. The cystamine layer is represented by the red line in Figure 2.7 and was characterised by blocking studies using $[Fe(CN)_6]^{4-}$ as a solution phase probe. These studies showed that the cystamine forms a layer on the gold surface, presumably through the thiol moiety. The cystamine carries a positive charge on the amine group, and this adsorption step is used as precursor step to the sphere deposition as the polystyrene spheres carry a negative charge due to sulfate groups present on the surface. Thus, electrostatic interactions can aid in sphere layer assembly. Gold coated (400 nm thick) silicon wafers were used as a substrate as this surface is suitably flat. Self-assembly of the spheres was achieved by immersing the cystamine coated slides in a 0.1% solution of 820 nm polystyrene spheres

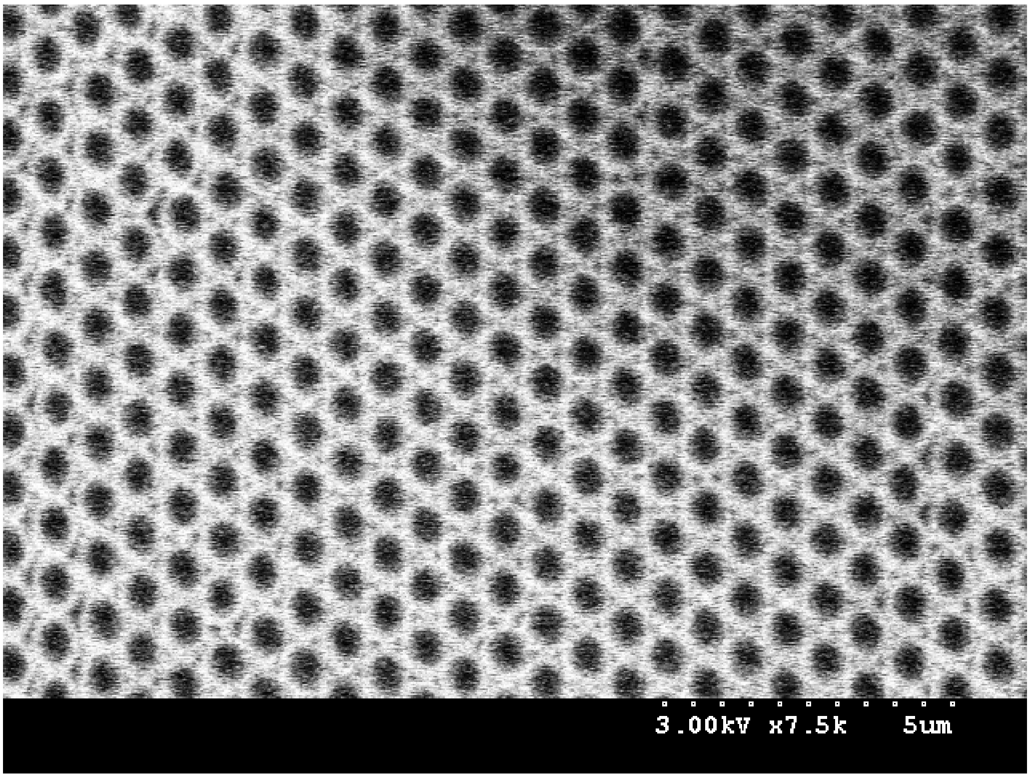

Fig. 2.8: Scanning electron micrograph of 820 nm polystyrene spheres assembled on a gold substrate, by evaporation of a 0.1% solution of spheres.

in water and evaporating to dryness at room temperature. This process can typically take several days.

Figure 2.8 shows an scanning electron microscopy (SEM) image of the resulting monolayer of 820 nm spheres assembled on gold. The voids between the spheres can be seen in the template. This figure shows that the spheres form well ordered close packed layers and although this packing can be described as hexagonal packing other types of packing have been observed in SEM images, such as cubic. Overall, the sphere assembly is most successful when room temperatures and pressures were used to evaporate the solvent. High temperature ($> 70^0$ C) and/or low pressure (-80 kPa) evaporation leads to well ordered layers, but the order does not extent beyond a few hundred micrometers. When evaporated at room temperature, several square centimeters can be successfully assembled and deposited, although this process is limited by the long times needed to evaporate a suitable amount of solvent to coat these large areas.

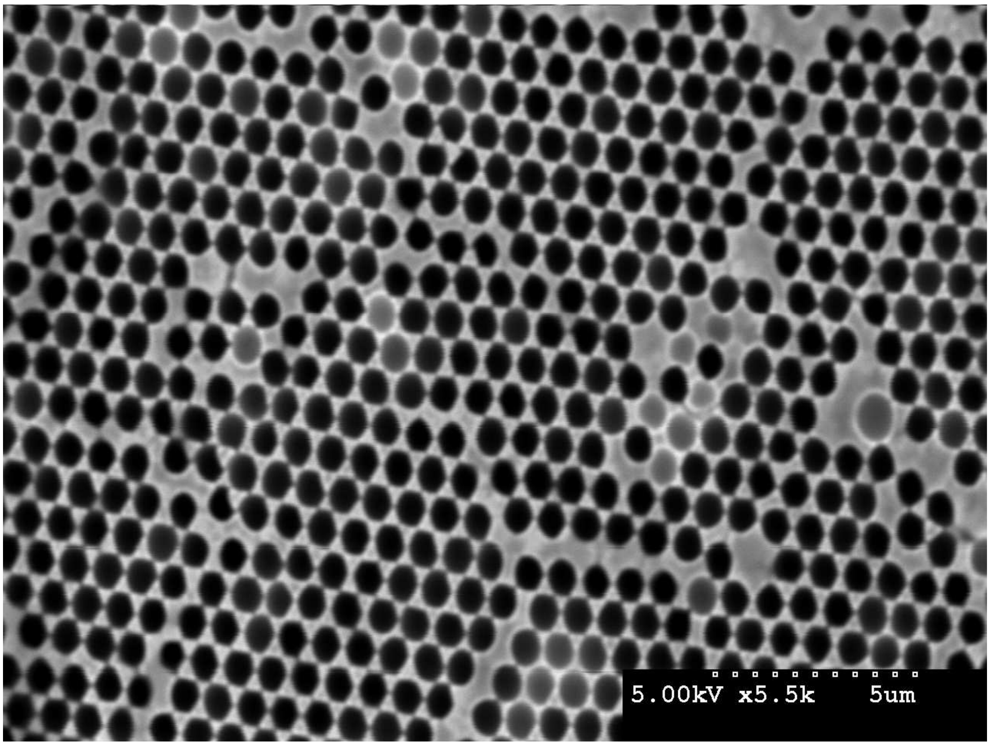

Fig. 2.9: Scanning electron micrograph of a macro-porous Au film formed by electrochemical deposition through a template of 820 nm polystyrene spheres assembled on a planar gold surface. Electrodeposition of gold was achieved at a potential of -0.95 V in a TG-25 RTU-Technic solution and passing approximately 0.35 $C.cm^{-2}$ of charge. The polystyrene spheres have been dissolved by sonication in THF.

The electrochemical deposition through these templates was achieved using a commercially available solution (TG-25 RTU-Technic Inc.) which contained 6.8 $g.L^{-1}$ of gold. A potential of -0.95 V versus Ag/AgCl (sat. KCl) was applied until a charge of approximately 0.35 $C.cm^{-2}$ was passed. This normally resulted in a layer thickness of approximately 700 nm and passing more or less charge results in a thicker or thinner gold layer. If the coulometric efficiency is assumed to be approximately 1, the charge need to completely cover the spheres can be calculated as 0.48 $C.cm^{-2}$. Therefore, passing a charge of approximately 0.36 $C.cm^{-2}$ should result in a layer approximately 700 nm thick. This relationship is obviously more accurate when all of the surface has been successfully coated with close packed spheres. The polystyrene spheres are then dissolved by sonication in THF for one hour. Figures 2.9 and 2.10 show SEM images at various magnification of the resulting nano-cavity assemblies.

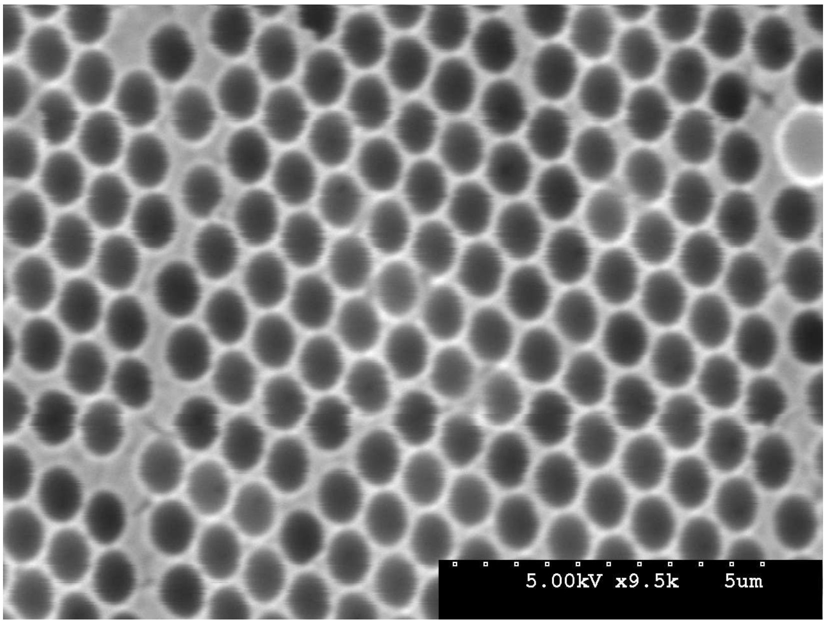

(a)

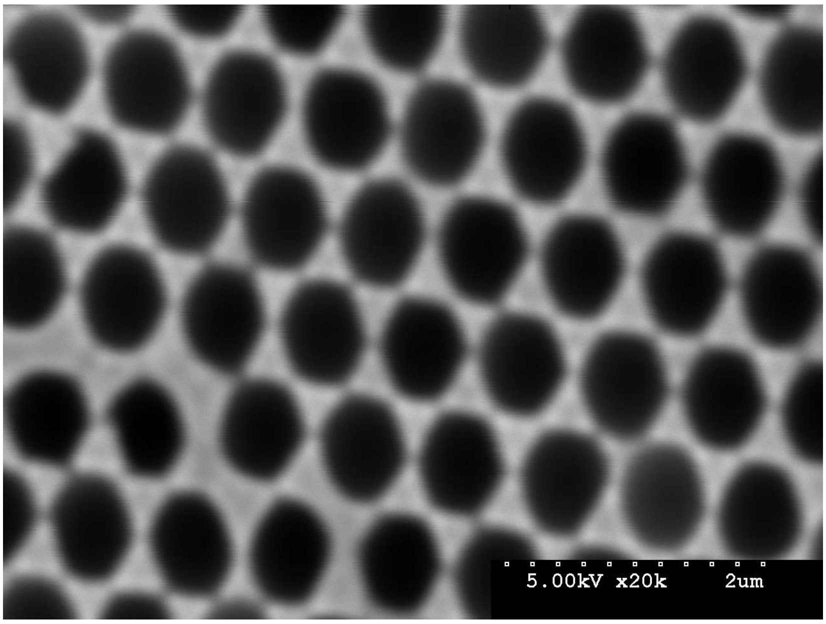

(b)

Fig. 2.10: Scanning electron micrograph of a macro-porous Au film formed by electrochemical deposition through a template of 820 nm polystyrene spheres assembled on a planar gold surface. Electrodeposition of gold was achieved at a potential of -0.95 V in a TG-25 RTU-Technic solution and passing approximately 0.35 C.cm^{-2} of charge. The polystyrene spheres have been dissolved by sonication in THF. The average size of the cavity opening is 600 nm.

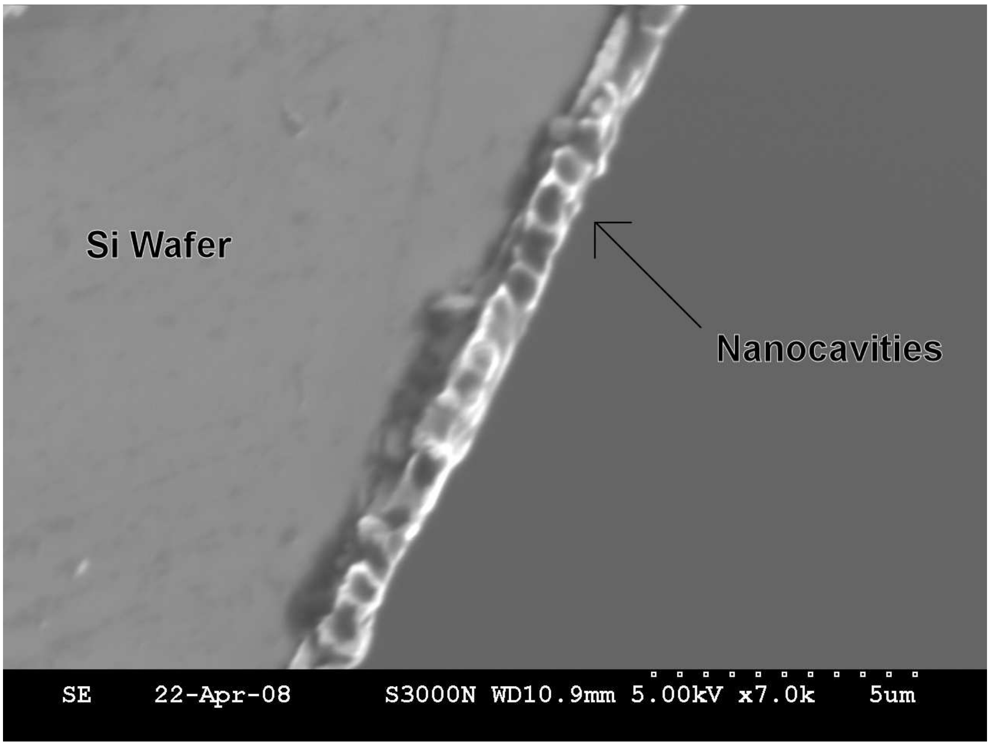

Fig. 2.11: Scanning electron micrograph of a macro-porous Au film, formed as previously described, viewed in parallel with the x-y plane of the substrate.

These images show that the cavity openings are approximately 600 nm in diameter. A small number of undissolved spheres can be seen in Figures 2.9 and 2.10a. For a 820 nm sphere a diameter of 600 nm is achieved at a thickness of either 700 or 120 nm depending on whether the cavity thickness is greater or smaller than the sphere radius. The electrochemical charge passed during the deposition step suggests that the cavity thickness is the former value, i.e. enough charge has been passed to deposited the gold to the former thickness. However, this calculation assumes 100% coulometric efficiency.

This uncertainty can be resolved by examining the thickness of the nano-cavity arrays using SEM. Figure 2.11 shows the side view of the nano-cavities deposited on a gold coated silicon wafer. This image was obtained by cracking a wafer and examining the edge. The silicon wafer, the 400 nm Au deposition and the spherical voids can be seen. The silicon (left side of the figure) is clearly the predominant part of the wafer and at the edge a small region of somewhat lighter shade can be attributed to the 400 nm thick deposited

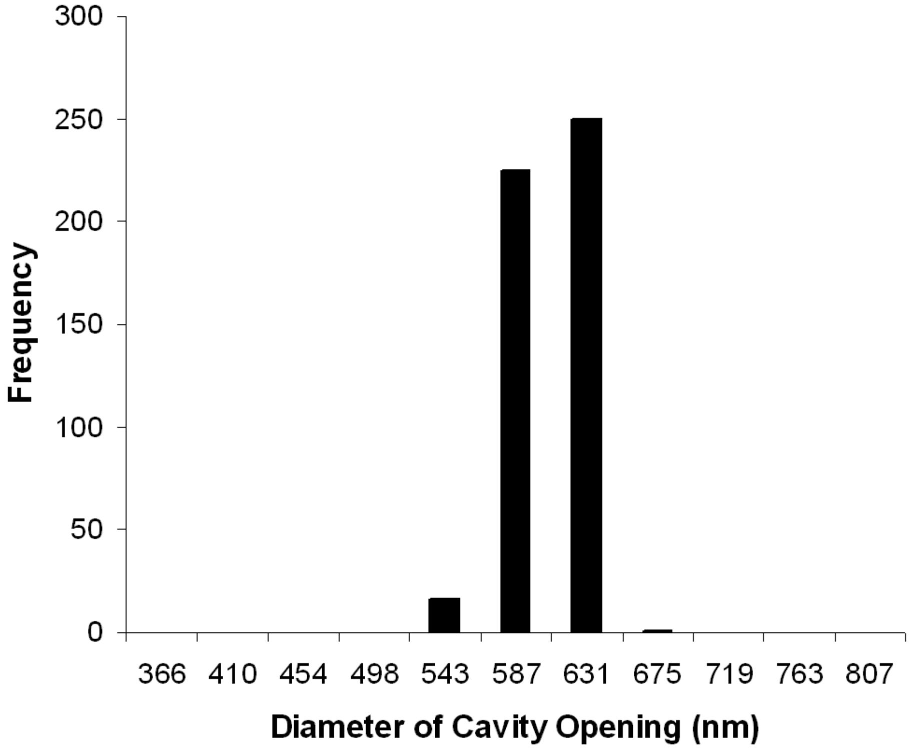

Fig. 2.12: Frequency distribution of the cavity opening diameter of Figure 2.9, as determined using Image J software.

gold. The cavities are clearly observed on top of this region. The cavities are approximately 700 nm thick in this image which suggests that the thickness obtained by monitoring the charge passed from the electrochemical deposition is a reasonable value.

The average cavity opening diameter was also investigated using image processing software (Image J) and Figure 2.12 shows a bar chart of the cavity opening diameter, which was obtained from Figure 2.9. The bar chart shows that the majority of the cavities have openings in the range between 587-630 nm. This is consistent with observations presented above.

Multi-layers of cavities can be formed by adsorbing more than a monolayer of spheres onto the substrate and depositing correspondingly more charge than that needed for monolayer cavity formation. This is achieved by increasing the concentration of the sphere deposition solution, typically to 1-10%, and

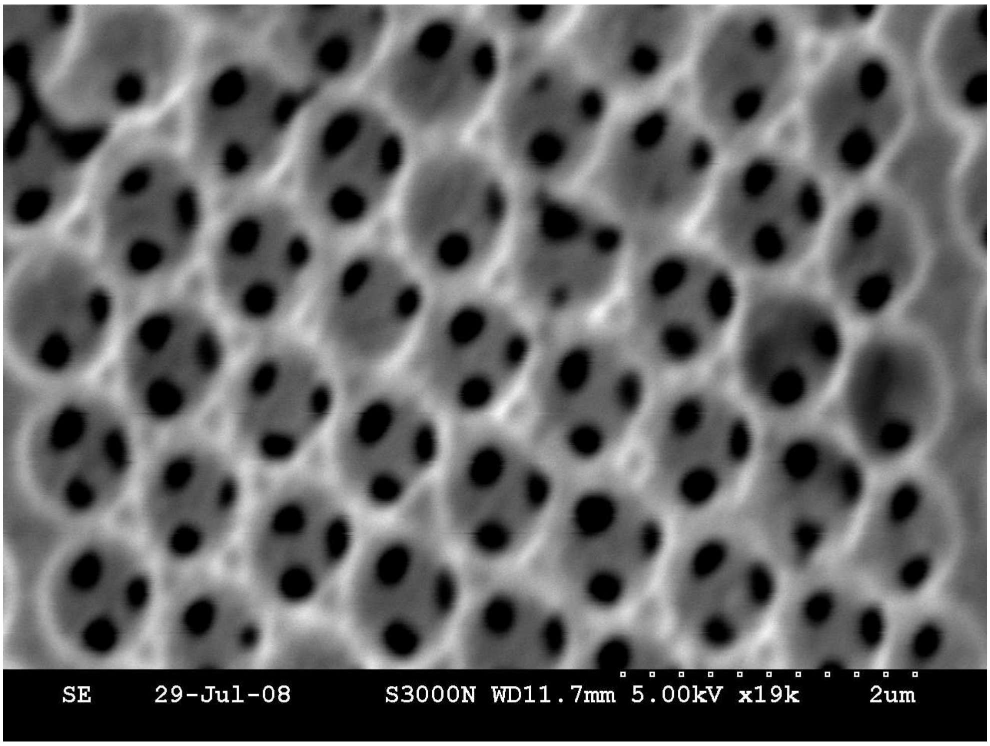

Fig. 2.13: Scanning electron micrograph of a multi-layer Au nanocavity film formed by electrochemical deposition through a three dimensional template of 820 nm polystyrene spheres assembled on a planar gold surface. Electrodeposition of gold was achieved at a potential of -0.95 V in a TG-25 RTU-Technic solution and passing approximately 0.8 C.cm^{-2} of charge. The polystyrene spheres have been dissolved by sonication in THF.

evaporating to dryness. This results in multilayers of spheres, through which gold can be deposited as previously described, creating a multi-layer array. Figure 2.13 is a SEM image of a multi-layer assembly, where the spheres have been dissolved in THF. Small holes ($\sim$ 150 nm) can be seen in the cavities giving entry to cavities underneath. These holes result from the inability of ions to deposit close to the contact points of the spheres. These images suggest that the spheres pack in a close packed fashion. Although not used subsequently in this study, these substrates offer some advantages over the 2-dimensional arrays previously described. The cavities are capable of providing localised surface plasmons, which can lead to enhancement of spectroscopic signals, but the larger surface area could lead to greater signal intensity. The ease with which these relatively complex 3-dimensional structures can be created demonstrates the power of this procedure.

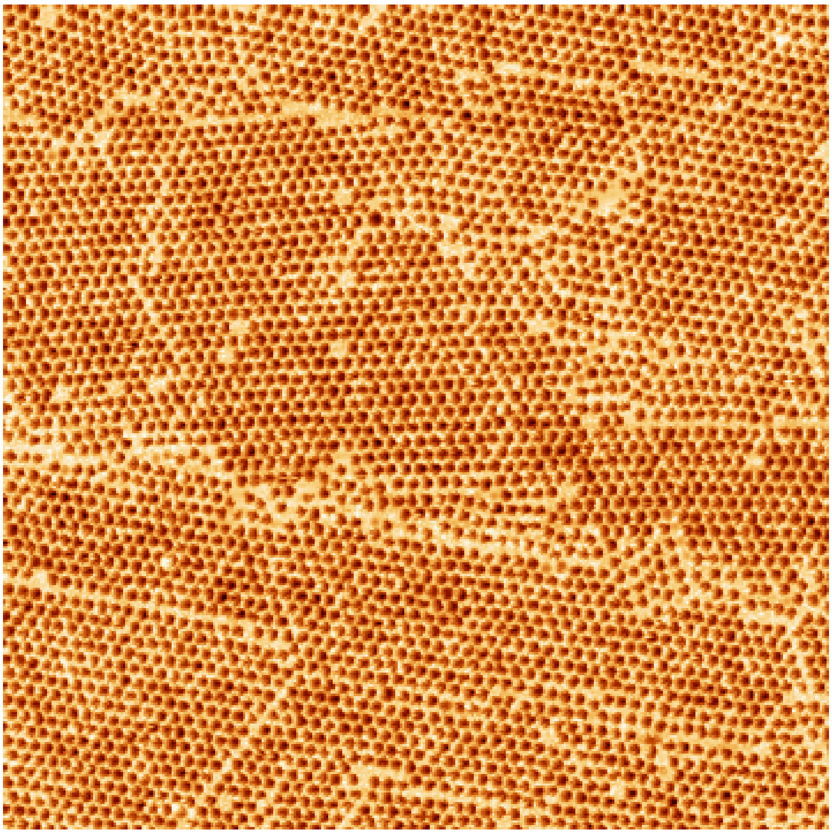

Fig. 2.14: Atomic force micrograph of a macro-porous Au monolayer film formed by electrochemical deposition through a template of 820 nm polystyrene spheres assembled on a planar gold surface. Electrodeposition of gold was achieved at a potential of -0.95 V in a TG-25 RTU-Technic solution and passing approximately 0.35 C.cm^{-2} of charge. The polystyrene spheres have been dissolved by sonication in THF. The image dimensions are 50 x 50 μm.

The nano-arrays can also be investigated using atomic force microscopy (AFM). Figure 2.14 shows an AFM image of a nano-cavity array obtained using tapping mode AFM. This image shows an ordered array of cavities over a 50 μm^2 area. This figure clearly shows the boundaries between close packed domains of cavities but the regular sub-micron spherical holes are observed which is consistent with the SEM data presented above.

2.4 Conclusion

This chapter has described the synthesis of a γ-CD di-functionalised with pyridine moieties for surface binding. This compound is used extensively in Chapters 3 and 4 to create CD platforms on platinum capable of molecular recognition and in the formation of CD molecular junctions. This chapter has also outlined the fabrication and cleaning procedures for several of the substrates that are used in the remaining sections of this thesis. These include gold and platinum disk macro-electrodes, platinum microelectrodes and nano-cavity arrays, all of which were fabricated during the course of this work. A key advantage of all these substrates is the ease with which they can be fabricated at low cost. This is in stark contrast with nano-lithographic techniques,[197, 217] which are frequently used for sculpting SERS substrates.

Micro-electrodes have been fabricated by sealing micrometer (25 μm) sized platinum wire in glass. The resulting surface was investigated using SEM and steady state cyclic voltammetry. The radius of the electrode was found to be approximately 13 μm by each technique. The RC constant of the electrode was investigated using electrochemical impedance spectroscopy (EIS) and was found to be 4.5 μs. These electrode are employed in Chapter 3 to investigate the speed of heterogeneous electron transfer from a metal center docked into CD monolayer to the electrode surface. The use of electrodes with small RC time constants is crucial for this process.

The creation of nano-cavity arrays by deposition of gold through a polystyrene sphere template was described and the resulting surfaces were investigated using SEM and AFM. These images showed regular sub-micron cavities, of average cavity openings of 600 nm, had been formed, after the spheres had been removed by sonication in THF. These surfaces are extremely useful as platforms which can enhance spectroscopic signals, such as Raman or fluorescence, and this is explored in Chapter 6.

Chapter 3

Surface immobilised γ-cyclodextrins: Electrochemical and spectroscopic characteristics

3.1 Introduction

The creation of platforms capable of molecular recognition is a major goal of surface modification.[2,5,58] Among host-guest systems the cyclodextrin family has been one of the earliest and widely studied due to its non-toxicity, its relatively simple synthetic pathways and its extensive and well characterised host-guest chemistry.[10,46,48] Immobilising cyclodextrins (CDs) on surfaces has been shown to be an attractive route to the creation of molecular recognition sites described in Chapter 1.[53,78,77,2] The development of CD monolayers as functional surfaces depends on several key issues, not all of which have been previously addressed. The creation of tightly packed CD monolayers is difficult and alkanethiol molecules are often co-adsorbed to achieve fully blocking layers. However, the effect of this process on the cavity orientation and its ability to bind guests is unknown. The differences between solution phase and interfacial binding were highlighted early in the study of CD monolayers,[62] but the origins of these differences are also unclear. The effect of varying the binding ligands on the inclusion constant has been characterised extensively in solution,[10] but this issue has not received as much attention for interfacial CD assemblies. Lastly, the rate of electron transfer across a CD-metal interface has not been investigated, but is likely to prove critical in any potential device applications.

As discussed in Chapter 1, the investigation of CD modified interfaces has been carried out by several groups.[88, 82, 68, 62, 96, 65] Kaifer and co-workers described a thiol modified β-CD which could detect μM levels of ferrocene in solution.[62] The concept of sealing or "backfilling" the gaps between the CD cavities was first forwarded in this publication. Kitano and co-workers have used thiolated CDs as sensors for several small molecules such as hydroquinone and phthalic esters.[70, 73, 71] CDs have been shown to interact through the face OH groups in the solid state,[234, 235] but the ability of adsorbed CDs to interact with each other has not been investigated fully, although Huskens has shown that methylation of the primary face decreases the order seen in AFM images of β-CD monolayers.[76] This was attributed to the breaking of inter-molecular H-bonding between the hydroxyl groups at the primary CD face. The largest of the common CDs, γ-CD, has not been as extensively utilised, but Suzuki and co-workers have reported a lipoyl group tethered γ-CD monolayer which could detect ferrocenecarboxylic acid in solution.[100] Suzuki also explored the difference in monolayers comprised of different isomers of di-substituted CDs.[101]

Many of these reports use co-adsorption of alkanethiols to backfill the defective sites on the electrodes between CD cavities.[74, 62, 63] However, as previously mentioned there has been little mention of the effect that this process has on CD orientation. The creation of receptor sites on platinum surfaces using a pyridine modified cyclodextrin, di-6^A, 6^B-deoxy-6-(4-pyridylmethyl)amino-γ-cyclodextrin (γ -CD-$(py)_2$), is described in this chapter. The effect of backfilling on the orientation of the di-substituted γ-CD is investigated. The importance of binding groups is also demonstrated and the thermodynamics of binding for the guest $[Co(biptpy)_2]^{3+}$ are probed. Several groups[62, 77, 71] have reported electron transfer at CD monolayers but the dynamics of this processes remain largely unexplored. Therefore, the rate of electron transfer from $[Co(biptpy)_2]^{2+}$ to the platinum surface is investigated.

3.2 Experimental

3.2.1 Apparatus

Cyclic voltammetry was performed in a conventional three electrode setup with a platinum mesh as the counter electrode and an Ag/AgCl saturated in KCl reference electrode using a CHI 660 or 660A electrochemical workstation. All solutions were deoxygenated with Argon prior to use and a blanket of Argon was maintained over the solutions during experimentation. The working electrode was prepared by polishing with alumina followed by electrochemical cleaning as described in Chapter 2.

AC voltammetry experiments were carried out on a CHI 660 electrochemical workstation using an excitation signal of 5 mV and at a frequency of 512 Hz. This excitation signal was chosen as it lies within the linear region of the current-overpotential relationship and this frequency was chosen as it is outside of the region where the capacitance changes significantly with frequency. Capacitance-time traces were constructed using AC voltammetry at potentials of 0 V on gold and 0.3 V on platinum. Capacitance-potential profiles were also constructed using AC voltammetry.

Raman spectroscopy was performed on a Horiba Jobin Yvon HR800UV using an Argon ion laser (458 nm) and the excitation wavelength was focused through a 10x objective lens on the electrode surface. Typical acquisitions were 10 seconds in length and performed ten times to acquire a spectrum. The electrodes were cleaned and roughened prior to use by a modification of the method described by Tian and co-workers.[236] Following the electrochemical cleaning the electrode potential was stepped between -0.2 V and 2.4 V 20000 times where the step length was 0.02 seconds in 0.5 M H_2SO_5. The potential was then held at 0 V for 400 seconds to fully reduce the surface followed by further cycling in 0.5 M H_2SO_5 between -0.2 V and 1.35 V until stable voltammograms were obtained. The average surface roughness after this treatment was 7.

Chronoamperometry was performed on a custom built programmable function generator-potentiostat, which had a rise time of less than 10 ns. This was used to apply potential steps of variable pulse width and amplitude directly to a two-electrode cell. A Pt foil and an Ag/AgCl reference electrode were combined to form a counter electrode. The foil lowered the resistance and provided a high-frequency path. The current-to-voltage converter was based on a Comlinear CLC 203 AI operational amplifier with a 1500 Ω feedback resistance and a response time of less than 10 ns. The chronoamperograms were recorded using a HP54201A digital oscilloscope in the 256X time-average mode.

Microelectrodes were fabricated as described in Chapter 2.

3.2.2 Materials

γ -CD-(py)$_2$ was synthesised as described in Chapter 2. [Co(biptpy)$_2$]$^{2+}$ and [Co(tpy)$_2$]$^{2+}$ were synthesised as described previously,[237] and obtained from the School of Chemical Sciences at the University of Birmingham, Edgbaston, Birmingham, B152TT, U.K.

Osmium bisbipyridyl 2-(4-adamantylphenyl)imidazo[4,5-f] [1,10]phenanthroline (Osmium-adamantyl) was synthesized as described in the literature for the ruthenium analogue.[238]

Monolayers of γ-CD-(py)$_2$ were formed by immersing the working electrode into a solution containing 100 μM γ -CD-(py)$_2$ overnight. Backfilling of the layers was performed by subsequently immersing the γ -CD-(py)$_2$ layers in a solution containing 2 mM 1-admantylamine and 0.2 mM 1-nonanethiol in ethanol. The adamantyl group has a strong affinity for the CD cavity and is expected to block the cavities while the alkanethiol fills the defects. Backfilled monolayers were thoroughly washed with Milli-Q water before use. Solutions of [Co(biptpy)$_2$]$^{2+}$ and [Co(tpy)$_2$]$^{2+}$ in the concentration range 1-40 μM were prepared in 90:10 H_2O/ACN v/v, with 0.18 M Na_2SO_4 as the supporting electrolyte by dissolving the cobalt complexes first in the acetonitrile.

3.3 Results and discussion

3.3.1 Adsorption of γ -CD-(py)$_2$ on electrodes

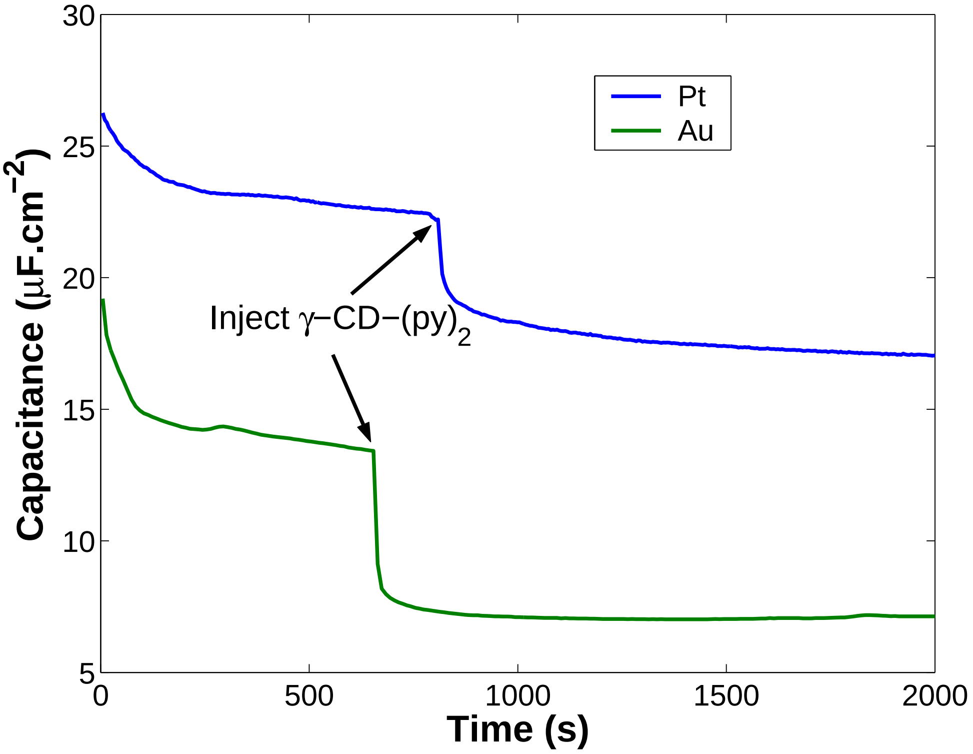

Fig. 3.1: Capacitance of gold and platinum electrodes at 0.3 V versus Ag/AgCl in 0.2 M Na_2SO_4 with addition of γ -CD-(py)$_2$ as indicated. The final concentration of the γ -CD-(py)$_2$ is 100 μM.

Pyridine has been used extensively as a surface binding molecule on several substrates[227, 33, 239] and therefore the pyridine founctionalised CDs were expected to adsorb readily onto gold and platinum electrodes. Figure 3.1 shows that the capacitance drops significantly after an injection of γ -CD-(py)$_2$, suggesting that the functionalised CDs adsorb on both surfaces. As explained in Chapter 1, this is a typical result for the formation of an organic type monolayer in aqueous solution. The plot also outlines a problem encountered throughout this section of the work i.e. the capacitance is seen to decrease over long times before addition of the γ -CD-(py)$_2$ to the solution (principally over the first 400 seconds). This is attributed to the fact the electrode has been electrochemically cleaned at the beginning of these experiments making

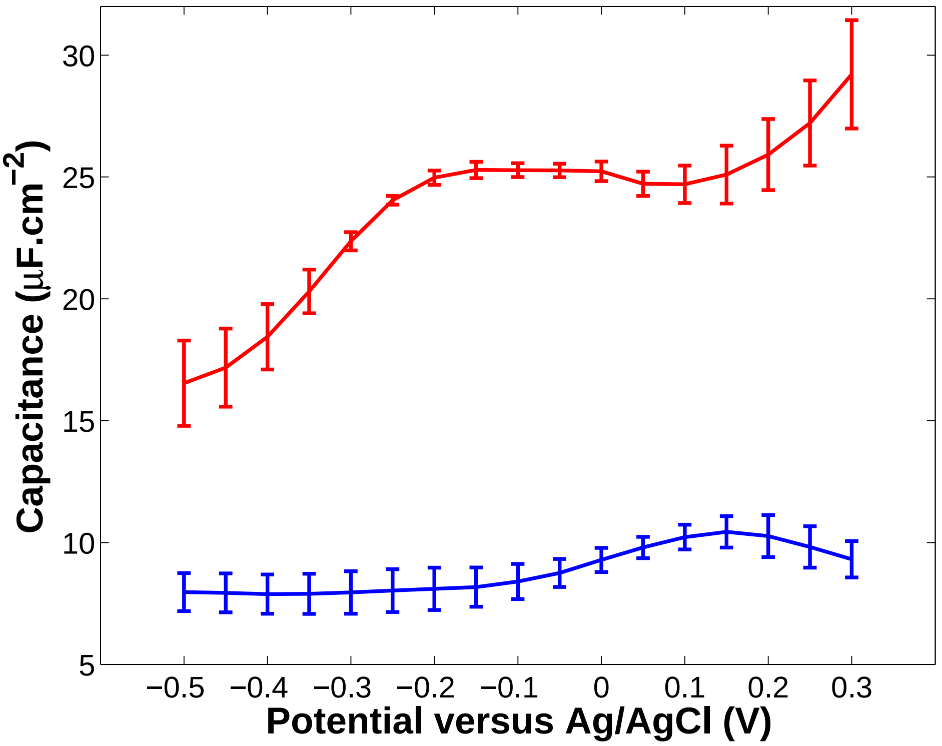

Fig. 3.2: Capacitance of gold electrodes in 0.2 M Na_2SO_4 at various potentials versus Ag/AgCl. The red line signifies the capacitance of bare electrodes and the blue line indicates the capacitance of electrodes modified with γ -CD-(py)$_2$.

it susceptible to adsorption of adventitious impurities from the bulk solution. It is important to note that the adsorption of these impurities proceeds at a slower rate than the CD adsorption, due to the differences in concentration of both species. The impurities are expected to be in the nano-molar range, therefore after 500 seconds approximately 1 x 10^{-13} moles may be transported by mass transfer to a 1 cm^2 site. Therefore, the adsorption of impurities should not greatly influence the subsequent adsorption of the functionalised CDs over this time range.

The reproduction of a blank measurement proved difficult for the reasons outlined above and the most reproducible results were achieved using freshly prepared electrodes. However, this simple experiment confirms that adsorption of γ -CD-(py)$_2$ is possible on both surfaces due to the large, punctuated capacitance drop upon addition of γ -CD-(py)$_2$ to the cell. The adsorption dynamics were not rigourously studied but appear to follow Langmuir first order kinetics

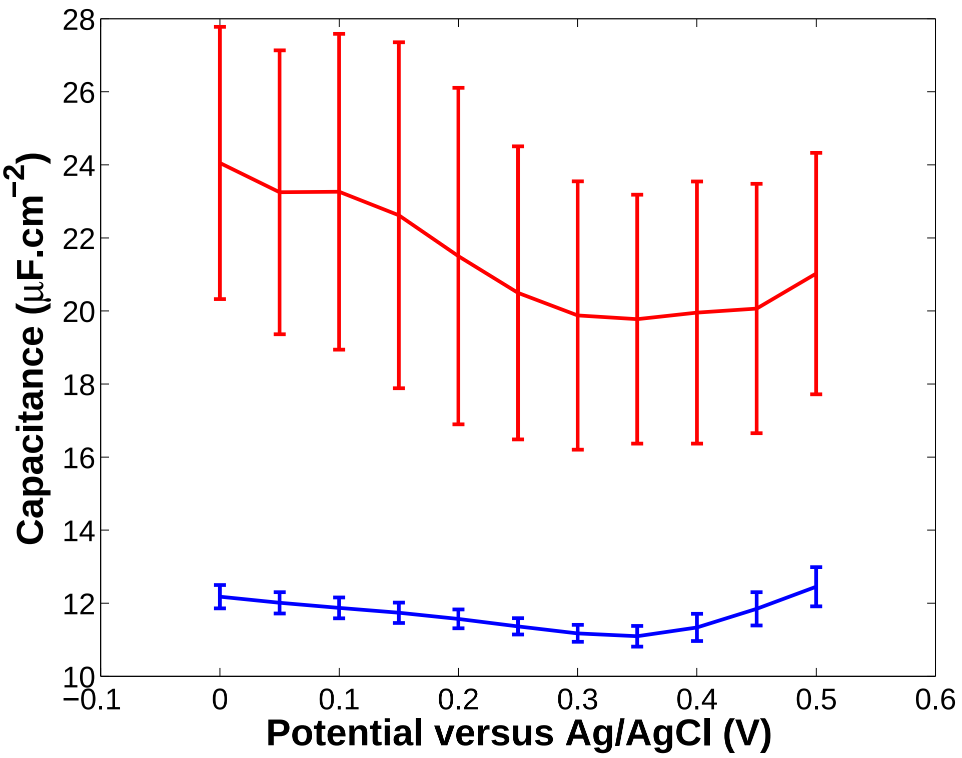

Fig. 3.3: Capacitance of platinum electrodes in 0.2 M Na_2SO_4 at various potentials versus Ag/AgCl. The red line signifies the capacitance of bare electrodes and the blue line indicates the capacitance of electrodes modified with γ -CD-$(py)_2$.

initially, before becoming dominated by mass transfer effects as the depletion region near the electrode grows with time.

The capacitance as a function of applied potential was then measured using AC voltammetry for both bare and modified substrates. The results can be seen in Figure 3.2 for gold electrodes and Figure 3.3 for platinum disk electrodes. These figures clearly show that the capacitance drops significantly for the modified electrode over the potential range investigated and that this final capacitance is approximately independent of applied potential, in accordance with the theory developed by Helmholtz.[16] The capacitance of the bare gold electrode shows significant potential dependence. This can be attributed to specific adsorption of sulphate ions at positive potentials and to possible surface re-construction effects at negative potentials. The capacitance after monolayer adsorption is lower due the decrease in the dielectric constant of the CD layer compared to the aqueous solution and to a greater separation of ions from the electrode surface. This capacitance after monolayer formation is very stable and also more reproducible than that of the bare electrode, presumably due to the fact that the effects of impurities in the double layer are negated due to the greater separation induced by the adsorbed layer.

It can also be seen that the final capacitance was lower on gold (approximately 8 μF.cm^{-2}) than platinum (approximately 10 μF.cm^{-2}), indicating perhaps greater packing density of the layer on gold. These values are consistent for CD molecules variously functionalised and adsorbed on gold.[88, 62] The value found for alkanethiol adsorption on gold is approximately 1-3μF.cm^{-2} depending on the chain length,[240] indicating that the CD layers are not as closely packed as the classical alkanethiol layer. This is almost certainly the result of steric hinderance as the maximum surface coverage of this molecule can be calculated as 7.4 x 10^{-11}mol.cm^{-2} for a hexagonally packed monolayer due to the larger dimensions of the CD compared to alkanethiol molecules, e.g. γ-CD is approximately 1.7 nm in diameter.

As the capacitance is approximately independent of applied potential, the theory developed by Helmholtz can be applied to calculate the dielectric constant of the layers, ϵ according to the following Equation,

$$C = \frac{(\epsilon \varepsilon_0)}{d} \tag{3.1}$$

The thickness of the layer (d) is estimated as 1.3 nm if one considers that the CD molecule is 0.78 nm deep and the pyridine linker is approximately 0.5 nm. Thus, the dielectric constant can be calculated as approximately 9 on gold and 15 on platinum for the layers. This can be compared to the dielectric constant for alkanethiol layers of 2.25, or of water of 80 and is consistent with that found for other CD monolayers[88] and is entirely consistent with a CD layer which potentially has water associated with the cavity. This relatively large dielectric constant may also indicate that the layers are not close packed.

3.3.2 Blocking studies of γ -CD-(py)$_2$ and backfilled layers

Backfilling of γ -CD-(py)$_2$ layers with 1-nonanethiol.

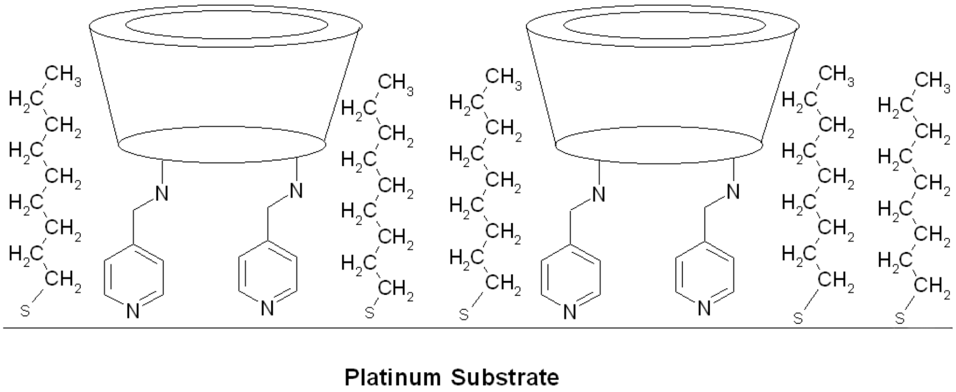

Fig. 3.4: Schematic of backfilled layer showing CD and thiol molecules on a platinum surface.

As previously discussed the maximum surface coverage of the γ -CD-(py)$_2$ can be theoretically calculated as 7.4 x 10^{-11} mol.cm^{-2} from the size of the CD cavity, assuming that the cavities are orientated perpendicular to the surface (i.e. as in Figure 3.4). However, the real surface coverage is almost certainly lower than this theoretically calculated value and it is reasonable to assume that there are small spaces between the CD molecules. The existence of these spaces, or pinhole defects, could compromise the ability of the system to detect target molecules, as any such molecule has two potential pathways for electron transfer. One route is through the CD cavity (encapsulation or inclusion of the molecule in the CD) while the other is through the defects in the CD layer. As the former is the desired outcome of the creation of immobilised CD layers it is of paramount importance that the defects in the layer, excluding the cavities, are filled. This can be achieved using short chain alkanethiol molecules as in Figure 3.4.

Backfilling has been used to patch defects in CD films before by several groups.[62] ,[96] ,[74] It is normally achieved by adsorbing a CD layer on the electrode surface prior to immersion in a solution containing the desired alkanethiol needed for sealing the defects. To avoid alkanethiol adsorption through the CD cavities an excess of a cavity guest is commonly included in the solution. In this case a 10 fold excess of adamantylamine over 1-nonanethiol in ethanol was used to backfill the CD layers. The binding constants for adamantane derivatives and nonanethiol are different by approximately an order of magnitude[48] (10^4 versus 10^3 respectively) so the nonanethiol molecules should not greatly displace the 1-adamantylamine molecules from the CD cavity. All of the previous work has focused on thiolated CDs, however there have been no studies where the co-adsorbed molecules have different binding moieties or any studies using pyridine as a CD surface linker. Due to potentially different bond strengths between pyridine, alkanethiols and platinum (the alkanethiol bond is likely to be the stronger) it is important to rigourously monitor the backfilling process to ensure that "stripping" of the pyridine bound molecules is not taking place. It is also critical to determine that the CD cavities are not permanently blocked by the backfilling process. While the bond energy of pyridine could not be found with platinum as a substrate, the binding of pyridine to gold polycrystalline electrodes has been reported to be above -40 $kJ.mol^{-1}$.[33] This compares to a bond energy of approximately -100 $kJ.mol^{-1}$ for the sulphur-gold bond,[5] plus the additional energy gained by lateral interactions (up to 4 $kJ.mol^{-1}$ per methylene group[21]). Notwithstanding the potentially stronger nature of the alkanethiol bond, the presence of two pyridine linkers and the incremental nature of such surface binding may result in a stronger interaction for the γ -CD-$(py)_2$ as a whole than for the mono-valent alkanethiol on platinum. It may also be kinetically slow for the alkanethiol to displace the di-valent CD. The following experiment was designed to test the assumption that the alkanethiol molecules do not displace γ -CD-$(py)_2$.

Figure 3.5 shows that the capacitance of a bare platinum electrode after 24 hours in the backfilling solution is significantly lower than the γ -CD-$(py)_2$ modified electrodes under identical conditions. The capacitance of the γ -CD-$(py)_2$ backfilled layer is approximately 9.5 ± 0.4 $\mu F.cm^{-2}$ whereas the pure alkanethiol layer shows capacitance values of 6.3 $\pm$ 0.4 $\mu F.cm^{-2}$. This is also probed layer using Raman spectroscopy, vide infra.

The difference in capacitance can be attributed to the presence of the CD molecules, which would allow closer approach, and greater flux, of ions to the

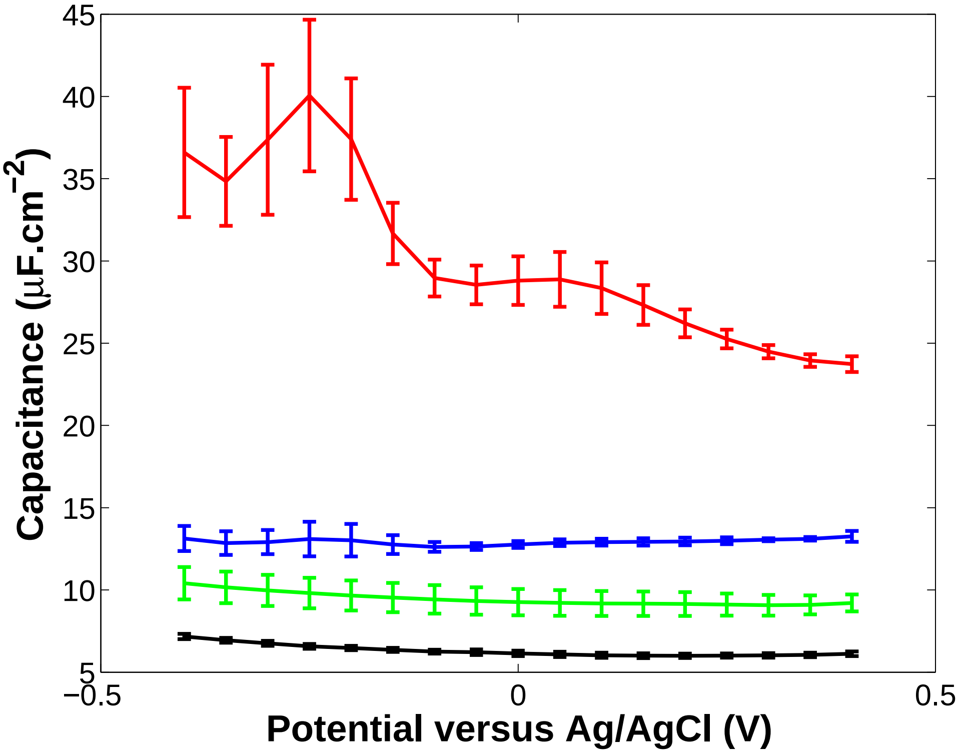

Fig. 3.5: Capacitance as a function of potential versus Ag/AgCl in 0.2 M Na_2SO_4 for bare platinum electrodes before (red) and after (black) 24hrs immersion in the backfilling solution and γ -CD-$(py)_2$ modified platinum electrodes before (blue) and after (green) under the same conditions.

electrode surface and therefore increase the capacitance due to the CDs permeable nature. The capacitance was monitored for several days until stable, time independent values were obtained. While the capacitance of the alkanethiol layer eventually fell to approximately 3-4 μF.cm^{-2} the capacitance of the CD layer stabilised at approximately 6-7 μF.cm^{-2}. Central to the assertion that the CD molecules are present in the layer is the observation that the capacitance values never equalise for the backfilled CD and alkanethiol layers and that the difference between them remain approximately constant. This result indicates that backfilling continued for longer than 24 hours, as it took several days to reach stable capacitance values for the backfilled CD layer. This is consistent with the fact that while inclusion is a dynamic process, the addition of thiol molecules to the layer is irreversible. Thus, any thiol molecules that are included bind irreversibly to the surface and potentially close the cavity. In order to exclude this possibility, the layers used to detect metal complexes were backfilled for approximately 40 hours only, although backfilling at longer times is discussed later.

Blocking behavior of γ -CD-$(py)_2$ and backfilled layers

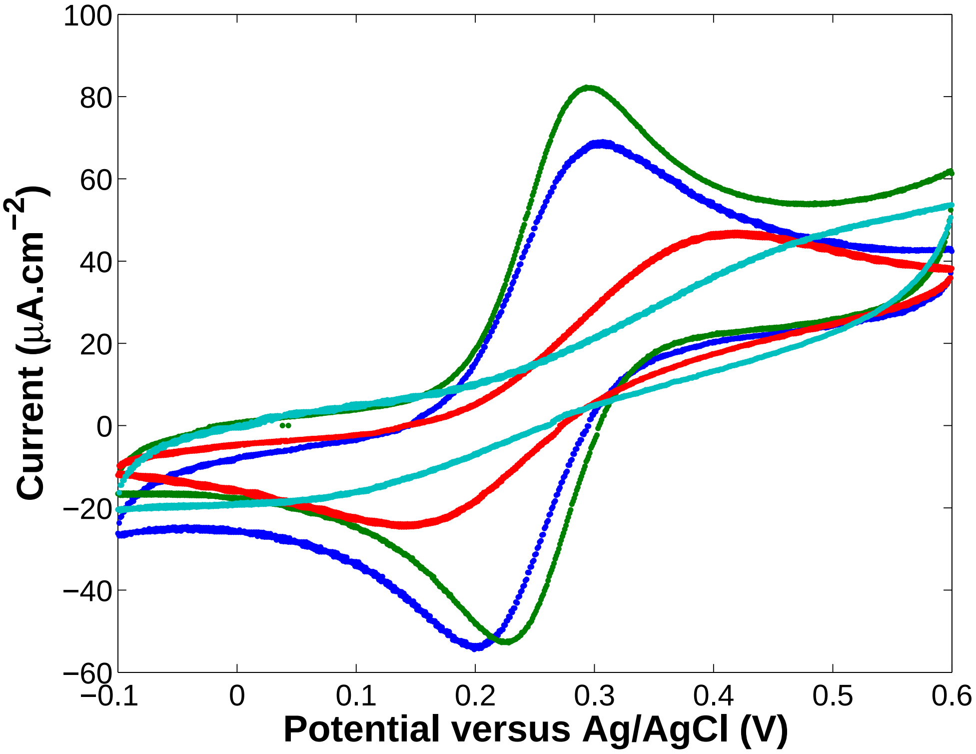

Fig. 3.6: CV of 2 mM $[Fe(CN)_6]^{4-}$ in 0.2 M sodium sulphate at bare platinum electrode (green), γ -CD-$(py)_2$ modified (blue) and backfilled (red) platinum electrodes. Also shown is the backfilled electrode in presence of 1-adamantylamine (light blue). All scans were performed at 0.1 V.s^{-1} and the third scan is presented.

The blocking properties of the layers described above have been investigated using 2 mM $[Fe(CN)_6]^{4-}$ as a solution phase probe. $[Fe(CN)_6]^{4-}$ has been used extensively as a blocking probe with alkanethiol[241, 23, 242] and CD monolayers,[66, 101, 70] due to its well defined electrochemistry and reversible electron kinetics. The mechanism of blocking is likely to be related to two effects, steric and electrostatic. Figure 3.4 shows the steric effect of blocking as the CD and alkanethiol molecules are drawn approximately to scale. The footprint area of alkanethiol molecules is approximately 0.2 nm^2 while the footprint area of

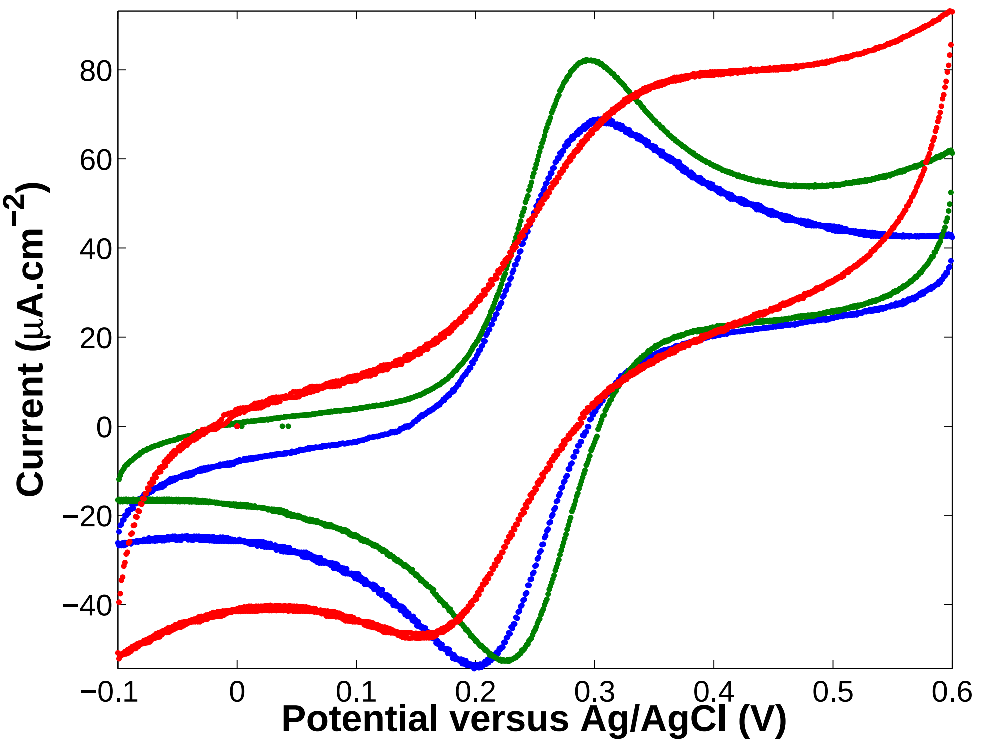

Fig. 3.7: CV of 2 mM $[Fe(CN)_6]^{4-}$ in 0.2 M sodium sulphate at bare platinum electrode (green) and γ -CD-(py)$_2$ modified (blue) platinum electrodes. Also shown is γ -CD-(py)$_2$ modified electrode in presence of 1-adamantylamine (red). All scans were performed at 0.1 V.s^{-1} and the third scan is presented.

the CD is approximately 4 nm^2. This indicates that steric blocking of the surface, especially close to the CD molecules may not be complete. However, the interaction between $[Fe(CN)_6]^{4-}$ and the alkanethiol layer is unfavorable due to the hydrophillic nature of $[Fe(CN)_6]^{4-}$ and therefore the distance of close approach between $[Fe(CN)_6]^{4-}$ and the electrode surface is greater, even at defective sites, due to electrostatic repulsions. Other more hydrophobic probes, such as ferrocene, would interact with the alkanethiol layer and show a less blocked surface. However, $[Fe(CN)_6]^{4-}$ was chosen as the probe molecule as it will not include with the CD cavity (unlike ferrocene) and therefore can give a better measure of the blocking at alkanethiol areas. However, as previously mentioned this blocking is both steric and electrostatic in origin, due to the hydrophillic nature of $[Fe(CN)_6]^{4-}$.

The response of bare and modified electrodes is given in Figures 3.6 and 3.7 while the statistics of the blocking effects are shown in Table 3.3.2. It can be seen that the peak to peak separation (ΔE_p) for the $[Fe(CN)_6]^{4-}$ is 67 mV on bare platinum, which is close to the ideal theoretical value of 57 mV for a reversible one electron transfer. This value increases at the CD layer to 109 ± 7 mV and the peak currents are suppressed by between 10 and 20%. This indicates that the effective area of the electrode has been reduced by the adsorption of the CD molecules as the kinetics of the reaction, as shown by the increase in ΔE_p, appear slower than the standard electron transfer rate k^0. The fractional surface coverage (θ) can be related to k^0 and the observed rate constant k_{obs} using Equation 3.2:[16]

$$k_{obs} = k^0(1-\theta) \tag{3.2}$$

which indicates that the decrease in electrode kinetics is related to the presence of the blocking film.

A further decrease in the heterogeneous electron transfer kinetics is observed at the backfilled layer which shows a very large ΔE_p (236 ± 26 mV) with currents reduced by more than 50%. Finally, Figure 3.6 shows that the electrode can be essentially completely blocked at the backfilled layer by an injection of adamantyl into solution to yield a final concentration of 1 mM in the electrochemical cell. As adamantyl is a well known CD guest molecule, with a free energy change upon complexation of approximately -27 $kJ.mol^{-1}$,[77] this result indicates the presence of un-blocked CD cavities in the layer. This result is consistent with the capacitance data presented in the last section. This result also suggests that the $[Fe(CN)_6]^{4-}$ can communicate with the electrode surface at least in part through the CD cavity. The diameter of $[Fe(CN)_6]^{4-}$ has been reported as 9 $\mathring{A}$[101] which is comparable to that of the γ-CD cavity (approximately 9 $\mathring{A}$). This indicates that in terms of size the $[Fe(CN)_6]^{4-}$ could be accommodated by the cavity although the hydrophobic nature of the interior of the CD makes this unlikely. Association of the $[Fe(CN)_6]^{4-}$ with the hydroxyl groups at the cavity entrance or encapsulated water molecules is more likely. It is clear, however, that electron transfer occurs at the CD sites rather than at other areas of the layer as when these are filled the current is almost totally suppressed.

Table 3.1: Peak to peak separations and current ratios for various modified electrodes in 2 mM $[Fe(CN)_6]^{4-}$ in 0.2 M sodium sulphate at a scan rate of 0.1 $V.s^{-1}$.

Electrode modification	E_{ox}-E_{red} (mV)	I_{ox}/I_0	I_{red}/I_0
Bare	67±4	NA	NA
γ -CD-$(py)_2$	109±7	0.80±0.09	0.93±0.10
γ -CD-$(py)_2$ + admantyl inj	186±18	0.32±0.05	0.53±0.08
Backfilled layer	236±26	0.49±0.03	0.35±0.08
Backfilled layer + adamantyl inj	NA	NA	NA

The effect of adamantyl on pure γ -CD-$(py)_2$ layers was also investigated as above and the resulting CV can be seen in Figure 3.7. The CV clearly shows that ΔE_p increases upon addition of the adamantyl and the peak currents are also significantly reduced (see Table 3.3.2). However, there is an additional increase in non-faradic current, perhaps attributable to a more complex double-layer. It is clearly evident, however, that electron mediation is possible notwithstanding the blocking effect of the CD cavities in the γ -CD-$(py)_2$ layer. This would suggest that the layer is not fully packed and this highlights the necessity for backfilling the monolayers.

These ΔE_p values and currents can be compared favorably to those found by Rubinstein and co-workers[23] for a $[Fe(CN)_6]^{4-}$ probe and octadecyl-thiol monolayers. For example a surface coverage of 99.5% yielded a 230 mV ΔE_p at 0.1 $V.s^{-1}$ and a coverage of 96.5% showed a ΔE_p of 100 mV and currents suppressed by 10% at the same scan rate.

Among the several studies that have been carried out on CD layers to characterise their blocking properties only Kaifer[62] has studied the properties of backfilled CD layers. ΔE_p values of 180 mV were found for $[Fe(CN)_6]^{4-}$ at Kaifer's backfilled layer, which is lower than that reported here. This difference is possibly attributable to the fact that Kaifer used pentanethiol to seal the defects in the CD layers which is likely to be less effective at blocking compared to the longer chain nonanethiol employed in this study due to the exponential distance dependence of electron tunnelling. Longer chain alkanethiols also from more crystalline films, with a smaller pinhole density.

Partially blocked surfaces: theoretical treatment and experimental results

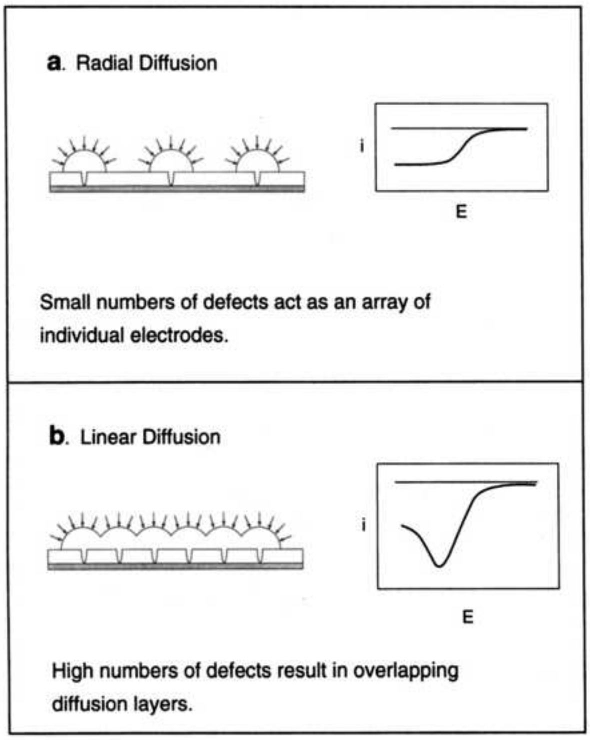

Fig. 3.8: Diffusion patterns and voltametric response for pinhole defects in a blocking layer. Adapted from Crooks and co-workers.[241]

Pinhole defects in a blocking layer can be considered as micro-electrode assemblies and can be subjected to similar theoretical treatments. The parameters that govern their electrochemical response are the fractional surface coverage, θ, the scan rate (or timescale) of the experiment, υ, the distance between the defects, d, and the average radius of the defects, r_0.[243] The density and distribution of the pinholes also influences the signal. Most experimental studies have dealt with pinholes in alkanethiol layers but CD layers are interesting systems to analyse as they can exhibit a potentially constant value for r_0, corresponding to the internal CD cavity radius, assuming a perpendicular CD orientation to the electrode surface. While it remains inherently possible that a di-substituted CD can adopt different orientations, this simplest conformation was assumed for the calculations in this section. The electrochemical data presented later for the backfilled CD layer suggests that it is reasonable

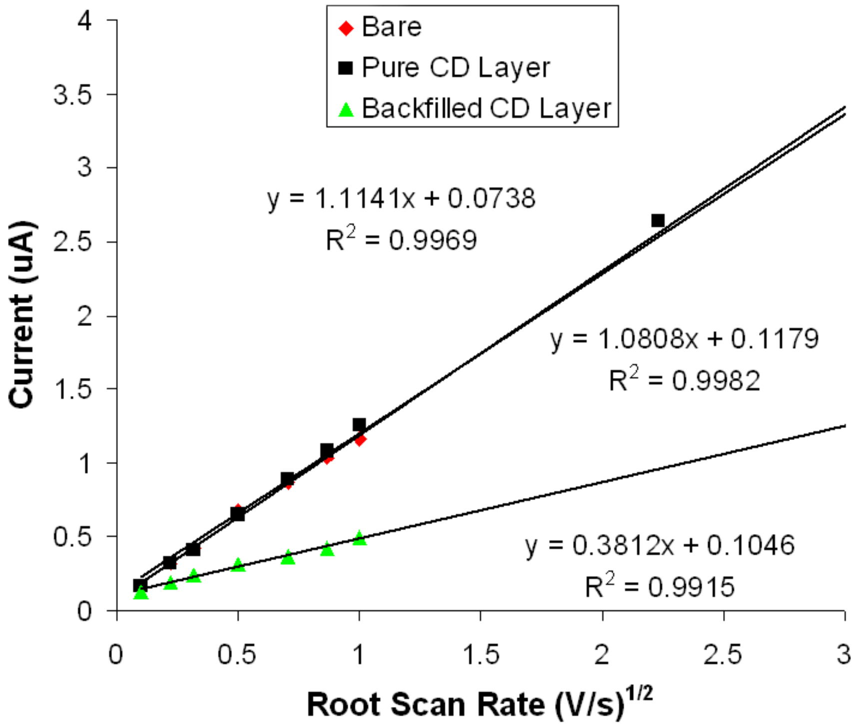

Fig. 3.9: Scan rate dependence for the oxidation peak of $[Fe(CN)_6]^{4-}$ in 0.2 M Na_2SO_4 at both bare and modified platinum electrodes.

to assume this CD orientation for the backfilled layer.

Figure 3.8 predicts two different electrochemical responses for pinhole layers at different experimental timescales. At short timescales (part a) the diffusion layer thickness δ is small compared to d and a spherical diffusion pattern typical of a micro-electrode dominates. The resulting signal is steady state and the current can be related to the density of pinhole defects. At longer timescales the diffusion layers of individual layers overlap (part b of Figure 3.8) and semi-infinite linear diffusion predominates, corresponding to the geometric area of the electrode, yielding peaks in the voltammogram. However, as the surface is significantly blocked, the kinetics of the reaction will appear slower according to Equation 3.2. The scan rate at which the transition from linear to spherical diffusion takes place has been called υ_{max} in several studies[241, 23] and this can be related to the average distance between defects, d, according to Equation

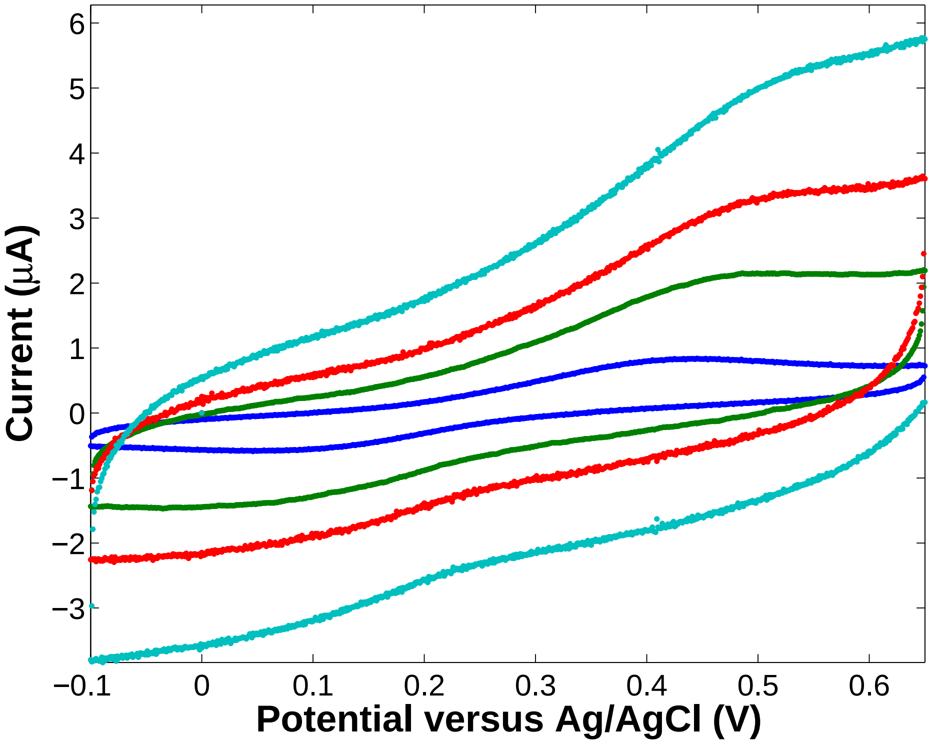

Fig. 3.10: Cyclic voltammogram of 2 mM $[Fe(CN)_6]^{4-}$ in 0.2 M Na_2SO_4 at backfilled CD platinum electrodes at 1 $V.s^{-1}$ (blue), 5 $V.s^{-1}$ (green), 10 $V.s^{-1}$ (red) and 20 $V.s^{-1}$ (light blue). The third scans are presented.

3.3:

$$d = \sqrt{\frac{(\frac{DRT}{F\upsilon_{max}})^{\frac{1}{2}} r_0}{4.44}} \tag{3.3}$$

where D is the diffusion co-efficient of the probe in $cm^2.s^{-1}$, R is the gas constant in $J.mol^{-1}.K^{-1}$, T is the temperature in Kelvin and F is Faraday's constant in $C.mol^{-1}$.

Figure 3.9 shows the scan rate dependence of the $[Fe(CN)_6]^{4-}$ probe at bare and modified electrodes. The diffusion co-efficient can be calculated from the slope of the bare electrode plot, according to the Randles-Sevçik Equation, as 1.4 ±0.1 x 10^{-6} $cm^2.s^{-1}$. The oxidation peak current for all the layers shows good linearity with the square root of the scan rate, although the slope of the backfilled layer is lower than that of the bare electrode, perhaps due to reduced effective surface area. Rubenstein and co-workers[23] estimated υ_{max} as the point where the current showed greater than 5% deviation from linearity with $v^{1/2}$ as it was supposed that the non-uniformity of the defects complicated the transition. However, the determination of v_{max} in the literature is somewhat arbitrary. The data presented here do not show any deviation from linearity, which would indicate that the defects in the film are not widely spread, as the voltammograms do not display any steady-state behavior at high scan rates. Figure 3.10 shows the current response at various scan rates for the backfilled electrode and indicates that the diffusion pattern is still linear, as no steady state current is observed. Although the current decreases and the peaks separate by approximately 100 mV beyond 5 V.s^{-1}, this is characteristic of Ohmic drop effects (approximately 20-30 mV) and the effect of slow heterogenous kinetics at high scan rates rather than steady state behavior. Therefore, it is impossible to estimate v_{max} from the data, but it is clear that it is much greater than 20 V.s^{-1}.

This conclusion can be justified with the following calculations. If v_{max} was 20 V.s^{-1} using Equation 3.3 and using the value found at the bare electrode as the diffusion co-efficient of $[Fe(CN)_6]^{4-}$, the value of d can be estimated as 6.9 x 10^{-7} cm. This density of pinholes can be converted into a surface coverage of approximately 4.4 x 10^{-12} mol.cm^{-2} assuming that each pinhole represents a CD cavity (as in the backfilled layer). As this surface coverage is very much lower than that predicted by theoretical footprint area (7.4 x 10^{-11} mol.cm^{-2}) it can be assumed that v_{max} is greater than 20 V.s^{-1}, as the peak splitting for the pure CD layer was seen to be significantly higher than the bare electrode in Table 3.3.2. How much greater can be estimated by assuming a value of d as 2.38 nm (this corresponds to a 1 nm gap between each CD cavity). This value of d can be converted into a surface coverage value of 3.7 x 10^{-11} mol.cm^{-2}, which is comparable with the footprint area, and using Equation 3.3 v_{max} can be calculated as 1420 V.s^{-1}. Therefore, it is clear that the high density of pinholes associated with the backfilled layer would have an overlapping diffusion layer even at high scan rates, which renders the transition to a steady-state behavior impossible to observe in the normal scan rate range.

Table 3.2: ΔE_p, closest ψ, k and θ values for various modified electrodes in 2 mM $Fe(CN)_6^{-4}$ in 0.2 M sodium sulphate at a scan rate of 0.1 V.s^{-1}.

Electrode modification	E_{ox}-E_{red} (mV)	ψ	k cm.s^{-1}	θ
Bare	67	3.16	1.31 x 10^{-2}	NA
γ -CD-(py)$_2$	108	0.441	1.84 x 10^{-3}	86%
γ -CD-(py)$_2$ + adamantyl inj	186	0.162	6.70 x 10^{-4}	95%
Backfilled layer	236	0.1	4.14 x 10^{-4}	97%

Estimation of θ from electron transfer kinetics

Nicholson[218] has developed a method for the estimation of the heterogenous electron transfer rate constant as a function of scan rate which can be summarised by the following equations:

$$\psi = \frac{k^0}{(D_0 \pi \frac{nF}{RT} \upsilon)^{1/2}} \tag{3.4}$$

where ψ is a dimensionless rate parameter which is related to ΔE_p;

$$\Delta E_p = f(\psi) \tag{3.5}$$

where ΔE_p is the peak to peak separation. Tables relating ΔE_p to ψ can be found in Nicholson's original text. The conditions for use of this method are that the switching potential of the scan is at least 60 mV after the peak potential and that the iR drop is not contributing significantly to ΔE_p. The first condition is clearly met as shown in Figure 3.6 and as values for ΔE_p in Table 3.3.2 were calculated at a scan rate of 0.1 V.s^{-1} the effects of Ohmic drop are expected to be minimal, due to the small currents observed at this scan rate.

The peak to peak separation data presented in Table 3.3.2 can therefore be converted to kinetic rate constants following this method. From these constants and using Equation 3.2 an estimation of the fractional surface coverage θ can be found, taking the rate found at the bare electrode as the standard rate constant (k^0). The k^0 and θ values obtained can be seen in Table 3.3.2. The pure γ -CD-(py)$_2$ layer has a θ of 86 %, which suggests that the CDs are not close packed, but significantly block the signal. The backfilled CD layer displays a θ value of 97 %, which suggests that the layer effectively blocks the $[Fe(CN)_6]^{-4}$ probe from the electrode surface. These calculations show that the γ -CD-$(py)_2$ layer in the presence of a large excess of adamantyl has a lower coverage than the backfilled layer, suggesting the presence of defects in the γ -CD-$(py)_2$ layer and justifying the backfilling process.

3.3.3 Metal complex inclusion at backfilled layers

Inclusion of Osmium-admantyl complex

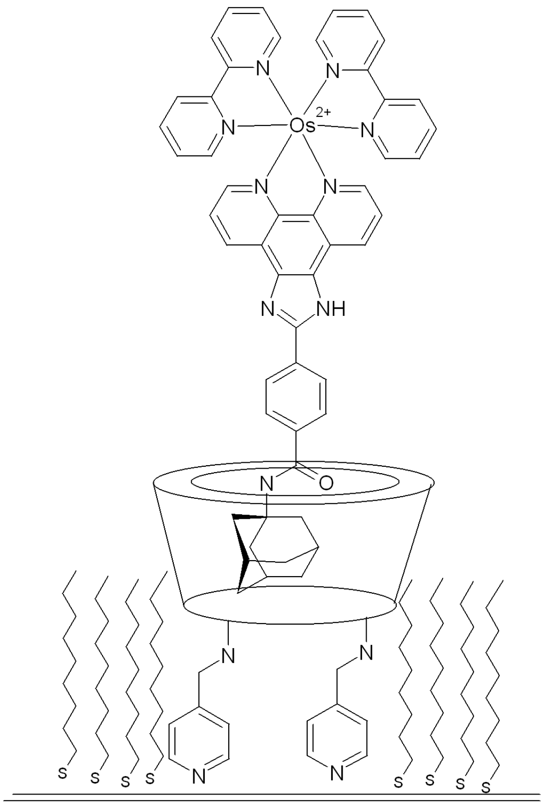

Fig. 3.11: Schematic showing the Osmium-admantyl complex non-covalently linking to the backfilled layer.

The ability to include or encapsulate transition metal complexes and demonstrate both covalent and non-covalent linkage in a single supramolecular assembly is an attractive feature of CD layers. The CDs can be covalently linked to the surface of metal electrodes and solution phase guests can non-covalently associate with the CD cavity. Figure 3.11 illustrates one possibility for an osmium dibipy-pic-adamantyl complex (Osmium-adamantyl) included in the backfilled layer. It has already been stated that to minimise solution phase interference, backfilled layers are the most suitable for inclusion studies. The effects of backfilling on layer structure, such as alkanethiol co-adsorption induced reorientation, are presented later. The inclusion of the admantyl group in these layers has also been observed in the previous section (although at larger

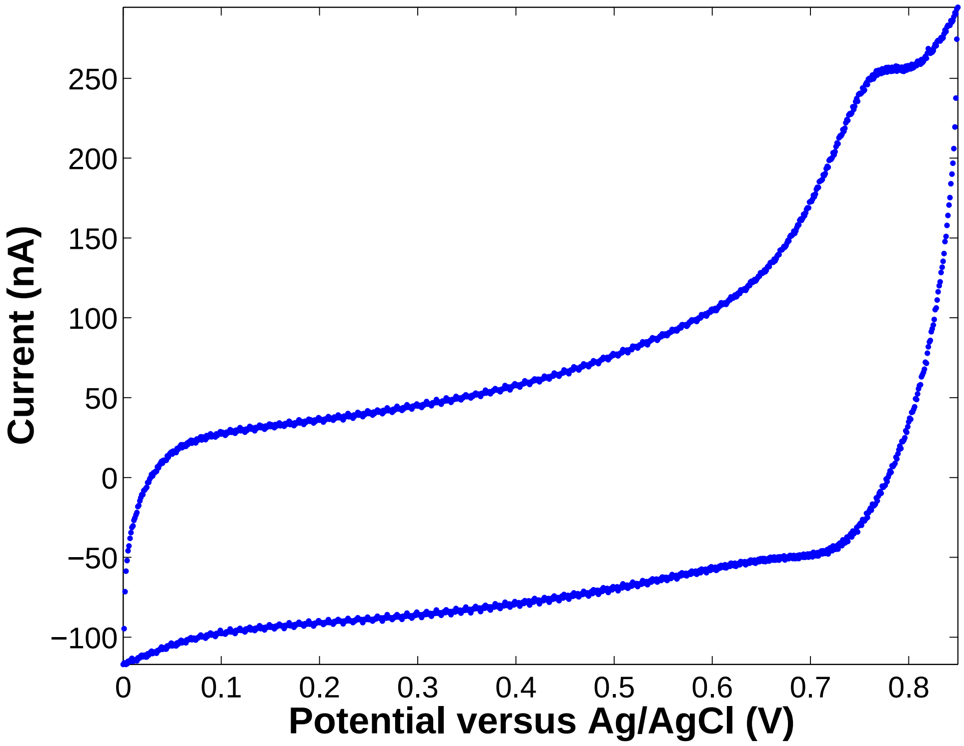

Fig. 3.12: CV of 45 μM Osmium-admantyl in aqueous 0.2 M Na_2SO_4 at the backfilled platinum electrode. The scan rate is 0.5 V.s^{-1} and the first scan is presented.

concentrations), and it is therefore expected that the Osmium-admantyl complex can also bind to the CD cavity. No signal from the osmium complex could be observed from the γ -CD-$(py)_2$ layer in the absence of co-adsorbed alkanethiols but Figure 3.12 shows a CV of the first scan of the backfilled CD layer in 45 μM Osmium-admantyl. Peaks at approximately 0.75 V can be seen that have been shown to be surface confined i.e. the peak current increases linearly with υ as opposed to the $\upsilon^{1/2}$ dependence expected for solution phase species. However, the CV also shows a rising background current in the positive region attributable to platinum oxidation. Therefore, further characterisation of this complex was deemed impossible in aqueous solvents as subsequent experiments proved that the layers are unstable at these high positive potentials. Thus, the CV presented is the first scan of a freshly prepared layer and the surface coverage Γ can be calculated as 1.3 x 10^{-11} mol.cm^{-2}. The free energy change associated with inclusion complex formation (ΔG) between this complex and β-CD has been found by our group to be -26 kJ.mol^{-1} in aqueous solution, which would indicate that the fractional occupancy of the cavities is close to unity, provided there are not large differences between the solution and interfacial binding constants.

Attempts were made to monitor the inclusion in acetonitrile, but no surface bound signals were visible in the voltammetry. The free energy of complexation for complex formation between the osmium complex and β-CD has been found by our group to be -26 kJ.mol^{-1} in aqueous solution, but this value is expected to decrease in non-aqueous media, due to a decrease in solvent polarity which reduces the hydrophobic-hydrophobic interactions that drive inclusion.

Inclusion of $[Co(biptpy)_2]^{2+}$

As the redox potential of the Osmium complex was in a region of platinum oxide formation, attempts were made to monitor inclusion using a cobalt complex ($[Co(biptpy)_2]^{2+}$) shown in Figure 3.13 which has a lower redox potential. Cobalt solutions were prepared in 90:10 H_2O:ACN with 0.18 M Na_2SO_4 as the supporting electrolyte. The solubility of the complex in this solution is approximately 60 μM. It is expected that the bi-phenyl group can include in the hydrophobic cavity while the more polar, charged metal center could potentially interact with the hydrophillic hydroxyl groups at the cavity entrance. The interaction of an Osmium complex with identical ligands with per-methylated β-CD in solution has been described by Pikramenou and the free energy change associated with complexation was found to be -24 kJ.mol^{-1}.[244] A larger value may be expected for binding to native CD, due to the potential for co-operative H-bonds.[245]

Figure 3.14 shows that the $[Co(biptpy)_2]^{2+}$ is capable of surface adsorption on bare platinum at concentrations of 13 μM $[Co(biptpy)_2]^{2+}$ as the peaks shown scale linearly with υ. Furthermore, the solution phase signal at this scan rate and concentration should be approximately 35 μA.cm^{-2}, which is significantly lower than the current seen in Figure 3.14. However, the voltammogram shows an extremely ill-defined response with broad peaks centered at 110 mV, perhaps indicating a lack of layer order. Figure 3.14 also shows the response of the γ -CD-$(py)_2$ layer in the same solution and indicates that the CD layer

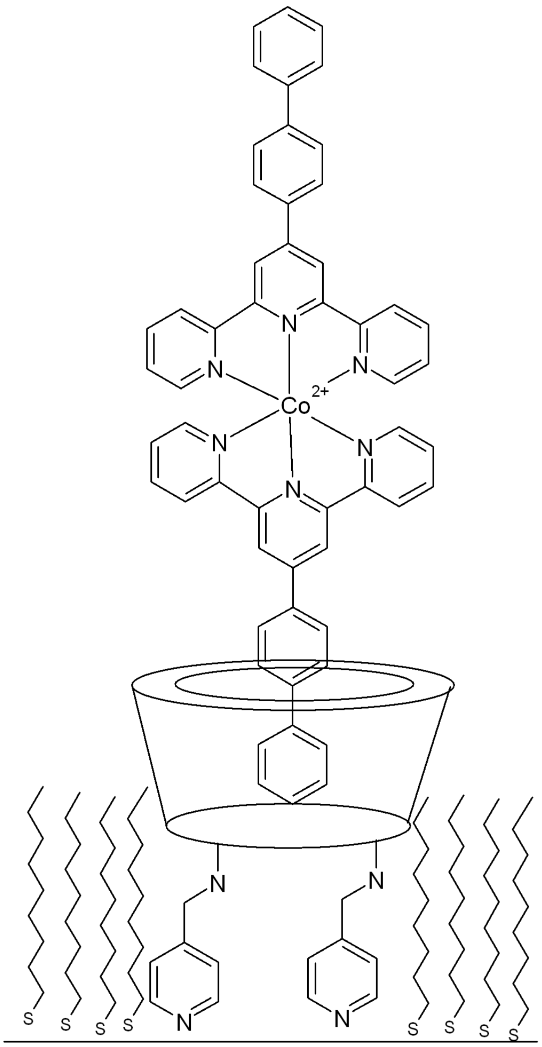

Fig. 3.13: Diagram showing the Co-bisterpy biphenyl complex, $[Co(biptpy)_2]^{2+}$, non-covalently linking to the backfilled layer.

completely blocks the $[Co(biptpy)_2]^{2+}$ surface adsorption. This total blocking is in contrast to the limited blocking shown by the γ -CD-(py)$_2$ layer to 1 mM $[Fe(CN)_6]^{4-}$ described earlier. While the concentration difference is certainly a factor in the improved blocking properties of the layers, the polarity of the probes indicates that the γ -CD-(py)$_2$ film is significantly less permeable to non-polar probes. This gives an important insight into the structure of the γ -CD-(py)$_2$ layer and suggests that the molecules are orientated so as the CD cavities are inaccessible to the solution (as in Figure 3.18 (top)).

Figure 3.15 shows the response of both backfilled CD layers and 1-nonanethiol

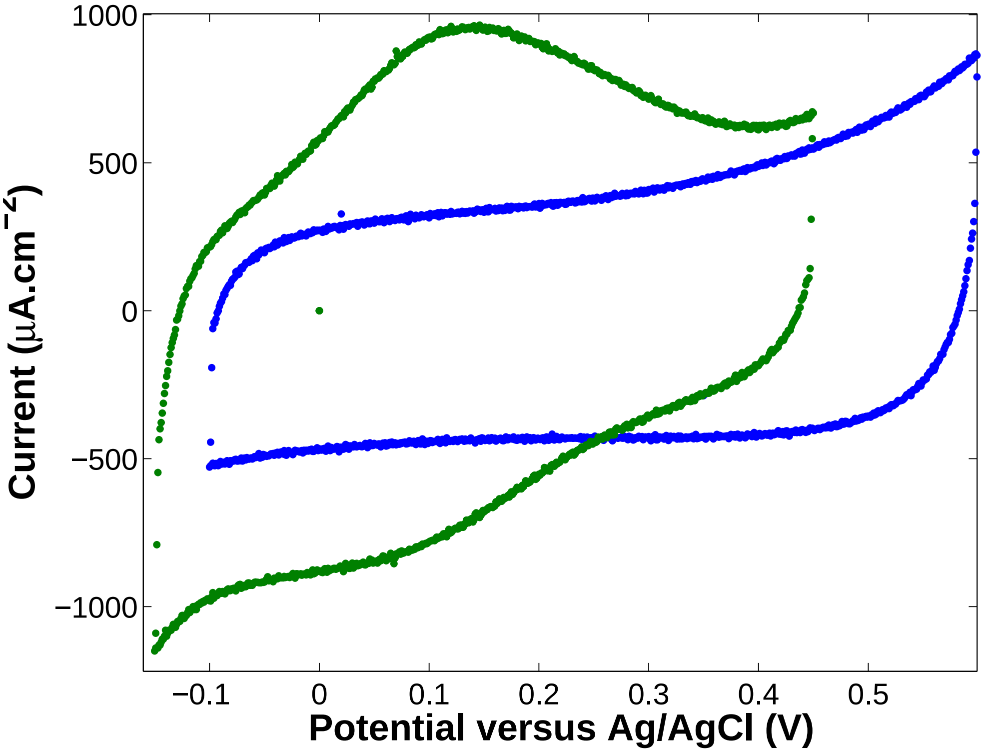

Fig. 3.14: CV of bare platinum (green) and γ -CD-(py)$_2$ layer on platinum (blue) in 13 μM [Co(biptpy)$_2$]$^{2+}$ in 90:10 H_2O:ACN with 0.18 M Na_2SO_4 as the supporting electrolyte. The scan rate is 20 V.s^{-1} and the third scan is presented.

layers to 13 μM [Co(biptpy)$_2$]$^{2+}$ solution. The presence of an electrochemical surface bound signal at the alkanethiol coated electrode deserves some comment. Alkanethiol monolayers have been shown to effectively block the reactions of solution phase polar probes such as [Fe(CN)$_6$]$^{4-}$ but in this case the non-polar [Co(biptpy)$_2$]$^{2+}$ complex associates with the non-polar alkanethiol layer. This result is consistent with the results of solubility experiments which show that [Co(biptpy)$_2$]$^{2+}$ is soluble in non-polar solvents such as hexane, despite the presence of the charged metal center. This non-specific adsorption on alkanethiol layers of cyclodextrin guests has been observed before, most notably by Huskens and co-workers,[82] who showed using AFM that such adsorption lacks order compared to that found at CD layers. The driving force for adsorption presumably arises from solvophobic or van de Waals effects, but results in random association with the monolayer, perhaps at defect sites. In addition, the [Co(biptpy)$_2$]$^{2+}$ signal at 1-nonanethiol layers is not reproducible

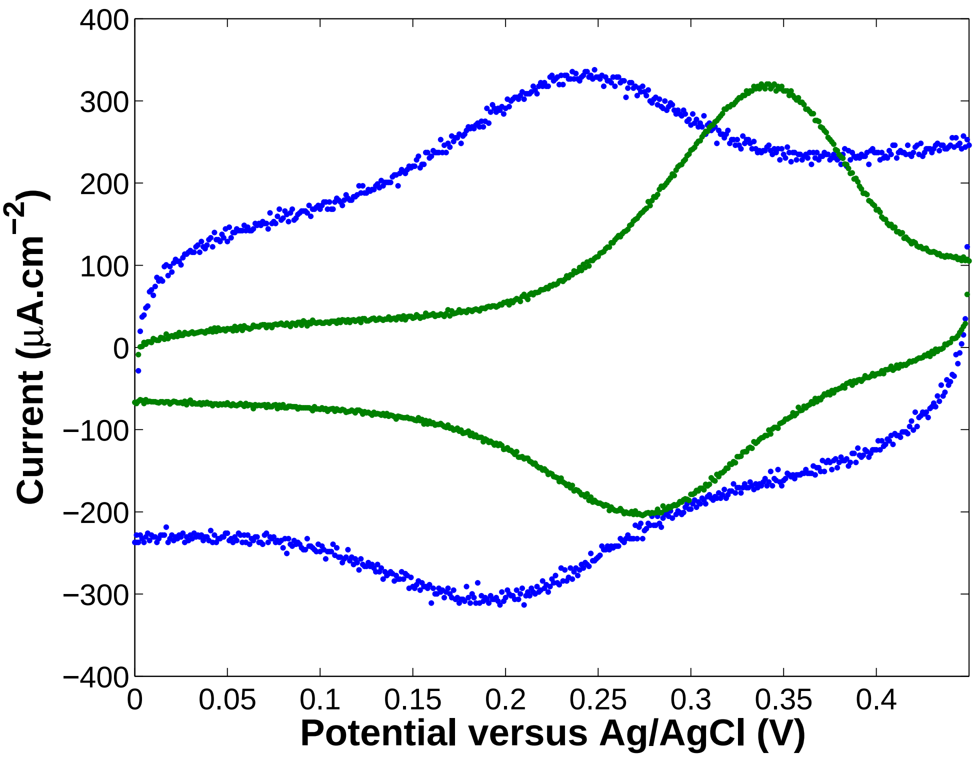

Fig. 3.15: CV of backfilled layer (blue) and 1-nonanethiol layer (green) on platinum in 13 μM [Co(biptpy)$_2$]$^{2+}$ in 90:10 H_2O:ACN with 0.18 M Na_2SO_4 as the supporting electrolyte. The scan rate is 20 V.s^{-1} and the third scan is presented.

between electrodes and this is likely a result of defect variation in layers assembled on different electrodes which has been well verified for alkanethiol layers on polycrystalline electrodes.[246] Figure 3.16 shows the response of four different 1-nonanethiol layers assembled on platinum to [Co(biptpy)$_2$]$^{2+}$ in solution and there is clear lack of reproducibility. The electrochemical signal shows variations in the kinetics and surface coverage of [Co(biptpy)$_2$]$^{2+}$ for different electrodes under identical conditions of layer formation and measurement. However, the response for the oxidation of Co^{+2} to Co^{+3} is never observed at potentials lower than that illustrated in Figure 3.15.

Figure 3.15 also shows the response of the backfilled CD layer to the presence of 13 μM [Co(biptpy)$_2$]$^{2+}$ in solution. This signal, at 220 mV, displays characteristics of a surface confined signal. The peak current scales linearly with

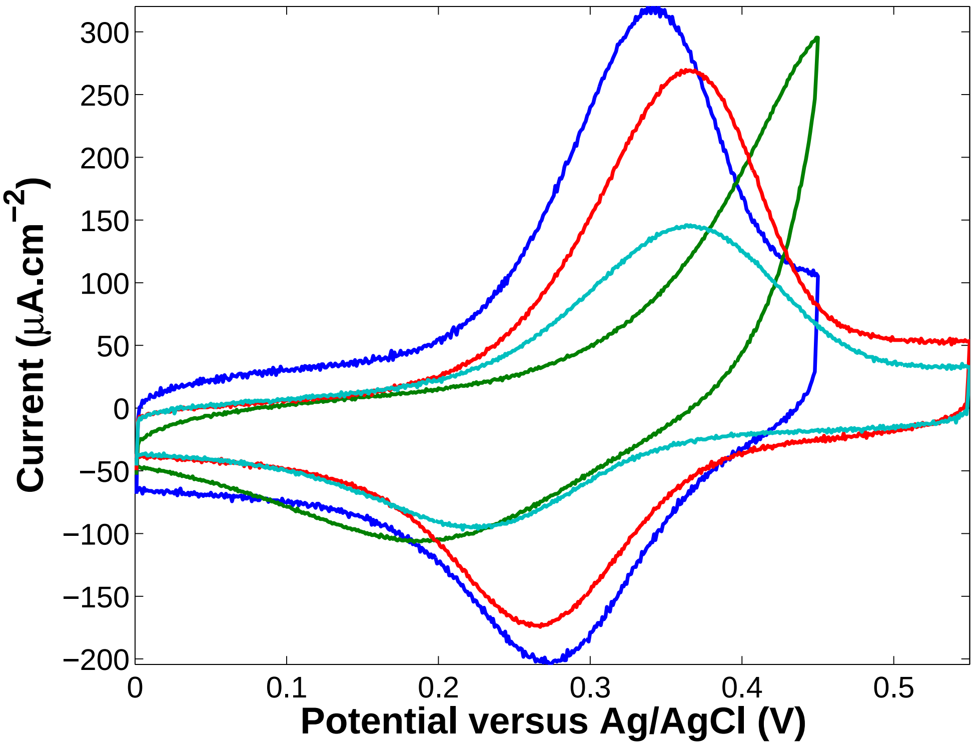

Fig. 3.16: CV of 1-nonanethiol layers on platinum in 13 μM [Co(biptpy)$_2$]$^{2+}$ in 90:10 H_2O:ACN with 0.18 M Na_2SO_4 as the supporting electrolyte. The scan rate is 20 V.s^{-1} and the third scan is presented.

scan rate, in accordance with the following Equation:

$$i_p = \frac{n^2F^2}{4RT}\upsilon A\Gamma \tag{3.6}$$

and this can be seen in Figure 3.17. The insert of this figure shows a plot of log scan rate versus log peak current which in the case of surface confinement should display a slope of unity and the experimental data clearly shows a nearly ideal response. The peak to peak separation (ΔE_p), which is ideally zero for surface confined species, is 40 mV at a scan rate of 20 V.s^{-1} and is therefore significantly less than that of a diffusive species at similar scan rates (i.e. $\simeq$ 60 mV). Finally, the full-width at half maximum is approximately 125 ± 10 mV which is somewhat higher than the theoretical value of 90 mV and the ratio of anodic and cathodic current is 1.16 ± 0.1 . These values indicate that the surface bound signal is not ideal, but also that it is approaching the theoretical values for a surface confined layer. The ratio of the anodic to cathodic currents

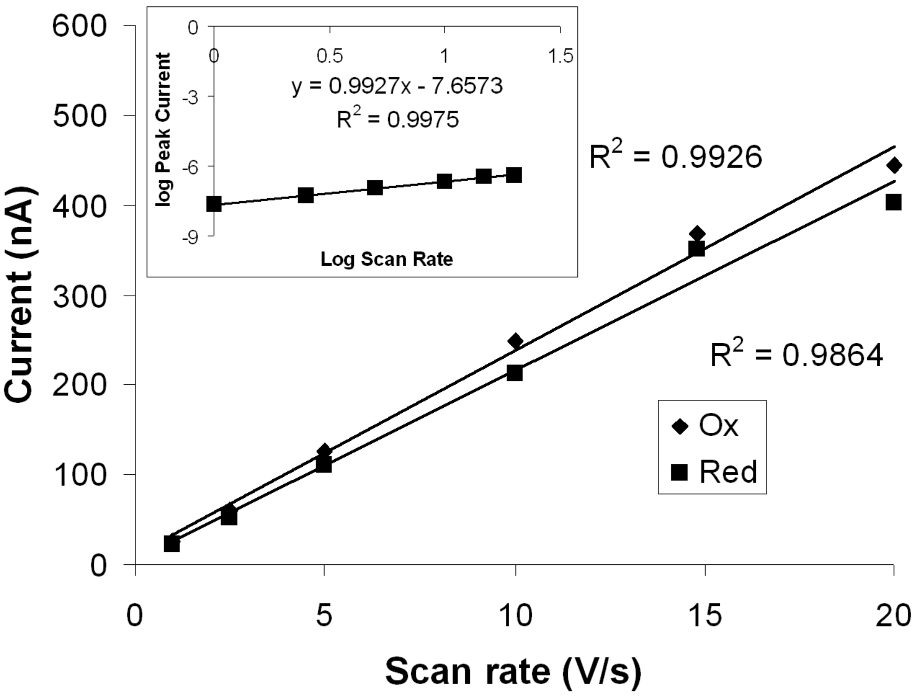

Fig. 3.17: Scan rate dependence of peak current of $[Co(biptpy)_2]^{2+}$ included in backfilled layer on platinum where bulk concentration of $[Co(biptpy)_2]^{2+}$ is 13 μM in 90:10 H_2O:ACN with 0.18 M Na_2SO_4 as the supporting electrolyte. Inset is the log of reduction current versus log scan rate for same data.

is interesting, as this shows that a similar amount of $[Co(biptpy)_2]^{3+}$ is present in the return scan.

This signal can be distinguished from that of the $[Co(biptpy)_2]^{2+}$ at the alkanethiol layer as it is approximately 90-100 mV more negative and it displays exceptional repeatability at different electrodes. It is also independent of electrode roughness, which is in contrast to the signal seen at the alkanethiol layers. The shift in redox potential is indicative of a different electronic environment from that of the alkanethiol layer and the greater repeatability suggests the presence of a reproducible binding site in the film, such as the CD cavity. It was described earlier that the $[Co(biptpy)_2]^{2+}$ will not interact with the γ -CD-$(py)_2$ layer before backfilling and it was suggested that this was because of a cavity orientation that mitigated against inclusion of the biphenyl group of the complex. However, after the layer is backfilled, the $[Co(biptpy)_2]^{2+}$ clearly displays a surface confined signal, significantly different to that at an alkanethiol

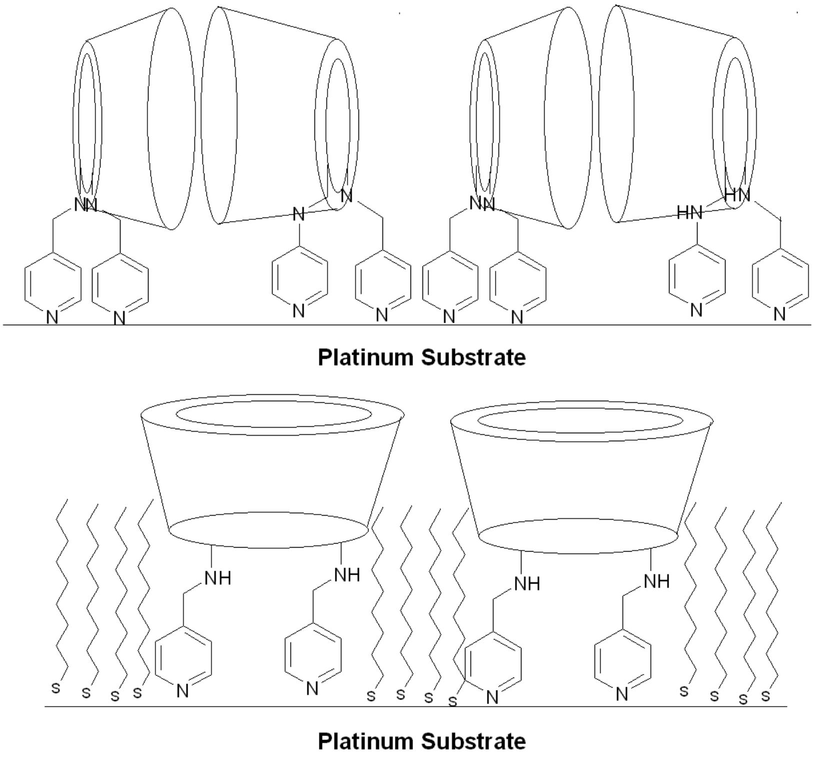

Fig. 3.18: Likely orientation of the γ -CD-(py)$_2$ on the platinum surface before (top) and after (bottom) backfilling with 1-nonanethiol.

layer, suggesting that inclusion into the CD cavity is now possible. This explanation would involve alkanethiol co-adsorption induced re-orientation of the CD cavity in the layer which facilitates inclusion, perhaps in manner like that shown in Figure 3.18.

Alkanethiol co-adsorption has been shown to cause reorientation of several primary adsorbates such as DNA[25] and viologen.[26] Previous work on cyclodextrins in our group has suggested cavity reorientation in β-CD-(py) monolayers on gold using SERS. The initial orientation was attributed to the formation of intermolecular interaction between CD cavities.[247, 248] It is possible that the co-adsorption of the 1-nonanethiol, which is a good length match of the γ -CD-(py)$_2$ molecule, disrupts such interactions and forces the cavities into a more upright orientation which renders them more amenable to cavity guests (see Figure 3.18).

Adsorption isotherm for Cobalt inclusion

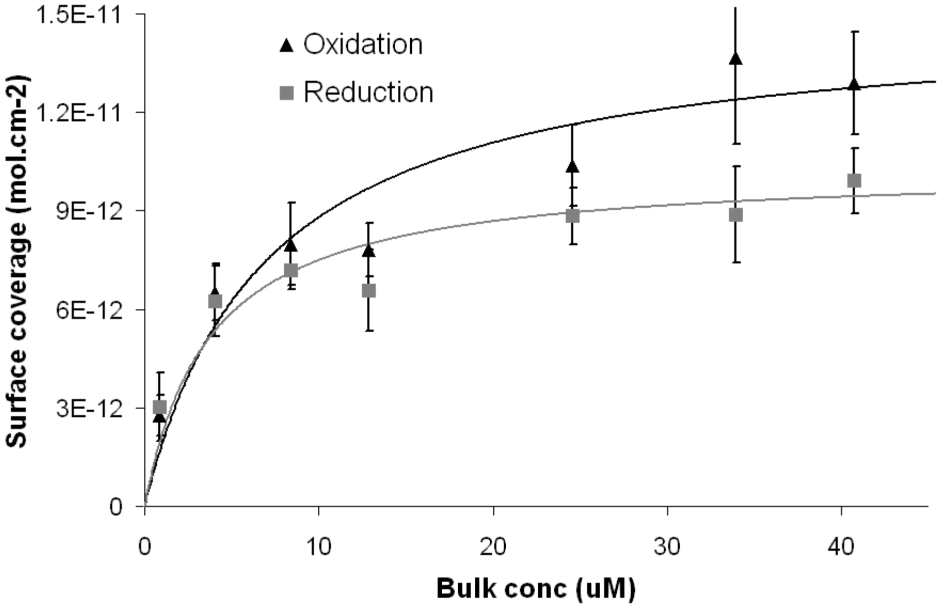

Fig. 3.19: Variation of surface coverage with bulk concentration of $[Co(biptpy)_2]^{2+}$ at backfilled layers on platinum for both oxidised and reduced forms. The solid lines are the best fits of the Langmuir isotherm.

Figure 3.19 shows the variation of surface coverage of oxidised and reduced $[Co(biptpy)_2]^{2+}$ at the backfilled layer with bulk concentration of $[Co(biptpy)_2]^{2+}$ as determined by CV. The reproducibility of the signal was impressive considering that the data is a combination of 12 different layers on polycrystalline electrodes. This is a far higher level of repeatability than the signal at the alkanethiol layer which reflects a greater overall layer reproducibility and the repeatability of the formal potential is consistent with inclusion as it suggests a reproducible binding site within the layer.

The solid lines are the best fits to the Langmuir isotherm as described by Equation 3.7:

$$\frac{\Gamma_i}{\Gamma_s - \Gamma_i} = \beta C_i \tag{3.7}$$

where Γ_i and C_i are the surface coverage and bulk concentration of species i, Γ_s is the saturation surface coverage, β is the adsorption coefficient of the

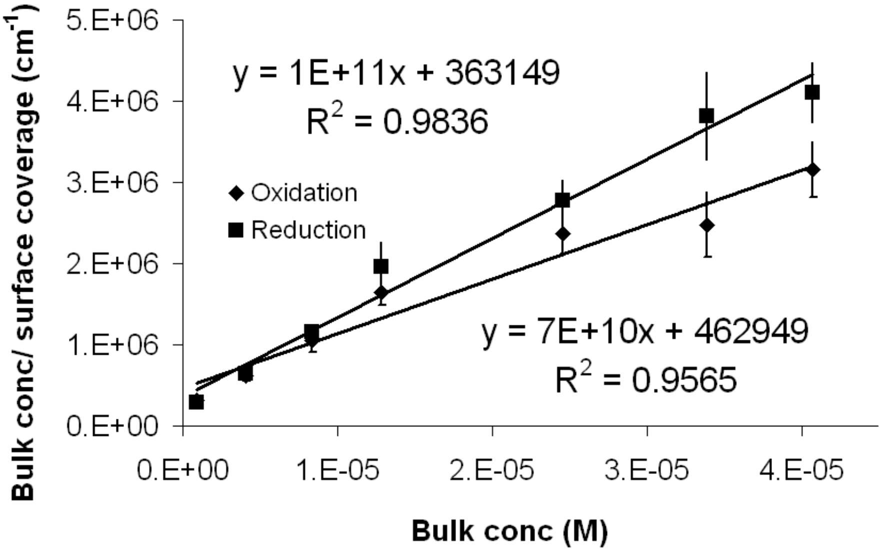

Fig. 3.20: Linearised Langmuir isotherm applied to experimental data for $[Co(biptpy)_2]^{2+}$ included at backfilled platinum layers.

adsorbing species i.

The Langmuir isotherm involves several assumptions such as no lateral interactions, either repulsive or attractive, between adsorbed species and that coverage does not proceed beyond a monolayer. It also assumes that all potential adsorption sites are equal. Despite these limitations the isotherm has proved to be widely applicable to guest inclusion in CD monolayers.[62,76,70] A linearised form of Equation 3.7 can be easily derived:

$$\frac{C_i}{\Gamma_i} = \frac{1}{\beta\Gamma_s} + \frac{C_i}{\Gamma_s} \qquad (3.8)$$

and β can be related to the free energy of adsorption ΔG_{ads} from:

$$-\Delta G_{ads} = RTln(\beta) \qquad (3.9)$$

where R is the gas constant and T the temperature in Kelvin. It is clear from Equation 3.9 that β is equivalent to K_{ass}.[62]

Figure 3.20 shows a plot of Equation 3.8 for the experimental data and displays good linearity for both oxidised and reduced forms of $[Co(biptpy)_2]^{2+}$. This confirms that the Langmuir isotherm is applicable to this system despite the approximations mentioned above and Table 3.3 shows the thermodynamic data which can be extracted from the isotherm.

The Langmuir plot reveals that the amount of $[Co(biptpy)_2]^{2+}$ bound into the cavities is approximately one tenth that of classical well packed monolayer and is approximately 20% of a fully packed γ-CD layer. Considering the large values found for K_{ass} it would appear that this saturation coverage is a reflection of the number of active CD cavities within the layer. While this value is lower than expected for a dense CD layer it is in accordance with that found by Kaifer[62] (2.5 x 10^{-11} mol.cm^{-2}) and Willner[98] (2.7 x 10^{-11} mol.cm^{-2}) for other CD monolayers. The discrepancy between the footprint area (7.4 x 10^{-11}mol.cm^{-2}) and these saturation values may due to several reasons. Steric hinderance by the terpyridine groups can be ruled out as a cause of the low surface coverage as maximum surface coverages for hexagonally packed terpyridine monolayers can be calculated as over 1 x 10^{-10} mol.cm^{-2}, although Campagnoli and co-workers reported a similarly small surface coverage of a cobalt terpyridine compound adsorbed directly to a platinum surface.[249] It also seems unlikely that the γ-CD-$(py)_2$ layer, which shows such effective blocking against the $[Co(biptpy)_2]^{2+}$ complex, is poorly packed. While it is possible that the backfilling process seals some of the CD cavities in the layer, an adsorption isotherm constructed after 90 hours of backfilling yielded results that are within experimental error with the data collected after 40 hours backfilling. This suggests that significant blocking or displacements of the cavities by the alkanethiols does not occur. Perhaps the most likely explanation for the low surface saturation coverages is that not all cavities are activated by the co-adsorption of the alkanethiol i.e. the backfilling process does not induce re-orientation of all CD cavities.

It has been previously noted that the free energy change associated with complexation of an osmium complex with identical ligands to the cobalt complex described here with a per-methylated β-CD was reported as -24 kJ.mol^{-1}.[244] The free energy change associated with complexation at the CD monolayer (ΔG_{ads}) determined at the backfilled γ-CD-$(py)_2$ interface for $[Co(biptpy)_2]^{2+}$ inclusion is significantly higher. Notwithstanding the differences in cavity size,

Table 3.3: Saturation surface coverage (Γ_{max}), association constants K$_{ass}$ and free energy of adsorption (ΔG_{ads}) for oxidised and reduced forms of the CD guest [Co(biptpy)$_2$]$^{2/3+}$ as determined from the Langmuir isotherm.

	$\Gamma_s(mol.cm^{-1})$	β/K_{ass}	$\Delta G_{ads}(kJ.mol^{-1})$
[Co(biptpy)$_2$]$^{2+}$	1.49 ± 0.25 x 10^{-11}	1.45 ± 0.46 x 10^5	-29.4 ± 0.7
[Co(biptpy)$_2$]$^{3+}$	1.03 ± 0.12 x 10^{-11}	2.68 ± 0.45 x 10^5	-30.9 ± 0.4

methylation of the primary face and the different metal center it is not unusual to observe higher K$_{ass}$ values at interfaces compared to solution phase systems. Kaifer[62] found that the interfacial K$_{ass}$ was an order of magnitude higher than the corresponding solution K$_{ass}$ while Kitano[72, 68] and others[76] have also observed this trend. As interfacial K$_{ass}$ constants have also been found to be lower than their solution phase counterparts[70] it is possible that subtle changes in the nature of CD-guest interactions occur upon CD immobilisation, which can either augment or diminish the binding constant. While a direct comparison cannot be made in this case to the corresponding solution phase system it is clear from the values of ΔG_{ads} seen in Table 3.3 that the binding strength is comparable to that found for strongly bound guests such as adamantane derivatives with β/γ-CD or pyrene with β-CD in solution.[48] These observations clearly show that the thermodynamic driving force for inclusion complex formation after immobilisation of the γ -CD-(py)$_2$ is still quite high. It is also interesting to note that the driving force for adsorption does not alter significantly as the complex becomes more charged. This is an indication that the charged metal center resides outside the CD cavity and does not significantly affect the inclusion process.

It is expected that the trivalent form of [Co(biptpy)$_2$] will dis-associate from the CD cavity as it is not present in the bulk solution (i.e. a new equilibrium will be established). This is consistent with the lower saturation coverage for the oxidised guest (1.03 x 10^{-11} mol.cm^{-2}) compared to the reduced form which is present in bulk solution. However, contrary to expectations a significant portion of the trivalent form remains associated with the layer even at low scan rates. This result can be rationalised in two ways depending on the dissociation rate. If the dissociation rate is slow such that the

$[Co(biptpy)_2]^{3+}$ molecules do not have sufficient time to exit the cavity before being re-reduced then the same molecules are being oxidised and reduced while remaining bound to the CD. However, if the rate of dissociation is very fast then local concentrations of $[Co(biptpy)_2]^{3+}$ could build up near the interface and a pseudo-equilibrium may be established between $[Co(biptpy)_2]^{3+}$ and the CD layer with an association constant, K_{ass}, corresponding to that shown in Table 3.3 for $[Co(biptpy)_2]^{3+}$. The inclusion is at least somewhat dynamic at 20 $V.s^{-1}$, as indicated by the drop in surface saturation coverage for $[Co(biptpy)_2]^{3+}$. However, at slow scan rates (typically 1 $V.s^{-1}$) the amount of $[Co(biptpy)_2]^{3+}$ decreases somewhat, suggesting that the $[Co(biptpy)_2]^{3+}$ exits the cavity to a greater extent at this slower scan rate.

The decrease in the amount of $[Co(biptpy)_2]^{3+}$ can be related to the scan rate and therefore to the amount of time spent in the oxidising region of the scan. This relationship suggests a slow dissociation step that would see all of the $[Co(biptpy)_2]^{3+}$ exit the cavity after 4 seconds in the oxidising region (or a scan rate of $V.s^{-1}$). This hypothesis suggests that at 20 $V.s^{-1}$ the cobalt complex does not exit the cavity immediately upon electron transfer and the presence of $[Co(biptpy)_2]^{3+}$ in the CV is due to the slow release of the oxidised form from the cavities. The principal cavity guest that is detectable electrochemically is ferrocene, but the behavior is different to that described here. It is generally accepted that ferrocene must exit the cavity before it becomes oxidised as it is not thermodynamically favorable for the charged metal center to remain inside the hydrophobic CD cavity.[78] However, the metal center in the cobalt complex resides outside the cavity and is already in a 2^+ oxidation state when it associates with the layer. Therefore, the charge on the complex would appear to have a little effect on the thermodynamics of binding. The kinetics of electron transfer will be discussed below, but the electron transfer step appears to be several orders of magnitude faster than the disassociation step. Therefore, the sequence of steps seems to be reversed compared to the accepted ferrocene sequence; i.e. the cobalt center is oxidised and then the complex disassociates from the CD layer.

Effect of biphenyl group on binding

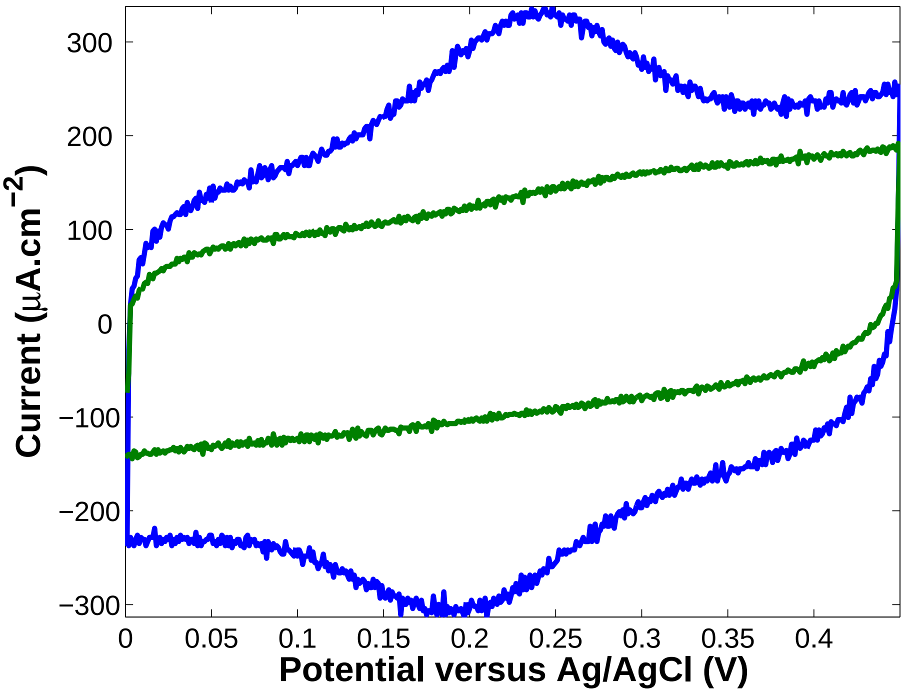

Fig. 3.21: CV of backfilled layer on platinum in the presence of 30 μM $[Co(biptpy)_2]^{2+}$ (blue) and 70 μM $[Co(tpy)_2]^{2+}$ (green) in 90:10 H_2O:ACN with 0.18 M Na_2SO_4 as the supporting electrolyte. The scan rate is 20 V.s^{-1} and the third scan is persented.

It has been stated that the biphenyl group is capable of binding with the CD cavities. The behavior at the backfilled CD layer of a bi-terpyridine cobalt complex identical to $[Co(biptpy)_2]^{2+}$ but without the biphenyl groups was investigated electrochemically using CV and the results are shown in Figure 3.21. This figure shows the response of the backfilled layer to 30 μM $[Co(biptpy)_2]^{2+}$ in blue and to 70 μM $[Co(tpy)_2]^{2+}$ in green. This figure shows that without the biphenyl docking ligand the cobalt complex cannot associate with the CD layer. In contrast to the complex with the biphenyl ligands the electrochemical signal from $[Co(tpy)_2]^{2+}$ is not observed at all ($[Co(tpy)_2]^{2+}$ $E^{0'}$ =150 mV in 90:10 H_2O:ACN with 0.18 M Na_2SO_4 as the supporting electrolyte). This control experiment indicates the importance of suitable docking ligands for effective CD binding.

3.3.4 Raman studies of γ -CD-(py)$_2$ monolayers

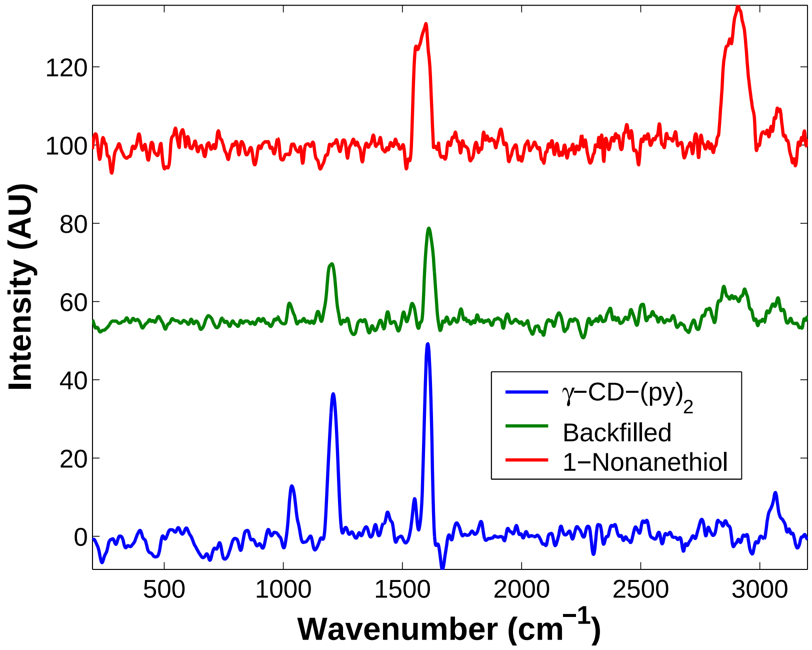

Fig. 3.22: Raman spectra of dry monolayers on roughened platinum electrodes using the 458 nm excitation line.

SERS has been used to characterise the functional groups present in all the monolayers previously described on platinum (Figure 3.22). A laser wavelength of 458 nm was chosen as it is closest to the surface plasmon band of roughened platinum. However, the SERS effect on platinum is seriously limited as this wavelength is still a poor match for the plasmon band, which is further towards the UV region.[250] Therefore, only limited information could be obtained from the layers and no signal from the CD itself was observed. However, the functional groups detected are those closest to the metal surface, suggesting a limited SERS effect.

Pyridine has been the subject of several SERS investigations on platinum and displays characteristic in plane vibrations modes at approximately 1000, 1200 and 1600 cm^{-1}.[236, 41] The γ -CD-(py)$_2$ layer is dominated by the pyridine in plane bending modes at 1035, 1209, 1550 and 1606 cm^{-1}. The band at 3066 cm^{-1} is attributable to pyridine aromatic C-H stretches. Figure 3.22 also shows the spectrum of 1-nonanethiol on platinum under identical acquisition parameters. This spectrum displays characteristic alkane C-H stretching at

2850-2946 cm^{-1} and a band at 1537-1624 cm^{-1} which may be attributable to a CH_2 bending mode.[251] There may also be a C-S stretch at 727 cm^{-1} although the signal to noise ratio in this spectral region is poor. Figure 3.22 also shows the spectrum of the backfilled layer and it contains bands from both functional groups. The pyridine bands appear with slight modifications at 1025, 1204, 1541 and 1610 cm^{-1}, while the alkane C-H stretching appears at 2850-2935 cm^{-1}. This spectrum is consistent with the electrochemical results presented earlier which described a mixed monolayer with both pyridine and alkanethiol linkers.

SERS has been used previously to probe β-CD-py layers on gold and a time dependent re-orientation of the CD cavity was suggested.[247] However, while SERS has the potential to probe the CD orientation change during the backfilling process, serious limitations in the intensity of the signal on platinum electrodes make this extremely difficult. As seen, the spectra are dominated by the surface linking groups as these are closest to the metal and as a consequence experience greatest enhancement of signal. For this reason the orientation of the CD cavities cannot be probed using SERS on platinum using this excitation wavelength. Attempts were also made to monitor the inclusion of the cavity guest $[Co(biptpy)_2]^{2+}$ at both the dry monolayer and using *in-situ* measurements. However, in the case of the dry monolayer, it proved impossible to wash the electrode without removing the $[Co(biptpy)_2]^{2+}$ from the cavity and high background signals from the acetonitrile made the *in-situ* measurements prohibitively difficult.

3.3.5 Chronoamperometric measurements

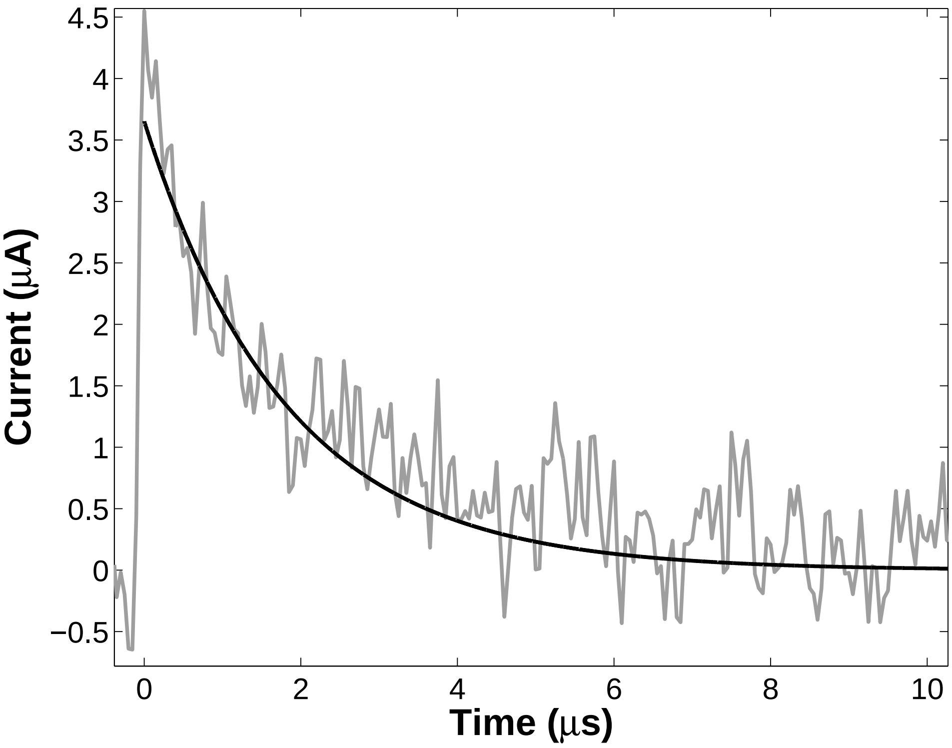

Fig. 3.23: Current-time transient observed at the backfilled layer in 90:10 water : acetonitrile with 0.18 M Na_2SO_4 as the supporting electrolyte. The step size was 0.069 mV and the platinum electrode radius was 12.5 μm. The solid line is a fit of Equation 3.10 to the data.

Chronoamperometry conducted on the microsecond timescale has been employed to probe the rate of electron transfer, k^0, across the monolayer electrode interface.[36, 249, 38] A potential step across the redox potential of an adsorbate can give rise to two distinct current transients. Firstly, a transient is observed due to double-layer charging and follows an exponential decay with a decay constant of $1/RC$, where RC represents the RC constant of the cell. This decay follows Equation 3.10;

$$i = \frac{\Delta E}{R} exp^{(-\frac{t}{RC})} \tag{3.10}$$

where ΔE is the size of the potential step in volts, R is the cell resistance and

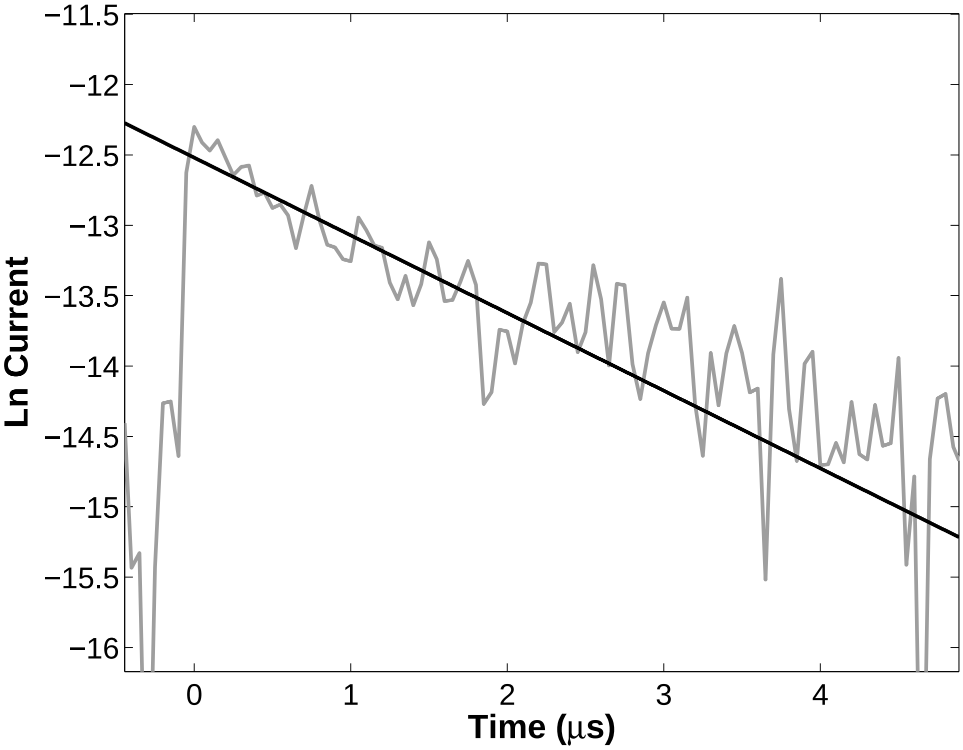

Fig. 3.24: Semi-log plot of data presented in Figure 3.23. The line shown is the best fit ($R^2 = 0.95$) of Equation 3.13, which corresponds to an RC constant of 1.8 x 10^{-6} s (intercept = -12.52).

C is the double layer capacitance.

The second transient observed is that of the faradaic current, i.e. the current resulting from the oxidation or reduction of the adsorbate and decays exponentially with a decay constant equal to the observed rate constant, k_f or k_b. Butler-Volmer theory relates the observed rate constant to the potential independent rate k^0 by:

$$k_f = k^0 exp(\frac{-\alpha nF\eta}{RT}) \tag{3.11}$$

$$k_b = k^0 exp(\frac{(1-\alpha)nF\eta}{RT}) \tag{3.12}$$

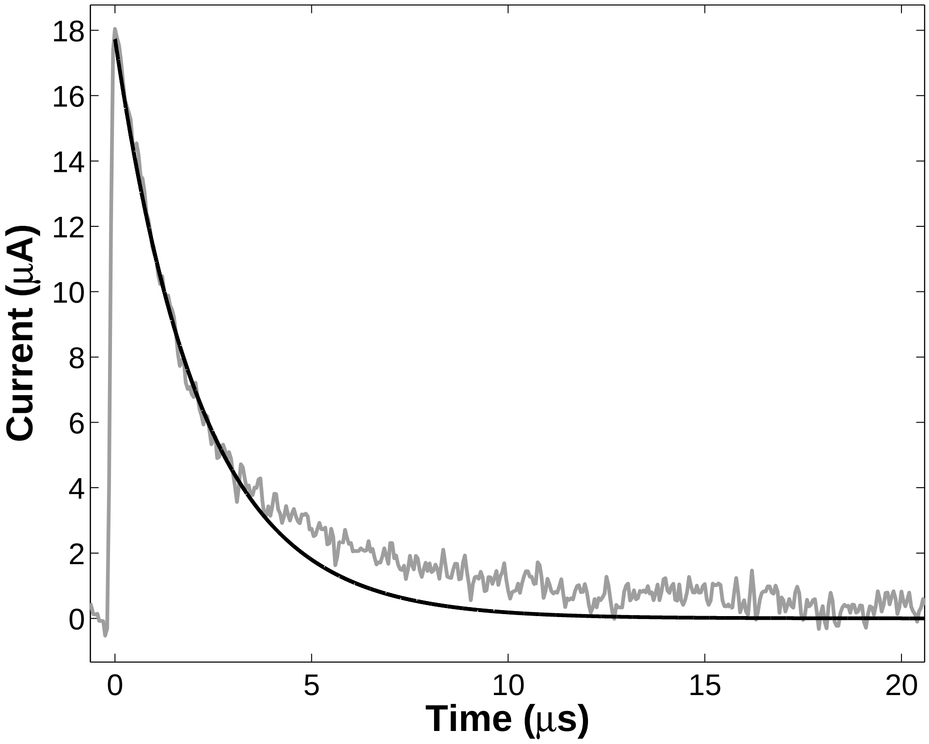

Fig. 3.25: Current-time transient observed at the backfilled layer in the presence of 20 μM $[Co(biptpy)_2]^{2+}$ in 90:10 water : acetonitrile with 0.18 M Na_2SO_4 as the supporting electrolyte. The overpotential was 80 mV and the platinum electrode radius was 12.5 μm. The black line is a fit to the RC decay.

where η is the overpotential, defined as the difference between the applied potential and the redox potential of the adsorbate and α is the transfer coefficient.

Figure 3.23 shows the current response of a 25 μm diameter platinum electrode in 90:10 H_2O: ACN with 0.18 M Na_2SO_4 as the supporting electrolyte where a backfilled layer has been assembled on the platinum electrode. Monitoring the current response in the absence of an electrochemically active guest yields information on the RC constant. This value needs to be 5-10 times smaller than the electron transfer step to acquire meaningful data. This figure also shows a fit of Equation 3.10 to the data, which confirms the single exponential nature of the decay. Figure 3.24 shows the semi-log plot of the data presented in Figure 3.23 and shows that a linear portion is obtained for approximately 4-5 μs after the potential step. The best fit line of this linear portion is also

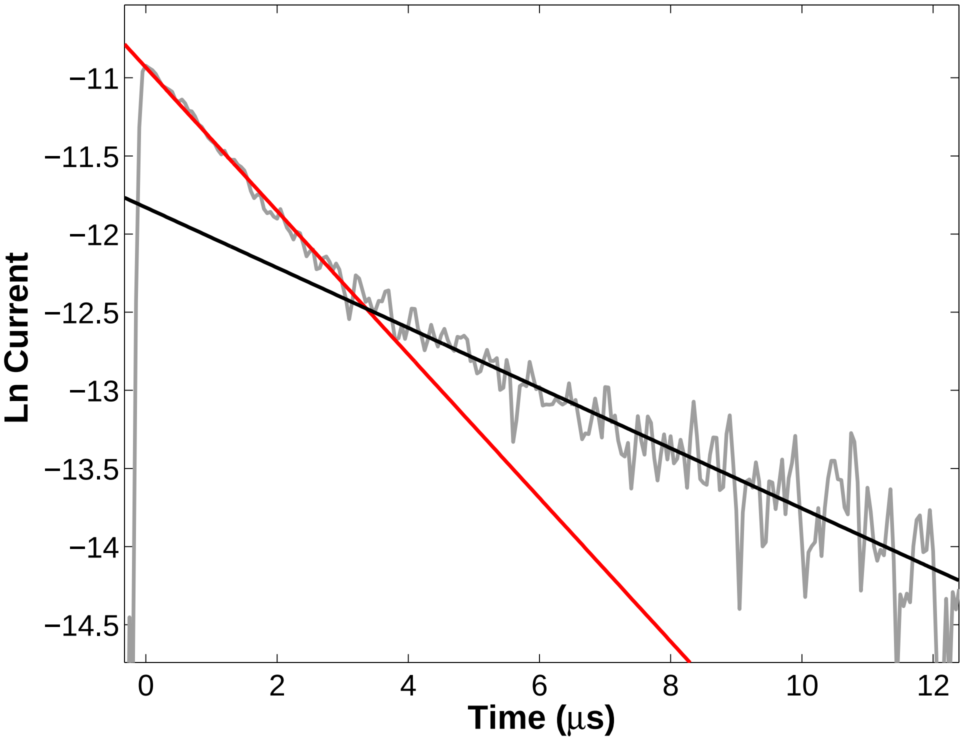

Fig. 3.26: 20 μM $[Co(biptpy)_2]^{2+}$ in 90:10 water : acetonitrile with 0.18 M Na_2SO_4 as the supporting electrolyte ΔE was 312 mV in this case and the platinum electrode radius was 12.5 μm.

shown. Taking the log form of Equation 3.10 yields:

$$Ln(i) = Ln(\frac{\Delta E}{R}) - \frac{t}{RC} \tag{3.13}$$

where ΔE is the magnitude of the potential step. Therefore, the inverse of the slope of the best fit line shown in Figure 3.24 corresponds to the RC constant. This value is 1.8 μs. This value is similar to, but slightly lower than, that determined by impedance spectroscopy in Chapter 2. This difference can be ascribed in part to the presence of the backfilled layer on the platinum electrode, which was not present during the impedance measurements, resulting in a lower capacitance value for the coated electrode (see Figure 3.5). Therefore, the RC constant is lower than previously seen for a bare platinum electrode but is consistent with that seen previously for coated platinum electrodes.[249, 252] The fast decay of the RC constant for the backfilled electrode means that the rate of electron transfer can be probed.

The rate of electron transfer of $[Co(biptpy)_2]^{2+}$ docked at the CD layer is of fundamental interest for several reasons. The host-guest nature of the interactions are highly versatile and are starting points for bio-mimetic systems. The rate of electron transfer across the CD cavity-guest interaction in a monolayer has not been probed before, although some studies have been carried out in solution.[110, 253, 245] The nature and speed of electron transfer across hydrophobic bridges has attracted much attention in recent years, due in part to the bio-mimetic nature of the such bridges.[110] Also, the rate of electron transfer would give insights into whether the complex dissociates from the cavity before electron transfer, as has been suggested for ferrocene type guests.[53]

Figure 3.25 shows the current-time transient recorded at a 12.5 μm radius platinum micro-electrode with a backfilled CD layer adsorbed in the presence of 20 μM $[Co(biptpy)_2]^{2+}$ after a potential step to an overpotential of 80 mV. The current response of such systems is expected to show bi-exponential behavior:

$$i_{(t)} = (\frac{\Delta E}{R})exp(\frac{-t}{RC}) + kQexp(-kt) \tag{3.14}$$

where the first term refers to the double-layer charging (ΔE is the potential step size) and a second term refers to the faradic response (where Q is the amount of faradic charge passed during the step). Therefore a plot of the natural log of the current versus the time should show two linear branches and Figure 3.26 shows a semi-log plot of the data presented in Figure 3.25. Two distinct linear branches are observed in this plot. As previously mentioned, the first of these corresponds to the RC constant, which is found to be 2.2 μs. This value is in good agreement with the investigation of the RC constant in the absence of $[Co(biptpy)_2]^{2+}$. The solid line in Figure 3.25 shows this RC transient decay and it is clear that there is a second transient present from this figure. This is clearly seen in Figure 3.26, where a linear branch can be seen from approximately 3-12 μs. This transient corresponds to the faradaic current and a rate constant of 2 x 10^5 s^{-1} is determined from this data.

The dependence of the observed rate constant on overpotential can yield the standard rate constant, k^0, according to Butler-Volmer formalism (Equations 3.12 and 3.11). Therefore, a plot of the natural log of k_f or k_b versus overpotential will yield the standard rate constant and the transfer co-efficient.

However, the creation of this plot was not possible for the system in question. The observed rate constant did not appear to depend on the overpotentials applied. In fact the rate did not significantly differ over the overpotential range of 86-171 mV. The reason for this is possibly related to the narrow range of overpotentials studied. However, a lack of layer stability at higher overpotentials restricted the available range. Therefore no reliable Tafel plots could be created.

Despite the problems outlined above, the rate of electron transfer can be at least estimated as approximately 1 x 10^5 s^{-1}, considering that k_{obs} is 2 x 10^5 s^{-1} at the relatively modest overpotential of 86 mV. This value is consistent with the observation that no significant peak splitting can be observed with increasing scan rate during CV measurements up to a scan rate of 100 V.s^{-1}. This value can be compared to a value of 3 x 10^4 s^{-1} for cobalt terpyridine complex linked to a platinum surface via a thiol group.[249] Ulstrup and co-workers have also investigated the rate of electron transfer from a cobalt terpyridine compound and found the rate of electron transfer to be approximately 2 x 10^3 s^{-1}. The distance between the metal centers and the electrode in these studies were comparable at approximately 7-8 $\mathring{A}$. The distance between the cobalt center and the electrode in this study is hard to estimate, but is probably in the region of 9-15 $\mathring{A}$, considering that the CD is 7.8 $\mathring{A}$ high. That the rate of electron transfer appears faster across a non-covalent interface compared to a directly bound system is surprising but differences in the re-organisation energy or the degree of electronic coupling to the electrode surface could provide an explanation. Unfortunately, the limitations of this experiment preclude further illumination of these issues. However, the rate of electron transfer is almost certainly faster than the disassociation rate of $[Co(biptpy)_2]^{2+}$ from the cavity, which was discussed earlier. Therefore, it would appear that the compound undergoes electron transfer and then disassociates from the CD, in contrast to the behavior described for ferrocene.

3.4 Conclusion

Adsorbed monolayers can be used to create molecular recognition sites on electrodes when the monolayer contains moieties capable of supramolecular host-guest interactions. The cyclodextrin family are among the most attractive targets for these systems as they display an extensive host guest chemistry. The use of transition metal complexes as guest molecules allows the binding events to be studied electrochemically. However, important issues must be explored to characterise any host-guest receptor system properly. These include the permeability of the layer to solution phase probes, the effect of co-adsorption of sealing alkanethiol molecules on CD cavity population and orientation, the thermodynamics of binding, the effect of docking ligands and the dynamics of electron transfer. In addition, SERS can provide a spectroscopic characterisation of the mixed monolayer. This Chapter has addressed these points.

This Chapter has described spontaneously adsorbed monolayers of γ-CDs functionalised with two aminomethyl-pyridine groups on platinum and gold electrodes. Electrochemical studies revealed that the layers are permeable to solution phase probes and that backfilling of the defects in the layer with 1-nonanethiol greatly increased the blocking ability of the adsorbed layers. SERS spectra of backfilled layers showed both pyridine and alkanethiol bands, indicating that backfilling with alkanethiols does not displace the pyridine moieties of the CDs. The exposure of the layers to a solution of inclusion complex, $[\mathrm{Co(biptpy)_2}]^{2+}$ was monitored electrochemically. Whereas no electrochemical signal was observed at the pure γ-CD-$(\mathrm{py})_2$ monolayer, a surface confined and highly reproducible redox process associated with the $[\mathrm{Co(biptpy)_2}]^{2/3+}$ couple was observed at the backfilled layer. This suggested that the backfilling process disrupts inter-CD interactions in the layer, causing orientational changes at the CD which permitted inclusion of the solution phase guest. The inclusion process in the mixed monolayer depended on the bulk concentration of $[\mathrm{Co(biptpy)_2}]^{2+}$ guest in solution and this dependence was fitted to the Langmuir isotherm. Experimental data indicated that the association constant was larger at the monolayer than for corresponding systems in solution, demonstrating that immobilisation of the CD does not impede complex formation.

The importance of the biphenyl ligands to the binding process is evidenced by comparison with a structurally analogous compound which lacks these ligands. The rate of electron transfer from the cobalt center to the metal (1 x 10^5 s^{-1}) appears to be several orders of magnitude faster than the disassociation of the compound from the CD layer (no significant disassociation at 20 $V.s^{-1}$).

In conclusion, a highly reproducible supramolecular interfacial assembly containing CD hosts has been formed and the creation of an inclusion complex with the cavity guest $[Co(biptpy)_2]^{2+}$ has been described. This system will be employed in the next chapter in the creation of tunnelling junctions incorporating host-guest receptors.

Chapter 4

Hg-Pt tunnelling junctions incorporating host-guest assemblies

4.1 Introduction

The fundamental nature of electron tunnelling in molecules has received significant attention over several decades.[109, 107, 142] Metal-insulator-metal (M-I-M) junctions predate the now common scanning probe techniques such as scanning tunnelling microscopy (STM),[129] but have become popular once more when combined with the well characterised alkanethiol self-assembled monolayers (SAMs) formed on metal electrodes. These systems have several advantages over scanning probe techniques such as ease of fabrication and relatively simple instrumentation.

Junctions have been fabricated both from two mercury drops (Hg-Hg)[124, 125, 135] and from a mercury drop and a solid metal plate (Hg-M)[126, 142, 141] where M is gold, silver or silicon.[147, 149] The conclusions drawn from each type of study are broadly similar; electron tunnelling is achieved by a non-resonant mechanism and the tunnelling co-efficient, β, is not significantly affected by small applied voltages. Rampi and Whitesides have extended this work to investigate tunnelling junctions incorporating redox centers and have demonstrated a potential depend signal that is linked to the redox couple.[143, 118, 128] However, the mechanism of electron transport in these systems remains unclear.

This chapter describes a novel Hg-Pt junction. Platinum is an attractive metal for use in conjunction with mercury as it amalgamates with the mercury at a much slower rate compared to other common electrode metals. Alkanethiols are the most commonly studied molecules in these type of junctions and are employed here to characterise the system. The incorporation of cyclodextrin (CD) layers and $[Co(biptpy)_2]^{2+}$ into the junctions is then described. The use of host-guest interactions to incorporate various molecules into the molecular junctions is demonstrated. The advantage of using CD layers is facile incorporation of a range of species into the junction. The tunnelling current appears to be influenced by the nature of guest molecules incorporated in the junction. Junctions with conjugated guests included in the CD cavities show larger currents compared to those with non-conjugated guests. Finally, the redox activity of $[Co(biptpy)_2]^{2+}$ can be shown to influence the current response of a CD monolayer junction and current transport mechanisms for this response are suggested.

4.2 Experimental

4.2.1 Apparatus

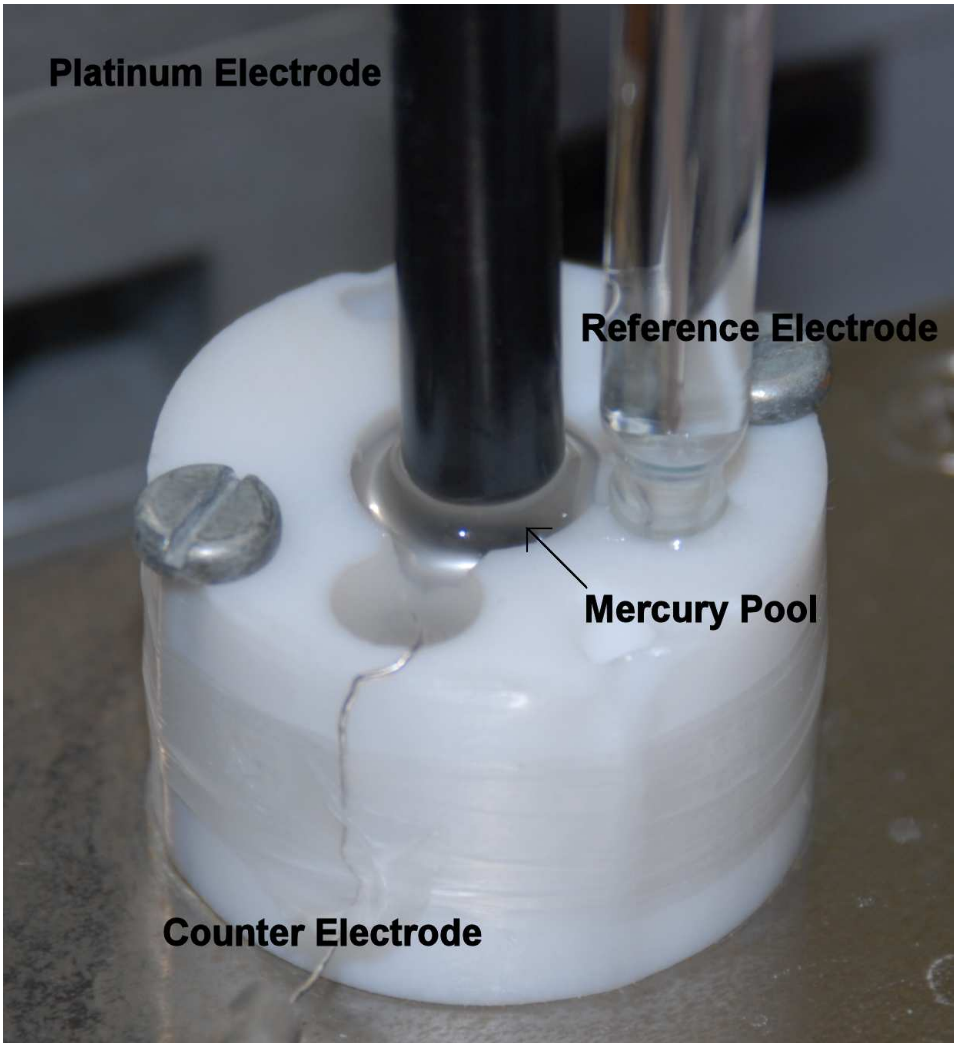

Fig. 4.1: Photograph of the cell used to form the Hg-Pt junctions.

Figure 4.1 shows the custom fabricated cell that was used during the course of these experiments. A mercury pool sits at the bottom of a well in a teflon block, where a contact is inserted to facilitate external potential control (note the contact is not shown in Figure 4.1 and is isolated from the solution). The cell allows electrolyte to sit on top of the mercury and has wells for both counter and reference electrodes, therefore facilitating the use of a four electrode system. The whole cell is fixed to the bottom plate of a piezoelectric stage and the platinum electrode (radius = 1 mm) is held directly over the mercury pool (radius = 5 mm) where it can be raised or lowered by the piezoelectric stage (Burleigh IW-700) as required. Potential control was exerted over both platinum and mercury by the use of a bi-potentiostat (model CHI900A).

The majority of experiments were carried out while moving the platinum electrode towards the mercury pool and simultaneously monitoring the current at this electrode. The speed of the approach was typically set at 25 μm.s^{-1} and variation of this rate did not significantly influence the results obtained. This displacement per second is obviously quite large when compared to a molecular layer, but the liquid nature of the mercury pool allows the pool to displace when the electrodes are brought into contact. The bias between platinum and mercury electrodes was maintained at 0.4 V unless otherwise stated during acquisition of the i-d curves.

The potential of the mercury electrode was typically held between -0.3 and -0.1 V to avoid desorption of the alkanethiols. The platinum electrodes were cleaned by manual polishing and electrochemical cycling in acid as described in Chapter 2. Monolayers of alkanethiols were prepared on platinum by immersing the cleaned electrode in a millimolar solution of the desired alkanethiol solution in ethanol for 24 h. Monolayers of alkanethiols on mercury were prepared by including the desired alkanethiol in the cell solution, typically at millimolar concentrations in a mix of ethanol/water (typically 25:75 v/v). The monolayers were formed on the mercury electrode at open circuit potential. Sodium sulfate was used as the electrolyte, typically at concentrations of 0.15 M. Mixed CD/alkanethiol monolayers were prepared on platinum as described in the last chapter. The junctions incorporating $[\mathrm{Co(biptpy)_2}]^{2+}$ as a CD binding guest were performed in solutions of 9:1 water/acetonitrile with 0.18 M sodium sulfate as the electrolyte, typically with 70 μM $[\mathrm{Co(biptpy)_2}]^{2+}$.

All solutions were deoxygenated with Argon prior to use.

4.2.2 Materials

γ -CD-(py)$_2$ was synthesised as described in Chapter 2. [Co(biptpy)$_2$]$^{2+}$ and [Co(tpy)$_2$]$^{2+}$ were synthesised as described previously.[237]

C$_{60}$ (99.9 %) was purchased from BuckyUSA.

4.3 Results and Discussion

4.3.1 General characteristics of Hg-Pt tunnelling junctions

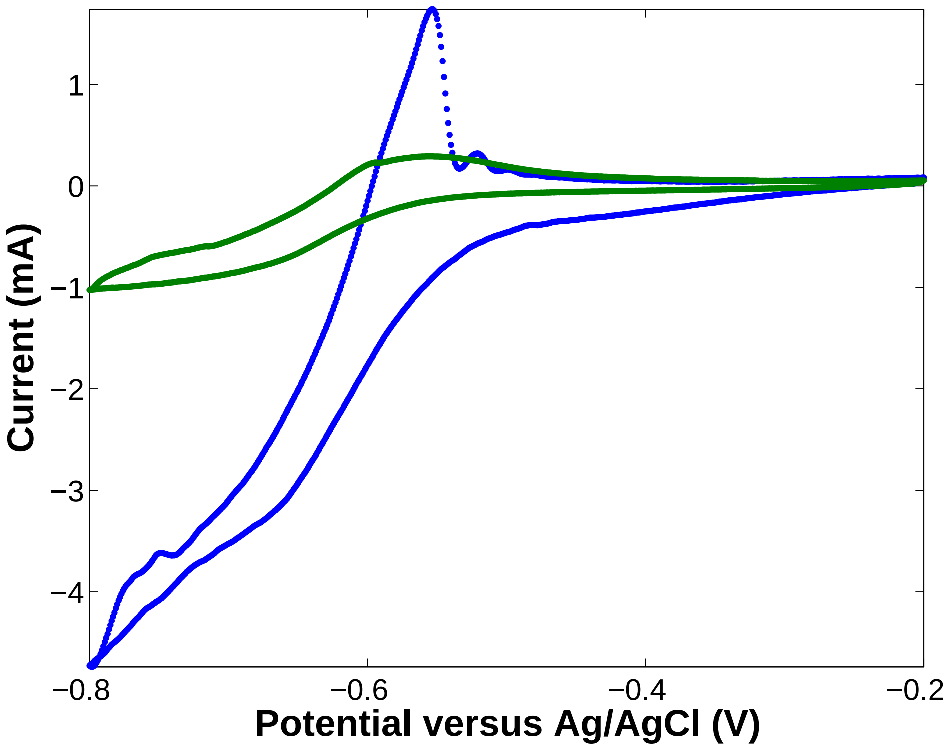

Fig. 4.2: CV of 4 mM methyl viologen at a Hg electrode in 20:80 ethanol:water with 0.16 M Na_2SO_4 as the supporting electrolyte. The green line is the response when the solution also contained 4 mM $C_{16}SH$. The scan rate is 1 $V.s^{-1}$ and the third scan is presented.

Alkanethiols have been used in M-I-M junctions by several groups[142, 124, 145, 149] and are employed here to characterise the Hg-Pt junctions as they yield a well defined current dependence on junction thickness. This is due to the close packing of the alkanethiols on metals. The solution typically contains the alkanethiol desired for assembly on the mercury electrode at milli-molar concentrations. Alkanethiols have been shown to effectively adsorb on mercury in several studies[30, 140] and Figure 4.2 shows that including 4 mM of $C_{16}SH$ in the electrolytic solution reduces the magnitude of the current seen at the

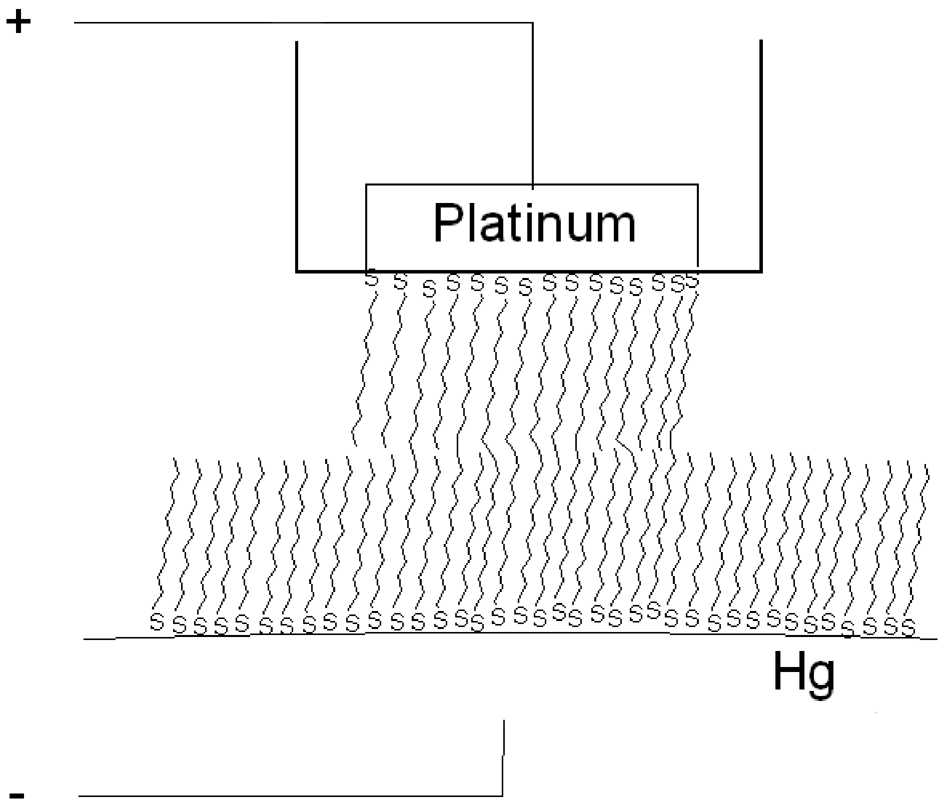

Fig. 4.3: Schematic of the Hg-SC_{11}-$C_{11}S$-Pt junction.

electrode from the solution phase probe methyl viologen significantly, which suggests the formation of a blocking layer. This blocking layer prevents the redox species from making direct contact with the electrode.

Figure 4.3 is a schematic of the type of junction assembled using $C_{11}SH$ monolayers adsorbed on both electrodes. Upon applying a potential bias to the junction current is expected to flow, as described in Chapter 1. The magnitude of this current is expected to depend on two factors; the distance across the junction, d, and the tunnelling co-efficient, β, such that:

$$i = i_0 exp^{-\beta d} \tag{4.1}$$

Figure 4.4 shows the i-d curve of the current at the platinum electrode as it

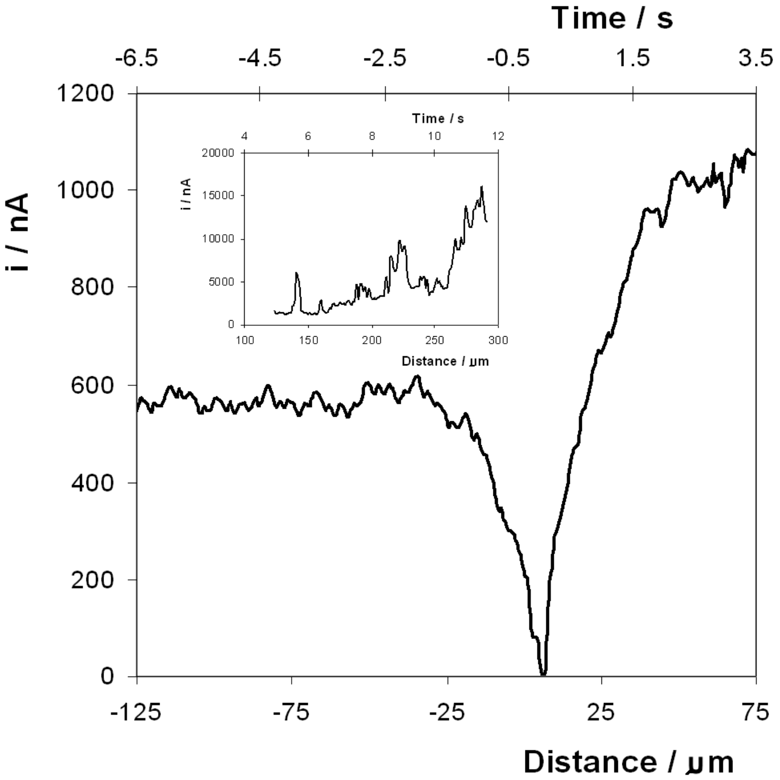

Fig. 4.4: Current-distance curve showing formation and characteristics of a C_{11}-C_{11} bi-layer Pt-Hg tunnelling junction at 0.4 V potential bias. The solution was composed of 9 mM $C_{11}SH$ in 1:1 ethanol: water with 0.1 M Na_2SO_4 as the supporting electrolyte. A $C_{11}SH$ layer was assembled on the platinum electrode before measurement. The inset shows the i-d characteristics at long times.

approaches and enters the mercury pool at a bias voltage of 400 mV at short and long distances. The lower x-axis shows the separation between the two electrodes while the upper x-axis shows the time, which can be useful for understanding the temporal characteristics of the junction. Several key features of junction formation and behavior can be seen in this figure. When the monolayer modified platinum electrode is far from the mercury surface the current is very low, at 560 ±29 nA, and independent of vertical displacement/time. This current most likely arises from Faradaic processes associated with low concentrations of impurities in the solution. As the electrode approaches the surface the current decreases due to blocking of any solution phase reactions as the solution is squeezed out. In addition, the double layer capacitance is likely to decrease due to the differences in dielectric constants of mercury and water. This feature was seen in approximately 70% of the alkanethiol bi-layer experiments and is in agreement with visual inspection of the junction at this point, which indicates that the two electrodes were in very close proximity.

Once the junction is formed, the current increases due to tunnelling across the bilayer before reaching a steady state value of 1060 ±30 nA when the platinum electrode is displaced approximately 75 μm from the point where the electrodes first make contact. It is perhaps important to note that because the mercury pool is mobile it distorts as the platinum electrode makes contact and the distance scale in Figure 4.4 may not accurately represent the extent to which this electrode penetrates the pool. The current plateau is consistent with the formation of a stable tunnelling junction with the magnitude of the current being controlled by the electrical properties of the monolayer. The time required to reach a stable tunnelling current is only 3 s.

In seeking to probe the electron tunnelling properties of molecular assemblies, a key issue is contact resistance which can cause the tunnelling current or rate to be underestimated. A distinctive feature of the approach used here is that the platinum electrode is mechanically moved even after the tunnelling junction is formed. This continuous movement provides an insight into the mechanical stability of the junction and how mechanical pressure affects the tunnelling current. The inset of Figure 4.4 shows the current behavior at longer times and relatively large current spikes are observed, which return to an approximately constant baseline value. These current spikes are typical for all alkanethiol measurements made for this system. Finally, as the platinum electrode is buried further into the mercury pool the current rises and eventually a metal-metal short occurs, causing the current to rise immediately to large values. The junction is effectively crashed at this stage.

A small percentage (<10%) of these types of approach do not result in the current characteristics described. In these measurements the current is seen to fall as the junction is closed but no subsequent rise is observed as is shown in Figure 4.5 for a C_{11}-C_{11} junction assembled in non-aqueous solvent. This suggests that these junctions possess significant trapped solvent which prevents close approach of the two monolayers. This behavior was particularly observed

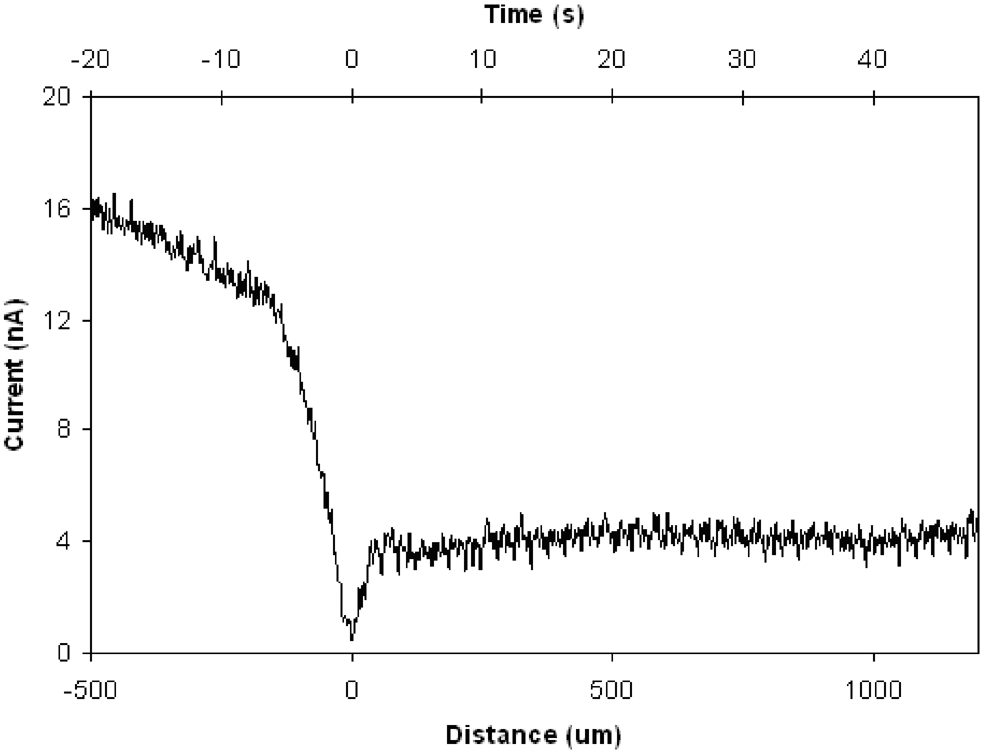

Fig. 4.5: Current-distance curve showing a C_{11}-C_{11} bi-layer Pt-Hg junction at 0.4 V potential bias that failed to show tunnelling current. The solution was composed of 6 mM $C_{11}SH$ in 1:4 toluene: acetonitrile with 0.1 M $TBABF_4$ as the supporting electrolyte. A $C_{11}SH$ layer was assembled on the platinum electrode before measurement.

at junctions where ionizable groups were present at the end of the alkane chain, e.g. carboxylic acids.

The spikes that appear in the tunnelling current are interesting features of this M-I-M junction and have not been observed at other M-I-M junctions described in the literature. The data portrayed in Figure 4.4 was obtained on a vibration isolation table to rule out vibrational interference. The magnitude and frequency of the current spikes are independent of the platinum displacement rate, v, for $10 < v > 50$ μm.s^{-1}, suggesting that mechanical translation does not induce the spikes. The spikes are possibly the result of defects in the mercury monolayer aligning with defects on the platinum. If this is the case, they can be considered temporary "shorts". The defects responsible for

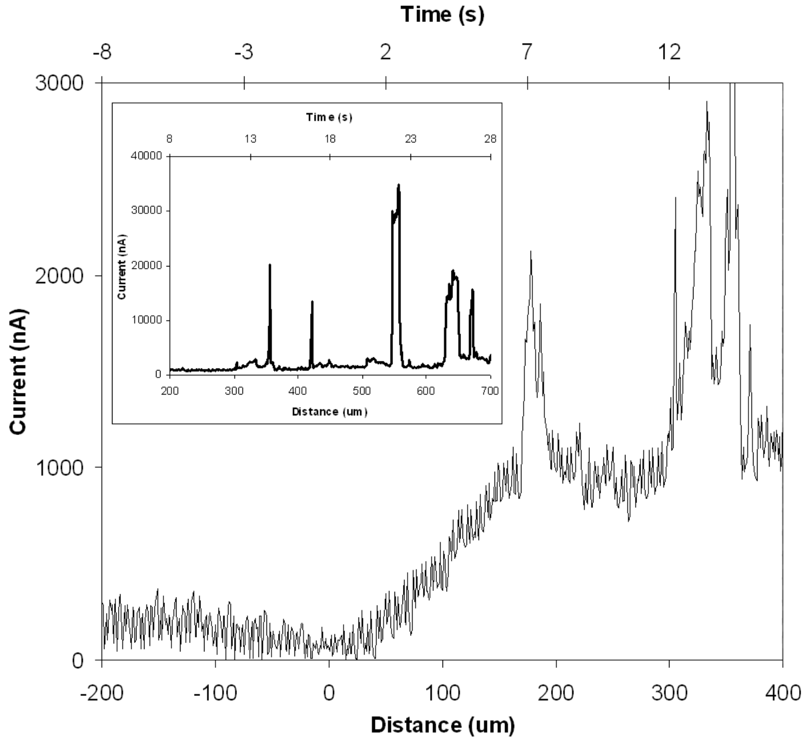

Fig. 4.6: Current-distance curve showing formation and characteristics of a C_{16}-C_9 bi-layer Pt-Hg tunnelling junction at 0.4 V potential bias. The solution was composed of 1 mM $C_{16}SH$ in 1:5 ethanol: water with 0.16 M Na_2SO_4 as the supporting electrolyte. A C_9SH layer was assembled on the platinum electrode before measurement. The inset shows the i-d characteristics at long times.

shorting have the capacity for self repair because of the mobility of the alkanethiol molecules on mercury. When the platinum becomes deeply embedded in the mercury these type of shorts intensify in both frequency and magnitude and possibly lead to the final metal-metal contact. However, this metal-metal contact shorting is often not seen until distances of up to a millimeter have been reached (see Figure 4.6).

Several studies of M-I-M junctions formed from mercury and other metals have emphasized the importance of a small junction area as key to reducing defects and therefore shorting. While most similar studies have been performed using significantly smaller junction areas[136] than the Pt-Hg junction (platinum electrode radius = 1 mm) some studies have also been carried out on junctions with comparable areas to those described here.[145] Rampi and Whitesides have recently evaluated the effect of surface roughness on the current response

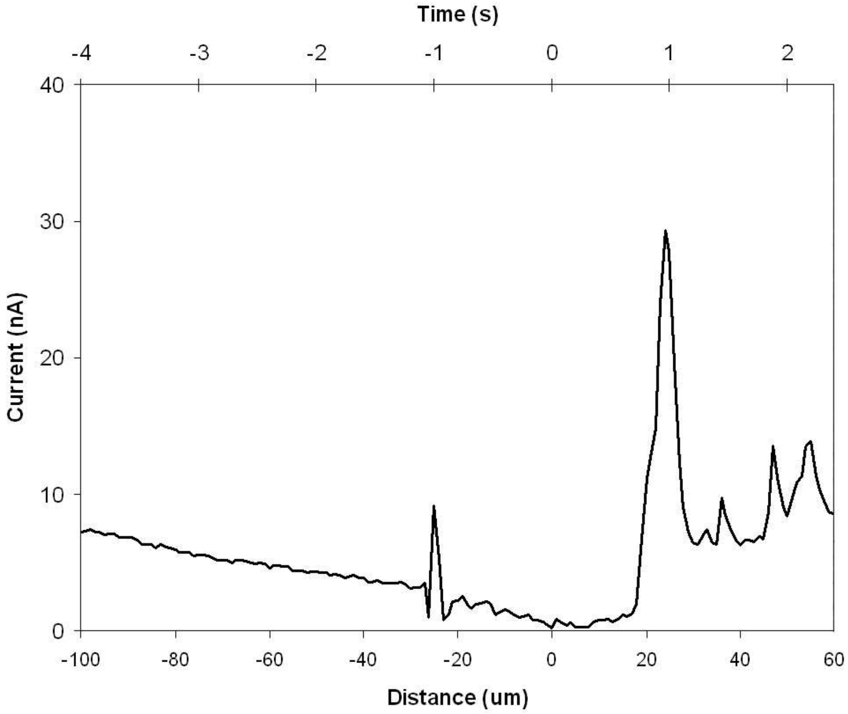

Fig. 4.7: Current-distance curve showing formation and characteristics of a C_{16}-C_{16} bi-layer Pt-Hg tunnelling junction at 0.4 V potential bias. The solution was composed of 1 mM $C_{16}SH$ in 1:5 ethanol: water with 0.16 M Na_2SO_4 as the supporting electrolyte. A $C_{16}SH$ layer was assembled on the platinum electrode before measurement.

of macroscopic junctions.[127] They found that while atomically flat template stripped silver surfaces yielded the most reproducible results, meaningful results could also be achieved using rougher electron beam deposited silver. The roughness factor of the polycrystalline electrodes used in this study was below two and it would appear that this may be a factor in the current spiking, as defects in the layer may be related to underlying features of the substrate.

Figure 4.6 shows the tunnelling current of an asymmetric alkanethiol junction also at 400 mV potential bias. In this case a C_9SH layer is pre-formed on the platinum electrode and 1 mM $C_{16}SH$ is included in the solution. This figure shows broadly similar characteristics to the C_{11} symmetric junction which indicates that the placement of the non-covalent interface, i.e. CH_3-CH_3 interface, in the junction does not significantly alter tunnelling behavior. Finally, Figure 4.7 shows the tunnelling current of a C_{16} bilayer junction at 400 mV

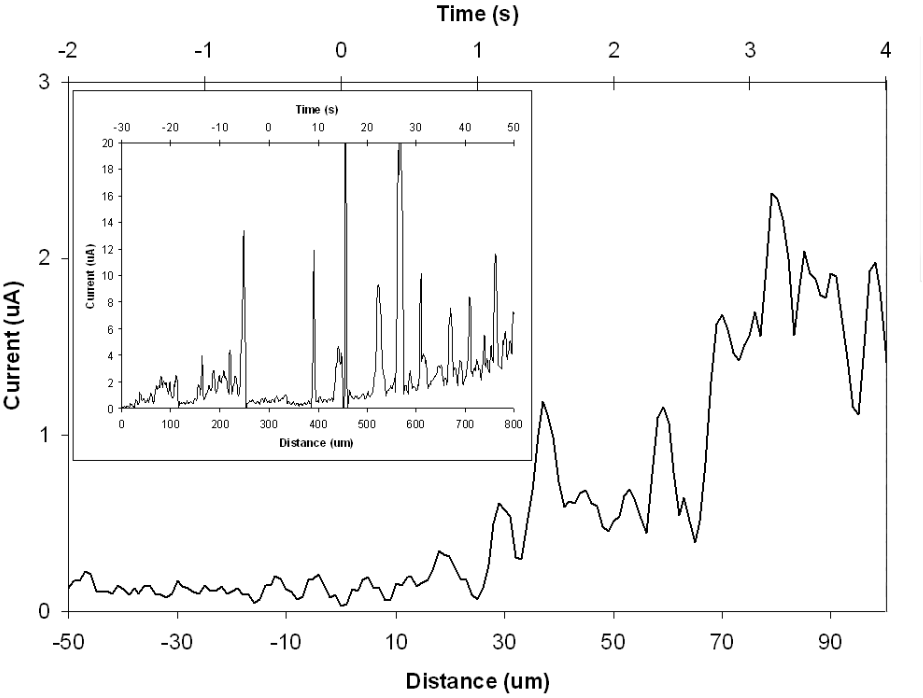

Fig. 4.8: Current-distance curve showing formation and characteristics of a C_{16} monolayer Pt-Hg tunnelling junction at 0.4 V potential bias in water with 0.2 M Na_2SO_4 as the supporting electrolyte. A $C_{16}SH$ layer was assembled on the platinum electrode before measurement. The inset shows the i-d characteristics at long times.

potential bias. Again, this figure shows similar characteristics to those shown above only the magnitude of the tunnelling current is greatly reduced due to the increased separation between the electrodes, due to the thicker alkanethiol layer.

Monolayer junctions can also be formed using the Hg-Pt method. Figure 4.8 shows the characteristics of a C_{16} layer assembled on the platinum electrode with no layer on the mercury at 400 mV potential bias. While this figure clearly shows characteristics comparable to the other examples shown, the current is somewhat lower than that expected for similar thickness bilayer junctions. Other studies have suggested a weaker tunnelling effect through monolayers due to poor contact at the non-bound electrode[254, 139] and this is a possible reason for the smaller current. Nonetheless, this experiment shows that determination of tunnelling current is possible with both mono and bilayers using this system.

4.3.2 Stability of alkanethiol Hg-Pt junctions

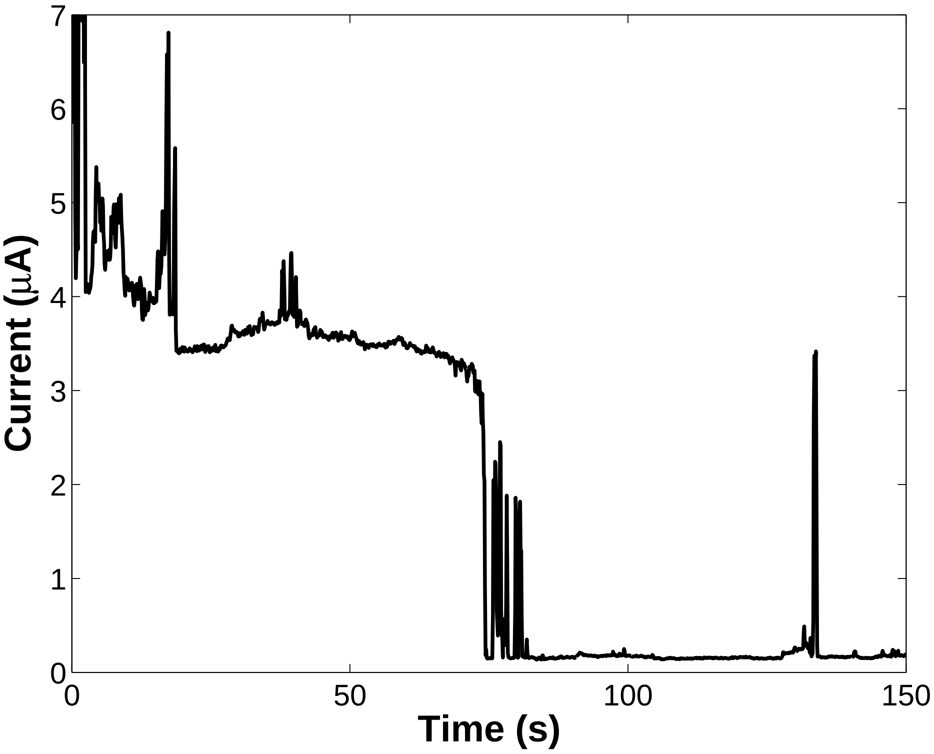

Fig. 4.9: Current-time trace of $C_{16}SH$ junction in water with 0.2 M Na_2SO_4 as the supporting electrolyte. The potential of the Pt and Hg electrodes is 0.1 and -0.3 V versus Ag/AgCl respectively. A $C_{16}SH$ layer was assembled on the platinum electrode before measurement.

The stability of the Hg-Pt alkanethiol junctions was investigated by monitoring the tunnelling current as a function of time. This experiment should indicate if the current spikes are related to the displacement of the platinum electrode. Figure 4.9 shows the current response of a $C_{16}SH$ layer junction to a bias voltage of 400 mV as a function of time. The trace shows similar spikes to those observed when the platinum electrode is in motion. The junction can also be seen to break (although not short) after 70 seconds, a result which compares favorably to other M-I-M junctions described in the literature.[137,138] As this experiment was performed on a vibration isolation table with no movement of the platinum electrode, the current spiking observed is unlikely to be related exclusively to the electrode displacement but also to other factors, most likely layer defects.

These results show that while the junctions are reasonably stable over time, breakdown can result in one of two ways. Firstly, the junction can break mechanically, whereby a metal-metal short is formed, as seen in the last section. Secondly, Figure 4.9 shows that the tunnelling can abruptly stop and the current can fall back to normal “solution” levels. This would appear to be due to the inter-calculation of solvent between the layers. This breakdown of tunnelling is naturally more prevalent when the electrodes are stationary, as opposed to the metal-metal shorting which is commonly seen when the platinum electrode is displaced into the mercury, and appears to be pressure driven.

4.3.3 Tunnelling spectroscopy

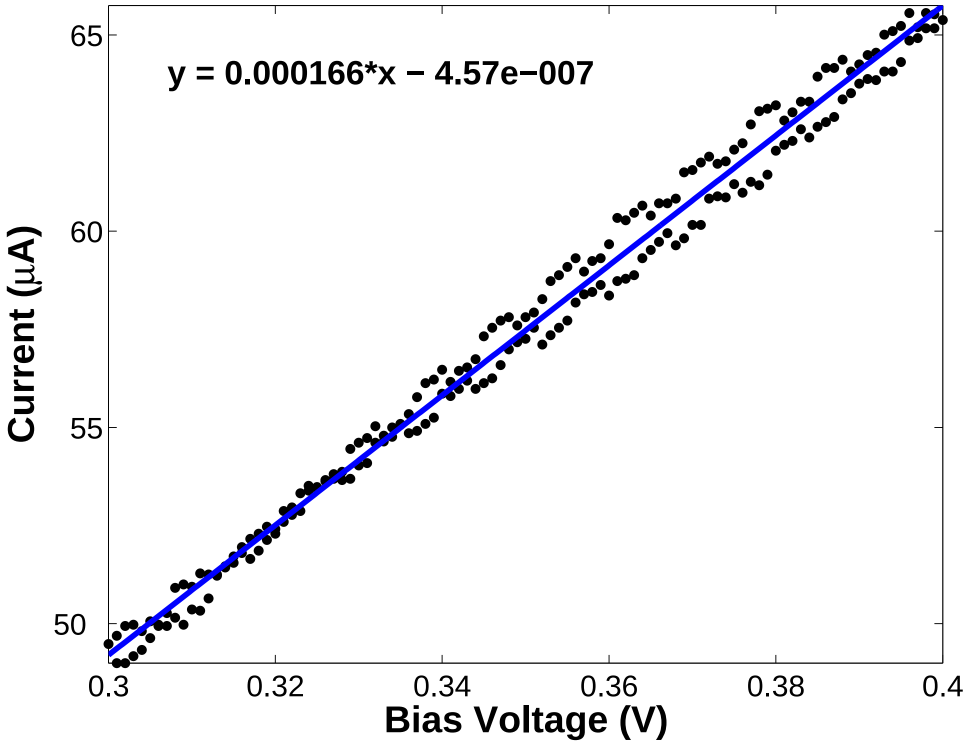

Fig. 4.10: Current-voltage curve of $C_{16}SH$ junction in water with 0.2 M Na_2SO_4 as the supporting electrolyte. The potential of the Pt electrode is varied between 0.3-0.4 V with respect to the potential of Hg pool (-0.3 V versus Ag/AgCl). A $C_{16}SH$ layer was assembled on the platinum electrode before measurement. The blue line indicated is a linear fit of the data with a correlation co-efficient of 0.99.

The current voltage (i-V) characteristics of molecules can be probed using the Hg-Pt junctions, however, the stability issues described above hamper the collection of i-V curves for these junctions. It would also appear that scanning the potential over time decreases the stability of the junction somewhat. Typically, most of the i-V curves collected show a degradation of the junction with scanning (i.e. the slope of the line gets progressively greater until metal-metal shorting is observed). Therefore, the use of fast scan rates yields the best i-V results in this case. Figure 4.10 shows an i-V curve obtained using a $C_{16}SH$ monolayer junction. Unfortunately, the solvent system limits the range of voltage that could be scanned, but it is also true that the junctions show greater

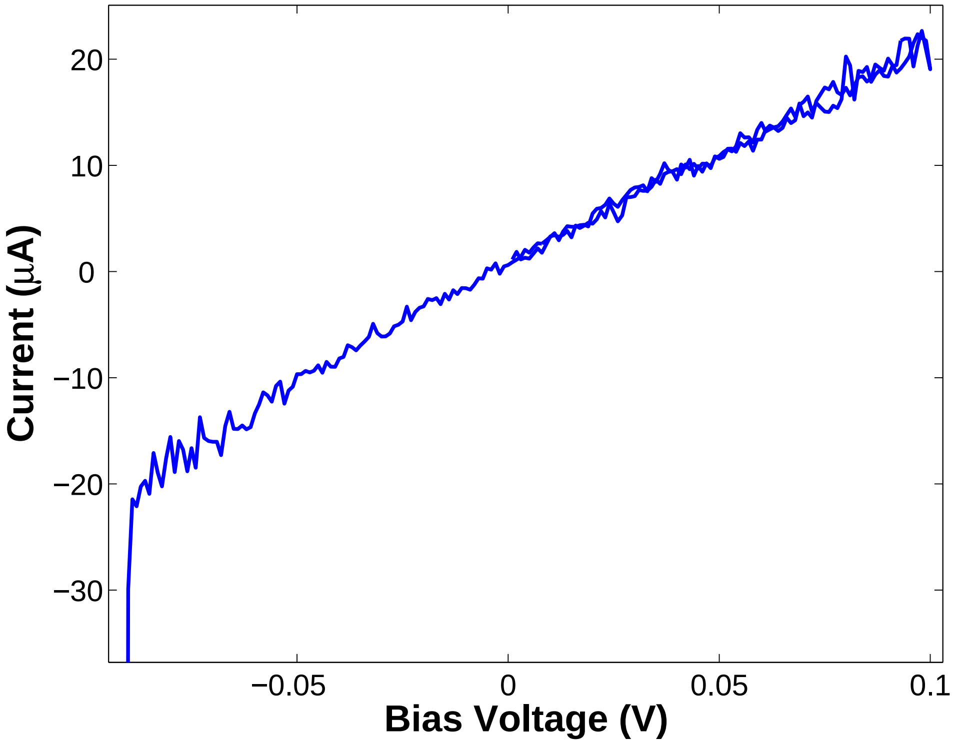

Fig. 4.11: Current-voltage curve of C_{11} bilayer junction. Solution composition is 9 mM $C_{11}SH$ in DMF with 0.1M $TBABF_4$ as the supporting electrolyte. The potential of the Pt electrode is varied between -0.1 and 0.1 V with respect to the potential of Hg pool (0 V versus the Fe/Fe^+ couple). A $C_{11}SH$ layer was assembled on the platinum electrode before measurement.

stability over small potential ranges. Nevertheless, the curve is clearly linear at bias voltages of 0.3-0.4 V. The i-V behavior of molecules is expected to be linear at low potential bias with an exponential current dependence at high potential bias. However, linear i-V curves at potential bias up to 0.4 V have been seen for Hg-Hg junctions by Slowinski and others.[138, 125] The blue line in Figure 4.10 shows a linear fit of the i-V data and can be extrapolated back to the origin. This suggests that the current is linear at these overpotenitals and can be modelled by:

$$i = \frac{1}{R}V \tag{4.2}$$

where R is the resistance of the junction in ohms. Figure 4.11 shows an i-V curve obtained in non-aqueous solvent, which permits a wider potential

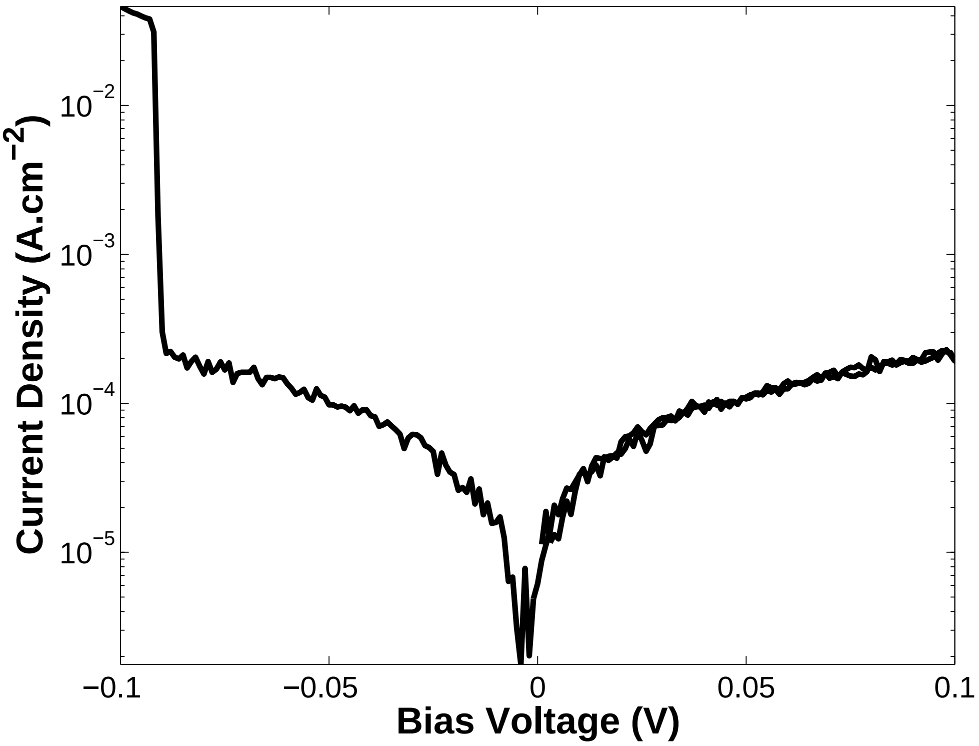

Fig. 4.12: Current-voltage curve of C_{11} bilayer junction. Solution composition is 9 mM $C_{11}SH$ in DMF with 0.1M $TBABF_4$ as the supporting electrolyte. The potential of the Pt electrode is varied between -0.1 and 0.1 V with respect to the potential of Hg pool (0 V versus the Fe/Fe$^+$ couple). A $C_{11}SH$ layer was assembled on the platinum electrode before measurement.

window, which exhibits linear characteristics around the origin. The junction can be seen to fail at about -0.09 V, possibly due to the stability issues discussed above. The equation of the best fit line through the data is $y = 0.0002186x + 2.2x10^{-7}$ with a correlation co-efficient of 0.9908, which confirms the linear current-overpotential behavior of the junction. In the literature, i-V curves are typically expressed on a log scale which can be seen in Figure 4.12. The large increase in current seen at about -0.09 represents junction failure, but otherwise the current is broadly symmetrical around the origin. Junction failure during i-V curve experiments is also reported in a recent paper by Rampi[127] and is attributed to the surface roughness of the solid metal electrode.

The resistance of the $C_{16}SH$ mono and C_{11} bilayer can be calculated as 6 kΩ and 4.5 kΩ respectively which is within the experimental error associated with multiple measurements of current-distance curves for the same layers. The greater resistance for the thinner $C_{16}SH$ layer can be attributed to the lack of a second covalent contact to the other electrode, as previously seen. Therefore, tunnelling across the interface between alkanethiol layers would appear to be more efficient than tunnelling across the CH_3-Hg interface. This conclusion has been made by several previous studies of M-I-M junctions and STM/AFM single molecule measurements.[254, 139]

In conclusion, these experiments show that while i-V curves were difficult to obtain due to stability problems, the i-V characteristics are in broad agreement with previous studies which show symmetric behavior around the origin at the potential biases explored here, i.e. up to at least 0.4 V.

4.3.4 Distance dependence of alkanethiol Hg-Pt junctions

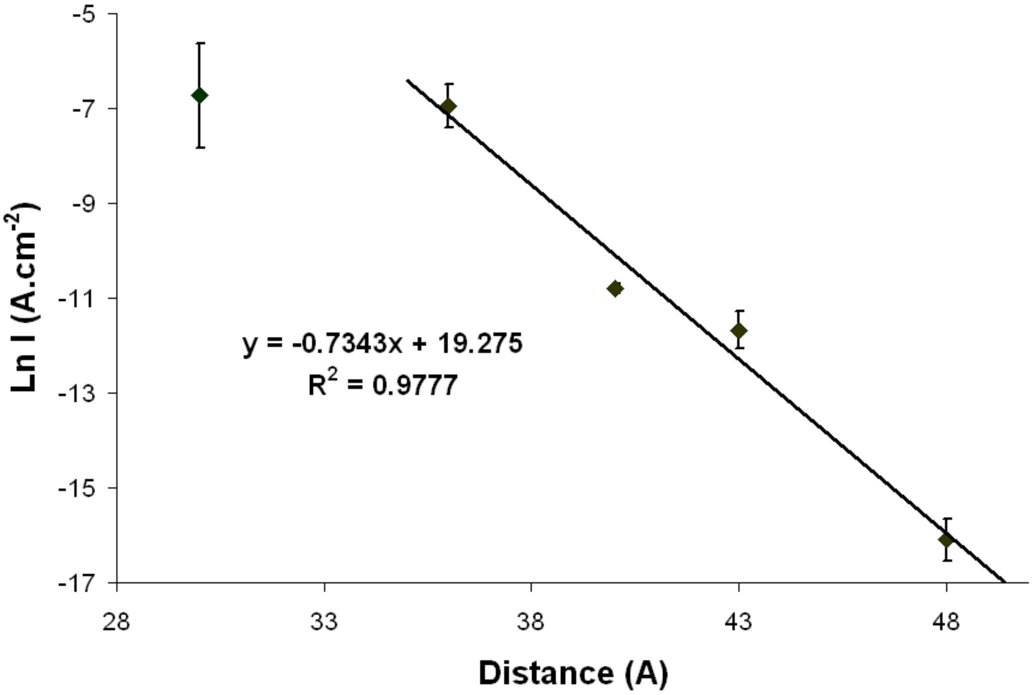

Fig. 4.13: Variation of the natural log of the tunnelling current density in Hg-Pt junctions at 400 mV bias voltage with junction thickness in angstroms. The error bars represent the standard deviations of at least five independent junction measurements.

The theoretical background described in Chapter 1 predicts that tunnelling current will decay exponentially with distance, according to Equation 4.1 if the current is due to non-resonant tunnelling. One of the most compelling reasons for using alkanethiol molecules in M-I-M junctions is the ease with which this relationship can be probed simply by varying the length of the alkane chain. Figures 4.13 and 4.14 show the natural log current dependence on distance in angstroms and per CH_2 respectively for alkanethiol bilayer junctions at a bias voltage of 400 mV as determined from multiple ($n \geq 5$) i-d measurements. The plots are generally linear but it is clear that the best fit is obtained by omitting the C_9-C_9 point. As seen on the graph the reproducibility associated with this point is the lowest and it is possible that the Hg-Pt junction described here is unsuitable for the measurement of thin alkanethiol layers. This may be

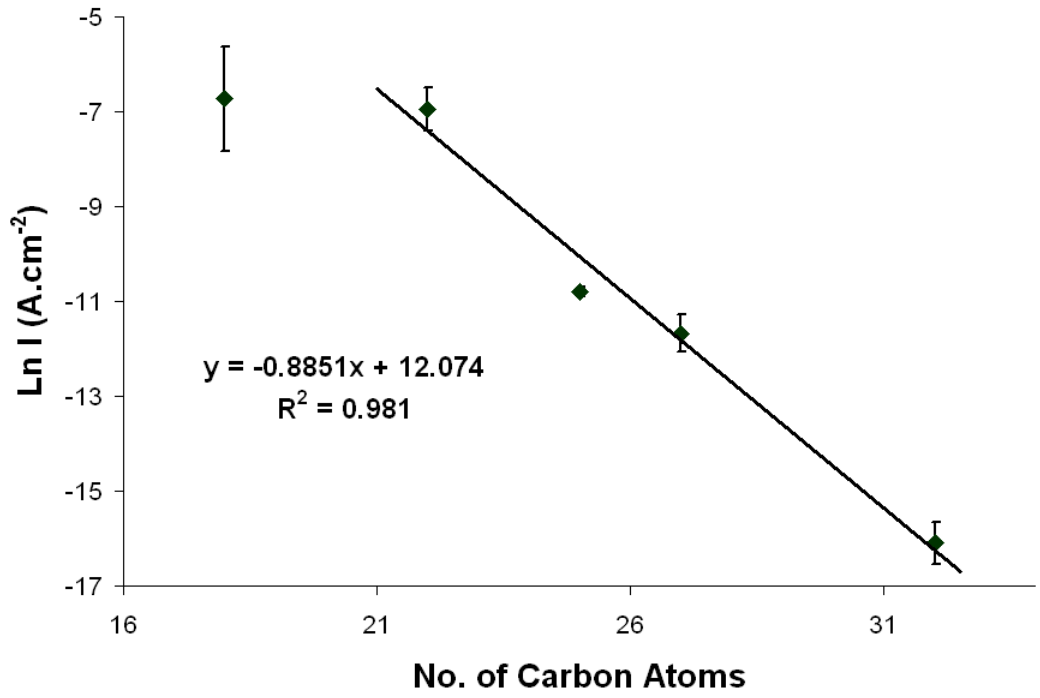

Fig. 4.14: Variation of the natural log of the tunnelling current density in Hg-Pt junctions at 400 mV bias voltage with the number of carbon atoms in the junction. The error bars represent the standard deviations of at least five independent junction measurements.

related to a higher degree of disorder in these layers or to poor stability of these thin layers to the pressure involved in junction formation. However, the good correlation co-efficients seen for the best fit lines suggests that Equation 4.1 is an appropriate model for the current variation with distance, at least at thick junction values.

The tunnelling co-efficient, β, can be found from the slope of a plot of the natural log of the tunnelling current versus distance, according to Equation 4.1. The values obtained for β of 0.73$\pm$ 0.006 $\AA^{-1}$ or 0.88$\pm$ 0.008 per CH_2 agree with the generally accepted values previously described in the literature by Slowinski[124] and Rampi[126] for similar M-I-M junctions. The barrier height at 0.4 V bias (E_{LUMO}-E_f) can be calculated as 2.53 eV, following Equation 4.3 introduced in Chapter 1;

Table 4.1: Average current densities at 400 mV bias voltage and resistances for alkanethiol Hg-Pt junctions and resistance per molecule.

Junction	I (A.cm^{-2})	R$_{junction}$ (k$\Omega.cm^2$)	R$_{molecule}$ (Ω)
C_9-C_9	1.2 x 10^{-3}	0.3	3.4 x 10^{17}
C_{11}-C_{11}	9.6 x 10^{-4}	0.4	4.2 x 10^{17}
C_9-C_{16}	2.0 x 10^{-5}	19.6	2.0 x 10^{19}
C_{11}-C_{16}	8.5 x 10^{-6}	47.1	4.8 x 10^{19}
C_{16}-C_{16}	1.0 x 10^{-7}	3921.6	3.8 x 10^{21}

$$\beta = 2\sqrt{\frac{2m^*(E_{LUMO} - E_f - eV/2)}{\hbar^2}} \tag{4.3}$$

This barrier is consistent with the Fermi levels of the electrode positioned approximately mid-way between the HOMO and LUMO of the bridging alkanethiol and compares well with the value (4 eV) found by Slowinski for a Hg-SAM-SAM-Hg junction.[135] This value reflects the relatively large energy barrier that alkanethiols present to tunnelling current and is consistent with the large HOMO-LUMO gap expected for alkanethiol molecules (up to 7-10 eV). Therefore, non-resonant tunnelling would appear to be the dominant tunnelling mechanism at these relatively low bias potentials. Indeed, for a theoretical barrier of 2.53 eV resonant tunnelling would only be expected at bias voltages greater than 5 V, according to Equation 1.9, which would correspond to electric field strengths of 1 GV.m^{-1}. This is above what previous studies have found M-I-M junctions are capable of sustaining,[141] and bulk polyethylene, for example, has a breakdown voltage of approximately 0.7 GV.m^{-1}. Therefore, resonant tunnelling is probably impossible for these alkanethiol junctions. However, the tunnelling barrier is almost certainly significantly lowered compared to the intrinsic barrier (the use of two different metals complicates this estimate, but the work functions of mercury and platinum are 4.5 and 5.6 eV respectively).

The average resistance of the layers can be calculated from the current values according to Equation 4.2. As the alkanethiol molecules can be considered as resisters in parallel, the resistance per molecule can be calculated as follows:

$$\frac{1}{R_{molecule}} + \frac{1}{R_{molecule}} + ... = \frac{1}{R_{junction}} = \frac{n}{R_{molecule}} \tag{4.4}$$

where n is the number of molecules in the junction. The area per molecule for alkanethiols has been reported as 0.2 nm^2 by Slowinski[138] so the number of alkanethiol molecules per square centimeter can be calculated as approximately 5 x 10^{14}. As bilayer junctions have been employed in this study this doubles the number of molecules present. These values are shown in Table 4.1 and are reasonably consistent with those found by Slowinski for M-I-M junctions in the literature.[135, 138] However, the use of these junctions for single molecule resistance measurements is limited by several factors, such as enhanced tunnelling at thin regions and the effect of neighboring molecules on the tunnelling current.

4.3.5 Evaluation of Hg-alkanethiol-Pt junctions

The Hg-Pt junctions described above represent a novel type of M-I-M junction. Alkanethiols have been used to characterise this system due to the large amount of research on alkanethiols sandwiched between other M-I-M junctions described in the literature. The results show for the first time that a solid polycrystal electrode can be used as a top contact of the junction. As previously seen the general results are broadly similar to other groups, but with a number of differences evident. The advantages of the system is that it is easily assembled as no special conditions are needed to prepare the platinum electrode. Platinum also does not amalgamate with mercury as quickly as is common for other electrode materials such as gold and silver. The electrochemical window is also greater for platinum in non-aqueous solvents, a feature that could prove important when systems less stable than alkanethiols are investigated.

The disadvantages of the system are mainly related to the stability of the junctions which is likely related to the roughness of the electrode as demonstrated by Rampi.[127] The results clearly show that while current-distance (i-d) curves are easily obtained and yield meaningful results which can be statistically analysed, obtaining i-V curves is more elusive. Only the most stable of junctions will yield these curves, making statistical analysis difficult. Another disadvantage of the junctions is the use of liquid mercury, which is volatile and toxic.

4.3.6 Junction formation with CD layers

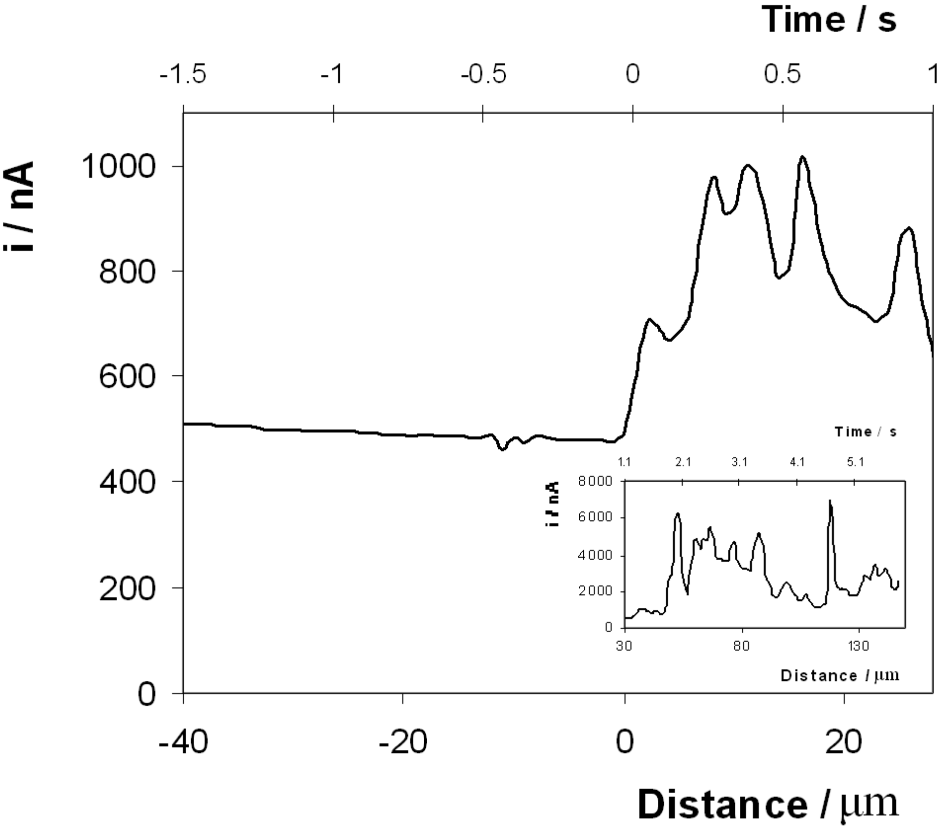

Fig. 4.15: Current-distance curve in 25:75 ethanol:water with 1 mM $C_{16}SH$ and 10 mM 1-adamantylamine with 0.15 M Na_2SO_4 as the supporting electrolyte. The potential of the Pt and Hg electrodes is 0.1 and -0.3 V versus Ag/AgCl respectively. A C_9SH backfilled CD layer was assembled on the platinum electrode before measurement.

The use of simple alkanethiols as dielectrics in Hg-Pt junctions was described in the previous section. However, junctions formed from compounds which are capable of forming non-covalent assemblies could yield potentially more interesting information, as non-covalent assemblies are highly versatile. Specifically, the role of non-covalent interactions in the conduction of electrons is likely to be crucial to further development of the field. The use of alkanethiols with terminating groups capable of forming H-bonds was briefly described by Rampi and Whitesides in Hg-Au junctions.[142] Using molecules such as CDs in tunnelling junction experiments has several advantages compared with conventional covalently linked systems. Firstly, the creation of complex systems can

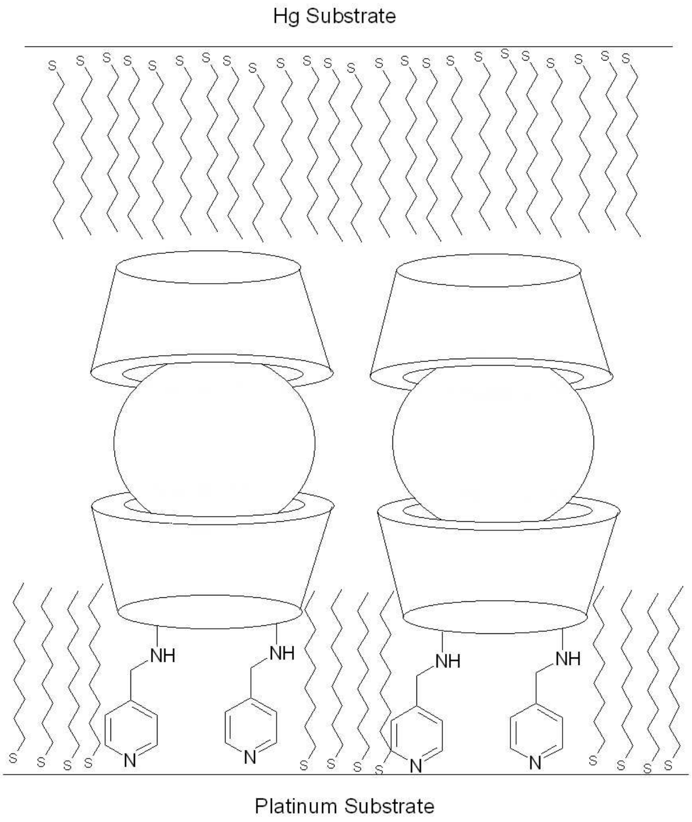

Fig. 4.16: Schematic diagram of the C_{60} junction.

be easily achieved using host-guest building blocks. Redox centers can therefore be easily included in junction experiments. Secondly, electron transfer across non-conjugated interfaces is of crucial importance in biological systems.

It has been shown in Chapter 3 that mixed alkanethiol-cyclodextrin (CD) monolayers can be formed on platinum using C_9SH and di-6^A, 6^B- deoxy-6-(4-pyridylmethyl)amino- γ-cyclodextrin, γ-CD-(py)$_2$. The CD host molecules in the layer can accommodate solution phase guests, such as 1-adamantylamine. Moreover, electrochemical blocking studies reveal that the mixed CD-C_9 layer in the presence of 1-adamantylamine effectively blocks the electrode surface from redox active solution phase species such as $[Fe(CN)_6]^{4-}$. This result suggests the mixed layer is tightly packed and that when the CD cavities are filled the defect density is low.

Figure 4.15 shows the tunnelling characteristics of a mixed C_9/CD C_{16} bi-layer junction, in which the CD cavities have been filled by the adamantane guest

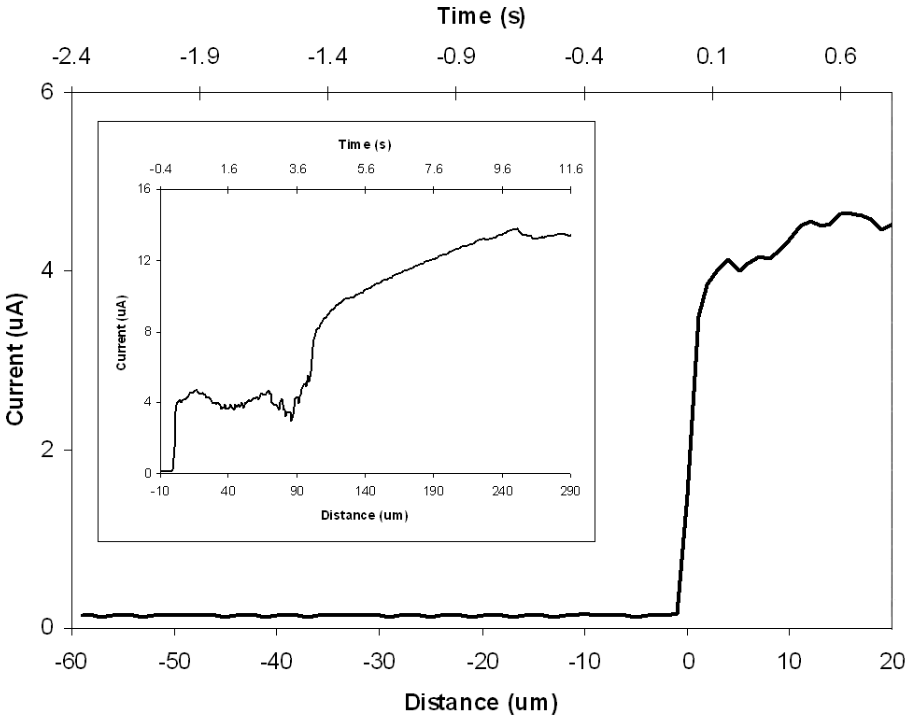

Fig. 4.17: Current-distance curve in 1:5 ethanol:water with 1 mM $C_{16}SH$ with 0.16 M Na_2SO_4 as the supporting electrolyte. The potential of the Pt and Hg electrodes is 0.1 and -0.3 V versus Ag/AgCl respectively. A C_9SH backfilled CD-C_{60} layer was assembled on the platinum electrode before measurement.

molecule. A $C_{16}SH$ layer was assembled on the mercury by addition of 1 mM of the alkanethiol to the contacting solution while the CD cavity was filled by addition of a ten fold excess of the cavity guest 1-adamantylamine over the alkanethiol, to avoid blocking the cavity. This figure shows that the current-distance behavior is broadly similar to that observed for pure alkanethiol bilayers. The current is seen to decrease slowly prior to junction formation which is attributed to isolation of the platinum electrode from the background solution. Following junction formation the current increases and current spikes, or temporary shorts, are also evident. As shown in the inset of Figure 4.15, spikes occur with greater frequency and intensity in the mixed CD layer than in pure alkanethiol SAMs. However, the current spikes appear to overlay a steady baseline as in the case of the alkanethiol junctions.

Repeated measurements put the average (n=6) current observed at this layer at 24 ± 14 μA.cm^{-2} at 400 mV bias potential (or 16.7 kΩ.cm^{-2} resistance). This shows that the conductivity of this layer is comparable to that of the C_9-C_{16} layer, suggesting that the CD layer, plus the adamantyl guest included in the cavity, is approximately as conducting as a C_9SH layer. As previously mentioned, 1-nonanethiol is expected to be a good length match to the γ-CD-(py)$_2$ molecule. Therefore, it would appear that similar tunnelling efficiency ($\beta \simeq 0.8$ $\AA^{-1}$) can be expected for the backfilled CD layers. This result is reasonable considering the relatively small degree of conjugation in the backfilled layer and the non-conjugated nature of the adamantyl guest.

Fullerene,[255] C_{60}, has been shown to form a stable inclusion complex with either one or two γ-CD molecules[229] and at γ-CD monolayers.[247,256] Therefore, the creation of a molecular junction with C_{60} included in the CD cavity is possible. The C_{60} is solubilised in methanol using CD at a ratio of 1:1. The backfilled CD layers are then exposed to this solution overnight with gentle stirring. The encapsulated CD layers are then used as one half of a junction and Figure 4.16 shows a schematic of such a junction formed in this way. However, there is a degree of uncertainty over the thickness of such a junction, as the orientation of second CD is unknown and this uncertainty limits an estimation of the tunnelling co-efficient.

To achieve the C_{60} junction the CD monolayer backfilled with C_9 alkanethiol was exposed to a solution of C_{60} capped with a single CD overnight to form a backfilled CD-C_{60} /C_{16} junction. Figure 4.17 shows the current-distance characteristics of this junction at 400 mV bias. The current can be clearly seen to increase upon junction formation to values greater than those seen for junctions incorporating adamantyl as a guest. Repeated measurements put the average (n=7) current seen as 240 ± 150 μA.cm^{-2} for the C_{60} layer. However, the thickness of the junction is difficult to estimate as the C_{60} is most likely associated with two CD units, as shown in Figure 4.16. Therefore, the tunnelling coefficient, β, cannot be easily estimated, but this junction is expected to be thicker than the adamantyl junction, as the adamantyl guest associates with only one CD unit. Therefore, the increase in conductivity would not appear to be due to a decrease in the junction thickness, but to the presence of the conjugated C_{60} molecule. The HOMO-LUMO gap in the

C_{60} (of the order of 2 eV[257,255]) is significantly less that expected for the adamantyl guest and therefore the tunnelling efficiency may be increased by the presence of these low-lying orbitals. Several studies on C_{60} films have been carried out[258,259] and Joachim and co-workers have reported the apparent single molecule resistance of a C_{60} molecule as 55 MΩ,[260] which is significantly less that the values typically seen for alkanethiols for a similar length (normally in the range of 10^3-10^5 MΩ).[11]

If the thickness of the junction is estimated at approximately 4.5 nm (considering that the C_{16}-C_9/CD layers should contribute approximately 4 nm), then a rough estimation of β is 0.44 $\mathring{A}^{-1}$, which is in close agreement with the value obtained by Rampi and Whitesides for junctions created from other conjugated molecules, such as oligophenylene thiol junctions.[126] This result demonstrates the host-guest chemistry of the CD can be successfully exploited to vary the tunnelling properties of the Pt-Hg junctions, in this instance comparing conductivity of an aromatic and non-aromatic guest.

4.3.7 Tunnelling characteristics of $[\mathrm{Co(biptpy)_2}]^{2+}$ in Hg-Pt junctions

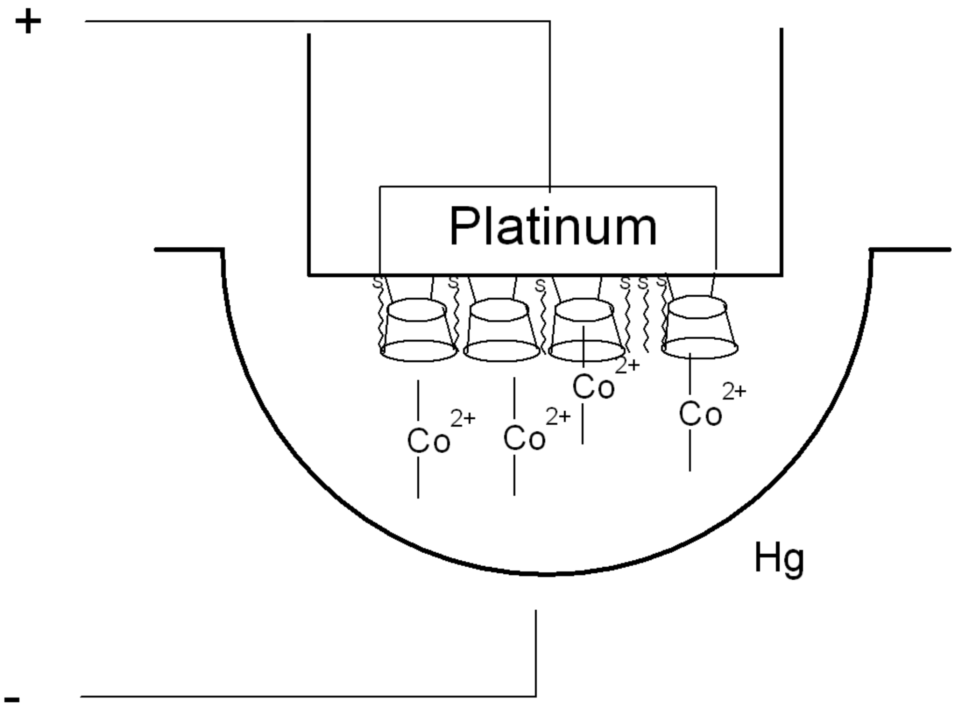

Fig. 4.18: Scheme of $[\mathrm{Co(biptpy)_2}]^{2+}$ in Hg-Pt junctions with a backfilled CD layer assembled on the platinum electrode.

The previous section has demonstrated that CD-guest interactions can be exploited to vary the magnitude of current seen at the Pt-Hg junctions. However, the HOMO-LUMO gap is still relatively large in these systems and the mechanism of electron transport is expected to be non-resonant tunnelling. In the case of macroscopic M-I-M junctions where the insulator is an alkanethiol layer (i.e., the work described in section 4.3.1) the HOMO-LUMO gap is of the order of 7 eV and the method of current transfer is one of non-resonant tunnelling at moderate potentials. Theory predicts that extremes of potential are needed to convert this mechanism to resonant tunnelling, i.e. where the HOMO/LUMO orbitals are in resonance with the occupied levels on the metal electrodes. Indeed, the potentials needed to achieve resonant tunnelling for alkanethiols could result in electric field induced desorption.

In general, where non-resonant tunnelling is the dominant current transport mechanism the magnitude of the current is independent of the individual applied potentials and responds only to the magnitude of the potential bias. In sharp contrast, junctions incorporating redox active guests have shown a marked current dependence on the magnitude of the potentials applied as the redox orbitals can be accessed.[117, 120, 122, 123] The redox active cobalt complex $[Co(biptpy)_2]^{2+}$ has been shown in Chapter 3 to associate with the backfilled layer and therefore is a suitable guest in the creation of redox active junctions. Figure 4.18 shows a schematic of the $[Co(biptpy)_2]^{2+}$ complex associated with the backfilled layer on platinum in a Pt-Hg junction where the mercury electrode is not modified. Modification of the mercury electrode was undesirable as any alkanethiol in solution could competitively displace the bound $[Co(biptpy)_2]^{2+}$ from the CD cavity. Therefore, monolayer junctions were employed for this study.

Figure 4.19 shows the current distance profiles for a junction formed in 90:10 water: acetonitrile with 0.18 M Na_2SO_4 as the supporting electrolyte (blue curve). The electrode potentials are 0.3 and -0.1 V for platinum and mercury respectively (Pt/Hg:0.3/-0.1) versus Ag/AgCl. This curve shows that the current rises substantially as the two electrodes are brought into contact. The current is seen to reach a peak value before falling to a semi steady-state value at which current spikes can be seen. The reason for this current peak is unclear but it should be noted that junction formation is a destructive process (i.e., capacitance studies before and after junction formation show that the backfilled CD layer is destroyed during this process). Madja and co-workers have previously seen current peaks in alkanethiol junctions during i-t measurements which they attributed to change in layer conformation.[125] It is possible that the peak seen in this study is a result of conformational changes resulting from destruction of the CD layer. Figure 4.19 also shows the current-distance profile for a junction formed in 70 μM $[Co(biptpy)_2]^{2+}$ in 90:10 water: acetonitrile with 0.18 M Na_2SO_4 as the supporting electrolyte (green curve). The electrode potentials in this experiment are Pt/Hg:0.1/-0.3 V versus Ag/AgCl. Both of these potentials are below the oxidation potential of $[Co(biptpy)_2]^{2+}$ (approximately 0.22 V when bound to the CD layer). As all available CD cavities are expected to be filled at a concentration of 70 μM, considering the association constant determined in Chapter 3, it would appear that the presence of the cobalt guest in the junction does not impact on the current response at these electrode potentials as the signal is broadly similar to that seen in the absence of $[Co(biptpy)_2]^{2+}$. One single, continuous rise is observed upon junction formation and is followed by a decrease in the observed current. This process can also be shown to be destructive. The absence of current spiking in this case could be evidence for a thicker junction as the $[Co(biptpy)_2]^{2+}$ molecules are included in the CD cavities.

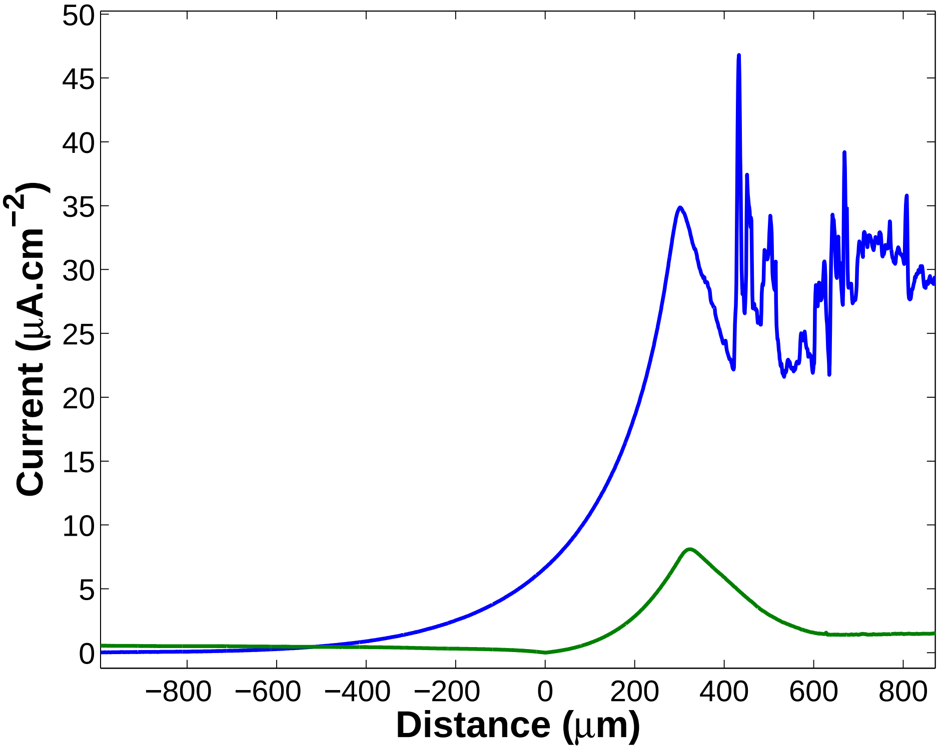

Fig. 4.19: Current-distance profiles for a junction formed in 90:10 water: acetonitrile with 0.18 M Na_2SO_4 as the supporting electrolyte (blue curve) and a junction formed in an identical solvent system with 70 μM $[Co(biptpy)_2]^{2+}$ present (green curve). The electrode potentials are: blue curve Pt/Hg: 0.3/-0.1 V and green curve Pt/Hg: 0.1/-0.3 V versus Ag/AgCl.

The junction behavior seen in Figure 4.19 is possibly attributable to tunnelling across the CD layer as the electrodes are brought into close approach. However, several differences are evident compared to the alkanethiol tunnelling junctions already described. The peak in the current profile seen in Figure 4.19 is not seen at the alkanethiol junctions. However, all the alkanethiol junctions were performed with alkanethiol molecules in solution, which may have a stabilising effect on the monolayers. The pure alkanethiol junctions were capable of several repeat measurements but the CD layer is destroyed during the course of a single junction experiment shown in Figure 4.19. The magnitude of current observed is also different compared to that seen for alkanethiol layers. The backfilled CD layer is anticipated to be approximately as thick as a conventional C_9 alkanethiol layer and previous studies have shown that the tunnelling co-efficient is also comparable to those layers. However, the magnitude of current observed is similar to that seen for alkanethiol junctions containing 25 carbons. This low signal can be attributed to several factors. The mercury-CD interface is not chemically bonded and this has been shown to be a crucial factor in tunnelling efficiency. It is also very likely that the hydroxyl groups at the entrance of the CD cavities are associated with solvent molecules. These groups are free to form H-bonds with the solvent in γ-CD, which make it the most soluble of the common CDs.[261] The cavity is also likely to contain some included water. The presence of these molecules in the junction would also reduce the tunnelling efficiency. This hypothesis is in agreement with the observation that the occurrence of current spikes is much less frequent for the CD junctions described here compared to the alkanethiol junctions.

4.3.8 Redox properties of $[Co(biptpy)_2]^{2+}$ in Hg-Pt junctions

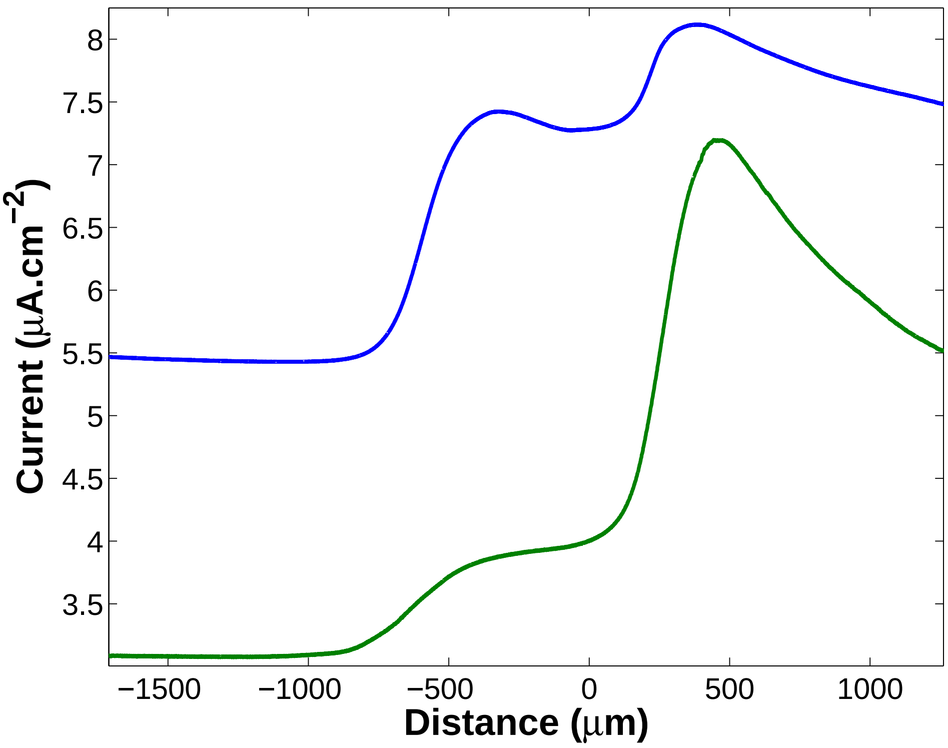

Fig. 4.20: Current-distance profiles for junctions formed in 70 μM $[Co(biptpy)_2]^{2+}$ in 90:10 water: acetonitrile with 0.18 M Na_2SO_4 as the supporting electrolyte. The electrode potentials are Pt/Hg: 0.3/-0.1 V versus Ag/AgCl. The blue curve is offset on the y-axis for clarity.

The main conclusion from Figure 4.19 is that the presence of $[Co(biptpy)_2]^{2+}$ in the Hg-CD-Pt junction does not significantly influence the current response compared to junctions formed in the absence of the complex at potentials below that of cobalt oxidation. However, when the individual electrode potentials are biased either side of the $E^{0'}$ of the complex the current response is markedly different. Figure 4.20 shows the current-distance profiles for junctions formed in 70 μM $[Co(biptpy)_2]^{2+}$ in 90:10 water: acetonitrile with 0.18 M Na_2SO_4 as the supporting electrolyte where the electrode potentials are Pt/Hg: 0.3/-0.1 V versus Ag/AgCl. The magnitude of the voltage bias is therefore identical to that in Figure 4.19. However, the current response in Figure 4.20 consistently shows two increases as opposed to the single increase seen in that figure. The second increase is a similar response to that seen for

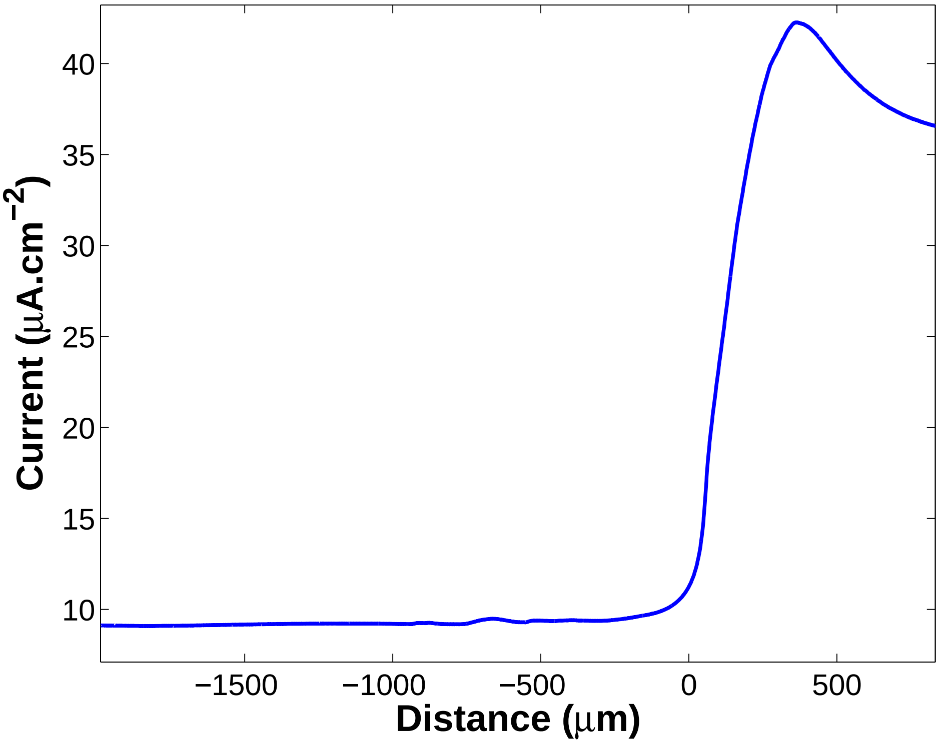

Fig. 4.21: Current-distance profile for a junction formed in 70 μM [Co(tpy)$_2$]$^{2+}$ in 90:10 water: acetonitrile with 0.18 M Na_2SO_4 as the supporting electrolyte. The electrode potentials are Pt/Hg: 0.3/-0.1 V versus Ag/AgCl.

junctions formed in the absence of [Co(biptpy)$_2$]$^{2+}$ at identical potentials or in the presence of [Co(biptpy)$_2$]$^{2+}$ where the junction potentials are too low to oxidise the cobalt. Therefore, the first increase appears to depend on the presence of [Co(biptpy)$_2$]$^{2+}$ in the junction and the application of a potential sufficient to oxidise the complex at the platinum electrode. Figure 4.20 shows two junction experiments of this type where an initial rise in current is followed by a second and final rise. Repeated measurements put the average (n=7) rise in current for the first process as 1.2 ± 0.6 μA.cm^{-2}.

Figure 4.21 shows the current-distance profile for a junction formed in 70 μM [Co(tpy)$_2$]$^{2+}$ in 90:10 water: acetonitrile with 0.18 M Na_2SO_4 as the supporting electrolyte. The electrode potentials are Pt/Hg: 0.3/-0.1 V versus Ag/AgCl. [Co(tpy)$_2$]$^{2+}$ is structurally similar to [Co(biptpy)$_2$]$^{2+}$ (Figure 4.22) but lacks the biphenyl ligands which are needed for CD binding. [Co(tpy)$_2$]$^{2+}$ has been shown in Chapter 3 to be inactive at the backfilled layer for this reason. The

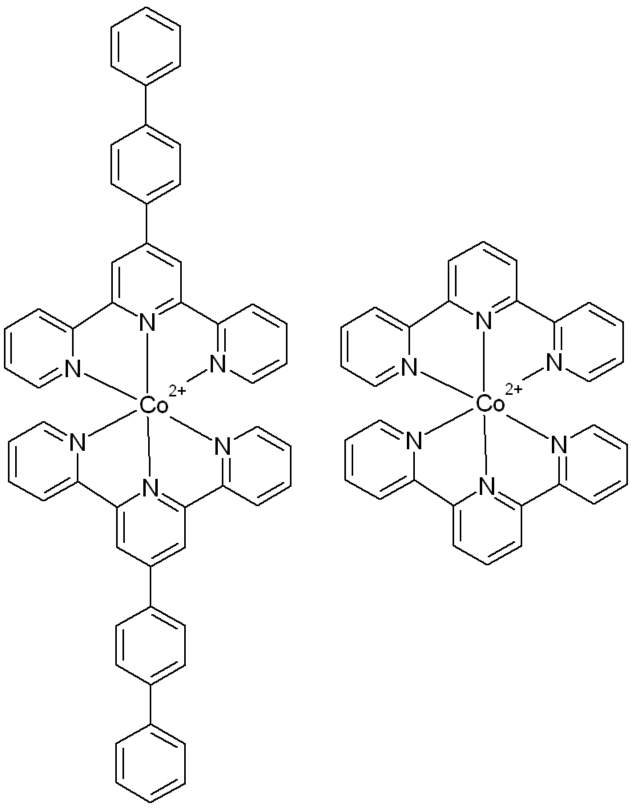

Fig. 4.22: Structures of $[Co(biptpy)_2]^{2+}$ (left) and $[Co(tpy)_2]^{2+}$ (right).)

potentials applied to the junction in Figure 4.21 are suitable for oxidation of $[Co(tpy)_2]^{2+}$ at the platinum and reduction at the mercury electrodes respectively. However, the current-distance profile is again broadly similar to those observed in the absence of a cavity guest or where the potentials applied are insufficient to oxidise the guest. As the potentials applied are sufficient to oxidise $[Co(tpy)_2]^{2+}$ this confirms it is blocked from the electrode surface as it is unable to bind to the CD layer. This experiment shows that host-guest interactions are crucial to the behavior of the junctions.

The initial increase in current appears to be a result of trapping $[Co(biptpy)_2]^{2+}$ in the junction at potentials where it can be oxidised at the platinum electrode. A redox cycling mechanism could be established between the two electrodes as the complex can be reduced at the mercury electrode. Therefore, the initial rise in current may be attributable to redox cycling, i.e. when a thin layer is trapped between the two electrodes, while the second rise could be attributed to tunnelling across the junction. Rampi and Whitesides have attributed a potential dependent rise in current in a macroscopic tunnelling junction to redox cycling of trapped $[Ru(NH_3)_6]^{2/3+}$.[144] This junction was composed of a $C_{10}COOH$ layer formed on two mercury drops with $[Ru(NH_3)_6]^{2/3+}$ in solution. When the junction closed the $[Ru(NH_3)_6]^{2/3+}$ was trapped electrostatically at the monolayer solution interface. The mechanism of current transport was proposed to be redox cycling, in which the current is expected to depend inversely on the distance between the electrodes, d:

$$i = \frac{nFADC}{d} \tag{4.5}$$

where n is the number of electrons transferred, F is Faraday's constant and D and C are the diffusion co-efficient and the bulk concentration of the redox active molecule respectively.

Using the average value for the initial current increase, i, as 1.2 μA.cm^{-2} and taking a diffusion co-efficient of 4 x 10^{-7} cm^2.s^{-1} (determined from CV of the probe $[Co(tpy)_2]^{2+}$, which is comparable in size and charge to $[Co(biptpy)_2]^{2+}$) the distance between the electrodes at the maximum of the first current peak can be calculated approximately 20 μm. This value is somewhat surprising as the platinum electrode moves at a rate of 25 μm.s^{-1} and so should close a gap of this magnitude in under a second. On the contrary, Figure 4.20 shows that the first rise in current persists for up to 40 seconds, despite the fast rate of displacement of the platinum electrode. On this basis, Rampi calculated a inter-electrode distance as 534 nm,[144] for the system described above, which is also an unrealistic value. One explanation for this discrepancy is the unknown nature of both the concentration and the diffusion co-efficient of the redox active molecule in the junction. It is possible that these may deviate significantly from the bulk solution values used in the calculation. It is also possible that the current observed is not due to a redox cycling mechanism.

In an attempt to probe a possible redox cycling mechanism in more detail the junction experiments involving $[Co(biptpy)_2]^{2+}$ seen in Figures 4.19 and 4.20 were repeated with 70 and 700 nM $[Co(biptpy)_2]^{2+}$ in solution. The free energy of adsorption (ΔG_{ads}) of $[Co(biptpy)_2]^{2+}$ with the backfilled layer was previously found to be -29 kJ.mol^{-1}, therefore, concentrations of 70 and 700 nM

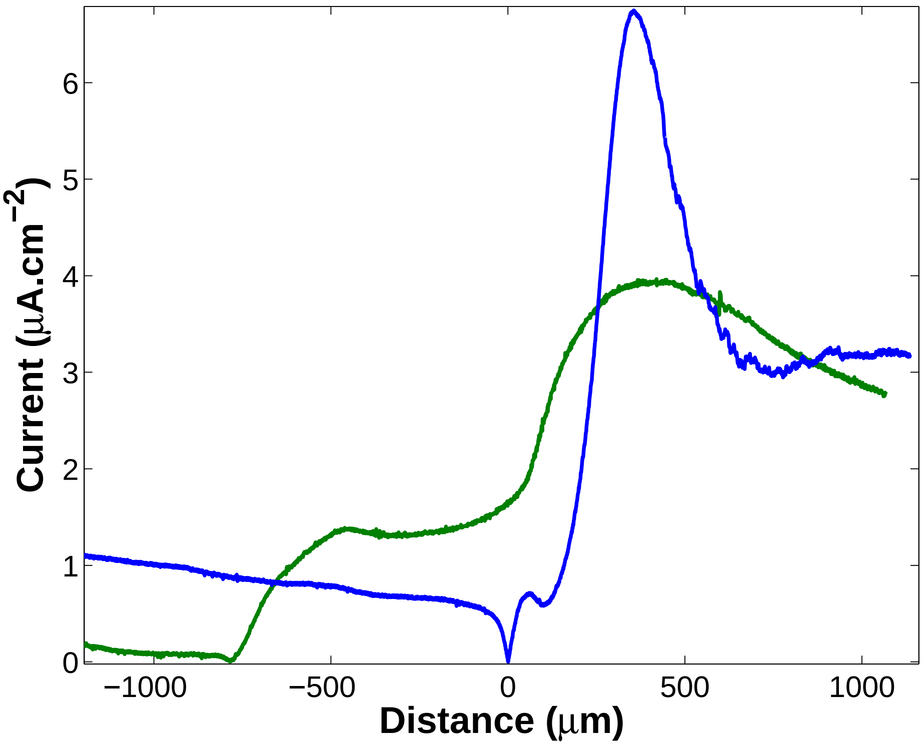

Fig. 4.23: Current-distance profiles for junctions formed in 70 *n*M $[Co(biptpy)_2]^{2+}$ in 90:10 water: acetonitrile with 0.18 M Na_2SO_4 as the supporting electrolyte. The electrode potentials are: blue curve Pt/Hg: 0.1/-0.3 V, green curve Pt/Hg: 0.3:-0.1 V versus Ag/AgCl.

$[Co(biptpy)_2]^{2+}$ represent a cavity occupancy of 1/100 and 1/10 respectively. If redox cycling is the dominant current transport mechanism the current observed should also decrease compared to the junctions formed with 70 μM $[Co(biptpy)_2]^{2+}$ present. The junctions formed at 70 nM showed only one current peak and were broadly similar to the junctions formed in the absence of $[Co(biptpy)_2]^{2+}$. Therefore, a cavity occupancy of 1/100 is clearly not enough to observe the first potential dependent peak. However, the junctions formed at 700 nM showed almost identical behavior to those seen at the higher concentration of $[Co(biptpy)_2]^{2+}$, as Figure 4.23 demonstrates. The blue curve in this figure represents a junction formed in 700 nM $[Co(biptpy)_2]^{2+}$ with electrode potentials of Pt/Hg: 0.1/-0.3 V while the green curve represents electrode potentials of Pt/Hg: 0.3/-0.1 V versus Ag/AgCl. The current responses are essentially identical to those observed at the same potentials for junctions formed in 70 μM $[Co(biptpy)_2]^{2+}$. Multiple measurements (n=5) reveal the magnitude of the initial rise in the current to be 1.5 ± 0.1 μA.cm^{-2} which is within the standard deviation of the measurement carried out at 70 μM [Co(biptpy)$_2$]$^{2+}$. Figure 4.23 also shows the characteristic dip in current upon junction formation for both curves. This dip in current was attributed to the closing of the junction for the alkanethiol junctions, indicating the insulation of the platinum electrode from the solution as it penetrated the mercury pool. Significantly, this dip can be seen before the initial rise in current for the green curve (Pt/Hg: 0.3/-0.1 V) which suggests that the electrodes are extremely close at this point (the scale on the figure may not accurately reflect the electrode separation). This observation contrasts with the value of 20 μm calculated for the distance between the electrodes using Equation 4.5. The similarity in the magnitude of current observed, using the two different concentrations, also contradicts the redox cycling mechanism, which would predict a decrease in observed current for junctions formed in more dilute solutions.

In summary, the use of [Co(biptpy)$_2$]$^{2+}$ in the junctions can be shown to give a potential dependent current response, which is not seen for molecules having similar redox potentials but lacking the CD docking ligands, such as [Co(tpy)$_2$]$^{2+}$. This indicates that host-guest interactions can be used to incorporate redox active metal complexes into the junctions. This is clearly evidenced by the incorporation of [Co(biptpy)$_2$]$^{2+}$ as a guest and the demonstration of a potential dependent current at potentials sufficient to access the redox orbitals. The average charge associated with this initial peak is 33 ± 18 μC.cm^{-2} (n = 5), which is approximately 23 times that needed to oxidize one monolayer of [Co(biptpy)$_2$]$^{2+}$ bound at the CD modified interface. This suggests that the [Co(biptpy)$_2$]$^{2+}$ molecules mediate more than one electron in this timescale.

Unfortunately, the inexact nature of the mercury-monolayer interface means that an estimation of the current transport mechanism is difficult. It is clear that the classical redox cycling mechanism fails to describe this system adequately. There may be differences in the bulk and junction concentrations or diffusion co-efficients as noted previously or a different mechanism may dominate the signal. The insulation of the platinum working electrode was only observed at low concentrations of [Co(biptpy)$_2$]$^{2+}$ which suggests some limited feedback current is obscuring this feature at higher concentrations. Therefore, it is possible that the observed current rise is due to another current mechanism, such as electron hopping.

4.3.9 Effect of electrode displacement

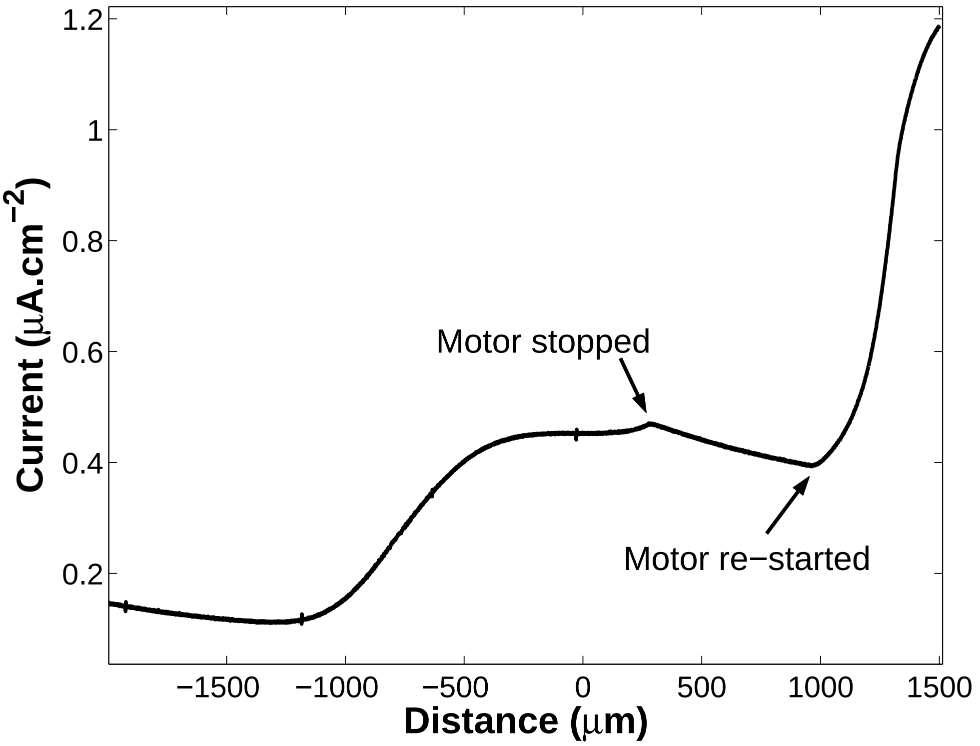

Fig. 4.24: Current-distance profiles for junctions formed in 70 μM $[\mathrm{Co(biptpy)_2}]^{2+}$ in 90:10 water: acetonitrile with 0.18 M Na_2SO_4 as the supporting electrolyte. The electrode potentials are: Pt/Hg: 0.3/-0.1 V versus Ag/AgCl. The platinum electrode's displacement was stopped as indicated.

The incorporation of $[\mathrm{Co(biptpy)_2}]^{2+}$ in the tunnelling junctions has been described in the previous section and a potential dependent current increase was observed along with a universal current increase which was evident in both the presence and absence of the redox active cavity guest. However, significant questions remain over the effect of the platinum electrodes displacement on the current response observed. Therefore, a series of experiments have been carried out where the platinum electrode has been stopped and the current monitored. Thus, current-distance curves are obtained, as seen in Figures 4.24 and 4.25, where the electrode is stationary for part of the measurements as indicated on the figures.

Figure 4.24 shows the effect of stopping the electrode displacement on the second, potential independent peak in a solution containing 70 μM $[\mathrm{Co(biptpy)_2}]^{2+}$.

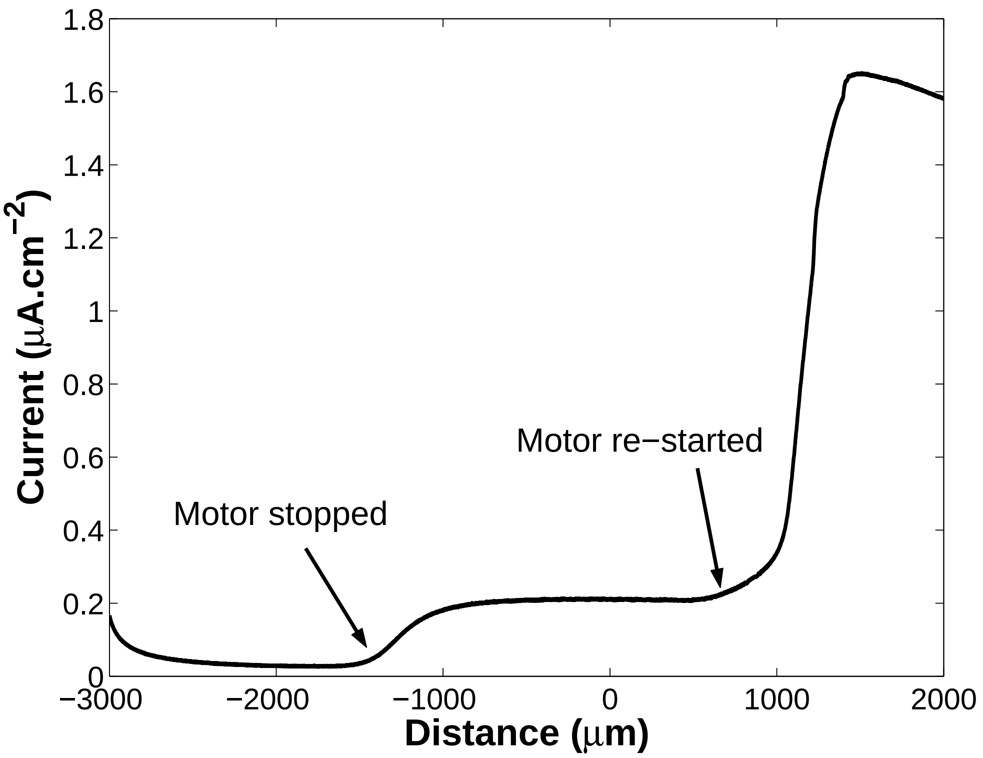

Fig. 4.25: Current-distance profiles for junctions formed in 70 μM $[Co(biptpy)_2]^{2+}$ in 90:10 water: acetonitrile with 0.18 M Na_2SO_4 as the supporting electrolyte. The electrode potentials are: Pt/Hg: 0.3/-0.1 V versus Ag/AgCl. The platinum electrode's displacement was stopped as indicated.

The curve shows the typical initial rise at approximately -1000 μm due to the cobalt complex (the distance indicated on the x-axis is not representative of the displacement in this case, as the motor is stopped as indicated). The motor is stopped at the onset of the second peak, as indicated in the figure, and the current is seen to decrease. This behavior is characteristic for the second current rise, i.e. once the electrode is stationary the current does not increase but falls in most cases. This suggests that this current peak is a direct result of the displacement of the platinum electrode. As described, this process is destructive to the monolayer and the current rise could be described as exponential in nature (and therefore perhaps described by Equation 4.1). Figure 4.24 also shows that upon re-starting the motor the current again increased and formed the familiar peak. Capacitance measurements revealed that after this experiment the CD-monolayer was destroyed, again suggesting that the process is of a mechanical nature.

Figure 4.25 shows the effect of stopping the platinum electrode on the initial, potential dependent, rise in current for a junction formed in an identical solvent system to that seen in Figure 4.24. In this experiment the electrode is stopped just as the current begins to rise from baseline values, as indicated in the figure. However, in contrast to the second peak, the current continues to increase and reaches a steady state value. This state appears to be stable over the timescale investigated here and the current only changes when the motor is restarted. At that point the current again rises and the familiar second peak is observed.

This experiment shows that the first rise is not dominated by the movement of the platinum electrode but that it is controlled by another process (the close approach of the mercury and platinum electrodes is obviously necessary). The first current peak therefore does not appear to be a mechanical process, as was found for the second peak. This observation is consistent with a redox activated signal, i.e., a mechanical process should not display a potential dependence, as in the case of the second peak. It should be noted that capacitance measurements were also carried out where the platinum electrode was withdrawn from the junction before the onset of the second peak, but after the occurrence of the first peak. The capacitance values in this case were similar to those seen before junction formation, indicating that the layer is not greatly altered by this first process. This is in sharp contrast to the second current peak, which appears to destroy the CD layer. Again, this observation suggests that the first peak is not a mechanical process, as previously noted.

In summary, the effect of electrode displacement is minimal on the first current increase, which as previously seen is predominately a function of the potential applied to the electrodes and the nature of the molecule in solution (i.e. CD active or inactive). However, the second peak, which is observed for all the CD-monolayer junctions in the presence and absence of $[\mathrm{Co(biptpy)_2}]^{2+}$ appears to be related to the electrode displacement and this suggests a mechanical process.

4.4 Conclusion

Tunnelling junctions provide powerful insights into electron transfer across either individual molecules or molecular assemblies.[147, 114, 139, 117] A number of elegant tunnelling junctions comprising assembled monolayers of either aromatic or aliphatic species have been described previously.[126, 124, 149] However, in order to probe central issues such as the impact of tuning redox states into resonance, distance dependence, or indeed the extent of delocalization, these approaches require significant synthetic effort. In contrast, exploiting host-guest chemistry in which electro-active metallo-guests self-assemble with immobilised cyclodextrins opens new possibilities. This strategy has a number of advantages over existing approaches. First, it avoids the complex synthesis usually required to covalently link several units together to form a molecular wire. Second, the impact of changing the electronic properties can be easily explored by changing the guest. Third, redox centers with and without “tails” capable of binding to immobilized CDs can be used to probe the impact of host-guest association on the tunnelling properties. Finally, as non-covalent interactions, such as H-bonding, stacking, van der Waals forces and hydrophobic-hydrophobic interactions are pervasive in biology, tunnelling junctions involving self-assembled wires based on these bonding motifs may be more relevant model systems for interrogating tunnelling in biosystems.

This chapter described a novel macroscopic Pt-Hg junction that has been characterized using alkanethiol bi-layers for the purpose of incorporating CD host-guest chemistry into molecular junction experiments. Non-resonant tunnelling is suggested as the most likely tunnelling mechanism and a tunnelling coefficient, β, of 0.88 per CH_2 has been observed. Host-guest interactions have been incorporated into the junctions by using the CD monolayers described in Chapter 3 as one half of a bi- and mono-layer junction. The bi-layer junctions revealed that the conductance of the mixed CD/C_9 layer is approximately the same as for pure alkanethiol layers when non-conjugated guests, such as adamantane, are included in the CD cavity. However, when C_{60} is included in the cavity the current is an order of magnitude greater. Uncertainty over the thickness of the junction means that β values cannot be obtained, but the electron transfer is clearly influenced by the nature of the CD guest. The redox active CD guest $[Co(biptpy)_2]^{2+}$ has been investigated in the mixed CD/C_9 monolayer junction. The current-distance curves show a potential dependent current, which is absent in the presence of $[Co(tpy)_2]^{2+}$, which lacks the biphenyl CD docking ligand. This potential dependent current is independent of electrode displacement, confirming that this behavior is mediated by host-guest assembly of the redox center into the layer.

In conclusion, host-guest interactions have been incorporated into molecular junction experiments. The nature of the guest appears to greatly influence the magnitude of current observed; junctions with conjugated guests show higher tunnelling currents compared to junctions with non-conjugated guests. This shows that the use of host-guest interactions can be exploited to vary the junction properties. The host-guest system can also be used to easily incorporate redox molecules in junctions and further work on molecular junctions is certain to concentrate on redox active dielectrics as they have important implications for the fabrication of molecular electronic devices.

Chapter 5

Fibrinogen adsorption and desorption from gold surfaces

5.1 Introduction

Immobilisation of biomolecules has received significant attention for many years and protein adsorption at the solid-liquid interface has been extensively studied.[13, 14, 162, 163] The plasma proteins are among the most popular due to the importance of protein binding to medical implants.[161] Fibrinogen is a large ($\approx$ 340 kDa) plasma protein that is involved in clotting.[154] It is converted to fibrin by thrombin and it is comprised of three non-identical disulfide linked chains, which are denoted α, β and γ respectively. The primary structures of these chains have been determined and can be consulted in the literature.[152]

Fibrinogen has been adsorbed at several interfaces, such as gold,[164] titanium,[175] and silica.[172] The kinetics of adsorption have been studied by several groups,[159] [, 171, 172, 170] but a clear consensus has not been reached as regards the mechanism of adsorption. The first-order Langmuir kinetic model is the most popular kinetic model in these studies,[13, 168, 170] but several authors claim that protein binding is more complex than this model describes.[13, 158] Fibrinogen layers have been extensively investigated using atomic force microscopy (AFM).[174, 175, 176, 177, 178, 160] The main conclusions from this work is that the substrate dramatically affects the adsorbed layer structure. Hydrophobic substrates, such as graphite, appear to spread the protein at the interface, resulting in a tightly bound layer.[174] However, adsorption at hydrophillic surfaces, such as mica, appears weaker, with AFM images showing less spreading and coverage of fibrinogen at these substrates.[177,178] The hydrophobicity of the substrate was also shown to effect the adsorption of protein layers in other studies.[185,179,] The effect of adsorption on titanium dioxide nanoparticles on the fibrinogen structure was investigated using Raman spectroscopy.[262] The amide I band was seen to shift to longer wavelengths for the adsorbed protein, indicating a decrease in the α-helix content of the protein, which is indicative of protein spreading.

Many studies have shown that the electrode potential has an effect on the adsorption of proteins at surfaces, which is presumably due to the charged nature of most proteins.[165,166,164] However, a key issue that remains relatively unexplored is the effect of electrode potential on the adsorbed layer. Some studies have suggested that the adsorption of negatively charged proteins can be influenced by application of a negative or positive potential, presumably due to electrostatic repulsions or attractions.[157] Desorption of proteins is normally an activated process, i.e. a change in temperature, ionic strength or pH is required to drive the process, but the possibility of electrochemically desorbing protein layers is relatively unexplored. The desorption kinetics of proteins have been explored in only a few studies,[179,180,181] where the proteins desorb off hydrophillic surfaces. Fibrinogen has been shown to be strongly adsorbed and spread at gold surfaces,[171] therefore electrochemical desorption could allow desorption from this surface. Other key issues are the kinetics of any electrochemical desorption and the effect of the adsorption-desorption process on the protein structure. The release of a protein from a surface could have applications such as model systems for agonist release from surfaces by electrochemical means or decontamination of surgical implements. The latter is important as fibrinogen is the one of the three principal blood proteins, after albumin and immunoglobulin.

This chapter describes the study of fibrinogen at gold-coated silicon wafers from aqueous solutions. The adsorption dynamics have been probed using

AC voltammetry to measure the capacitance change upon adsorption. The adsorbed layer has been characterised using a variety of techniques such as AFM, SEM and fluorescence microscopy. The rate of fibrinogen desorption upon application of a negative potential is investigated by measuring the capacitance change and by fluorescence spectroscopy. The effect of this process on the activity of the protein is also probed.

5.2 Experimental

5.2.1 Apparatus

Cyclic and AC voltammetry was performed in a conventional three electrode setup with a platinum mesh as the counter electrode and an Ag/AgCl saturated in KCl reference electrode using a CHI 660 electrochemical workstation. All solutions were deoxygenated with Argon prior to use and a blanket of Argon was maintained over the solutions during experimentation. The working electrode was Au coated (400nm) silicon wafers, which are close to atomic flatness. AC voltammetry experiments were carried out using an excitation signal of 5 mV and at a frequency of 512 Hz.

The kinetic and potential dependence of the Oregon Green fibrinogen was investigated by monitoring the intensity of the fluorescence using a Horiba Jobin Yvon HR800UV spectrometer using an Argon ion laser (488 nm calibrated using the silicon phonon and Rayleigh line) as the excitation wavelength focused through a 10x objective lens on the electrode surface. Typical acquisitions were 1 second in length and performed once to acquire a spectrum.

Raman spectroscopy was performed using a Horiba Jobin Yvon HR800UV, calibrated as described above. The excitation wavelength was focused through a 10x objective lens on the electrode surface. Typical acquisitions were several minutes in length and performed three times to acquire a spectrum.

Electronic absorption spectra were measured on a Shimadzu 3500 UVVis/NIR spectrophotometer. Emission spectra were recorded on a Cary Eclipse Fluorescence spectrophotometer. Scanning electron microscopy was carried out using a Hitachi S-3000N scanning electron microscope. Fluorescence microscopy images were recorded with a confocal fluorescence microscope (LSM 50, Zeiss) using a 64x oil immersion objective (NA = 1.4). An argon ion laser provided 488 nm as the excitation wavelength. The scanned images contain 512x512 pixels. A 505 nm long pass filter was used to remove the excitation wavelength. Atomic force images were obtained using a Nanoscope III (Digital Instruments) and silicon tapping mode tips (Veeco Probes HMX-10).

The structural integrity of the desorbed fibrinogen was investigated by SDS PAGE gel (10%) electrophoresis, by comparing the fibrinogen mobility before and after adsorption.

5.2.2 Materials

Fibrinogen (65%) was obtained from Sigma Aldrich Chemical Company. Fibrinogen solutions in the concentration range 10-600 μM were prepared in phosphate buffered solution (PBS) and 0.1 M $HNaCO_3$. PBS consisted of 0.01 M phosphate buffer, 0.0027 M potassium chloride and 0.137 M sodium chloride, pH 7.4, at 25^0C. Oregon Green Fibrinogen (90%) was obtained from Invitrogen.

Oregon Green labelled fibrinogen solutions were prepared in 0.1 M $HNaCO_3$ (pH = 7.4). These salts also acted as the electrolyte in the electrochemical experiments.

Fibrinogen layers were formed on gold by immersion of the electrode in fibrinogen solutions ($\geq$ 60 μM) overnight. The working electrode was rinsed copiously with Milli-Q water before use.

SDS-PAGE analysis was kindly performed by Ciaran De Chaumont at the Royal Collage of Surgeons in Ireland (RCSI).

5.2.3 Spectroscopic characterisation of fibrinogen

Figure 5.1 shows the UV-vis and fluorescence spectra of Oregon Green fibrinogen. Oregon Green is a fluorescein derivative and it can be shown that there are approximately 100 dye molecules per protein molecule. The maximum absorbance, seen at 496 nm, is attributed to the organic dye (ε = 85000 $M^{-1}.cm^{-1}$). The band at 275 nm can be attributed to the aromatic amino acid groups in the protein. From the ratio of these values the number of dye molecules per protein can be found, assuming that all dye present is conjugated to the protein. The absorbance at 328 nm is attributed to Oregon green

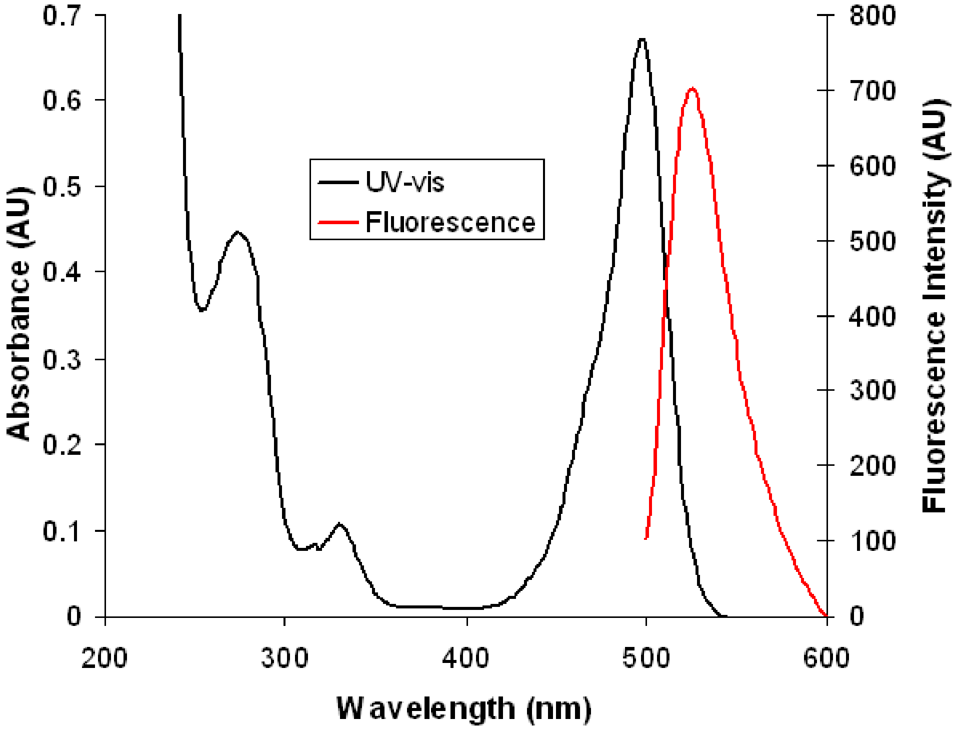

Fig. 5.1: UV-vis spectrum of 29 μg/mL Oregon Green Fibrinogen in 0.1 M $HNaCO_3$ and fluorescence spectrum of 1 μg/mL Oregon Green Fibrinogen in 0.1 M $HNaCO_3$. The fluorescence spectrum was obtained using an excitation wavelength of 496 nm.

as fluorescein shows a similar band.[219] Figure 5.1 also shows the fluorescence spectrum for a 1 μg.mL solution of Oregon Green Fibrinogen at the excitation wavelength of 496 nm. The maximum emission is seen at 526 nm.

Figure 5.2 shows the Raman spectrum of solid fibrinogen at an excitation wavelength of 488 nm. The principle bands and assignments can be seen in Table 5.1. The bands which show the greatest intensity are the CH stretching modes at 2927 cm^{-1} and the ring breathing modes at 995 cm^{-1}. This is in agreement with previous Raman studies of solid fibrinogen.[262]

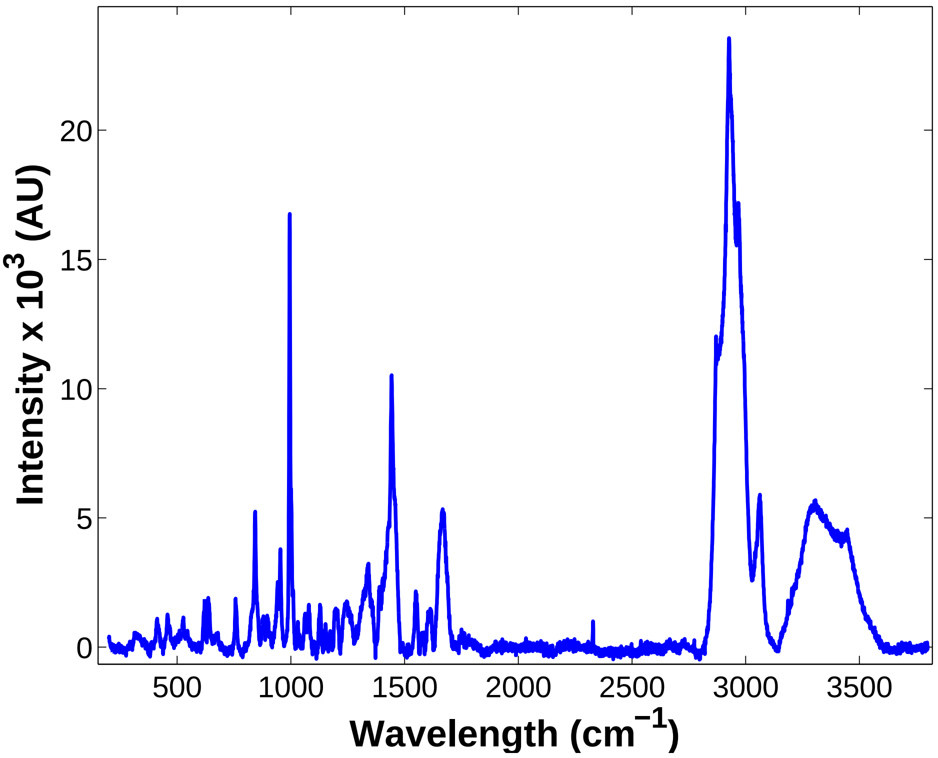

Fig. 5.2: Raman spectrum of solid fibrinogen using a 488 nm excitation laser line.

Table 5.1: Spectral data and assignments for the dominant modes of solid fibrinogen.

Wavenumber (cm^{-1})	Assignment
3300	NH stretching
3060	Aromatic CH stretching
2927	Aliphatic CH stretching
1670	Amide I
1610	Aromatic C=C stretching
1550	Aromatic ring vibration
1443	CH_2 deformation
1250	Amide III
995	phenylalanine ring breathing
843	symmetric CNC stretch

5.3 Results and Discussion

5.3.1 Adsorption dynamics of fibrinogen

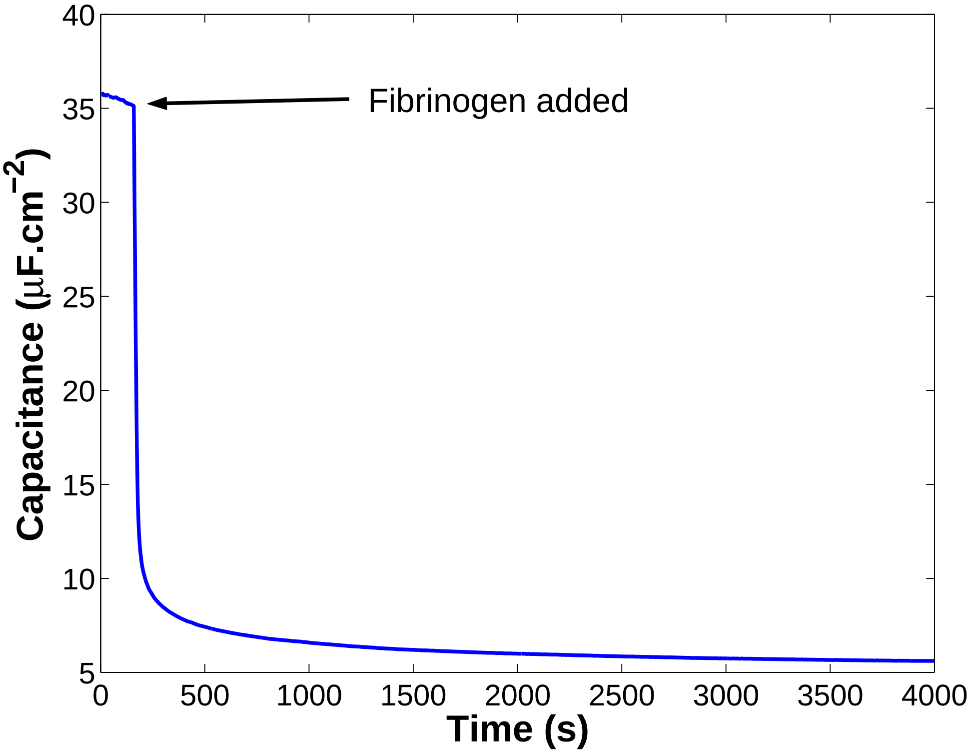

Fig. 5.3: Capacitance-time curve for gold electrode at OCP versus Ag/AgCl immersed in PBS to which fibrinogen was added, at the indicated time, to yield a final cell concentration of 264 μg/mL.

As seen in Chapter 1, the double-layer capacitance is a convenient and sensitive tool for the study of adsorbed organic molecules. The adsorption of fibrinogen on gold was studied by monitoring the capacitance change upon addition of fibrinogen to an electrochemical cell. Figure 5.3 shows the capacitance at the open circuit potential (OCP) of a gold electrode over time in PBS before and after the addition of fibrinogen to the cell (final concentration 264 μg/mL). The time at which the addition of the fibrinogen took place is indicated on the figure. The capacitance before the addition of the protein is approximately 35 μF.cm^{-2} which is typical of a clean electrode in an aqueous solution. The addition of the fibrinogen leads to an immediate drop in the capacitance, which can be attributed to the adsorption of the protein to the gold surface. This

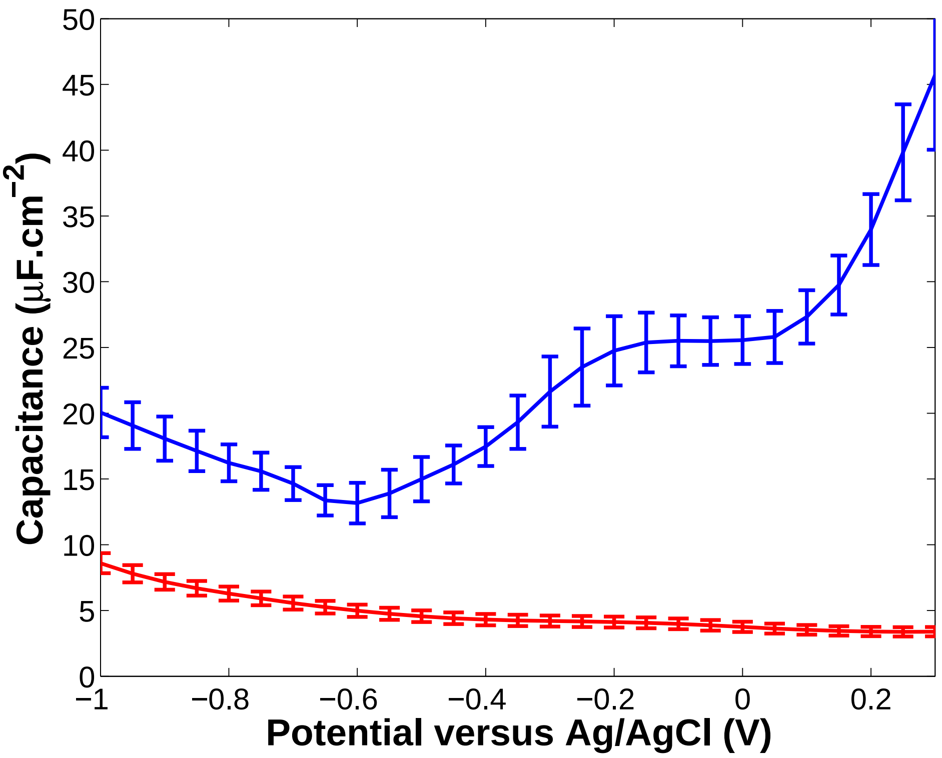

Fig. 5.4: Capacitance-potential profile for bare (blue) and fibrinogen coated (red) gold electrodes in blank PBS. The curves were obtained by stepping the potential from the OCP (~0.3 V) in the negative direction.

figure confirms that fibrinogen spontaneously adsorbs onto gold electrodes. Mass transfer of the protein to the gold surface was minimised by performing the experiment with a high concentration of fibrinogen in solution. The time needed to supply enough protein to reach the surface coverage, as determined later in this chapter, is approximately 3 seconds. This would indicate that mass transfer effects do not dominate the curve, but that the binding kinetics is the limiting step.

The capacitance of the electrodes, before and after exposure to a fibrinogen solution, as a function of potential was monitored and Figure 5.4 shows the capacitance-potential profiles for both bare and fibrinogen modified electrodes. The modification was performed overnight to reach saturation coverage of the protein. The bare electrode shows typical values for aqueous solutions and has a marked potential dependence. In contrast, the fibrinogen coated electrodes display a much lower capacitance, which is consistent with the adsorption of

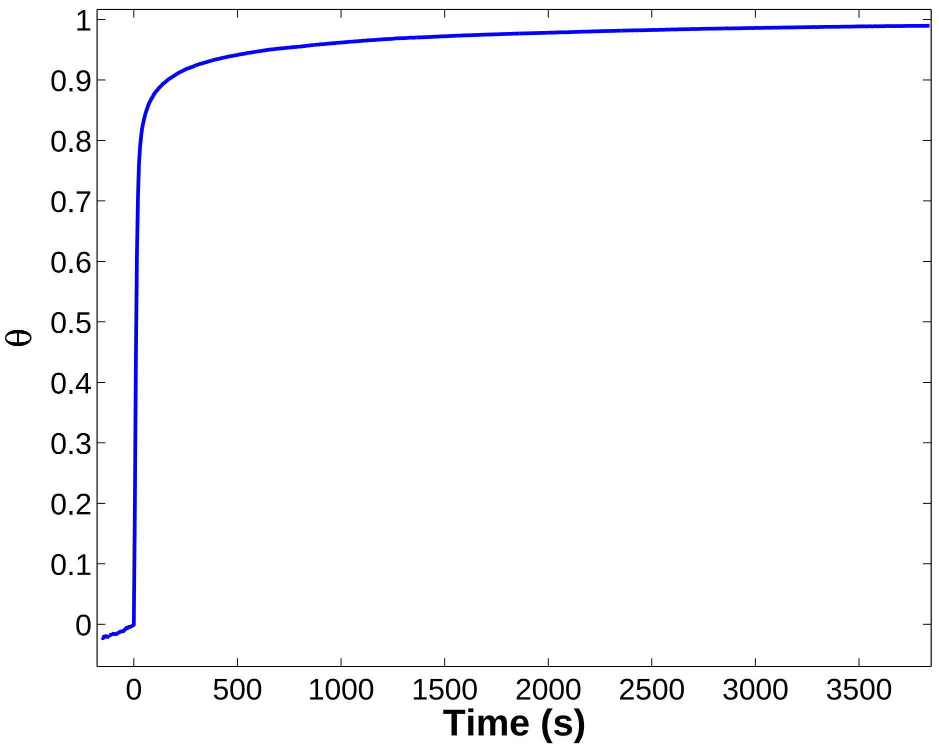

Fig. 5.5: Fractional surface coverage, θ, at a gold electrode versus time for 264 μg/mL fibrinogen in PBS.

a layer with a lower dielectric constant than bulk water. The coated electrode capacitance is also much less potential dependent, which indicates the presence of a blocking layer. The capacitance of the coated layer can be seen to rise as the electrode potential becomes more negative, which could indicate that the negatively charged fibrinogen is being lost from the surface. Determination of the average layer thickness is difficult, but the data in Figure 5.9 suggest that 5 nm is a reasonable approximation. This would yield a dielectric constant of approximately 20 for the adsorbed protein, following the Helmholtz model.

The fractional surface coverage, θ, can be found from the capacitance values using Equation 5.1:[240]

$$\theta = \frac{C_0 - C_t}{C_0 - C_f} \tag{5.1}$$

where C_0 is the bare electrode capacitance, C_t is the capacitance at time t and

C_f is the final electrode capacitance. This equation can be used to create curves plotting θ against time as shown in Figure 5.5. In this figure the capacitance data seen in Figure 5.3 has been converted to fractional surface coverage values using Equation 5.1. The capacitance was monitored at longer times than that shown in Figure 5.5 until repeatable values were obtained to find C_f, the capacitance of the fully formed layer.

The adsorption dynamics of the fibrinogen can be investigated by fitting the θ-t curves with common simple adsorption models. If the adsorption is controlled purely by diffusion, the plots should follow Equation 5.2;

$$\theta(t) = k_d\sqrt{t} \tag{5.2}$$

where k_d is ;

$$k_d = \frac{2CD^{1/2}}{B\pi^{1/2}} \tag{5.3}$$

where D is the diffusion co-efficient, B is the number of particles per unit area at saturation coverage and C is the concentration of the bulk solution.

The first order Langmuir kinetic model is expressed as;

$$\theta(t) = 1 - exp(-k_L t) \tag{5.4}$$

where k_L is the Langmuir first order adsorption rate constant. A modification of Equation 5.4 is the Langmuir diffusional model;

$$\theta(t) = 1 - exp(-k_m\sqrt{t}) \tag{5.5}$$

where k_m is equal to $2D^{1/2}C/B\pi^{1/2}$. Finally a second order Langmuir model, with a Langmuir second order constant k_{so}, can also be used;

$$\theta(t) = 1 - (k_{so}t)^{-1} \tag{5.6}$$

It has been suggested in the literature that protein adsorption dynamics are too complex to be accurately modelled by the relatively simple models outlined above. Despite the possibly complex nature of the dynamics, Langmuir first order kinetics (Equation 5.4) have been used repeatedly to describe protein adsorption.[13, 168, 170]

Table 5.2: Average kinetic rate constant, k_{ave}, and correlation co-efficient, R^2, for simple adsorption models.

Model	k_{ave}	R^2
Langmuir 1st order	0.037 ± 0.01 s^{-1}	0.74
Langmuir 2nd order	0.041 ± 0.005 s^{-1}	0.87
Langmuir diffusive	0.16 ± 0.04 s$^{-1/2}$	0.74
Pure diffusive	0.020 ± 0.0007 s$^{-1/2}$	0

The fit statistics for each of the models described here, applied to the adsorption data presented in Figure 5.5, can be seen in Table 5.2. The R^2 values for fits corresponding to each of these models are all below 0.9, which indicates poor correlation between the model and the experimental data. The diffusional based model is expected to be a poor model for the data since the maximum surface coverage can be supplied to the surface after approximately three seconds, where the approximate diffusion layer thickness, δ, follows Equation 5.7.

$$\delta = \sqrt{2Dt} \tag{5.7}$$

As the adsorption takes longer than this time, it is clear that mass transport does not significantly influence the data. For this reason the Langmuir diffusional model is also a poor match for the curve. The first order Langmuir adsorption model can be used to model the data for approximately the first 20 seconds of adsorption, but significant deviations are observed after this time. The Langmuir second order model provides the best fit to the curve, but the molecular bases for a two-step adsorption process are unclear. Therefore, it is clear that none of the above models can be used to adequately describe the whole range of data presented in Figure 5.5. It is possible that the protein adsorption is influenced by more complex events than binding kinetics, such as the spreading of the adsorbed protein on the surface over time. Some kinetic studies of this spreading process have been performed[172, 171, 263] and models have been developed that combine Langmuir type adsorption, mass transport effects and protein spreading. However, in the absence of a study of concentration effects on the adsorption kinetics these models cannot be rigourously tested and therefore, were not applied to this system. In conclusion, the adsorption kinetics of fibrinogen have been shown to be complex, but initially fast at this concentration, with $\theta = 0.8$ after only 30 seconds. This fast process is followed by a slower adsorption process, which sees the remaining 20 % of the surface occupied over a timescale of approximately 4000 seconds.

5.3.2 Characterisation of fibrinogen layers

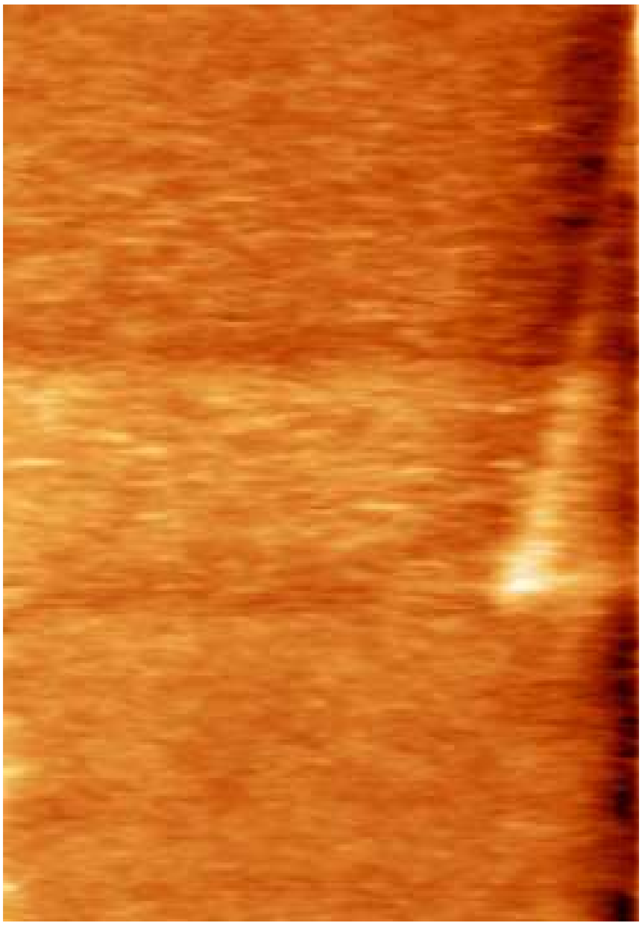

Fig. 5.6: AFM image of a bare Au coated silicon wafer. The image dimensions are 2 μm by 1.4 μm.

The electrochemical characterisation of the fibrinogen layer has been described in the previous section. This section describes the characterisation of the layer using non-electrochemical techniques to gain an insight into the layer structure. Atomic force microscopy (AFM) is a powerful tool that can give topographical information about a surface. AFM has been used by several groups to characterise fibrinogen layers on a variety of substrates.[174, 175, 176, 177, 178] Figure 5.6 shows an AFM image of a bare vapor deposited gold coated silicon wafer. This image confirms that there are no significant structures on the surface, which is consistent with the smooth surface of the silicon wafer. The roughness profile for this bare gold coated silicon wafer can be seen in Figure 5.9 and shows that the average height of the surface features is approximately 2 nm.

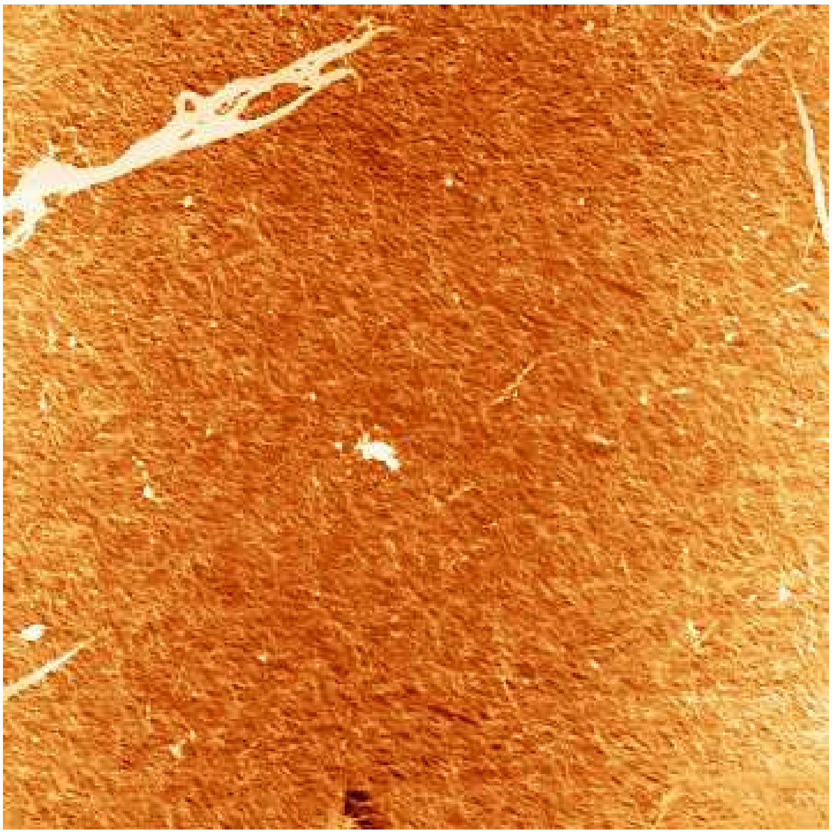

Fig. 5.7: AFM image of fibrinogen coated Au electrode. The image dimensions are 40 μm by 40 μm

The AFM images obtained from the fibrinogen coated slides are markedly different to that obtained for the bare slide and are shown in Figures 5.7, 5.8 and 5.10, while a roughness profile of Figure 5.8 can be seen in Figure 5.9. These figures show several significant features following exposure to the fibrinogen solution. Figure 5.7 shows a 40 $\mu\mathrm{m}^2$ portion of the surface and suggests that the protein has formed a fibre-like layer over the whole substrate and this effect has been observed at other studies.[177,178] However, there are also features which suggest that protein adsorption has proceeded beyond a monolayer in some places. This multi-layer adsorption has been observed before for protein layers.[13] The white streaks seen in Figure 5.7 appear to be due to agglomeration of large amounts of protein. Figure 5.8 shows a 20 $\mu\mathrm{m}^2$ area of the substrate showing a feature like that of a clump of protein. The height profile for this image can be seen in Figure 5.9 and shows that the clump is approximately 2 μm wide and is at least 40 nm high, compared to an approximate

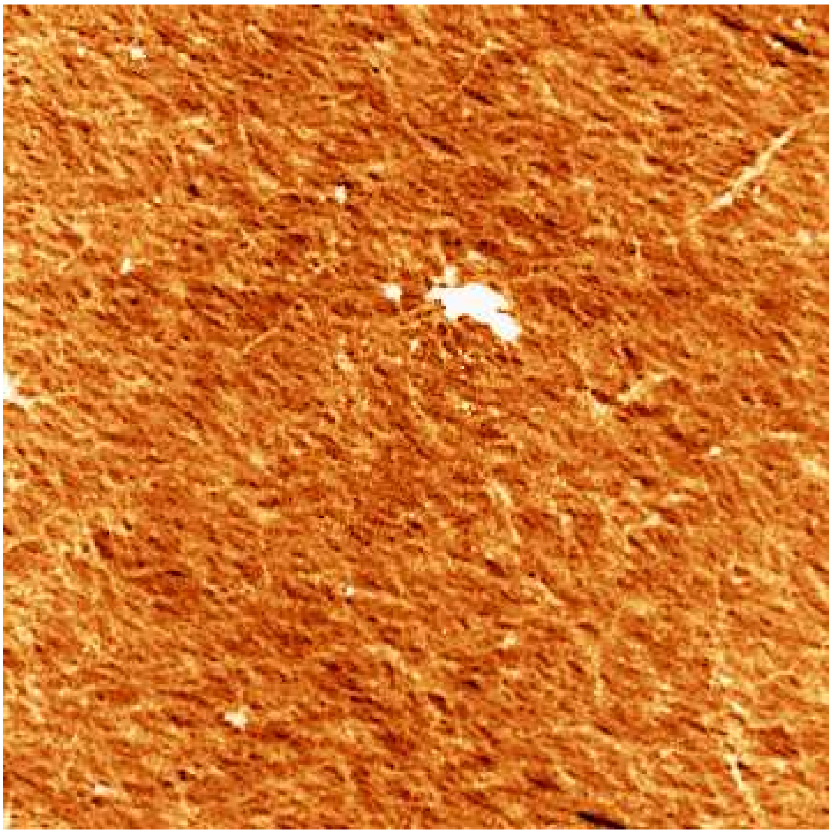

Fig. 5.8: AFM image of fibrinogen coated Au electrode. The image dimensions are 20 μm by 20 μm.

height of 10 nm for the rest of the surface. Both of these feature heights are significantly greater than those seen at the bare slide.

The AFM images presented here suggest two distinct patterns of fibrinogen adsorption on gold. There is a base-layer of protein which covers the whole surface and appears to be in a fibrous, strand like structure on the surface. A strand like conformation is strongly suggested by Figure 5.10, which shows an AFM image of a 10 μm^2 area of the substrate. This figure shows a highly cross-linked network of protein and this cross-linking has been observed before in some studies.[160] It has been suggested that this cross-linking is a result of the uneven charge distribution of the rod-like fibrinogen molecule. The ends of the molecule display positive charges, while a negative charge resides on the central part of the protein and this could lead to electrostatic interactions between protein molecules. The figures shown suggest an amorphous strand like structure for the base layer of fibrinogen. In addition to this layer, there

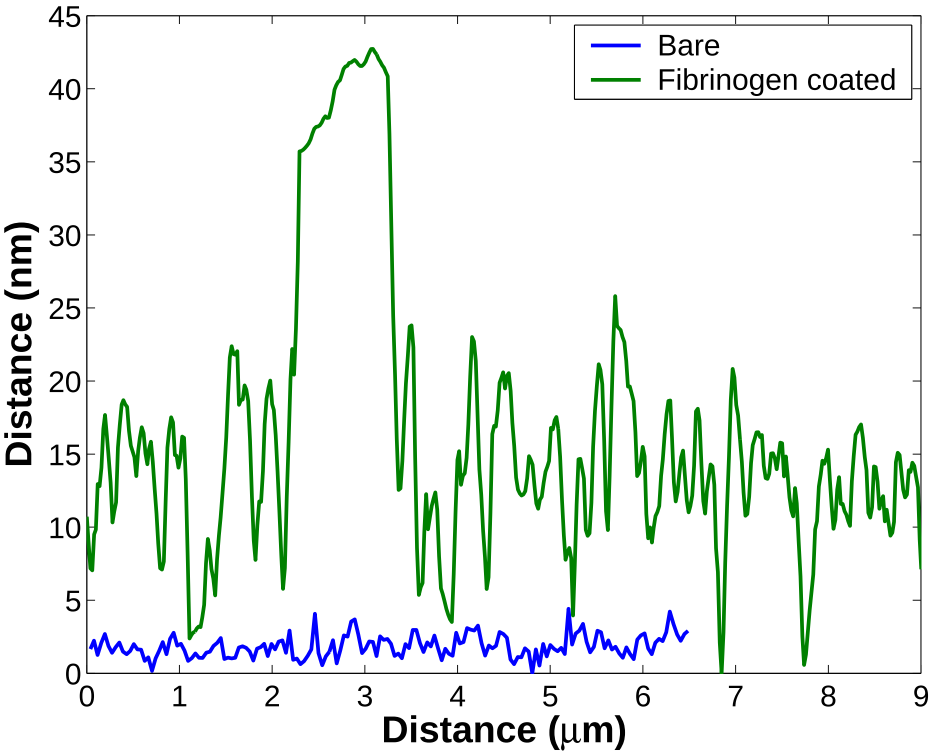

Fig. 5.9: AFM height profiles of bare and fibrinogen coated gold coated silicon wafers.

appears to be some areas where large amounts of protein are adsorbed together in a large streak or clump. The reason for this multi-layered adsorption is unclear, but may be due to precipitation of the protein from solution during overnight deposition and adsorption of these large precipitates onto the base layer. In conclusion, the AFM images show that the protein is broadly spread as a fibrous structure across the surface and that there are areas where multi-layers of the protein are adsorbed even after rinsing.

Fluorescently labelled proteins can be useful in protein adsorption studies as the intensity of the signal is high compared to the other possible signals obtained off surfaces (such as the inherently weak Raman scatter), unless significant surface quenching occurs. Therefore, a dye labelled fibrinogen, Oregon Green Fibrinogen, was adsorbed onto the substrates in a manner analogous to that for normal fibrinogen. Oregon Green is a fluorescein derivative and has excitation/ emission peaks at 494 and 526 nm, respectively (see Figure 5.1).

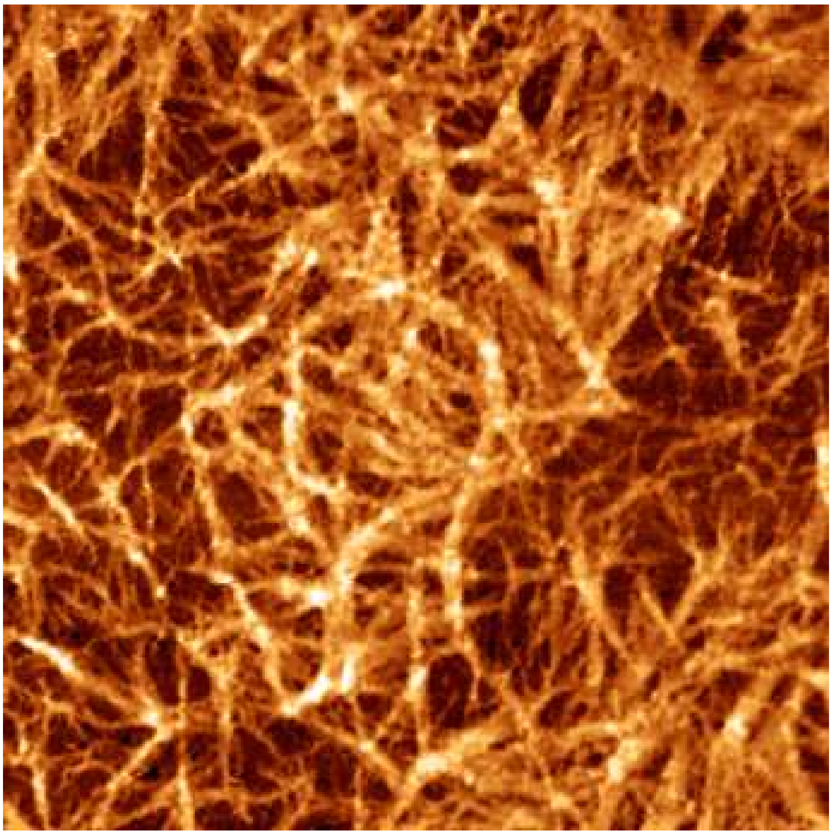

Fig. 5.10: AFM image of fibrinogen coated Au electrode. The image dimensions are 10 μm by 10 μm

Figure 5.11 shows a confocal fluorescence image of the resulting layer using a 488 nm laser excitation source. This figure confirms an adsorption pattern similar to that observed from the AFM images. There appears to be a base-layer of fibrinogen which is evenly spread over the whole surface as the fluorescence is seen from all over the slide. However, some intense, fluorescent signals are observed from macroscopic features on the slide that are like strands or streaks, in agreement with the AFM investigation presented earlier. Figure 5.12 shows the intensity profile across these streaks. Narrow intense bands can be seen at approximately 200 and 760 μm which are 2-4 times as intense as the signal coming from the rest of the slide. As stated above, the presence of these large stands of protein could be due to precipitation of the protein from solution and adsorption of these strands onto the base-layer of adsorbed fibrinogen. Figure 5.12 also shows the emission profile of a gold coated slide in the absence of a protein layer, which confirms the fluorescent signal from the fibrinogen is well

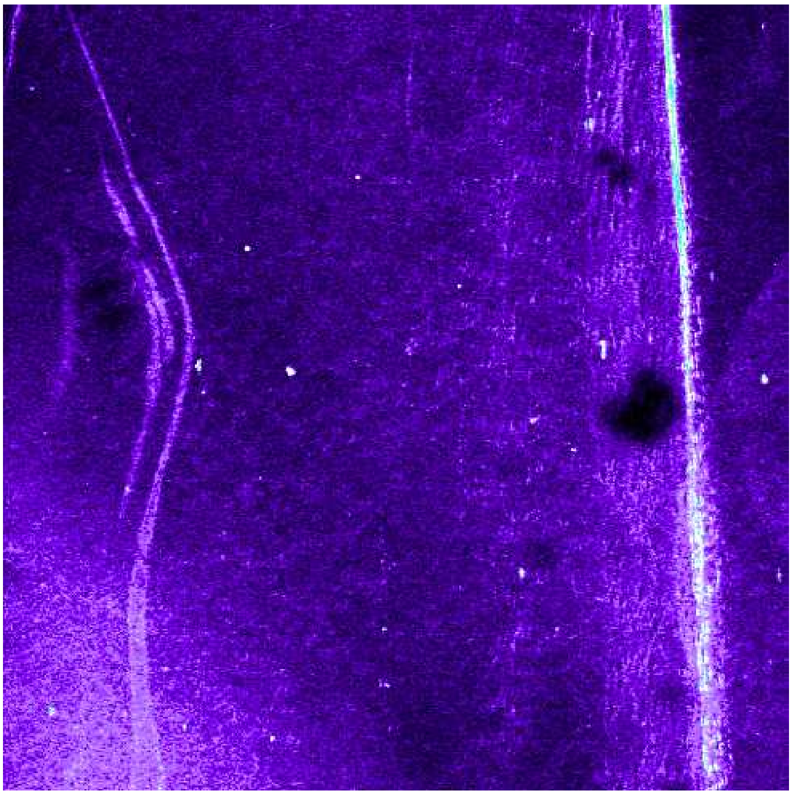

Fig. 5.11: Fluorescence microscopy image of Oregon Green Fibrinogen adsorbed onto a gold substrate. The excitation wavelength was 488 nm and the image dimensions are 900x900 μm. A 505 nm long pass filter was used to remove the excitation wavelength.

in excess of background.

The base-layer coverage of protein observable in the AFM and fluorescence microscopy images presented above is not visible using scanning electron microscopy, (SEM), but the large features observed on the substrate can be imaged successfully. Figure 5.13a shows an SEM image of a bare gold slide and no significant features can be observed, which is consistent with the AFM image of the same unmodified substrate. Figure 5.13b shows an SEM image of a clump of protein on the substrate. This figure shows several dramatic features. The principle two are the coral-like structure which is chiefly confined to the left of the figure and the strand-like structure that can be seen in the left of center and the far right of the figure. The coral-like structure is reminiscent of the features seen in Figure 5.10, as the scale bar shows in Figure 5.13b, the feature dimensions are similar. However, the strand-like structure is also

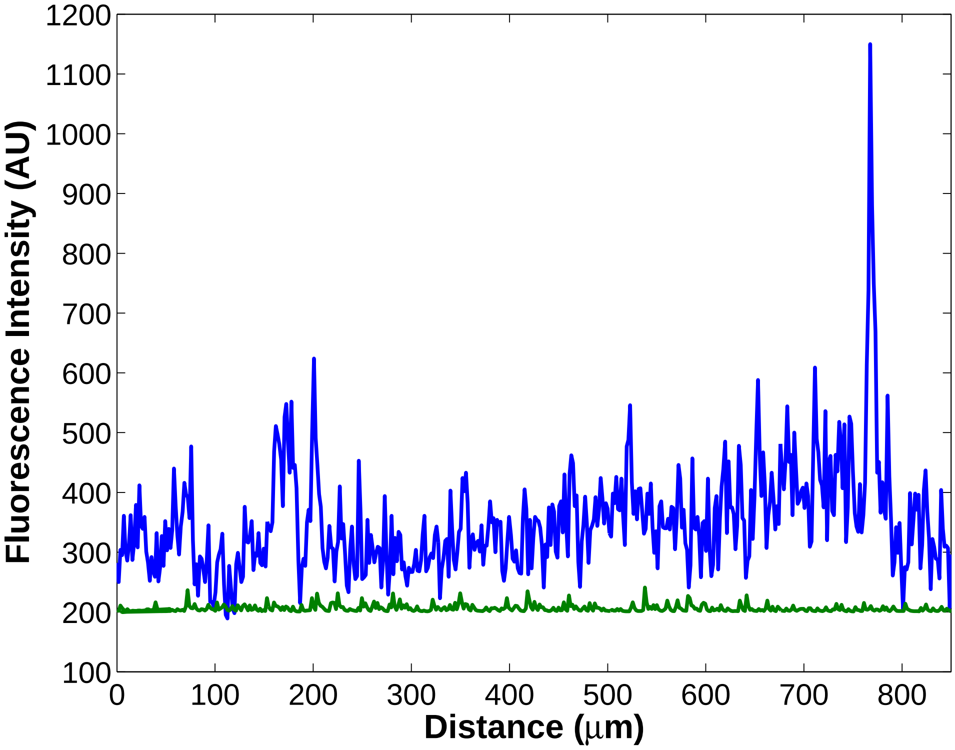

Fig. 5.12: Fluorescence intensity profile across an Oregon Green Fibrinogen layer adsorbed on gold slide (blue) and a bare gold slide (green). The excitation wavelength was 488 nm.

similar to all the AFM images obtained. It is possible that the over-layer of protein adopts several conformations, two of which are seen in Figure 5.13b.

The layers were investigated using Raman spectroscopy exciting at 633 nm to maximise any SERS effect, although the SERS effect is not expected to be significant given the smoothness of the gold surface. The Raman process is inherently weak, with only 1 every 10^6 photons undergoing inelastic scattering and the sensitivity is further reduced for protein layers as proteins are poor Raman scatterers. Therefore, the sensitivity is such that it was not possible to observe protein signals except at the clumps of protein. Figure 5.14 shows a Raman spectrum obtained at the same feature as that shown in the SEM image presented in Figure 5.13b. It should be noted that the spot size of the Raman microscope was approximately 3 μm in diameter, but that the signal did not significantly change when focused on a different area of this protein feature. Figure 5.14 shows the CH stretching region and as seen in Figure 5.2 this

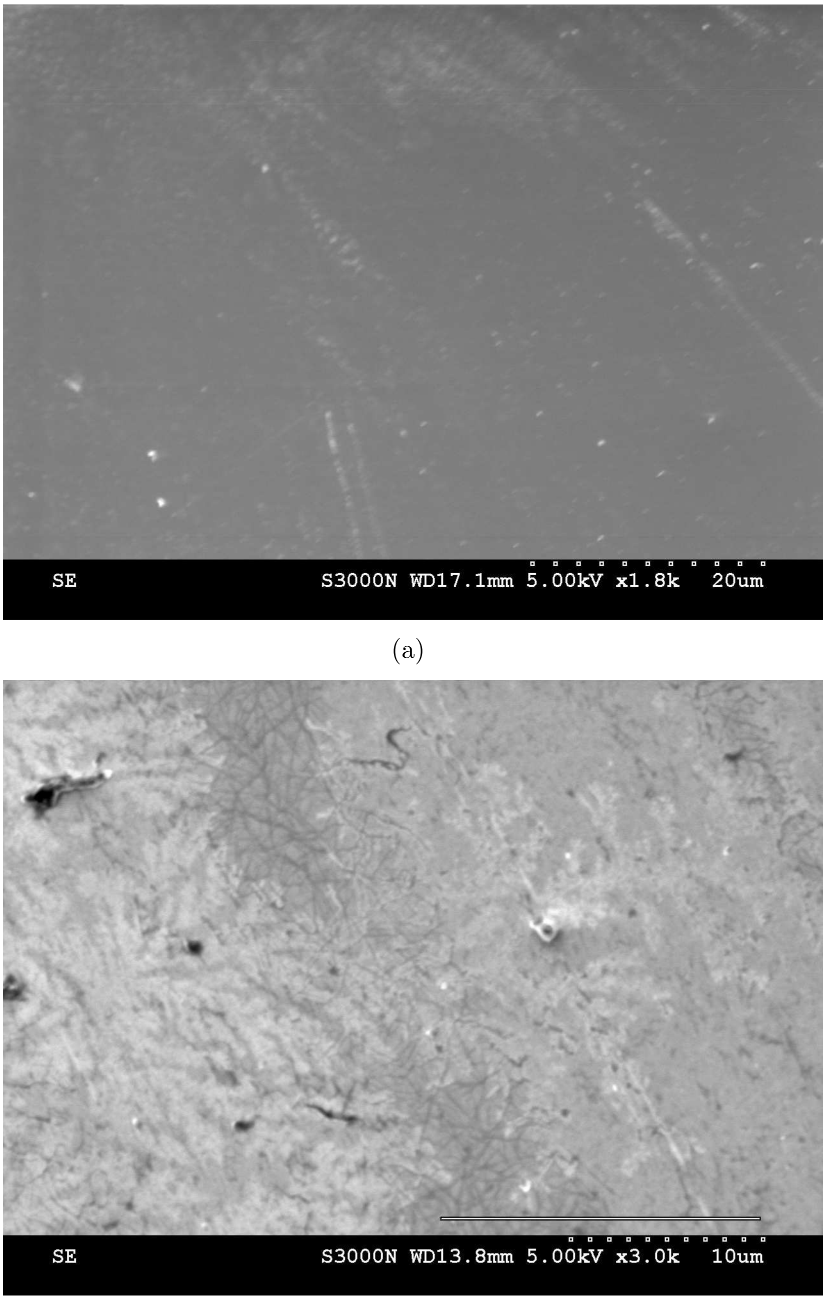

(a)

(b)

Fig. 5.13: SEM image of bare gold coated silicon wafer (a) and of a large clump of fibrinogen adsorbed on gold coated silicon wafer (b).

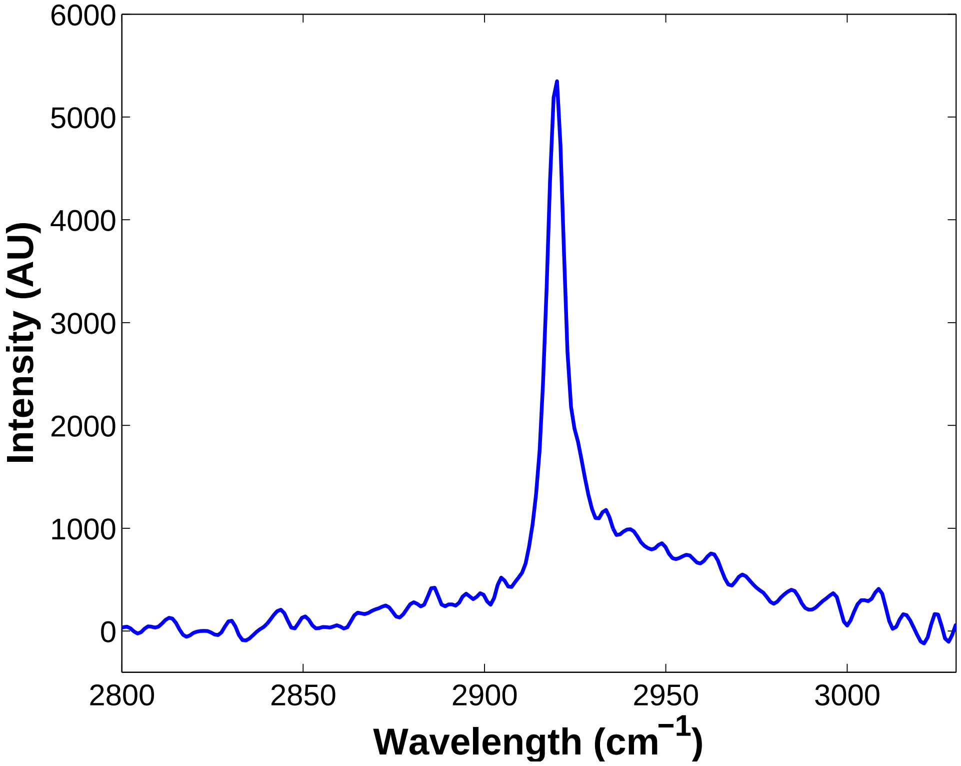

Fig. 5.14: Raman spectrum of the CH stretching region of a fibrinogen layer adsorbed on gold coated silicon wafer. The excitation wavelength was 633 nm.

region is the most intense in the protein spectrum. The peak at 2924 cm^{-1} is a good match for the most intense feature seen in Figure 5.2 for CH stretching in the solid state, which leads to the conclusion that at least one of the features seen in Figure 5.13b are due to fibrinogen adsorption. CH stretching modes may be also observed from adventitious adsorbates, but given the AFM and confocal fluorescence images previously presented it seems likely that these modes may be identified with protein adsorption. Unfortunately, the signal was not intense enough to get structural or conformational information from the spectrum and the peak shown in Figure 5.14 is the only peak that can be attributed to the protein. This is not surprising, however, as the CH stretching is the most intense region of the spectrum, as previously noted.

5.3.3 Desorption of fibrinogen

Effect of electrode potential on fibrinogen desorption

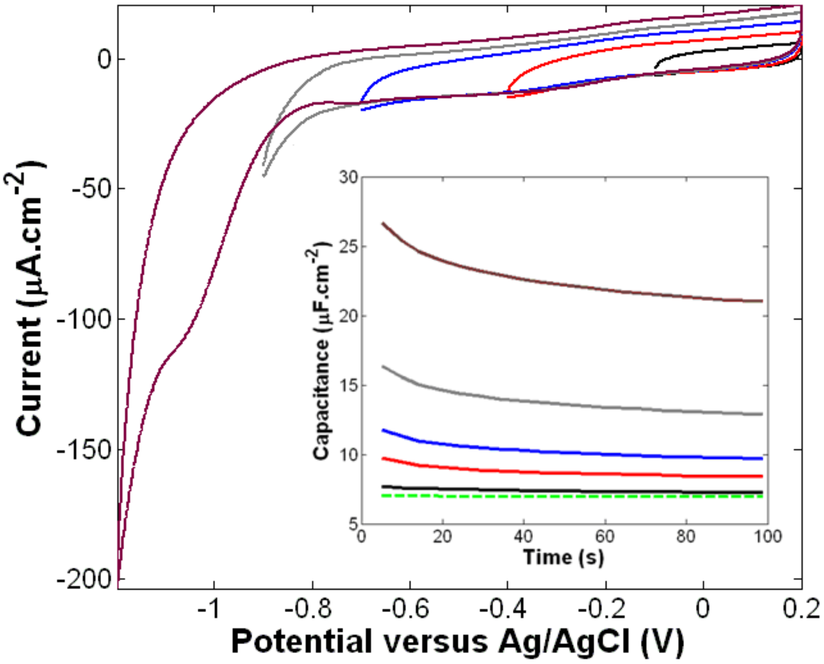

Fig. 5.15: CVs of fibrinogen coated gold electrode in PBS at increasingly negative potential windows (black: -0.1 V, red: -0.4 V, blue: -0.7 V, grey: -0.9 V and brown: -1.2 V). The scan rate is 0.1 V.s^{-1} and the first scan is presented. Inset: the capacitance before (green) and immediately after each CV (the colours are matched).

The adsorption of biomolecules such as proteins on electrode surfaces has been extensively investigated in recent years.[13, 161, 162] However, the effect of electrode potential on the adsorbed layer is a relatively unexplored area. The prospect of electrochemically induced desorption of proteins could be useful in the context of delivery of small volumes of highly concentrated protein in a short time, or for decontamination of metallic surfaces, e.g. medical instruments. The section investigates the effect of electrode potential on the fibrinogen layer. Fibrinogen is negatively charged overall[164] and application of a negative potential is anticipated to lead to electrostatic repulsion and desorption. Figure 5.15 shows a series of window opening CVs where a fibrinogen coated electrode was scanned in an increasingly negative direction from the

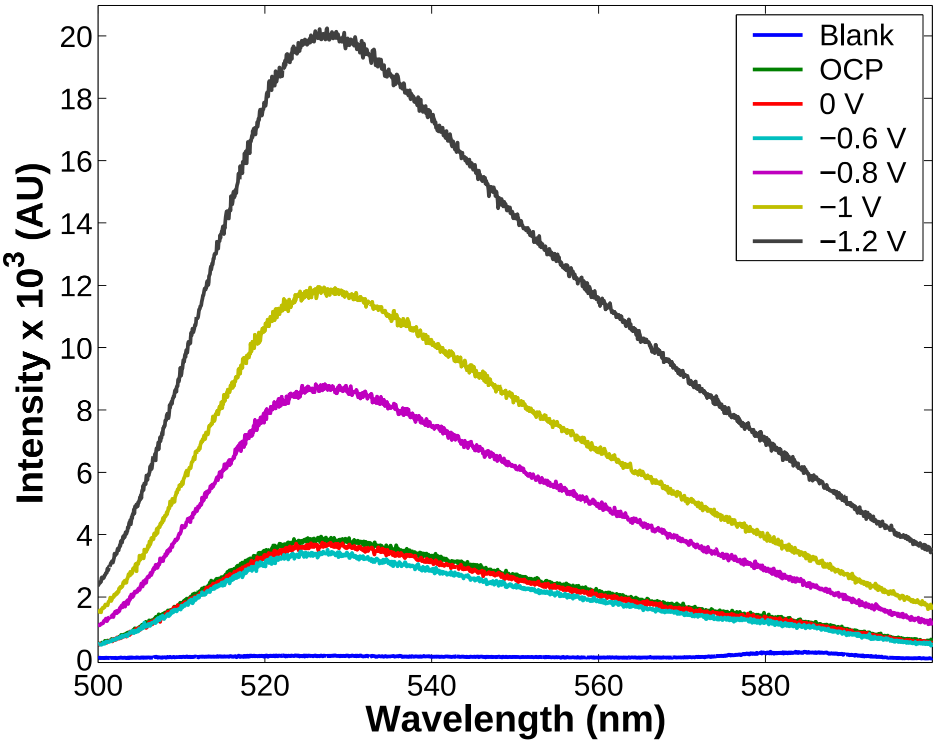

Fig. 5.16: Fluorescence spectra of an Oregon Green Fibrinogen layer on a gold substrate held at progressively negative potentials versus Ag/AgCl in aqueous solution with 0.1 M $NaHCO_3$ as the supporting electrolyte. The blue curve at the bottom is the signal in the absence of the Oregon Green fibrinogen layer. The excitation wavelength is 488 nm. The spectra were obtained focused on the electrode surface using a confocal microscope.

OCP (approximately 0.2 V), up to -1.2 V. This potential is clearly near the cathodic background limit in PBS and more negative potentials were not investigated.

The capacitance of the electrode was investigated at the OCP before this series of CVs and in between each CV. The inset of Figure 5.15 shows capacitance-time traces after each scan. The capacitance measurements are performed at the OCP to avoid any background interference. Initially, the capacitance of the electrode is approximately 7 μF.cm^{-2} (green curve in the inset of Figure 5.15) and the capacitance rises to a final value of approximately 27 μF.cm^{-2} after scanning to -1.2 V. This capacitance is reminiscent of that observed for a clean electrode (see Figure 5.4) and suggests that the fibrinogen layer has been desorbed from the electrode at this negative potential, presumably due to

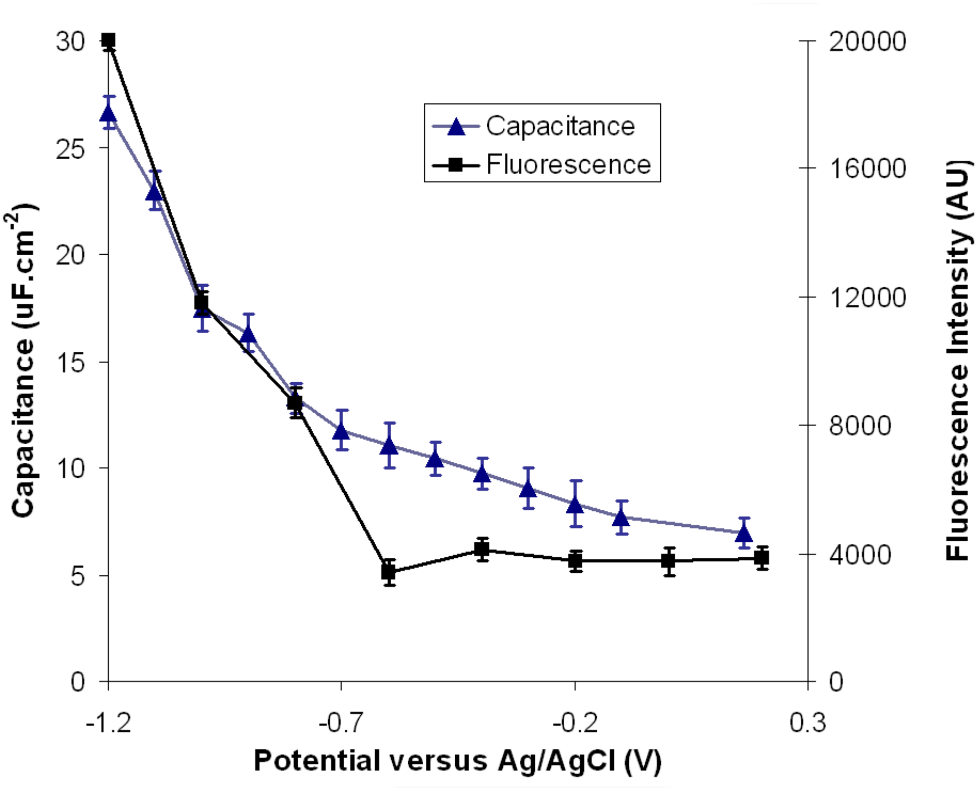

Fig. 5.17: Capacitance of a fibrinogen layer (from the data shown in Figure 5.15) and fluorescent intensity of Oregon Green Fibrinogen layer as a function of potential versus Ag/AgCl.

electrostatic repulsion. It is also likely that the negative potential reduces the di-sulphide bridges in the protein, or any sulphur-gold interactions that may be present, which would aid desorption. This may account for the irreversible wave observed at approximately -1 V in Figure 5.15. Interestingly, the inset shows that the capacitance falls over time, when measured between each scan, which may indicate the re-adsorption of the protein, or parasitic impurities in solution. However, the key conclusion from Figure 5.15 is that the protein can be desorbed by the application of negative potential.

The effect of application of a negative potential on the fibrinogen layer was also investigated using the fibrinogen labelled with Oregon Green, by monitoring the intensity of the fluorescence from the surface as a function of potential. The result can be seen in Figure 5.16 for an Oregon Green fibrinogen layer held at various negative potentials and excited using a 488 nm laser source.

This figure shows that the fluorescence intensity is approximately constant until the application of potentials more negative than -0.8 V, wherein the signal *increases*. The application of a potential of -1.2 V leads to a three fold *increase* of the fluorescent signal compared to the initial signal. The blue curve at the bottom of the figure is the signal in the absence of the Oregon Green Fibrinogen layer on the gold confirming that the observed signal is due to the presence of the dye at the surface. This is supported by the λ_{max} of the emission at 526 nm, which corresponds to the solution phase emission λ_{max} of Oregon Green Fibrinogen (see Figure 5.1).

Figure 5.17 shows a plot of both fluorescent intensity of the Oregon Green Fibrinogen layers and capacitance of a fibrinogen layer versus applied potential on gold electrodes. This data was extracted from Figures 5.15 and 5.16 and it is clear that the increase in the fluorescence signal occurs at potentials similar to those where the capacitance shows that the protein begins to desorb. This suggests that the increase in the fluorescent signal is related to the protein desorption. If the dye molecules are close to the gold surface, significant quenching of the fluorescence can be expected.[219] The quantum yield of Oregon Green has been reported as 0.97,[264] but the fluorescence signal seen in Figure 5.12, while significantly greater than background, is not as large as expected for a dye with such as large quantum yield, indicating significant surface quenching. Oregon Green is not redox active in this potential window and therefore faradic processes associated with the dye are not expected to be a cause of the signal increase. Therefore, the increase in signal is attributed to the removal of surface quenching of the dye as the protein desorbs, which explains the matching trends in the capacitance and fluorescence data. The confocal microscope is focused on the electrode surface, but the confocal volume also includes the area above the surface, up to 200 μm in the z-direction. Therefore, the fluorescence increases as the protein desorbs from the surface and out of range of the surface quenching effects, while remaining at least temporarily in the confocal volume. These experiments suggest the removal of the protein from the surface can be controlled electrochemically by the application of a negative potential.

Desorption kinetics of fibrinogen from gold surfaces

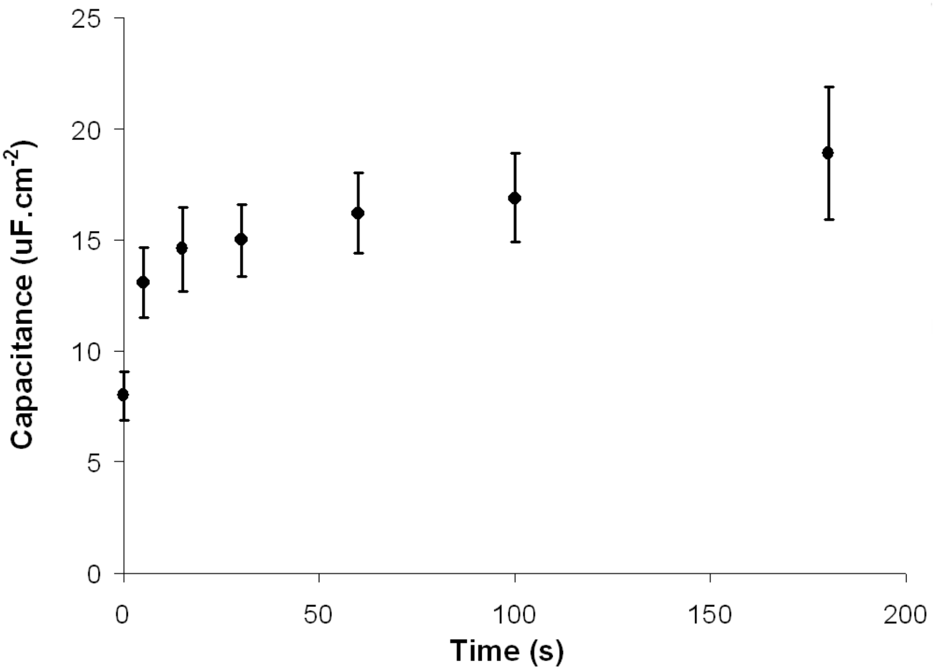

Fig. 5.18: Capacitance of fibrinogen layers measured at OCP as a function of time spent at -1.2 V versus Ag/AgCl. The error bars are the standard deviation of three independent measurements.

The previous section exploited capacitance and fluorescence studies to show that fibrinogen desorbs from a gold surface at negative potentials. The kinetics of this desorption process can also be investigated by both of these methods.

Figure 5.18 shows the capacitance measured at the OCP as a function of time spent at a potential of -1.2 V. The capacitance was measured at the OCP as there are significant background currents observable at -1.2 V. This experiment was performed by monitoring the capacitance of a fibrinogen layer at the OCP before and after application of a potential of -1.2 V for various times. Fresh fibrinogen layers were prepared for each time point. The capacitance at time zero is the initial capacitance and is approximately 7 μF.cm^{-2}, which is in agreement with the previous capacitance studies. The figure shows the capacitance change is initially fast; approximately half the change in capacitance occurs in the first five seconds. It has been found that after 180 seconds the capacitance does not appreciably change. Therefore, this value, of approx-

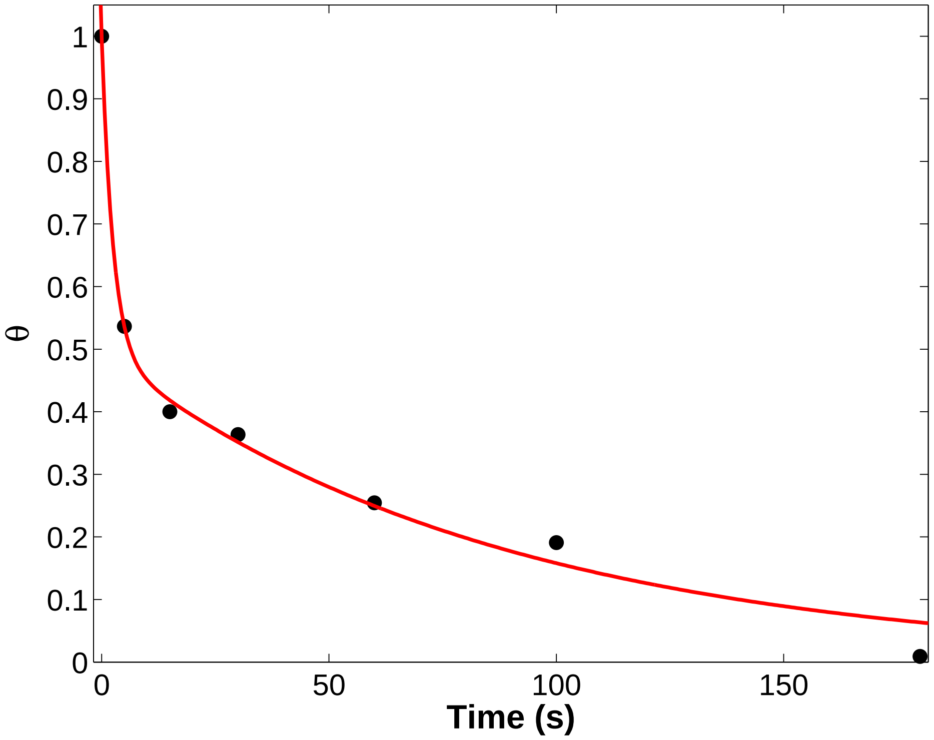

Fig. 5.19: Fractional surface coverage, θ, of fibrinogen layers as a function of time spent at -1.2 V versus Ag/AgCl. The red line represents a bi-exponential fit.

imately 19 μF.cm^{-2} can be considered the final capacitance. This value is somewhat lower than that seen at clean electrodes at similar potentials (see Figure 5.4), which may indicate some residue protein resides on the surface.

The capacitance values can be converted to fractional surface coverage, θ, values in a manner analogous to that for the protein adsorption experiments using the initial and final capacitance values (C_0 and C_f respectively) by the following equation:

$$\theta = \frac{C_f - C_t}{C_f - C_0} \tag{5.8}$$

where C_t is the capacitance at time t. Figure 5.19 shows θ as a function of time where θ has been calculated using Equation 5.8. The desorption of proteins (by a change of pH of the solution[181] or desorption into blank electrolyte[180]) from surfaces has received some attention in the literature and the main models used are the Langmuir model,[180] although some studies suggest a diffusion based kinetic model is more appropriate,[13] as diffusion of the large protein molecules from the surface is slow.

The first order Langmuir desorption model is the simplest and assumes that the rate of change of surface coverage is proportional to the surface coverage;

$$\frac{d\theta}{dt} = -k\theta \tag{5.9}$$

Integration of this equation yields;

$$\theta = exp^{-kt} \tag{5.10}$$

However, this model is a poor match for the data displayed in Figure 5.19 and shows a correlation coefficient of 0.73, suggesting a more complex mechanism. Figure 5.19 shows a bi-exponential fit of the experimental data and it is clear that this model is more successful than the single exponential Langmuir model. The correlation co-efficient of the fit shown in Figure 5.19 is 0.99 and the rate constants are $k_1 = 0.400 \pm 0.065\ s^{-1}$ and $k_2 = 0.011 \pm 0.001\ s^{-1}$. This indicates that the desorption is initially fast, with over half of the surface coverage lost after polarization at -1.2 V for 10 seconds ($k_1 = 0.4\ s^{-1}$). It is surprising therefore that the second rate constant should be slower than the first, as the stabilising lateral interactions would be weakened as the protein desorbs. However, as the capacitance measurements are performed at the OCP, the desorbed protein may re-adsorb, which would increase the surface coverage and decrease the observed desorption rate. This may explain why the second desorption rate is significantly slower than the first. It is also possible that some of the protein is more strongly bound, perhaps due to greater spreading of protein that is nearest the surface.

The desorption kinetics can also be explored using the fluorescence signal from

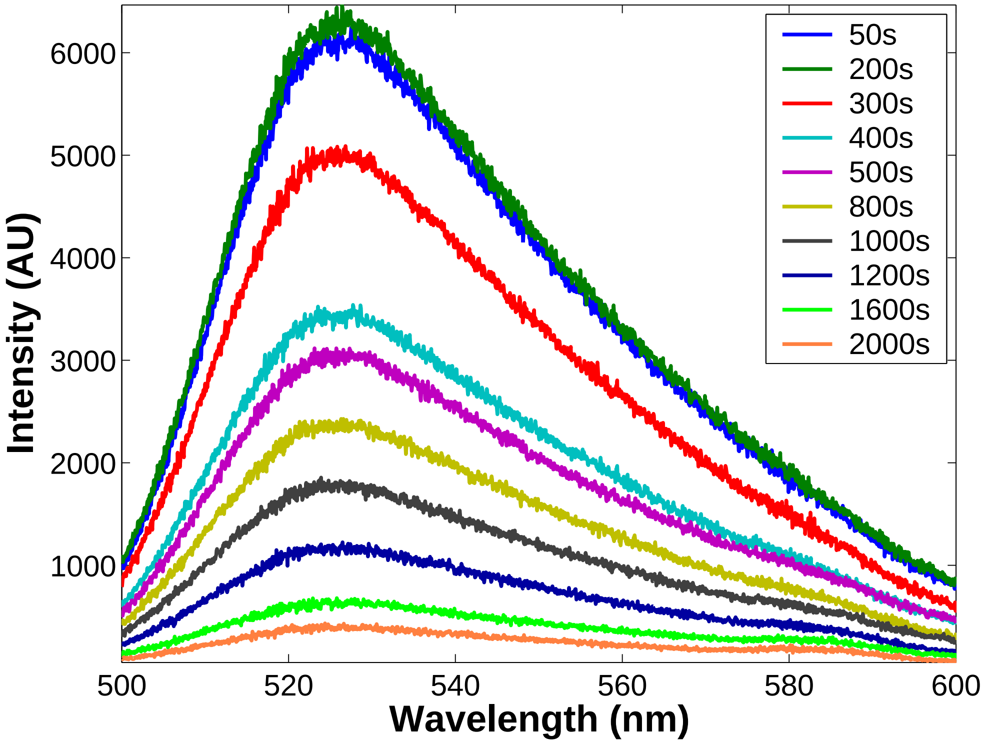

Fig. 5.20: Fluorescence spectra at various times of an Oregon Green Fibrinogen layer on a gold substrate at a potential of -1.2 V versus Ag/AgCl in aqueous solution with 0.1 M $NaHCO_3$ as the supporting electrolyte. The excitation wavelength is 488 nm. The spectra were obtained focused on the electrode surface using a confocal microscope.

Oregon Green Fibrinogen adsorbed onto gold substrates. Figure 5.20 shows a series of fluorescence spectra obtained from an Oregon Green Fibrinogen layer held at a potential of -1.2 V in aqueous solution with 0.1 M $NaHCO_3$ as the supporting electrolyte. Figure 5.21 shows a plot of fluorescence intensity versus time which was constructed using data from Figure 5.20. These figures show that the fluorescence intensity initially increases over the first 200 seconds before falling steadily to less than 10 % of the initial value after 2000 seconds. This process was seen to be irreversible, i.e. holding the potential at the OCP after this scan did not revive the fluorescence signal. Therefore, the decrease of the signal over the relatively long time scale is potentially due to the diffusion of the protein away from the surface.

The increase in fluorescence intensity over the first 200 seconds is an interesting feature of this experiment but is consistent with the pattern seen for the

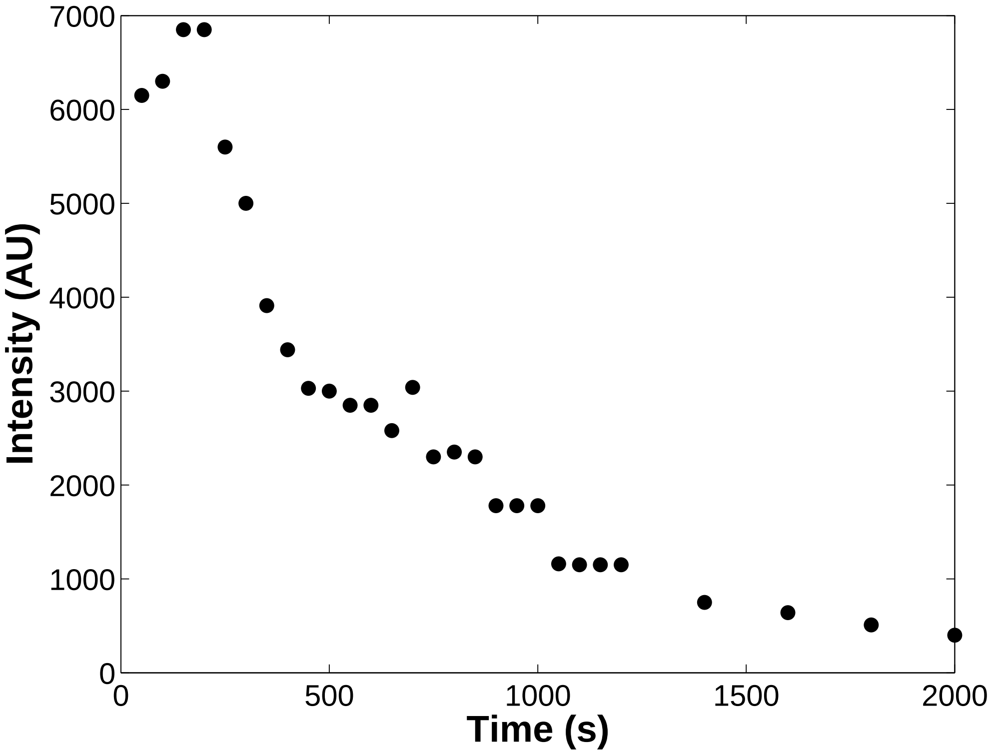

Fig. 5.21: Fluorescence intensity (at λ_{max}) of an Oregon Green Fibrinogen layer at a gold electrode at -1.2 V versus Ag/AgCl as a function of time in aqueous solution with 0.1 M $NaHCO_3$ as the supporting electrolyte. The excitation wavelength is 488 nm.

fluorescence intensity as a function of applied potential experiments (Figure 5.16). In that case the fluorescence intensity was seen to rise as the potential applied became more negative and this was attributed to a decrease in dye quenching due to an increase in the protein-surface distance as the protein desorbed. Therefore, the initial increase in signal, over the first 200 seconds, can be attributed to the protein desorbing and moving out of range of the surface quenching effects but still within the confocal volume. At longer times, the protein diffuses out of the confocal volume and the signal decreases. It is interesting to note that the capacitance data suggest that the desorption process is practically complete after approximately 180 seconds, which is a good match for the timescale over which the fluorescence signal increases. The subsequent decrease in signal can be attributed to diffusion of the protein out of the confocal laser volume and as a 10x objective was used to focus the laser onto the surface this area is relatively large (approximately 100-200 μm

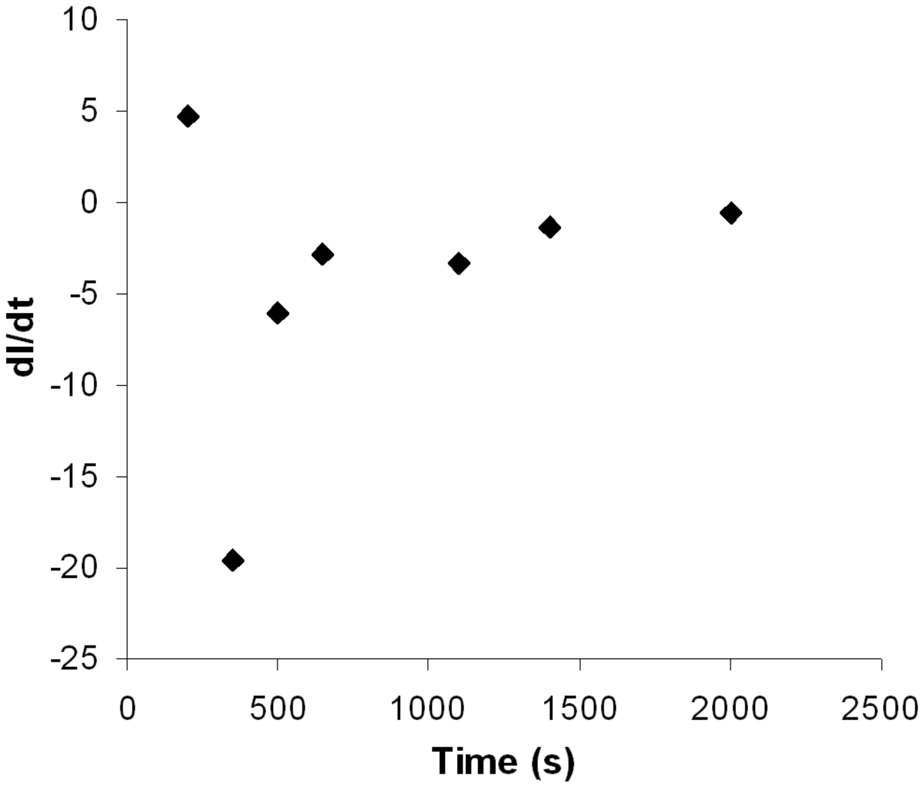

Fig. 5.22: Plot of change in fluorescence intensity with time (dI/dt) as a function of time for a fibrinogen coated gold electrode at -1.2 V versus Ag/AgCl.

in the z direction), which accounts for the long time scale for this diffusional event. As this signal constantly decreases this shows that the protein does not re-adsorb at this potential but is released into the solution. Finally, this figure suggests that the overwhelming majority of the fibrinogen is desorbed from the surface, as the signal falls to less than 10% of the initial intensity. The extent of desorption observed here is significantly higher than that found for other surfaces.[179, 180, 181] Therefore, the electrochemical desorption that has been described here appears to be more efficient, as at least 90% of the protein appears to desorb.

The decrease in the fluorescence signal after 200 seconds has been attributed to diffusion of the dye away from the electrode surface. Therefore, the change in fluorescence intensity over time (dI/dt) should correspond to the flux of the protein out of the confocal laser volume. The flux (J) in or out of a region can

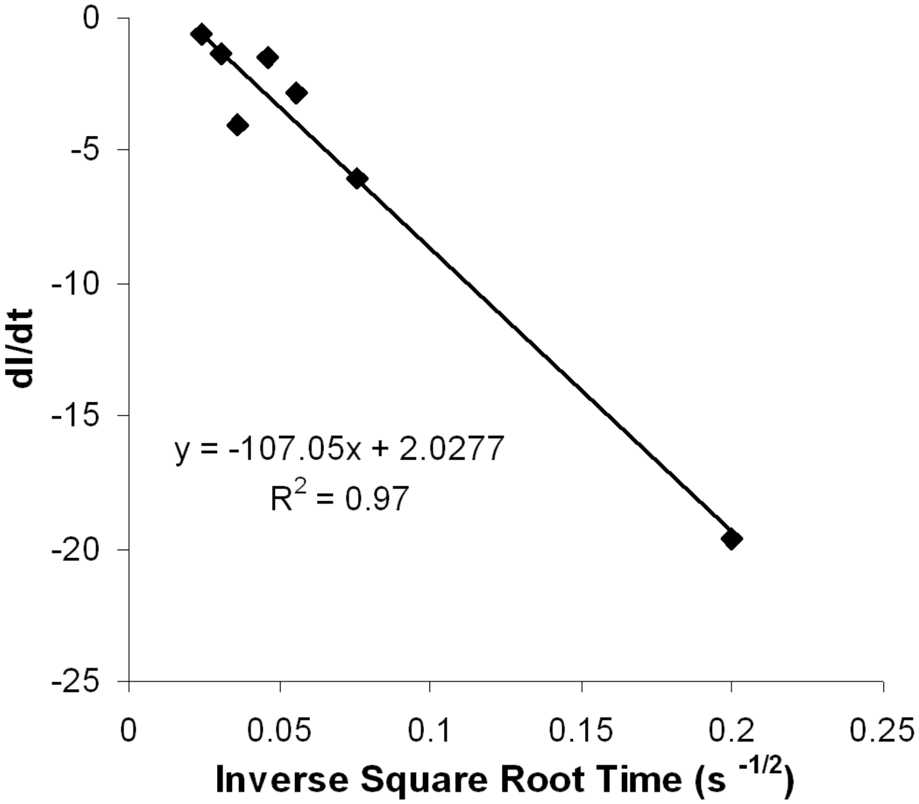

Fig. 5.23: Variation of dI/dt of a fibrinogen coated gold electrode at -1.2 V versus Ag/AgCl with the inverse square root of time.

be characterised by Fick's first law, which states that the flux is proportional to the concentration gradient at the interface, which has been shown to be dependent on the inverse of the square root of time:[265]

$$J(x=0,t) = D\frac{\partial C}{\partial x} = \frac{DC}{\sqrt{D\pi t}} \tag{5.11}$$

where D is the diffusion co-efficient and C is the concentration at the surface. The diffusion co-efficient of fibrinogen has been reported[266] as 2.24 x 10^{-7} $cm^2.s^{-1}$.

Figure 5.22 shows a plot of dI/dt versus time. The initial increase in the fluorescent signal leads to a positive value for dI/dt at low time values. However, the dI/dt values soon become negative, which reflects the decrease in the fluorescent signal. The magnitude of the change slows over time, until it approaches zero at approximately 2000 seconds. If diffusion of the protein out of the confocal laser volume is the reason for the fall in intensity then the flux (or dI/dt) should follow a $t^{-1/2}$ dependence, in accordance with Equation 5.11. Figure 5.23 shows a plot of dI/dt versus $t^{-1/2}$, excluding the data reflecting the initial increase in fluorescent signal. This plot is broadly linear, ($R^2 = 0.97$), which shows that Equation 5.11 is a suitable model for the experimental data. The slope of this plot is -107, which should correspond to $DC/\sqrt{D\pi}$ according to Equation 5.11. However, the use of fluorescence intensity instead of concentration is this study must be accounted for. The concentration can be related to the fluorescence intensity by considering the final fluorescent intensity in solution after desorbing the protein, and estimating the amount of protein desorbed from the surface, using 6.3 x 10^{-13} mol.cm^{-2} as the coverage of the protein as determined in the next section. Therefore, if $I = kC$, k can be estimated as 3.49 x 10^{12}. This means that the slope can be related to the diffusion co-efficient by $slope = DkC/\sqrt{D\pi}$. This yields a diffusion co-efficient of 0.19 cm^{-2}.s^{-1}, which is clearly very large compared to the literature value of 2.24 x 10^{-7} cm^{2}.s^{-1}.[266] The reason for this discrepancy may be related to the conversion of fluorescence intensity into concentration, or to limitations in Equation 5.11.

In conclusion, the decrease in fluorescent signal can be attributed to the diffusion of the protein away from the gold surface and it appears that re-adsorption is negligible at -1.2 V.

Effect of desorption on fibrinogen structure

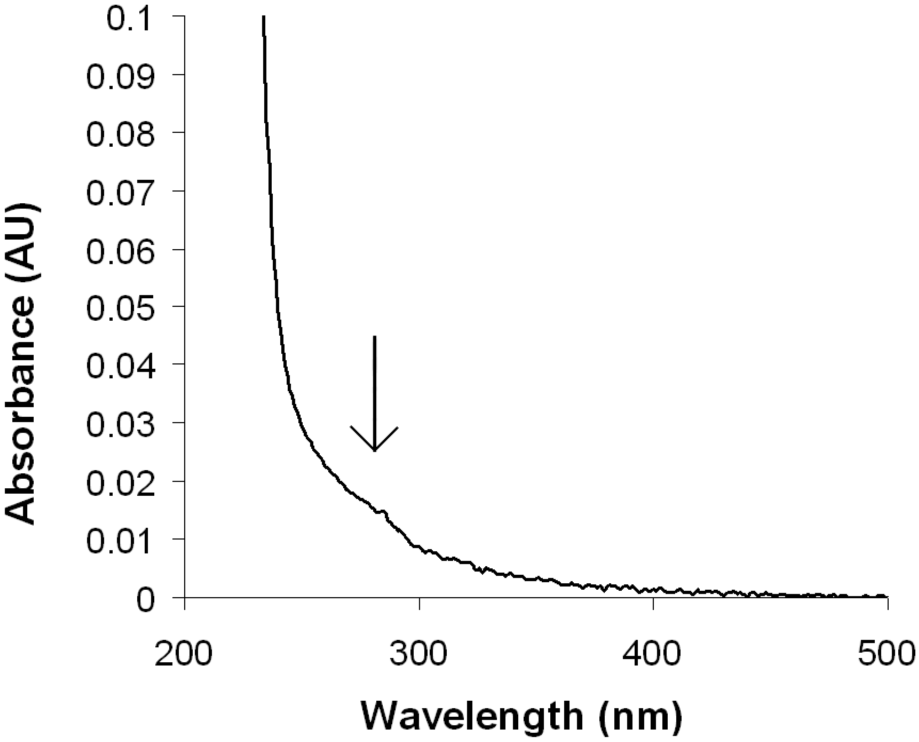

Fig. 5.24: UV-vis spectra of desorbed fibrinogen in 0.1 M $NaHCO_3$. The native protein spectrum can be seen in Figure 5.1.

It has been seen in the previous section that the vast majority of the adsorbed fibrinogen can be desorbed by the application of a negative potential to the electrode. Therefore, if desorption of fibrinogen layers is performed into blank electrolyte solutions, the presence of the fibrinogen in solution can be probed by spectroscopic methods such as UV-vis and fluorescence spectroscopy. Figures 5.24 and 5.25 show the UV-vis and fluorescence spectra of solutions containing desorbed fibrinogen and desorbed Oregon Green labelled Fibrinogen respectively. These layers were desorbed from a large area (approximately 14 cm^2) electrode into blank electrolyte by applying a potential of -1.2 V for 180 seconds. It has been reported[266] that fibrinogen has an extinction co-efficient ($E^{1\%}$) of 15.1 at λ_{max} of 280 nm. The UV-vis spectrum in Figure 5.24 shows a weak but detectable band in this region, which is indicated on the figure.

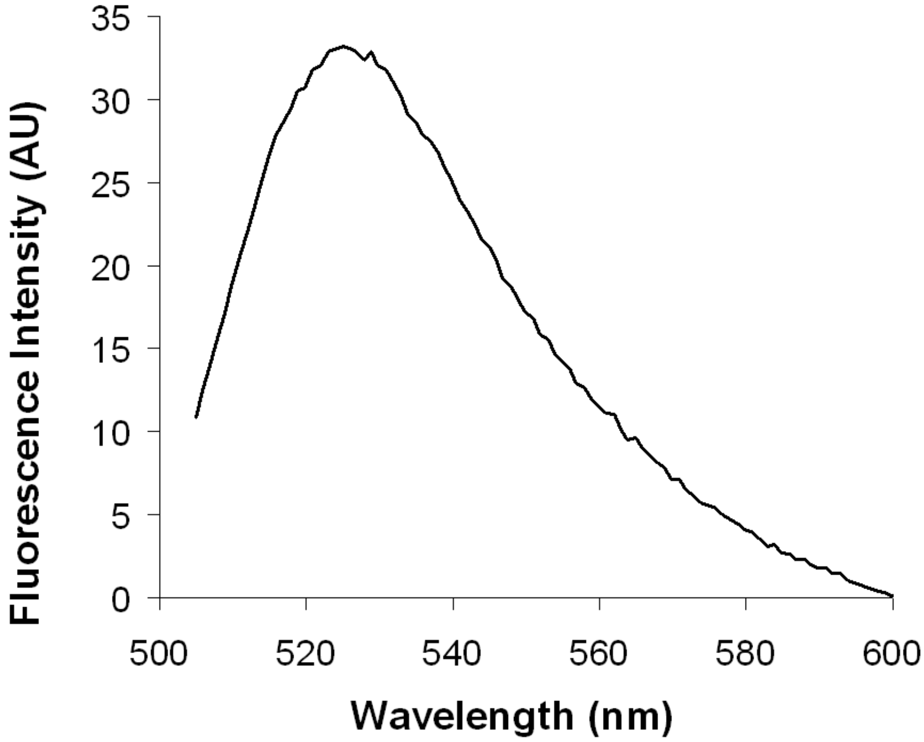

Fig. 5.25: Fluorescence spectra of desorbed Oregon Green Fibrinogen in 0.1 M $NaHCO_3$, obtained using an excitation wavelength of 496 nm. The emission of the dye labelled protein can be seen in Figure 5.1.

The curve rises sharply at approximately 240 nm which is in good agreement with the spectra presented in Figure 5.1 for fibrinogen before adsorption. The fluorescence spectrum seen in Figure 5.25 shows a peak at 526 nm which is also in good agreement with the data presented in Figure 5.1. The difference in sensitivity between these techniques is evident from the figure. The amount of fibrinogen in solution can be estimated from the UV-vis analysis as approximately 3 μg. Assuming that all the fibrinogen has desorbed from the surface, this corresponds to a fibrinogen surface coverage of approximately 0.2 μg.cm^{-2}, or 6.3 x 10^{-13} mol.cm^{-2} according to the UV-vis data. The surface coverage can also be calculated using the fluorescence data and in that case the somewhat lower surface coverage of approximately 70 ng.cm^{-2} is found. This may be a result of the discrepancies between the concentration of the fibrinogen in the solutions from which adsorption took place, as the layers for the

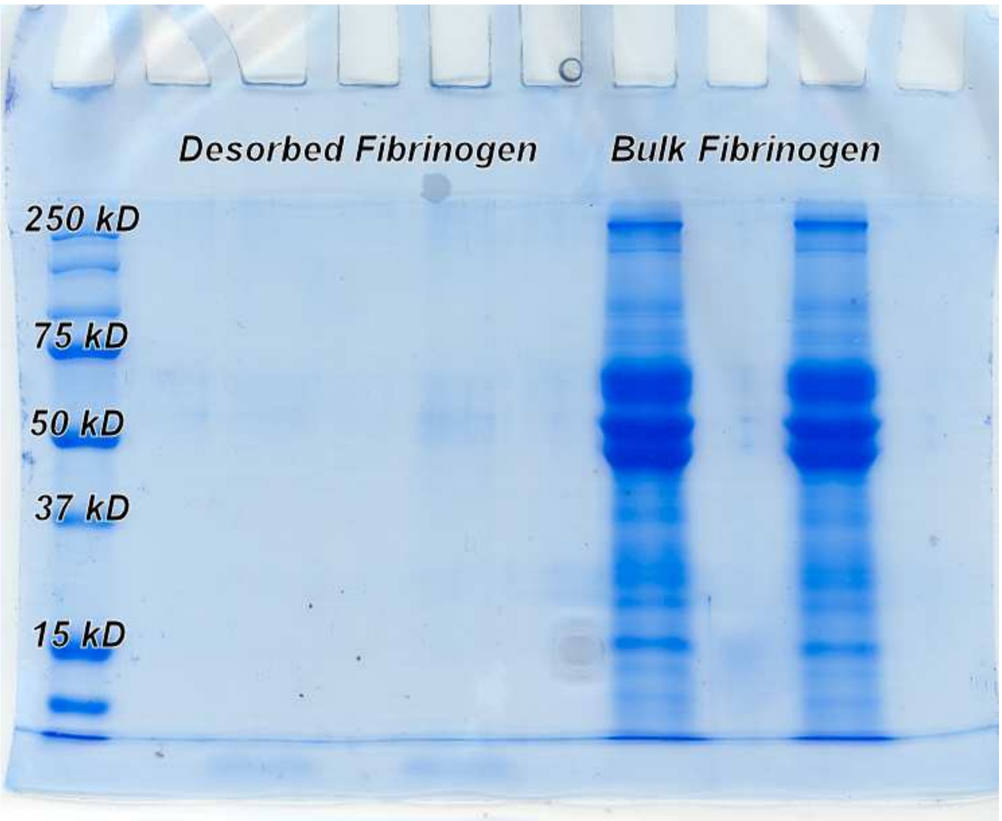

Fig. 5.26: Migration of fibrinogen on a SDS PAGE gel (10%) before (bulk) and after (desorbed) the adsorption/desorption cycle.

UV-vis work were prepared in solutions which had a 10 fold excess of fibrinogen compared to the solutions used for the fluorescence studies. The extent of protein-dye conjugation could also lead to discrepancies between these two methods, due to uncertainty in the ratio of dye to protein. The UV-vis and fluorescence spectra presented in Figure 5.1 suggest that there are approximately 100 dye molecules per protein molecule. This can be found by calculating the concentrations of the protein (λ_{max} = 280 nm, $E_{1\%}$ = 15.1 L.g^{-1}.cm^{-1}) and dye (λ_{max} = 490 nm, ε = 85000 M^{-1}.cm^{-1}). However, this assumes that all the dye is conjugated and the supplier (Invitrogen) claims a ratio of 15 dye molecules per protein molecule. Therefore, the amount of fibrinogen desorbed into solution could lie between 200-1000 ng depending on this ratio.

The maximum surface coverage of fibrinogen has been reported as approximately 1 μg.cm^{-2},[13] on a variety of surfaces such as glass or nylon, which would indicate that the surface coverage described here is not at saturation levels. However, the constancy of the capacitance after overnight deposition appears to contradict this observation. It is possible that the extent of protein spreading has an influence on the maximum surface coverage.

Many studies have shown that the adsorption of proteins on bare metal surfaces leads to the denaturation of the protein as the protein irreversibly changes its secondary structure to interact with the substrate upon surface binding.[13] This process is commonly called spreading and is frequently seen for fibrinogen at hydrophobic surfaces.[177, 178] The structure of the desorbed fibrinogen has been investigated using gel electrophoresis studies of both native and desorbed fibrinogen samples. Figure 5.26 shows the migration of native and desorbed fibrinogen on a SDS PAGE gel (10%). The desorbed fibrinogen was obtained by performing a bulk adsorption-desorption experiment. This involved subjecting a 3 cm^2 gold electrode in 50 μg of fibrinogen in PBS to a series of potential steps from OCP to -1.2 V. The time spent at the OCP was 12 minutes and the adsorption kinetic data discussed above indicates that approximately 90% of the surface is covered in this time. The potential was then stepped to -1.2 V for 180 seconds as described above for desorption studies. This process was repeated, under gentle solution agitation, for 90 hours. If 0.6 μg of protein is adsorbed and desorbed in every cycle then, by agitation of the solution, all of the protein should go through the adsorption-desorption process at least once in this time period, although nothing is known about the propensity of previously desorbed material for re-adsorption.

Figure 5.26 shows that the active fibrinogen migrates principally to the 50 kD level. The desorbed fibrinogen is much less concentrated but faint traces can also be seen at this level, indicating the presence of some active protein. However, the majority of the desorbed fibrinogen appears to be fragmented as there are significant traces which run in front of the solvent front visible at the bottom of the figure. These fragments are likely to be less than 10 kDa. Efforts to concentrate the protein on spin filters also indicated that the protein was fragmented. This fragmentation appears to be a direct result of the adsorption-desorption process (it has been previously noted that the disulfide bridges may be reduced by application of -1.2 V), but it is unclear at which step the damage occurs. However, it is clear that the protein structure is seriously compromised by the adsorption-desorption cycle on bare gold.

5.4 Conclusion

Protein adsorption is one of the most commonly studied biochemical processes and is important for several areas such as biocompatibility of clinical implants and fouling of equipment in the food processing industry.[13,161] Electrodes are common substrates for studying adsorption of biomolecules and are useful as the energy levels of the electrons in metal can be easily controlled. This can lead to interesting and advantageous systems, such as those where the redox activity of proteins is exploited, and a large body of work explores this concept through various proteins and surface linkers.[267,268] However, there is another important, but rarely studied, effect that application of electrode potential can have on adsorbed protein layers; electrostatically driven desorption. This could potentially enable control over the accumulation and release of protein from an interface.

This chapter has described spontaneously adsorbed fibrinogen layers at gold surfaces. The kinetics of adsorption were explored, but a simple model was not found that could fit the experimental data. This would indicate that complex processes, such as protein spreading over time have an influence on the adsorption kinetics. The topographical structure of the layer was investigated using atomic force microscopy and fluorescence microscopy. While the protein appeared to adsorb evenly as a fibrous structure over the whole surface, streaks or aggregates of protein were also observed in these images even after extensive washing of the electrode with Milli-Q water. These aggregates were observed using scanning electron and Raman microscopy. The Raman spectrum confirmed the presence of protein in the clump as the CH stretching peaks are clearly evident. In conclusion, the fibrinogen layer appears to be somewhat heterogeneous in nature, which is perhaps consistent with denaturation of the protein.

The effect of application of negative electrode potential on the adsorbed fibrinogen layer was investigated using both capacitance and fluorescence techniques. The capacitance of the layer (measured at OCP) is seen to rise as the electrode is subjected to increasingly negative potentials. The fluorescence signal also shows a very similar increase, indicating that the dye-labelled protein is moving away from the surface, leading to less efficient surface quenching of the fluorescence signal. The kinetics of desorption at -1.2 V were also explored using both capacitance and fluorescence measurements. The capacitance data indicate that the desorption kinetics can be fit using a bi-exponential model, where the initial rate is faster than the second rate. The fluorescence data indicate that re-adsorption at -1.2 V does not occur and that more than 90% of the protein is desorbed. The diffusion of the protein out of the confocal laser volume follows a $t^{-1/2}$ dependence. Finally, the effect of this adsorption-desorption cycle was investigated and it was found that significant damage to the protein conformation occurred.

In conclusion, this chapter demonstrates that significant control can be exercised over adsorbed fibrinogen layers by altering the electrochemical potential. The disruption of the protein conformation is disappointing from the perspective of protein delivery. However, pre-modification of the gold surface with molecules such as alkanethiols to protect the protein structure could allow desorption of active protein from an interface. However, the destruction of the protein activity may have applications in areas such as decontamination of metals exposed to proteins, e.g. sterilisation of surgical equipment.

Chapter 6

Protein adsorption and desorption at nano-porous surfaces

6.1 Introduction

Structuring materials with nanoscale features is currently a popular and exciting area of interfacial science.[189, 190, 191] This is due to the novel optical properties that these materials display when compared to the bulk material. Specifically, the interaction of light with a surface can be altered by incorporation of features of similar scale to the wavelength of the light used. Surface plasmons can be localised on a metallic surface by nanoscale features,[190] leading to enhancement of spectroscopic signals such as Raman[202] or fluorescence.[215]

These surfaces provide new challenges and opportunities to many areas of surface science and much work has focused on nanoparticles. Although considerably less studied, nano-void arrays have also received attention and are easily and reproducibly created using lithography techniques.[197] A further advantage is the possibility of filling these nano-void arrays with analytes. Brolo and co-workers have described the creation of gold nano-hole arrays[217] for both Raman[269] and fluorescence enhancement.[215] However, these substrates are fabricated using focused ion beam milling. The creation of nanocavity arrays by nanosphere lithography has been described by Bartlett[202, 206, 207, 212] and others.[208] A key advantage of metal nano-cavities is the ease with which these features can be reproducibly controlled by self-assembly of a template of polystyrene spheres, through which gold or other metals[204] can be electrodeposited. The spheres are then dissolved to leave behind an array of nanocavities. These methods are simple and cost effective compared with electron lithographic methods. Furthermore, the cavity diameter can be easily changed by the use of a different sphere size and the cavity shape and opening can be controlled by monitoring the charge passed during the electrodeposition step.[202] These substrates generate interesting and complex localised surface plasmons that depend on several factors including the cavity depth and the angle of incidence of the light source.

However, many possibilities remain for the modification of these nano-structured materials with organic layers, such as those described in the last three chapters. A key objective is to selectively modify these structures so as to promote binding at certain sites, such as inside the cavity where any plasmonic enhancement is potentially greatest. The adsorption and desorption of molecules, such as proteins, could provide information on the diffusion into and out of the cavities. The enhancement offered by the cavities to spectroscopic signals such as fluorescence or Raman also offer possibilities for molecular detection. As the substrates are gold they can also be employed as electrodes, which results in greater control over the system.

Nano-cavities may be used to create more complex supramolecular systems, such as that shown in Figure 6.1. This figure shows an agonist protein adsorbed at the walls of a nano-cavity and a lipid bilayer spanning the cavity opening. Parallel work in our group is being carried out to investigate the stability of this bilayer-cavity structure and the possibility of incorporating membrane proteins, such as integrins. A key objective is the electrochemical release of the agonist protein from the cavity walls, which could lead to interaction between the two proteins. The plasmonic enhancement provided by the cavity could enhance spectroscopic signals, such as Raman, to monitor this interaction. The keys issues for this system to be realised are the release rate and transit

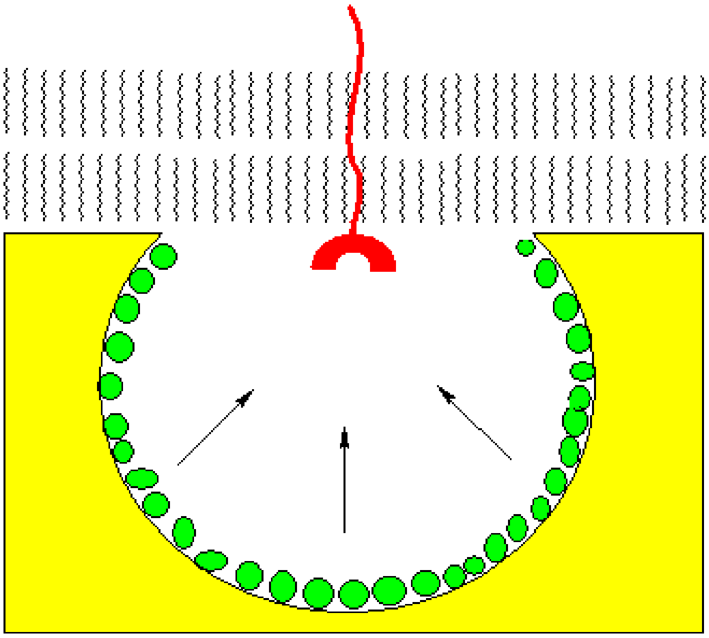

Fig. 6.1: Schematic of an agonist protein layer (green) adsorbed at the walls of a 820 nm diameter nano-cavity. A lipid bilayer spans the cavity opening and a second protein (red), which can interact with the first, is immobilised in the bilayer. Electrochemical release of the agonist protein should lead to an interaction with the lipid protein, after sufficient time has passed for diffusion from the cavity walls to the bilayer.

time of the agonist protein from the cavity walls, and the preservation of the activity of the agonist protein during the adsorption-desorption cycle.

This chapter describes the use of nano-cavities as substrates for fibrinogen adsorption, as a model system for the agonist described above. Dye labelled fibrinogen is available commercially at moderate cost. The selective modification of the top versus the interior surfaces of the substrate is demonstrated. The filling of the cavities and the adsorption of protein is determined by fluorescence microscopy. The desorption of the protein is probed to gain insights on the diffusion out of the cavity. This behavior is compared to that observed for planar gold surfaces, as described in Chapter 5.

6.2 Experimental

6.2.1 Apparatus

The kinetic and potential dependence of the Oregon Green labelled fibrinogen release was investigated by monitoring the intensity of the fluorescence using a Horiba Jobin Yvon HR800UV spectrometer using an Argon ion laser (488 nm calibrated using the silicon phonon and Rayleigh line) as the excitation wavelength focused through a 10x objective lens on the electrode surface. Typical acquisitions were 1 second and performed once to acquire a spectrum.

Raman spectroscopy was performed using a Horiba Jobin Yvon HR800UV spectrometer, calibrated as described above. The excitation wavelength was focused through a 10x objective lens on the electrode surface. Typical acquisitions were 30 seconds and performed three times to acquire a spectrum.

Fluorescence microscopy images were recorded with a confocal fluorescence microscope (LSM 50, Zeiss) using a 64x oil immersion objective (NA = 1.4). An argon ion laser provided 488 nm and 514 nm excitation wavelengths. The scanned images contain 512x512 pixels.

The protein was desorbed by applying a potential of -1.2 V to the nano-cavity array, which served as the working electrode in a three electrode cell. The working electrode was situated at the bottom of the cell and the counter and reference electrode were placed over the working electrode. A platinum mesh was employed as the counter electrode and the reference electrode was Ag/AgCl saturated in KCl. A CHI 660 electrochemical workstation was used to apply the desired potentials.

Electronic absorption spectra were measured on a Shimadzu 3500 UVVis/NIR spectrophotometer. Emission spectra were recorded on a Cary Eclipse Fluorescence spectrophotometer.

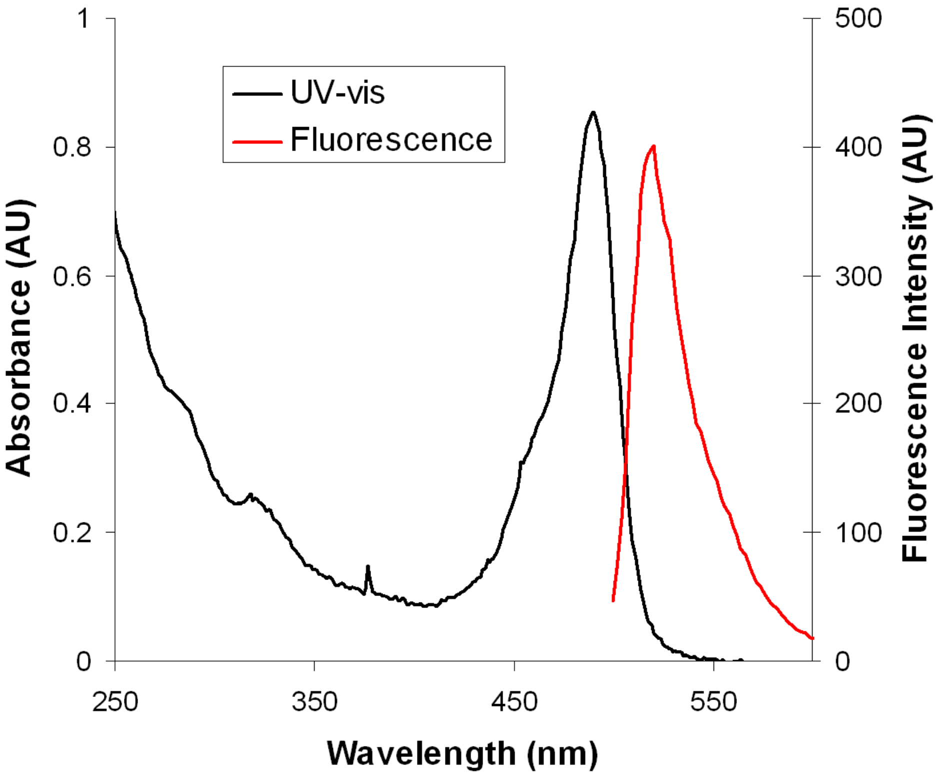

Fig. 6.2: UV-vis spectrum of 10 μM fluorescein in methanol and fluorescence spectrum of 32 μM fluorescein in methanol. The fluorescence spectrum was obtained using an excitation wavelength of 490 nm.

6.2.2 Materials

Fluorescein solutions (3 mM) were prepared in methanol. Oregon Green labelled fibrinogen solutions were prepared in 0.1 M $HNaCO_3$ (pH = 7.4). This salt also acted as the electrolyte in the electrochemical experiments. The nano-cavities were sonicated in solutions of fluorescein or Oregon Green Fibrinogen to fill the cavities. Nano-cavities were prepared as described in Chapter 2.

Figure 6.2 shows the UV-visible and fluorescence spectra of fluorescein in methanol. This figure shows that fluorescein has an absorbance maximum in the visible at 490 nm and a maximum in emission intensity at 520 nm.

6.3 Results and Discussion

6.3.1 Fluorescein filled nano-cavity arrays

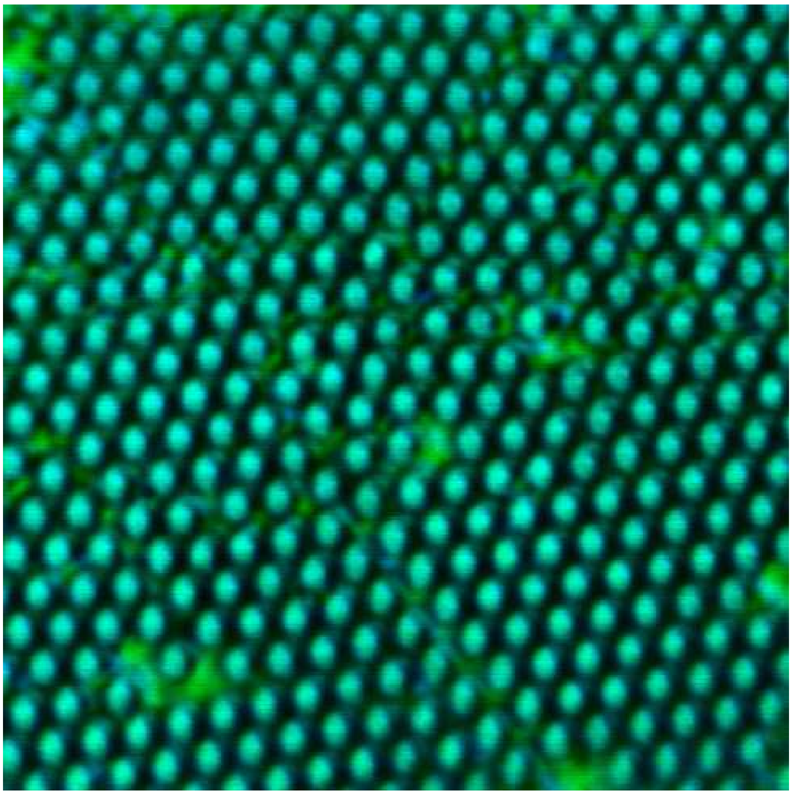

Fig. 6.3: Fluorescence microscopy image of fluorescein inside the nano-cavity arrays. The solvent used was methanol and the excitation wavelength was 514 nm. The image dimensions are 15 by 15 μm.

The use of arrays of nano-particles[216] or nano-holes[215] as fluorescent enhancing platforms has been demonstrated in the literature. Nano-cavities may provide fluorescent enhancement, due to the localised surface plasmons that are a feature of these substrates. A key objective of this chapter is to probe the adsorption and electrochemically controlled release of fibrinogen using fluorescence spectroscopy at the nano-cavity arrays. This can potentially be achieved using the dye labelled fibrinogen described in the last chapter, Oregon Green Fibrinogen. However, investigation of dye (i.e no bound protein) filled cavities should give information on the characteristics of the intensity, e.g. strength and excitation wavelength dependence.

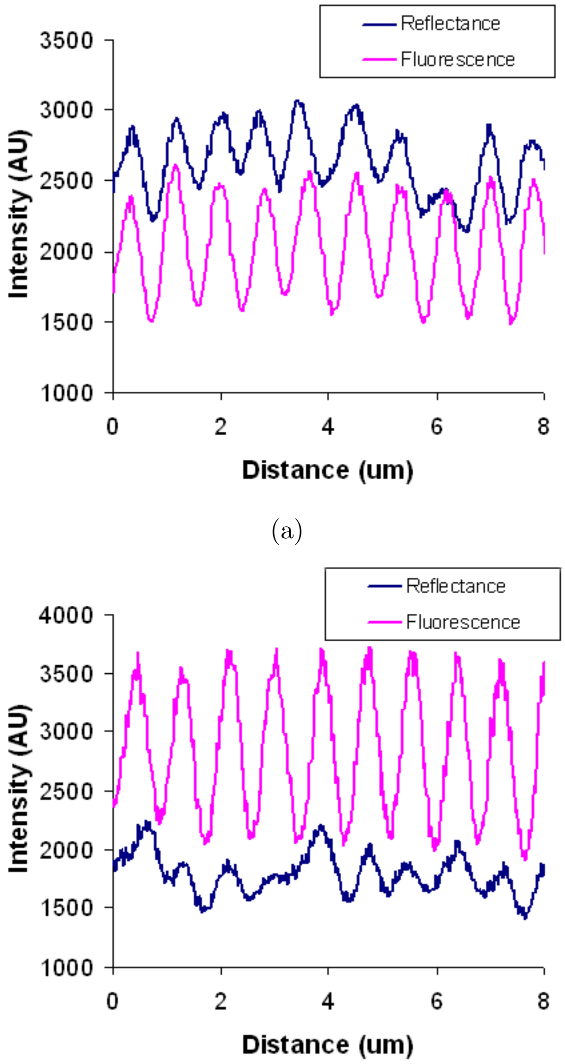

(a)

(b)

Fig. 6.4: Fluorescence and reflectance profiles using an excitation wavelength of 514 nm for (a) methanol filled cavities and (b) fluorescein filled cavities.

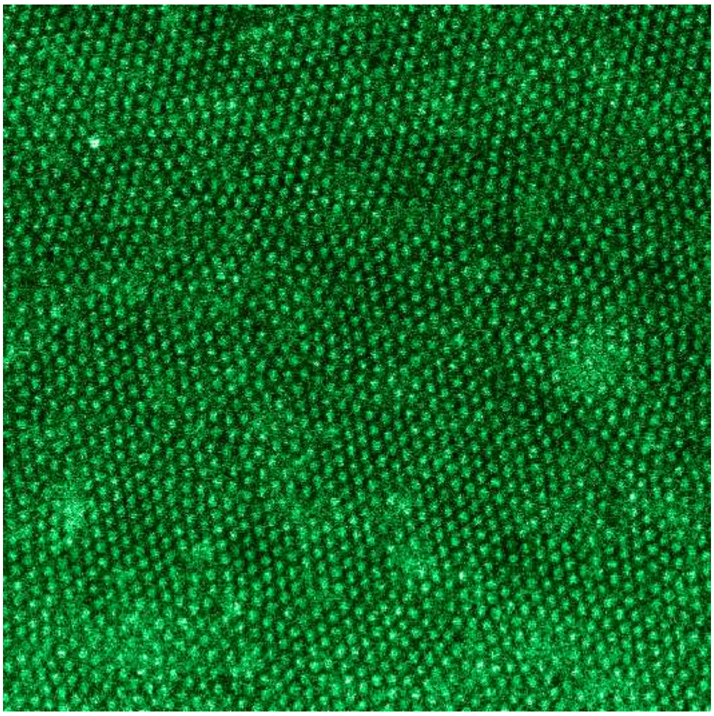

Fig. 6.5: Fluorescence microscopy image of fluorescein inside the nano-cavity arrays. The solvent used was methanol and the excitation wavelength was 488 nm. The image dimensions are 38 by 38 μm.

Figure 6.3 shows a fluorescence microscopy image of fluorescein in solution filled nano-cavity arrays. Sonication for one hour was required to fill the cavities, which were then washed with Milli-Q water. This figure clearly shows the nano-cavities but is a combination of both reflectance and fluorescence signals. It should be noted that it is possible to resolve the cavities from the reflectance signal alone, i.e. in the absence of any fluorescent dye, the cavities can still be seen. In the images presented here, the fluorescence signal is coloured green and the reflectance is coloured blue. Figure 6.3 is a mix of the two colours, but is primarily green, which suggests that the fluorescence signal is dominant.

The reflectance and fluorescence signals can be separated, and sent to different detectors, by a judicious choice of filters and the intensity of each signal can be compared. This is achieved by splitting the signal and using two detectors to monitor the reflectance and the fluorescence. If, for example, the excitation wavelength is 488 nm, the reflectance can be measured by using a 420 nm long pass filter, while the fluorescence can be measured by using a 505 nm long pass filter. Figure 6.4 shows the distance-intensity profile for both the reflectance and fluorescence signals at cavities with and without the dye, measured using an excitation wavelength of 514 nm. This figure shows that in the absence of dye the ‘fluorescence’ signal is approximately equal to that seen for the reflectance. This is likely to be due to an instrumentation problem, whereby the fluorescence filters do not effectively screen the reflectance. This problem is greatest when using the 514 nm laser line, but is considerably less at the 488 nm line. However, in the presence of the dye the fluorescence signal is much greater than the reflectance signal. The amplitude of the fluorescence signal on passing through the cavity region is also enhanced compared to that seen for methanol filled cavities. This is clearly due the presence of the fluorophore emission, which adds to the ‘fluorescence’ signal observed at the methanol filled cavities, by approximately 600 counts. There appears to be approximately 9 cavities in the 8 μm profile shown in the figure, which would correspond to a cavity diameter of approximately 800 nm, which is in close agreement with the SEM studies presented in Chapter 2. This suggests that the polystyrene spheres are close packed, as their diameter is 820 nm. However, some defective areas are also visible, which are attributed to domain boundaries between close packed areas.

The effect of varying the excitation wavelength has also been explored. Figure 6.5 shows a fluorescence microscopy image of fluorescein filled nano-cavities using an excitation wavelength of 488 nm. This wavelength is preferred to 514 nm as the issues with reflected light in the fluorescence channel are considerably less. In this and all further figures the reflectance and fluorescence signals have been separated as described above. However, only the fluorescence signal will be shown in the interest of clarity. Figure 6.5 shows that the cavities can also be observed at this wavelength, but the image is generally less intense than that seen when using an excitation wavelength of 514 nm. As shown in Figure 6.2, 488 nm is a better match for the maximum fluorescein absorbance than 514 nm. This effect may be due to a greater resonance of the 514 nm excitation light with the surface plasmon band of the substrate or to the greater reflectance background observed when using 514 nm. The reflectance background is significantly less when using 488 nm as an excitation source and this wavelength was primarily used for the protein studies described later.

6.3.2 Selective modification of nano-cavity arrays with alkanethiols

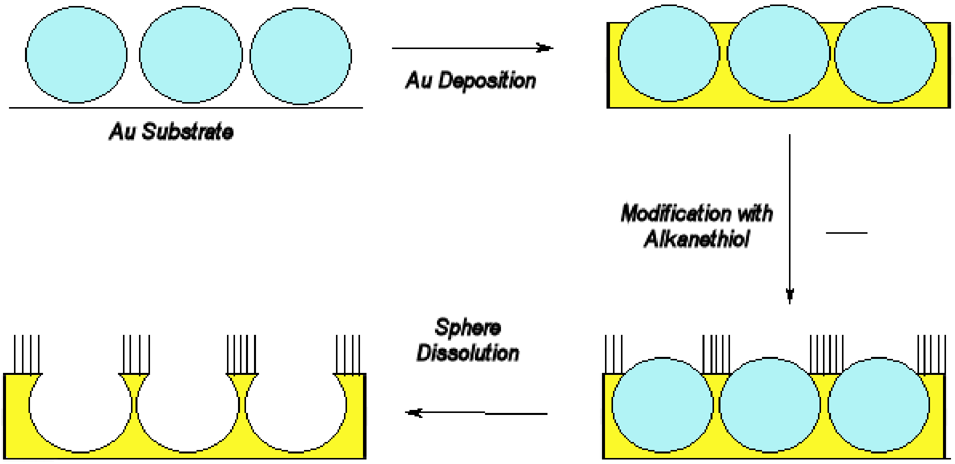

Fig. 6.6: Schematic (not drawn to scale for clarity) of nano-cavities selectively modified with an alkanethiol layer.

A key objective of this work is the selective modification of the nano-cavity arrays. In particular, the modification of the non-cavity regions is attractive, as this would facilitate studies of the cavity plasmons only. The gold ridges between cavities and any potential defects in the arrays could be coated with a blocking layer, leaving only the cavities as active sites on the substrate. Assembly of any blocking layer would have to take place before the dissolution of the polystyrene spheres, as indicated in Figure 6.6. This figure shows the stepwise modification of the gold substrate with the polystyrene spheres followed by the deposition of gold around the spheres as described in Chapter 2. The substrate is then exposed to a solution of the relevant alkanethiol, which can form a layer only on the top surface. The subsequent removal of the spheres should leave the substrate selectively modified and the internal regions of the cavities available for further modification.

To achieve this selective modification, a C_9SH layer was formed on the nano-cavities before dissolving the polystyrene spheres. The Raman spectra of the substrate before and after this dissolution process is shown in Figure 6.7. The green curve in this figure shows the spectrum before the sphere dissolution and is dominated by the polystyrene bands.[270] Both aromatic and aliphatic

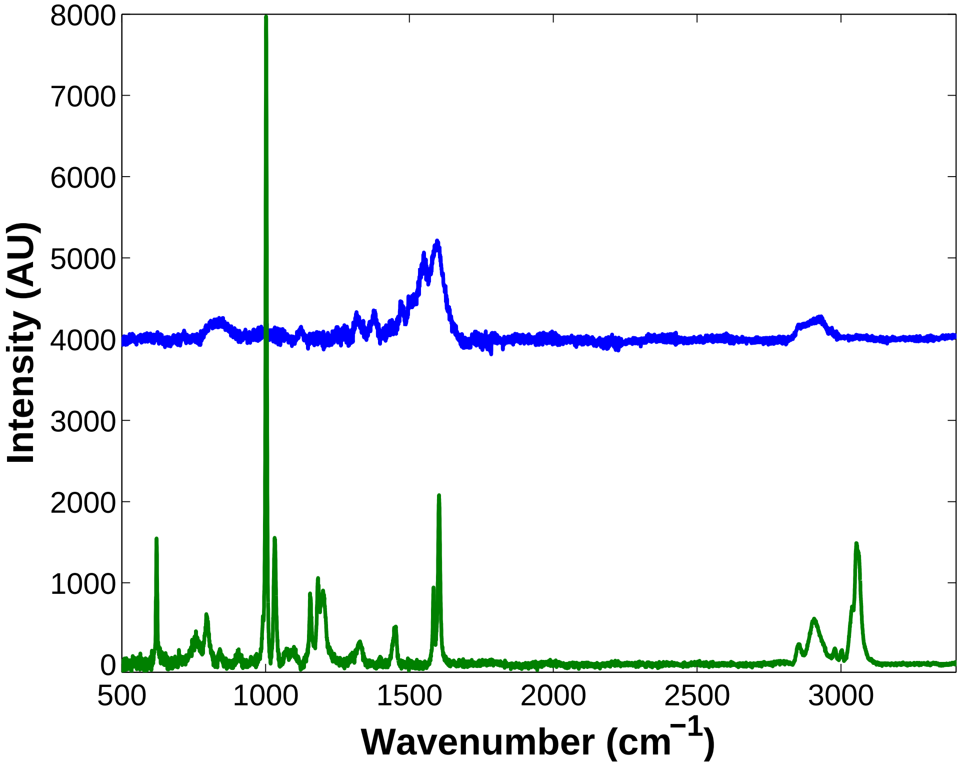

Fig. 6.7: Raman spectra of nano-cavity arrays treated with 1-nonanethiol before (green) and after (blue) polystyrene sphere dissolution.

stretching can be seen either side of 3000 cm^{-1}. The other main peaks are attributable to the aromatic C-H deformation observed at 1001 cm^{-1} and at 1200 cm^{-1} and aromatic C=C stretching seen at 1602 cm^{-1}. The peak at 621 cm^{-1} can be attributed to the aromatic ring deformations. There are no signals attributable to alkanethiol modes present in this spectrum, but this can be rationalised by considering the significantly greater concentration of polystyrene at the surface.

The blue spectrum in Figure 6.7 shows the same sample as above without the polystyrene spheres (these are dissolved by sonication in THF for 1 hour). This spectrum has lost all of the characteristic bands of polystyrene, but bands attributable to alkanethiol moieties can be seen. The aromatic CH stretching above 3000 cm^{-1} is not observed, but stretching modes are observed at 2850-2950 cm^{-1} which is characteristic of aliphatic stretching. The aromatic C-H deformation bands at 1001 cm^{-1} and at 1200 cm^{-1} are completely lost, as is the aromatic ring deformation band at 621 cm^{-1}. Some weak CH$_2$ scissor vibrations are evident at 1470 cm^{-1}, whereas the band at 850 cm^{-1} can be attributed to C-S vibrations. It is difficult to assign the broad band seen at approximately 1590 cm^{-1}, but this may be a background peak attributable to the gold surface. However, as the characteristic polystyrene peaks have been lost, but bands attributable to straight chain alkanes are evident, it can be concluded that the sonication process in THF did not remove the adsorbed alkanethiol layer. As the only part of the gold surface not exposed to the alkanethiol solution is the internal cavity walls, it would appear that selective modification of the substrate is possible. In this case, a simple alkanethiol was chosen to modify the non-cavity regions but by extension, any molecule capable of forming a gold-sulphur bond could be used.

6.3.3 Fibrinogen filled cavities

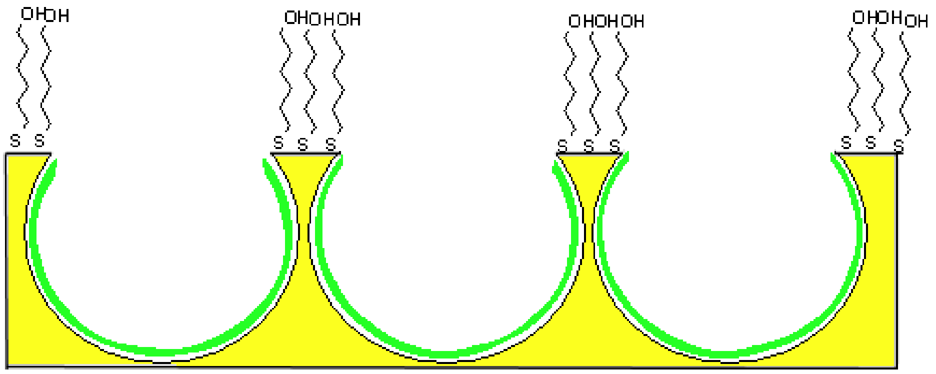

Fig. 6.8: Schematic (not drawn to scale for clarity) of nano-cavities modified with a protein layer (green) and a protein resistant layer on the interior and exterior of the cavities respectively.

The regio-selective modification of nano-cavities has been demonstrated in the last section. This feature is important when the modification of the cavity interior is desired and can be achieved by the use of a two step surface modification process. The last chapter has demonstrated the ability of fibrinogen to adsorb to planar gold surfaces and explored the effect of electrode potential on the adsorbed layer. The use of nano-structured substrates for protein adsorption is attractive for several reasons. The enhancement provided by such substrates could allow easier detection of the protein molecules, especially if fluorescence or Raman spectroscopy is employed. There are also possibilities for further development of this system such that the protein is released from the cavity to interact with a species outside the cavity or within a lipid bilayer spanning the cavity opening.

The adsorption of fibrinogen on planar substrates has been demonstrated in the last chapter. As this process was facile, the adsorption of fibrinogen should be possible on the gold nano-cavity substrates. However, the localisation of the fibrinogen adsorption in the interior of the cavities is important if the study of the protein release and transit time out of the cavity is to be achieved. Otherwise, the protein is released from both the edges of the cavities and from the cavity interior. Several spontaneously adsorbed or self-assembled monolayers have been shown to resist protein adsorption.[32,158] While the most effective are layers with ethylene glycol terminating groups, it has been shown

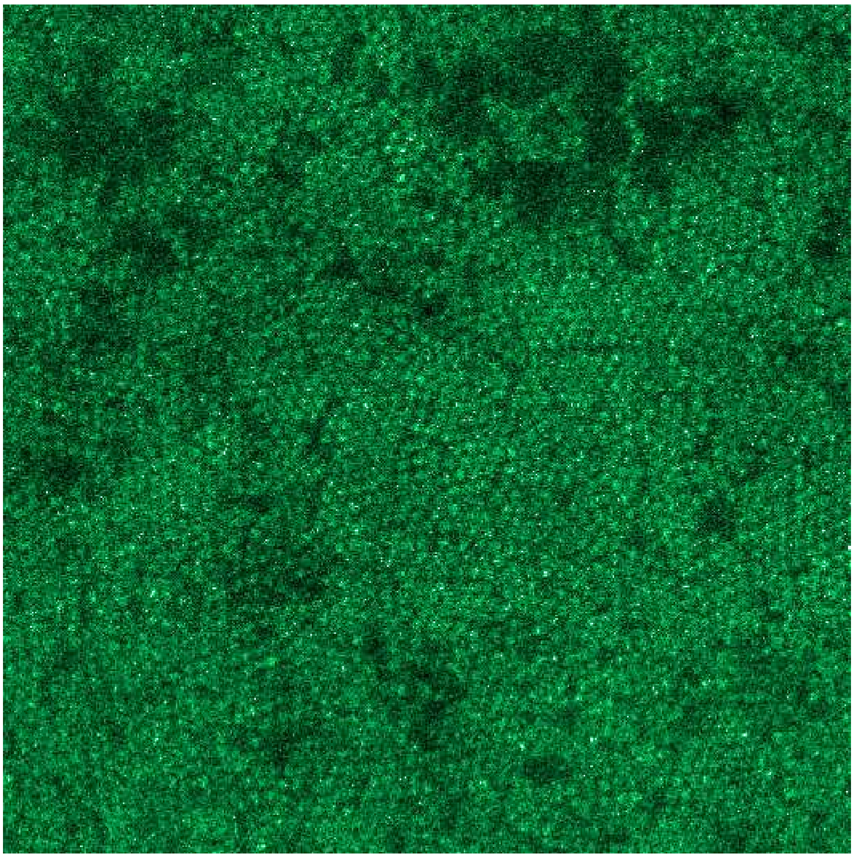

Fig. 6.9: Fluorescence microscopy image of Oregon Green Fibrinogen inside nano-cavity arrays, which are edge modified with $HS(CH_2)_6OH$. The excitation wavelength is 488 nm and the image dimensions are 47 μm by 47 μm.

that layers with hydroxyl terminating groups can limit fibrinogen adsorption to 30% of a full monolayer.[158] Therefore, the nano-cavity top surface was exposed to a solution of 1 mM $HS(CH_2)_6OH$ in ethanol before dissolution of the polystyrene spheres by sonication in THF. It has been previously shown that the sonication in THF does not remove a nonanethiol layer from the top surface of the substrate and although a different alkanethiol was employed here it is not expected that a change in alkanethiol would result in different behavior. The substrates were then sonicated in a solution of Oregon Green Fibrinogen to create a protein layer on the interior of the cavity (represented schematically in Figure 6.8). One hours sonication was assumed to be sufficient to fill the cavities. Chapter 5 probed the kinetics of adsorption of fibrinogen on planar gold and it was seen that this process is relatively fast on this timescale, i.e. the adsorption process is virtually complete after one hour.

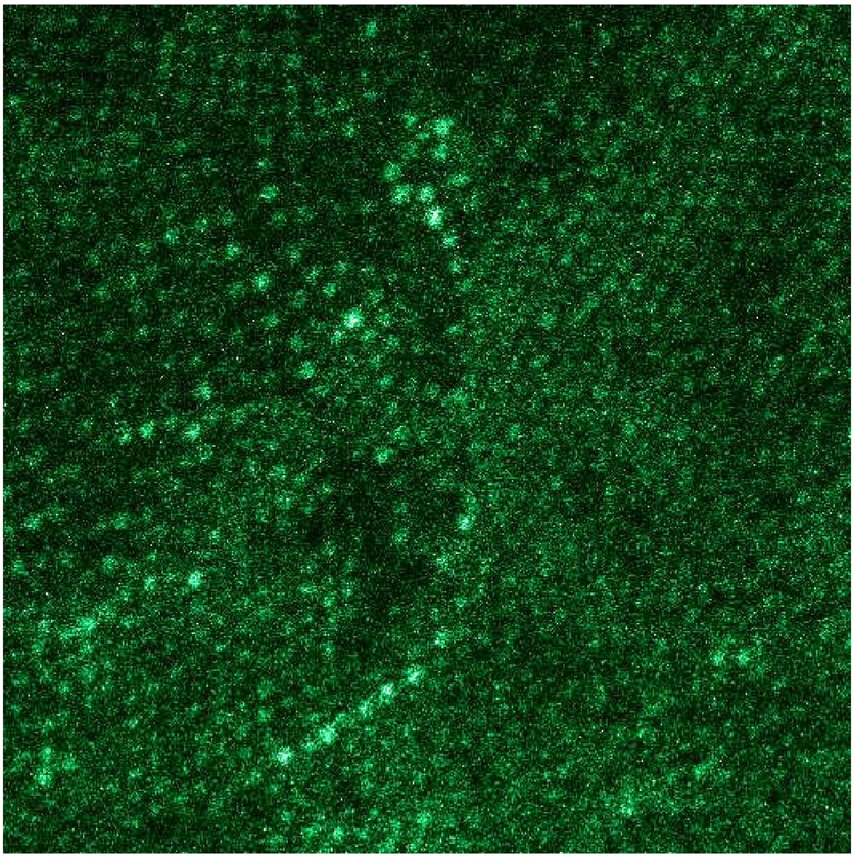

Fig. 6.10: Fluorescence microscopy image of Oregon Green Fibrinogen inside nano-cavity arrays, which are edge modified with $HS(CH_2)_6OH$. The excitation wavelength is 488 nm and the image dimensions are 28 μm by 28 μm.

The use of fluorescence microscopy to image the dye-labelled fibrinogen was described in the last chapter and the technique can be also used to monitor the protein inside the cavities. Figures 6.9 and 6.10 show two different nano-cavity substrates with Oregon Green Fibrinogen adsorbed inside the cavities using a 488 nm laser excitation source. Similar to the figures described above, the reflectance has been separated and only the fluorescence signal is shown. These figures show the nano-cavity array structure, which suggests that the incorporation of the protein inside the cavities has been successful. Significantly, the signal from areas where no cavities are observed (i.e. defects in the packing of the spheres before gold deposition) is dramatically reduced compared to the cavity areas. The fluorescent intensity for the cavity area is approximately 3500 counts, but for the non-cavity region the intensity is approximately 550 counts. This suggests that adsorption of the protein resistant layer on these

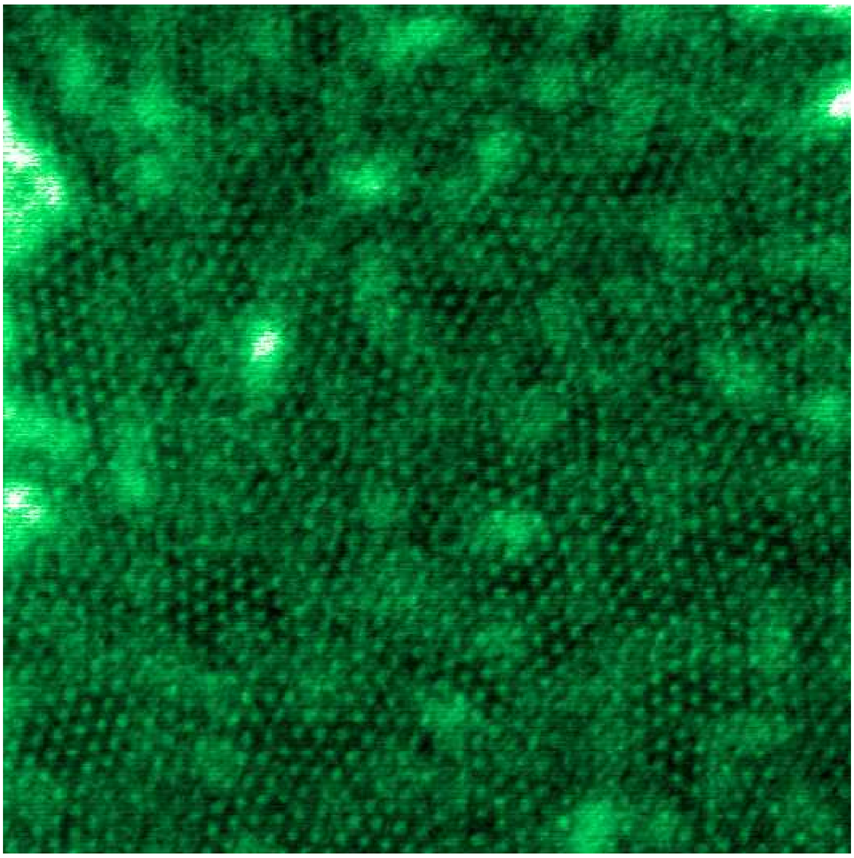

Fig. 6.11: Fluorescence microscopy image of Oregon Green Fibrinogen inside nano-cavity arrays, which are edge modified with $HS(CH_2)_6OH$. The excitation wavelength is 514 nm and the image dimensions are 32 μm by 32 μm.

defective areas has reduced the protein adsorption.

Figure 6.11 shows the nano-sphere arrays with Oregon Green Fibrinogen adsorbed inside the cavities at an excitation wavelength of 514 nm. As the Oregon Green dye is similar to fluorescein, 514 nm is a further away from the maximum absorbance of the Oregon Green dye than 488 nm. However, the fluorescence signal seen at this wavelength is significantly higher than that seen when using 488 nm as the excitation wavelength. This observation is consistent with the study using fluorescein filled cavities and is possibly due to a greater reflectance background at this wavelength.

The fluorescein filled cavities were more defined and substantially brighter compared to the protein filled cavities. This is due to the differences of concentration of fluorophore in the respective solutions. The fluorescein concentration was in the milli-molar range and the image was obtained by the trapping the solution inside the cavities. While fluorescein is expected to adsorb at the gold surface, the concentration in solution (3 mM) should be much greater than that at the surface. The Oregon Green Fibrinogen is surface active and is expected to form a layer at the gold surface, but is adsorbed from solutions in the low micro-molar range. This results in a greater concentration at the cavity walls compared to the solution. If the adsorption solution concentration is in the micro-molar range and the protein surface coverage is of the order of 6 x 10^{-13} mol.cm^{-2}, as determined in the last chapter, the fluorescence signal, based on the number of molecules present, from the surface should be an order of magnitude higher than that in solution. However, this calculation neglects surface quenching and plasmonic enhancement effects. In spite of these factors, which are difficult to estimate, the signal is likely to be dominated by the adsorbed protein species.

6.3.4 Effect of potential on fibrinogen at cavities

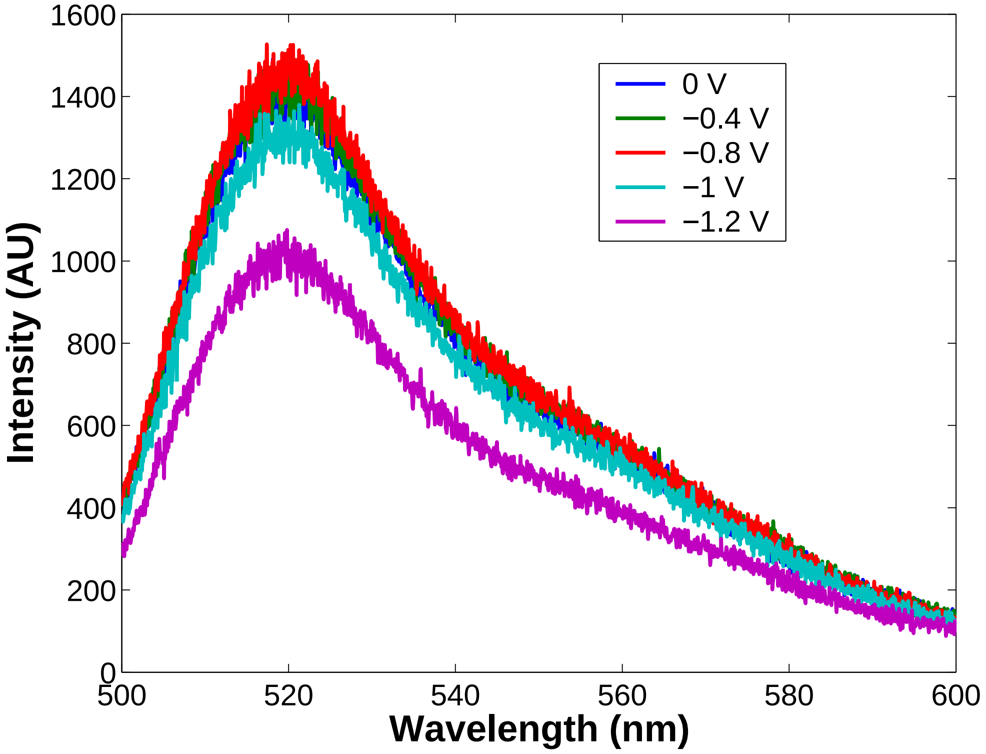

Fig. 6.12: Fluorescence spectra of an Oregon Green Fibrinogen layer deposited within gold nano-cavities held at progressively more negative potentials versus Ag/AgCl in aqueous solution with 0.1 M $NaHCO_3$ as the supporting electrolyte. The excitation wavelength is 488 nm and the spectra were obtained focused on the electrode surface using a confocal microscope. All the curves were stable with time, except the -1.2 V curve, which showed a decrease. In that case, the curve presented was obtained after 20 seconds polarisation.

The last section described the formation of Oregon Green Fibrinogen layers in the nano-cavity substrates. Therefore, the effect of electrode potential on the adsorbed layers can be explored, as in the last chapter, as the nano-cavities are a conducting substrate. Exploring the time dependence of the signal at potentials capable of desorbing the protein could give information on the diffusion off the cavity walls and out into solution. This is likely to be of a more complex nature than that seen at a planar gold surface.

Fibrinogen is negatively charged overall[164] and application of a negative potential leads to electrostatic repulsion and to protein desorption, as demonstrated in the last chapter. This should influence the fluorescence signal observed

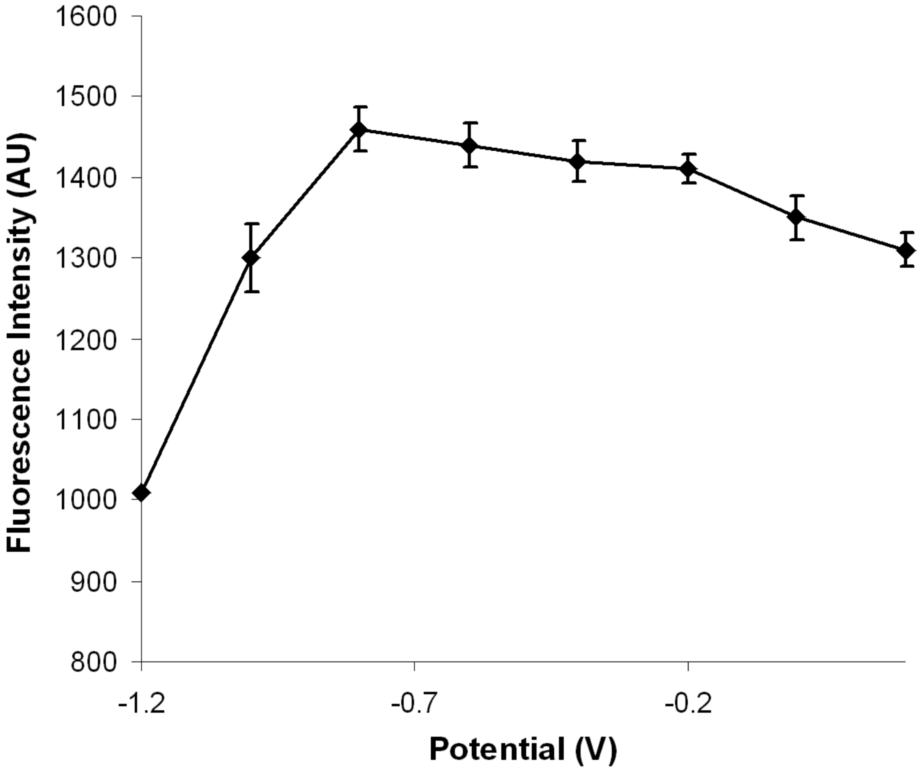

Fig. 6.13: Fluorescent intensity of Oregon Green layers as a function of potential versus Ag/AgCl at gold nano-cavity substrates. The excitation wavelength is 488 nm. The error bars are the standard deviations of three separate measurements but are not extended to the -1.2 V point as it is not stable over time.

from the surface and Figure 6.12 shows that the fluorescence spectra of Oregon Green Fibrinogen adsorbed at the nano-cavity substrate at various applied potentials. As previously described, a protein resistant layer was adsorbed on the cavity edges to localise protein adsorption inside the cavities. The fluorescence peak in these spectra shows broadly similar characteristics to that seen in the previous chapter for Oregon Green Fibrinogen at planar surfaces. However, the difference in intensity of the spectra obtained from the two substrates is very significant. The laser power intensity used at the nano-cavity substrate was of the order of 1 x 10^4 less than that used for the planar surfaces, but the resulting fluorescence intensities in the spectra are similar. The spectra seen at the planar surfaces were approximately 5000 counts, but at the nano-cavity substrates the same fluorescence intensity is achieved using laser power reduced by a factor of 1 x 10^4. This suggests that the nano-cavity substrate can enhance the fluorescence intensity of the dye considerably. After the intensities have been matched and surface area normalisation is carried out the enhancement factor is approximately 500 compared to the planar surface. This is similar, but somewhat larger, to the fluorescent enhancement reported by Brolo and co-workers for oxazine at nanohole arrays.[215] However, it should be noted that the effect of surface quenching has been neglected in this calculation.

The dependence of the fluorescence spectra on applied potential can be seen in Figure 6.12, while Figure 6.13 shows a plot of fluorescence intensity versus potential. These figures show that the fluorescence intensity increases slightly as the electrode potential changes from OCP (approximately 0.2 V) to -0.9 V. This behavior is consistent with that observed at the planar gold surfaces in the last chapter. However, the fluorescence intensity decreases at the nano-cavity substrates when potentials more negative than -0.9 V are applied, which is in marked contrast to the behavior of the dye-labelled protein at the planar surface. At the planar surface the fluorescence intensity increases five fold on moving from a potential of -0.6 V to -1.2 V. The decrease in the fluorescence signal seen at the nano-cavities over this potential range is less extreme. It should be noted that the spectra were all time independent except when the potential was biased to -1.2 V. This would indicate that kinetic effects do not influence the signal until this potential is reached. The time dependence of the signal at 1.2 V is discussed in the next section.

The reason for this difference between the planar and nano-cavity substrates is likely to be related to the difference between the substrate structure. Both surfaces are expected to quench the fluorescence when the protein is closely bound to the surface. However, the nano-cavity substrate can also enhance the signal and this enhancement is not expected to be uniform throughout the cavity.[211] A further difference is the variation of diffusion out of the cavity and away from a planar surface. Bartlett has shown that the enhancement at these type of cavities can be greatest away from the cavity walls.[211] Therefore, it is possible that the decrease in fluorescence observed in Figure 6.13 is due to protein exiting the cavity and leaving the enhancement area altogether.

6.3.5 Time dependence of fluorescence signal

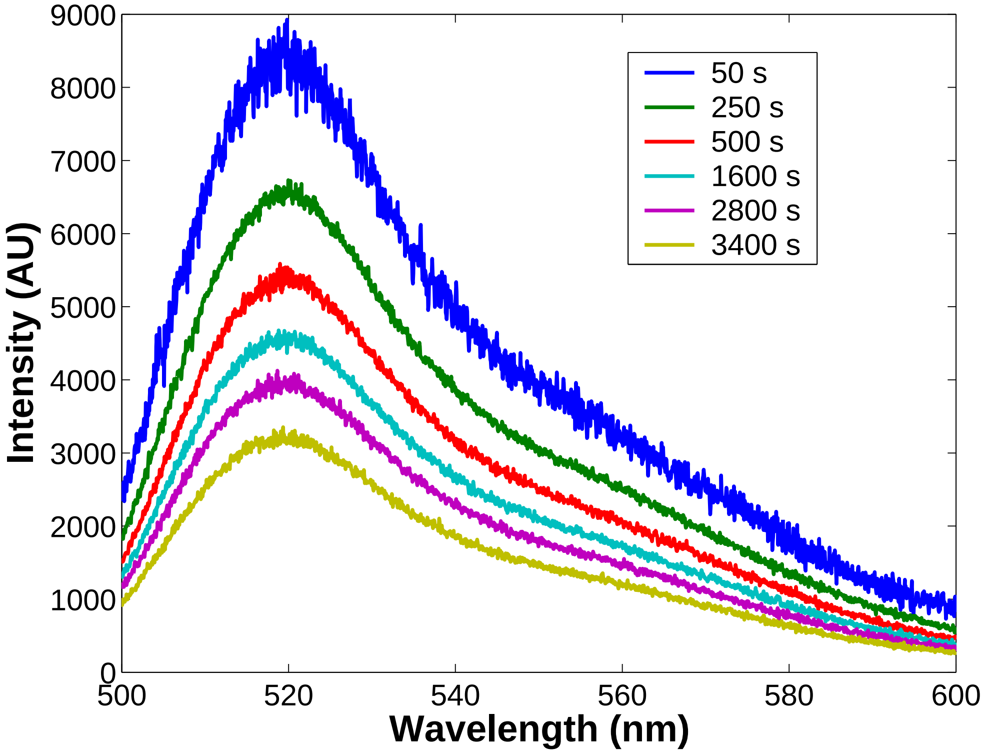

Fig. 6.14: Fluorescence spectrum intensity at various times of an Oregon Green Fibrinogen layer on a gold nano-cavity substrate at a potential of -1.2 V versus Ag/AgCl in aqueous solution with 0.1 M $NaHCO_3$ as the supporting electrolyte. The excitation wavelength is 488 nm. The spectra were obtained focused on the electrode surface using a confocal microscope.

The potential dependent fluorescent signal of Oregon Green Fibrinogen adsorbed in gold nano-cavities was presented in the last section and was found to be in sharp contrast to the behavior seen for the same protein at planar surfaces. The time dependence of the fluorescence signal at -1.2 V could give an idea into the differences in diffusion away from the two substrates. Figure 6.14 shows the fluorescence spectrum of Oregon Green Fibrinogen adsorbed at the nano-cavities, where a protein resistant layer was adsorbed on the cavity edges to localise protein adsorption inside the cavities as previously described. This figure shows that the intensity of the signal decreases with time, which is consistent with the protein diffusing out of the cavity and out of the confocal laser volume (approximately 100-200 μm in the z direction). This behavior was also observed at the planar surface in the previous chapter.

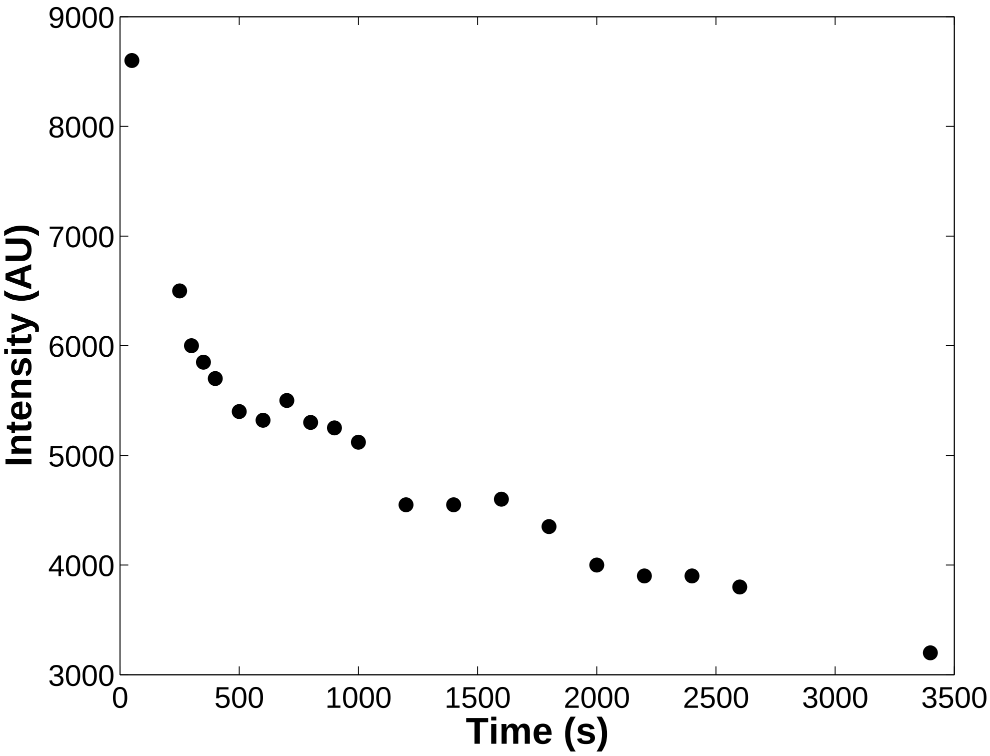

Fig. 6.15: Fluorescence intensity (at λ_{max}) of an Oregon Green Fibrinogen layer at a gold nano-cavity substrate at -1.2 V versus Ag/AgCl as a function of time in aqueous solution with 0.1 M $NaHCO_3$ as the supporting electrolyte. The excitation wavelength is 488 nm.

Figure 6.15 shows the fluorescence intensity, at λ_{max}, as a function of time. This plot is broadly similar to that seen for the same experiment using planar gold as the substrate. However, one significant difference can be seen in the intensity behavior over the first 200-250 seconds of the plot. At the planar surface, the fluorescence intensity was seen to rise over this time scale and this was attributed to the decrease in quenching of the dye by close proximity to the surface. Significantly, no such increase is observed in Figure 6.15. This suggests that the decrease in signal is due to the protein leaving the confocal volume only, i.e., surface quenching effects are undetected.

The decrease in the fluorescence signal is likely to involve diffusion of the dye out of the cavities and away from the electrode surface. As seen in Chapter 5, the change in intensity over time (dI/dt) can be equated with the flux of the protein out of the confocal laser volume. The flux (J) in or out of a region can

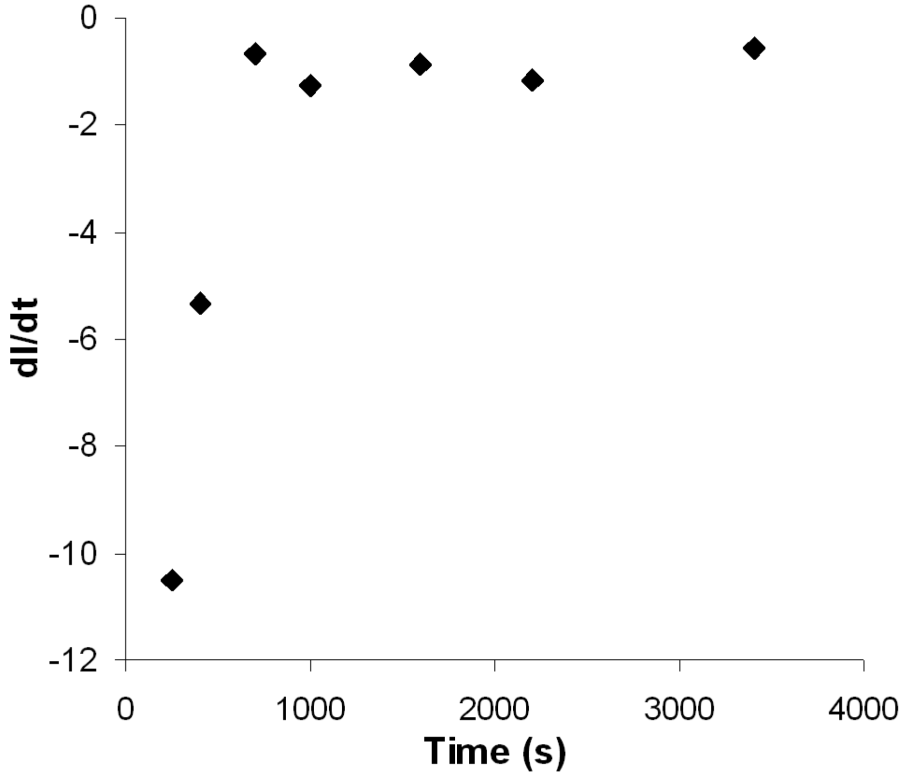

Fig. 6.16: Change in fluorescence intensity with time, dI/dt, for a fibrinogen coated gold nano-cavity array electrode at -1.2 V versus Ag/AgCl as a function of time.

be characterised by Fick's first law, which states that the flux is proportional to the concentration gradient at the interface, which has been shown to be dependent on the inverse of the square root of time:[265]

$$J(x=0,t) = D\frac{\partial C}{\partial x} = \frac{DC}{\sqrt{D\pi t}} \tag{6.1}$$

where D is the diffusion co-efficient (the diffusion co-efficient of fibrinogen has been reported[266] as 2.24 x 10^{-7} $cm^2.s^{-1}$) and C is the concentration at the surface.

Figure 6.16 shows dI/dt as a function of time. It can be seen that the change in intensity is initially fast and that dI/dt decreases with time but does not reach zero. If dI/dt depends on diffusion out of the confocal laser volume then

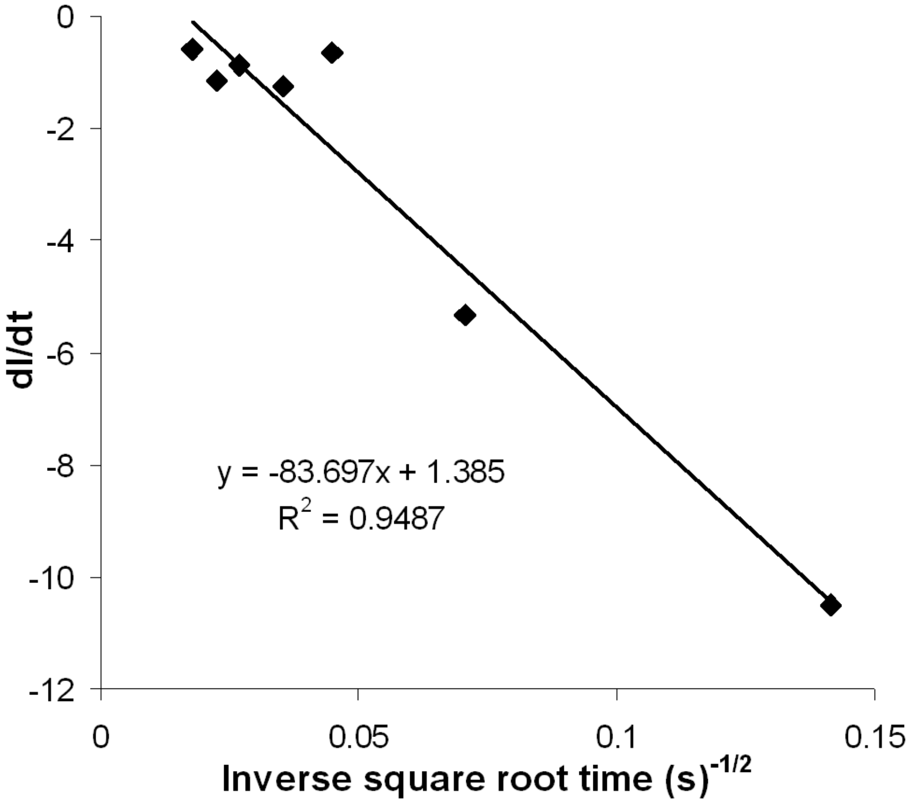

Fig. 6.17: Variation of dI/dt for a fibrinogen coated gold nano-cavity array electrode at -1.2 V versus Ag/AgCl with the inverse square root of time.

a plot of dI/dt versus $t^{-1/2}$ should be linear. Figure 6.17 shows such a plot and it can be seen that the data are approximately linear ($R^2 = 0.95$). This suggests the decrease in the fluorescent signal is related to diffusion.

The confocal volume is significantly larger in the z direction (100-200 μm) than the cavity dimensions (820 nm diameter). However, the diffusion process appears much slower than that seen at the planar surface, which indicates that the presence of the cavities influences the signal. At the planar surface, the fluorescent intensity had fallen to below 10% of the initial value after 2000 seconds. At the nano-cavity substrate the fluorescence intensity is approximately 45% of the initial value at the same time. Even after 3400 seconds the intensity of the signal had fallen to only ~30% of the initial signal. This indicates that the diffusion away from the cavities is slower than that seen at the planar surface. Once the protein moves out of the cavity the diffusion away from the patterned surface should be the same as that seen at the planar surface, therefore it would appear that the limiting step is the diffusion of the protein out of the cavity. This result is unsurprising considering that the cavity opening is approximately 600 nm, while the fibrinogen molecule is approximately 50 nm in length.

The slope of the plot seen in Figure 6.17 is -84, which should correspond to $DC/\sqrt{D\pi}$ according to Equation 5.11. However, the use of fluorescence intensity instead of concentration is this study must be accounted for. This was described in Chapter 5, where if $I = kC$, k can be estimated as 3.49 x 10^{12}. This means that the slope can be related to the diffusion co-efficient by $slope = DkC/\sqrt{D\pi}$. This yields a diffusion co-efficient of 0.117 cm.s^{-1}, which is clearly too large compared to the literature value of 2.24 x 10^{-7} cm^2.s^{-1}.[266]. However, a larger value (0.19 cm.s^{-1}) was obtained using this method at the planar surface, which indicates that the diffusion away from the nano-cavity surface is slower than that seen at the planar surface, by approximately 20 %. This is consistent with the diffusion out of the cavity being the rate determining step in the process.

6.3.6 Raman of fibrinogen at cavities

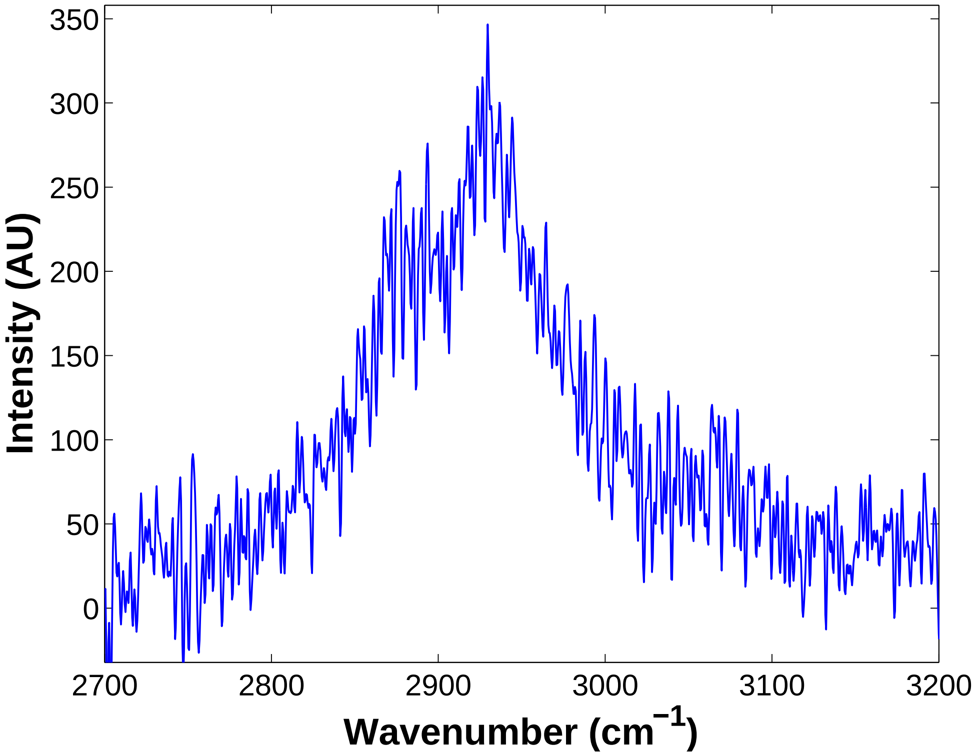

Fig. 6.18: Raman spectrum of the CH stretching region of a fibrinogen layer adsorbed at a gold nano-cavity substrate. The excitation wavelength was 514 nm. A reference spectrum of solid fibrinogen can be seen in Chapter 5.

The nano-cavity substrates have been shown to be interesting platforms for the binding of proteins. In particular, there appears to be significant enhancement of the fluorescent signal of a dye labelled protein. This enhancement is attributable to the presence of plasmons confined inside the cavity which augment the electric field experienced by the dye leading to a brighter emission. While the enhancement of the fluorescent signal could find applications in areas such as sensing, the use of these confined plasmons to enhance Raman signals is much more common. This is due to the greater structural information that Raman spectroscopy can provide compared to fluorescence spectroscopy. Bartlett has reported an enhancement factor of 10^7 for a benzene thiol layer adsorbed at similar nano-cavity substrates.[202] Therefore, the investigation of fibrinogen (which is not dye labelled) adsorbed at these substrates may provide an enhanced Raman signal.

Figure 6.18 shows the CH stretching region of a Raman spectrum obtained at the nano-cavity substrates in the presence of adsorbed fibrinogen. The excitation wavelength chosen was 514 nm. Unfortunately, the only peak observable in the spectrum was that of the aliphatic CH stretching. This is unsurprising considering that this band is the most intense observed in the spectrum of solid fibrinogen (shown in Chapter 5). The band appears at 2927 cm^{-1} in the solid spectrum and Figure 6.18 shows that it appears at a very similar value (2930 cm^{-1}) when adsorbed at the nano-cavities. There are no further peaks attributable to protein bands in the spectrum and this is perhaps due to the rather weak protein scatter. As an example, the amide I region is approximately 25% as intense as the CH stretching in the solid fibrinogen spectrum. This would equate to an intensity of 75 AU on Figure 6.18, which would make such a peak extremely hard to distinguish. However, as no Raman signals were observable off planar gold surfaces with monolayer fibrinogen coverage it is clear that some modest enhancement is occurring. This however, is certainly lower than the enhancement reported by Bartlett.[202] Our group has also recently detected a 10^7 increase in SERS signal for a ruthenium dye solution present in the nano-cavities. It is also clear from Figure 6.7 that the alkanethiol molecules adsorbed at the edges can be detected using SERS. It has been suggested[211] that for thick cavities, i.e. where the cavity height is greater than the sphere radius, the largest enhancement is observed away from the cavity walls. This may indicate that the signal from the adsorbed protein is not significantly enhanced, as compared to molecules present in the cavities in the solution phase, such as the ruthenium dye described above. However, the lack of enhancement compared to Bartlett's values, which were obtained for adsorbed benzenethiol layers, suggests that the system described here requires further optimisation for Raman studies. This optimisation would include probing the frequency of the surface plasmon band of the nano-cavity substrates.

The fluorescein filled cavities have also been investigated using Raman spectroscopy. In this case, the excitation wavelength was chosen as 633 nm to avoid the fluorescein absorption band. However, no Raman signal was evident from the substrate at this wavelength, which would suggest that the plasmon absorbance lies below 600 nm. This would also demonstrate that some enhancement is seen for the protein Raman spectrum obtained using 514 nm as an excitation wavelength. Bartlett has investigated the position of the surface plasmon band as a function of film thickness for 600 nm diameter cavities[202] and has found that the band shifts towards longer wavelengths, such as 500-600 nm, as the film thickness increases. However, some uncertainty exists over the exact maximum of the surface plasmon band in such studies as they are typically broad bands.

6.4 Conclusion

The incorporation of nanoscale features such as nanoparticles or nano-cavities has attracted a large amount of interest in recent years.[189, 190, 191, 208, 217, 206, 211] This is due to the interesting properties that these structures can impart to an interface compared to an unmodified substrate. While much work has been carried out on the modification of nanoparticles with molecular layers,[213, 271, 272] the use of nano-cavity arrays as substrates for molecular adsorption is relatively unexplored,[202, 269, 273] in spite of the interesting and beneficial features of these systems.

This chapter has described the use of gold nano-cavity structures as substrates for adsorption of fibrinogen. It has been demonstrated that these substrates can be investigated in a number of non-destructive ways, such as fluorescence microscopy and Raman spectroscopy. These spectroscopic techniques are ideally suited to these substrates as they can enhance both fluorescent and Raman signals and this offers a key advantage over planar surfaces, explored in Chapter 5, for sensing and even perhaps structural characterisation of layers. The Raman enhancement for this system was modest and no structural information could be obtained using the conditions explored in this study, although it is possible that optimisation of the system could lead to acquisition of such data. However, the fluorescence signal showed significant enhancement compared to the planar gold surface and an enhancement factor of approximately 500 was suggested.

A second key advantage of the nano-cavity arrays as substrates for molecular adsorption is the ease with which they can be selectively modified. This chapter has shown that by exploiting the blocking properties of the polystyrene spheres the exterior of the nano-cavities can be modified, which localises any further adsorption into the actual cavity. This selective modification gives greater control over which molecules are enhanced and by a judicious choice of layers only molecules inside the cavity can be detected. The adsorption of fibrinogen inside the cavities has been demonstrated by fluorescence microscopy and Raman spectroscopy, which suggests that the protein is indeed localised inside the cavity. This was achieved by the adsorption of a protein resistant layer on the cavity exterior. The system could be improved in two ways. Firstly, the use of a SAM with ethylene glycol terminating groups would be completely protein resistant.[158] Secondly, a layer that could protect the protein structure from the destructive effects of the gold surface could be assembled inside the cavity. This would ensure the structural integrity of the adsorbed and desorbed protein, something that Chapter 5 suggested was compromised by the immobilisation of the protein on the surface.

The effect of application of negative potential to the protein modified nano-cavity arrays was investigated and compared to that seen for planar surfaces, which were described in Chapter 5. The fluorescence intensity was seen to decrease as the potential applied became more negative and co-incided with the potentials needed for electrostatic repulsion of the negatively charged protein from the surface. This may be attributable to a decrease in the plasmonic enhancement experienced by the protein as it exits the cavity. The time dependence of the signal showed that the diffusion of the molecules out of the confocal laser volume was slower than that seen for planar surfaces, which reflects the complex geometry of the cavities. Diffusion out of the cavities was proposed as the rate determining step in the process and it seems likely that a significant amount of the protein does not leave the cavity in the timescale investigated.

In conclusion, the nano-cavities have been shown to be attractive platforms for surface modification. They allow site specific adsorption to a reasonable degree. Furthermore, this site specific adsorption allows selective enhancement of non-destructive signals such as Raman and fluorescence spectroscopies. This renders these substrates advantageous for several applications such as sensing and the creation of supramolecular systems.

Chapter 7

Conclusions and future work

The focus of this thesis has been the creation of functional surfaces using the adsorption of organic molecules, typically cyclodextrin (CD), alkanethiol or protein molecules. These systems could be considered as primitive molecular wires, or resisters. Alternatively, a primary motivation for the study of proteins at interfaces is the possibility of creating systems capable of replicating biological systems, at least to some degree. Structural changes in proteins would be significantly easier to detect in such similar, but simpler, systems.

Chapter 3 has described the use of cyclodextrin layers for molecular recognition purposes and it was found that co-adsorption of alkanethiol molecules appears to have a significant influence on the CD orientation. The thermodynamics of binding of a cobalt metal complex guest were determined and an estimate of the rate of electron transfer from the metal center to the electrode was presented. Future work could include the use of CD dimers to extend this 'molecular wire' further out into solution. This could be possible as the cobalt guest has two docking ligands, at opposite ends of the molecule. The insights on the thermodynamics of binding and kinetics of electron transfer given in Chapter 3 need to be carefully considered in designing such extended systems.

Chapter 4 has described the use of CD layers in novel Hg-Pt tunnelling junctions. It was found that the nature of the CD guest had an influence on the magnitude of the junction superexchange current. A potential dependent current was observed when an electrochemically active guest was included in the cavity. However, the mechanism of electron transfer for this process is uncertain. Future work could involve probing the nature of this electron transport. The variation of the signal with temperature could provide some insights into the dominant mechanism. Electron hopping, for example, is expected to show Arrhenius type behavior.

Chapter 5 has described the adsorption of fibrinogen layers at planar gold surfaces. These layers have been characterised using AFM and, in the case of Oregon Green labelled fibrinogen, confocal microscopy. The desorption of these layers by application of a potential of -1.2 V has been investigated using both capacitance and fluorescence measurements. This study has shown that the protein can be desorbed at this potential, but SDS-PAGE gel electrophoresis indicates that the protein is significantly fragmented by the adsorption-desorption process. This may be of interest in the sterilisation of surgical instruments and future work might investigate the effect of negative potential on other more dangerous proteins adsorbed at surfaces such as stainless steel.

Chapter 6 has described the localisation of Oregon Green labelled fibrinogen at nano-cavity assemblies. The release of the protein from the cavities has been monitored using confocal fluorescence microscopy and it has been shown to be slower than that seen at planar surfaces. A significant enhancement is observed in the fluorescence signal seen at the nano-cavities compared to the planar surfaces and further work might involve determining the real enhancement by comparing to a similar number of molecules in solution. Future work could also involve the release of a protein capable of interacting with a molecule fixed at the cavity entrance (e.g. a membrane protein bound to a bi-layer spanning the cavity opening). This concept was introduced in the introduction to Chapter 6, however, the most immediate concern is the activity of the released protein. It is clear from Chapter 5 that the fibrinogen is structurally compromised by the time it is released from the gold surface, but modification of the interior of the cavity with a protecting monolayer would appear to be one solution to this problem. Determining the optimum conditions for releasing active protein is clearly a challenge for the future.

References

[1] Rubinstein, I., Steinerg, S., Tor, Y., Shanzer, A., and Sagiv, J. *Nature* **332**, 426 (1988).

[2] Kaifer, A. E. and Gomez-Kaifer, M. *Supramolecular Electrochemistry.* Wiley-VCH, London, (1999).

[3] Chidsey, C. E., Bertozzi, C. R., Putvinski, T. M., and Mujsce, A. M. *J. Am. Chem. Soc.* **112**, 4301 (1990).

[4] Finklea, H. O. and Hanshew, D. W. *J. Am. Chem. Soc.* **114**, 3173 (1992).

[5] Forster, R. J., Keyes, T. E., and Vos, J. G. *Interfacial Supramolecular Assemblies.* Wiley, Chichester, (2003).

[6] Lindsay, S. *Devices based on molecular electronics.* US patent 6673424, (2004).

[7] Tour, J. M. *Molecular Electronics.* World Scientific, New Jersey, (2003).

[8] Harada, A. *Acc. Chem. Res.* **34**, 456 (2001).

[9] Wenz, G. *Angew. Chem. Int. Ed.* **33**, 803 (1994).

[10] Connors, K. A. *Chem. Rev.* **97**, 1325 (1997).

[11] Akkerman, H. B. and de Boer, B. *J. Phys.: Condens. Matter* **20**, 1 (2008).

[12] McCreery, R. L. *Chem. Mater.* **16**, 4477 (2004).

[13] Brash, J. L. and Horbett, T. A. *Proteins at Interfaces Physicochemical and Biochemical Studies.* American Chemical Society, Washington, DC, (1987).

[14] Horbett, T. A. and Brash, J. L. *Proteins at Interfaces II, Fundamentals and Applications.* American Chemical Society, Washington, DC, (1995).

[15] Farrell, M. M. *Electroanalysis in the nanodomain: quinone monolayers and nanometer dimensioned electrodes.* PhD thesis, Dublin City University, (2003).

[16] Bard, A. J. and Faulkner, L. R. *Electrochemical Methods, Fundamentals and Applications.* Wiley, New York, second edition, (2001).

[17] Finklea, H. O. *Encyclopedia of Analytical Chemistry-Self assembled monolayers on electrodes.* Wiley, London, (2000).

[18] Love, J. C., Estroff, L. A., Kriebel, J. K., Nuzzo, R. G., and Whitesides, G. M. *Chem. Rev.* **105**, 1103 (2005).

[19] Lee, J. G., Lee, J., and Jr., J. T. Y. *J. Am. Chem. Soc.* **126**, 440 (2004).

[20] Andreoni, W., Curioni, A., and Gronbeck, H. *Int. J. Quantum Chem.* **80**, 598 (2000).

[21] Atkins, P. and de Paula, J. *Physical Chemistry, 7th Ed.* Oxford, New York, (2002).

[22] Laibinis, P. E. and Whitesides, G. M. *J. Am. Chem. Soc.* **114**, 9022 (1992).

[23] Sabatani, E. and Rubinstein, I. *J. Phys. Chem.* **91**, 6663 (1987).

[24] Lee, M. and Chung, C. *Bull. Korean Chem. Soc.* **20**, 1 (1999).

[25] Arinaga, K., Rant, U., Tornow, M., Fujita, S., Abstreiter, G., and Yokoyama, N. *Langmuir* **22**, 5560 (2006).

[26] Reipa, V., Yeh, S. M., Monbouquette, H. G., and Vilker, V. L. *Langmuir* **15**, 8126 (1999).

[27] Demoz, A. and Harrison, D. J. *Langmuir* **9**, 1046 (1993).

[28] Miller, C., Cuendet, P., and Gratzel, M. *J. Phys. Chem.* **95**, 877 (1991).

[29] Li, Z., Chang, S. C., and Williams, R. S. *Langmuir* **19**, 6744 (2003).

[30] Slowinski, K., Chamberlain, R. V., Miller, C. J., and Majda, M. *J. Am. Chem. Soc.* **119**, 11910 (1997).

[31] Smalley, J. F., Finklea, H. O., Chidsey, C. E. D., Linford, M. R., Creager, S. E., Ferraris, J. P., Chalfant, K., Zawodzinsk, T., Feldberg, S. W., and Newton, M. D. *J. Am. Chem. Soc.* **125**, 2004 (2003).

[32] Erol, M., Du, H., and Sukhishvili, S. *Langmuir* **22**, 11329 (2006).

[33] Stolberg, L., Richer, J., and Lipkowski, J. *J. Electroanal. Chem.* **207**, 213 (1986).

[34] Southampton-Electorchemistry-Group. *Instrumental Methods in Electrochemistry.* Horwood Publishing, Weinheim, (2001).

[35] Acevedo, D. and Abruna, H. D. *J. Phys. Chem.* **95**, 9590 (1991).

[36] Forster, R. J. and Faulkner, L. R. *J. Am. Chem. Soc.* **116**, 5444 (1994).

[37] Forster, R. J. and Faulkner, L. R. *J. Am. Chem. Soc.* **116**, 5453 (1994).

[38] Forster, R. J. and O'Kelly, J. P. *J. Phys. Chem.* **100**, 3695 (1996).

[39] Brennan, J. L., Keyes, T. E., and Forster, R. J. *Langmuir* **22**, 10754 (2006).

[40] Forster, R. J., Pellegrin, Y., Leane, D., Brennan, J. L., and Keyes, T. E. *J. Phys. Chem. C* **111**, 2063 (2007).

[41] Cai, W. B., She, C. X., Ren, B., Yao, J. L., Tian, Z. W., and Tian, Z. Q. *J. Chem. Soc., Faraday Trans.* **94**, 3127 (1998).

[42] Szejtli, J. and Osa, T. *Comprehensive supramolecular chemistry-volume 3.* Elsevier Science, Weinheim, (1996).

[43] Uekama, K., Hirayama, F., and Irie, T. *Chem. Rev.* **98**, 2045 (1998).

[44] Li, S. and Purdy, W. C. *Chem. Rev.* **92**, 1457 (1992).

[45] Takahashi, K. *Chem. Rev.* **98**, 2013 (1998).

[46] Khan, A. R., Forgo, P., Stine, K. J., and D'Souza, V. T. *Chem. Rev.* **98**, 1977 (1998).

[47] Schneider, H. J. *Angew. Chem. Int. Ed.* **30**, 1417 (1991).

[48] Rekharsky, M. V. and Inoue, Y. *Chem. Rev.* **98**, 1875 (1998).

[49] Inoue, Y., Hakuski, T., Liu, Y., Tong, L., Shen, B., and Jin, D. *J. Am. Chem. Soc.* **115**, 475 (1993).

[50] Matsue, T., Evens, D. H., Osa, T., and Kobayashi, N. *J. Am. Chem. Soc.* **107**, 3411 (1985).

[51] Gonzalez, B., Cuadrado, I., Alonso, B., Casado, C. M., Moran, M., and Kaifer, A. E. *Organometallics* **21**, 3544 (2002).

[52] Conn, M. M. and Rebek, J. *Chem. Rev.* **97**, 1647 (1997).

[53] Kaifer, A. E. *Acc. Chem. Res.* **32**, 62 (1999).

[54] Hapiot, F., Tilloy, S., and Monflier, E. *Chem. Rev.* **106**, 767 (2006).

[55] Ariga, K., Hill, J. P., and Endo, H. *Int. J. Mol. Sci.* **8**, 864 (2007).

[56] de Namor, A. F. D., Cleverley, R. M., and Zapata-Ormachea, M. L. *Chem. Rev.* **98**, 2495 (1998).

[57] Diamond, D. and McKervey, M. A. *Chem. Soc. Rev.* , 15 (1996).

[58] van Velzen, E. U. T., Engbersen, J. F., and Reinhoudt, D. N. *J. Am. Chem. Soc.* **116**, 3597 (1994).

[59] Matsue, T., Fujihira, M., and Osa, T. *J. Electroana. Chem.* **128**, 1473 (1981).

[60] Matsue, T., Fujihira, M., and Osa, T. *J. Electroanal. Chem.* **126**, 500 (1979).

[61] Odashima, K., Kotato, M., Sugawara, M., and Umezawa, Y. *Anal. Chem.* **65**, 927 (1993).

[62] Rojas, M. T., Kiiniger, R., Stoddart, J. F., and Kaifer, A. E. *J. Am. Chem. Soc.* **117**, 336 (1995).

[63] Almirall, E., Fragoso, A., and Cao, R. *Electrochem. Commun.* **1**, 10 (1999).

[64] Damos, F. S., Luz, R. C. S., and Kubota, L. T. *Electrochim. Acta* **53**, 1945 (2007).

[65] Weisser, M., Nelles, G., Wohlfart, P., Wenz, G., and Mittler-Neher, S. *J. Phys. Chem.* **100**, 17893 (1996).

[66] Nelles, G., Weisser, M., Back, R., Wohlfart, P., Wenz, G., and Mettler-Neher, S. *J. Am. Chem. Soc.* **118**, 5039 (1996).

[67] Weisser, M., Nelles, G., Wenz, G., and Mettler-Neher, S. *Sens. Actuators, B* **38-39**, 58 (1997).

[68] Kitano, H., Taira, Y., and Yamamoto, H. *Anal. Chem.* **72**, 2976 (2000).

[69] Meada, Y. and Kitano, H. *J. Phys. Chem.* **99**, 487 (1995).

[70] Kitano, H. and Taira, Y. *Langmuir* **18**, 5835 (2002).

[71] Endo, H., Nakaji-Hirabayashi, T., Morokoshi, S., Gemmei-Ide, M., and Kitano, H. *Langmuir* **21**, 1314 (2005).

[72] Maeda, Y., Fukuda, T., Yamamoto, H., and Kitano, H. *Langmuir* **13**, 4815 (1997).

[73] Fukuda, T., Maeda, Y., and Kitano, H. *Langmuir* **15**, 1887 (1999).

[74] de Jong, M. R., Huskens, J., and Reinhoudt, D. N. *Chem. Eur. J.* **7**, 4164 (2001).

[75] Beulen, M. W., Bugler, J., Lammerink, B., Geurts, F. A., Biemond, E. M., van Leerdam, K., van Veggel, F. C., Engbersen, J. F., and Reinhoudt, D. N. *Langmuir* **14**, 6424 (1998).

[76] Beulen, M. W., Bugler, J., de Jong, M. R., Lemmerink, B., Huskins, J., Schonherr, H., Vansco, G. J., Boukamp, B. A., Wieder, H., Offenhauser, A., Knoll, W., van Veggel, F. C., and Reinhoudt, D. N. *Chem. Eur. J.* **6**, 1176 (2000).

[77] Ludden, M. J. W., Reinhoudt, D. N., and Huskens, J. *Chem. Soc. Rev.* **35**, 1122 (2006).

[78] Crespo-Biel, O., Ravoo, B. J., Huskens, J., and Reinhoudt, D. N. *Dalton Trans.* , 2738 (2006).

[79] Huskens, J., Mulder, A., Auletta, T., Nijhuis, C. A., Ludden, M. J. W., and Reinhoudt, D. N. *J. Am. Chem. Soc.* **126**, 6784 (2004).

[80] Crespo-Biel, O., Peter, M., Bruinink, C. M., Ravoo, B. J., Reinhoudt, D. N., and Huskens, J. *Chem. Eur. J.* **11**, 2426 (2005).

[81] Nijhuis, C. A., Sinha, J. K., Wittstock, G., Huskens, J., Ravoo, B. J., and Reinhoudt, D. N. *Langmuir* **22**, 9770 (2006).

[82] Huskens, J., Deij, M. A., and Reinhoudt, D. N. *Angew. Chem. Int. Ed.* **41**, 4467 (2002).

[83] Nijhuis, C. A., Oncel, N., Huskens, J., Zandvliet, H. J. W., Ravoo, B. J., Poelsema, B., and Reinhoudt, D. N. *Small* **2**, 1422 (2006).

[84] Ludden, M. J. W., Peter, M., Reinhoudt, D. N., and Huskens, J. *Small* **2**, 1192 (2006).

[85] Ludden, M. J. W., Li, X., Greve, J., van Amerongen, A., Escalante, M., Subramaniam, V., Reinhouldt, D. N., and Huskens, J. *J. Am. Chem. Soc.* **130**, 3574 (2008).

[86] Ludden, M. J. W., Mulder, A., Tampe, R., Reinhoudt, D. N., and Huskens, J. *Angew. Chem. Int. Ed.* **46**, 4104 (2007).

[87] Nijhuis, C. A., Yu, F., Knoll, W., Huskens, J., and Reinhoudt, D. N. *Langmuir* **21**, 7866 (2005).

[88] Henke, C., Steinem, C., Janshoff, A., Steffan, G., Luftmann, H., Sieber, M., and Galla, H. J. *Anal. Chem.* **68**, 3158 (1996).

[89] Michalke, A., Janshoff, A., Steinem, C., Henke, C., Sieber, M., and Galla, H. S. *Anal. Chem.* **71**, 2528 (1999).

[90] Qian, J., Hentschke, R., and Knoll, W. *Langmuir* **13**, 7092 (1997).

[91] Morales, G. R., Silva, T. R., and Galicia, L. *J. Solid State Electrochem.* **7**, 355 (2003).

[92] Liu, H., Li, H., Ying, T., Sun, K., Qin, Y., and Qi, D. *Anal. Chim. Acta* **358**, 137 (1998).

[93] He, P., Ye, J., Fang, Y., Suzuki, I., and Osa, T. *Anal. Chim. Acta* **337**, 217 (1997).

[94] Chmurski, K., Temeriusz, A., and Bilewicz, R. *J. Inclusion Phenom. Macrocyclic Chem.* **49**, 187 (2004).

[95] Shahgaldian, P., Hegner, M., and Pieles, U. *J. Inclusion Phenom. Macrocyclic Chem.* **53**, 35 (2005).

[96] Lee, J. Y. and Park, S. M. *J. Phys. Chem. B* **102**, 9940 (1998).

[97] Choi, S. J., Choi, B. G., and Park, S. M. *Anal. Chem.* **74**, 1998 (2002).

[98] Lahav, M., Ranjit, K. T., Katz, E., and Willner, I. *Chem. Commun.* **3**, 259 (1997).

[99] Bollo, S., Yanez, C., Sturm, J., Nunez-Vergara, L., and Squella, J. *Langmuir* **19**, 3365 (2003).

[100] Suzuli, I., Murakami, K., Anzai, J., Osa, T., and He, P. *Mater. Sci. Eng., C* **6**, 19 (1998).

[101] Suzuki, I., Murakami, K., and Anzai, J. *Mater. Sci. Eng., C* **17**, 143 (2001).

[102] Chamberlain, R. V., Slowinska, K., Majda, M., Buhlmann, P., Aoki, H., and Umezawa, Y. *Langmuir* **16**, 1388 (2000).

[103] Yamamoto, H., Maeda, Y., and Kitano, H. *J. Phys. Chem. B* **101**, 6855 (1997).

[104] Hill, W., Fallourd, V., and Klockow, D. *J. Phys. Chem. B* **103**, 4707 (1999).

[105] Lindsay, S. *J. Chem. Ed.* **82**, 727 (2005).

[106] Chen, F., Hihath, J., Huang, Z., Li, X., and Tao, N. J. *Annu. Rev. Phys. Chem.* **58**, 535 (2007).

[107] Tao, N. J. *Nat. Nanotechnol.* **1**, 173 (2007).

[108] Bumm, L. A., Arnold, J. J., Cygan, M. T., Dunbar, T. D., Burgin, T. P., II, L. J., Allara, D. L., Tour, J. M., and Weiss, P. S. *Science* **271**, 1705 (1996).

[109] Reed, M. A., Zhou, C., Muller, C. J., Burgin, T. P., and Tour, J. M. *Science* **278**, 252 (1997).

[110] Balzani, V. *Electron Transfer in Chemistry vol I-V.* Wiley, Weinheim, (2001).

[111] Fan, F. F., Yang, J., Dirk, S. M., Price, D. W., Kosynkin, D., Tour, J. M., and Bard, A. J. *J. Am. Chem. Soc.* **123**(2454) (2001).

[112] Li, X., He, J., Hihath, J., Xu, B., Lindsay, S. M., and Tao, N. *J. Am. Chem. Soc.* **128**, 2135 (2006).

[113] Leatherman, G., Durantini, E. N., Gust, D., Moore, T. A., Moore, A. L., Stone, S., Zhou, Z., Rez, P., Lui, Y. Z., and Lindsay, S. M. *J. Phys. Chem. B* **103**, 4006 (1999).

[114] Wold, D. J. and Frisbie, C. D. *J. Am. Chem. Soc.* **123**, 5549 (2001).

[115] Salomon, A., Cahen, D., Lindsay, S. M., Tomfohr, J., Engelkes, V. B., and Frisbie, C. D. *Adv. Mater.* **15**, 1881 (2003).

[116] Xu, B. and Tao, N. J. *Science* **301**, 1221 (2003).

[117] Tao, N. J. *Phys. Rev. Lett.* **76**, 4066 (1996).

[118] Duati, M., Grave, C., Tcbeborateva, N., Wu, J., Mullen, K., Shaporenko, A., Zharnikov, M., Kriebel, J. K., Whitesides, G. M., and Rampi, M. A. *Adv. Mater.* **18**, 329 (2006).

[119] Metzger, R. M. *Acc. Chem. Res.* **32**, 950 (1999).

[120] Albrecht, T., Moth-Poulsen, K., Christensen, J. B., Guckian, A., Bjornholm, T., Vos, J. G., and Ulstrup, J. *Faraday Discuss.* **131**, 265 (2006).

[121] Haiss, W., Albrecht, T., van Zalinge, H., Higgins, S. J., Bethell, D., Hobenreich, H., Schiffin, D. J., Nichols, R. J., Kuznetsov, A. M., Zhang, J., Chi, Q., and Ulstrup, J. *J. Phys. Chem. B* **111**, 6703 (2007).

[122] Chen, F., He, J., Nuckolls, C., Roberts, T., Klare, J. E., and Lindsay, S. *NanoLett.* **5**, 503 (2005).

[123] Gittins, D. I., Bethell, D., Schiffrin, D. J., and Nichols, R. J. *Nature* **408**, 67 (2000).

[124] Slowinski, K., Fong, H. K. Y., and Majda, M. *J. Am. Chem. Soc.* **121**, 7257 (1999).

[125] Slowinski, K. and Majda, M. *J. Electroanal. Chem.* **491**, 139 (2000).

[126] Holmlin, R. E., Haag, R., Chabinyc, M. L., Ismagilov, R. F., Cohen, A. E., Terfort, A., Rampi, M. A., and Whitesides, G. M. *J. Am. Chem. Soc.* **123**, 5075 (2001).

[127] Weiss, E. A., Chiechi, R. C., Kaufman, G. K., Kriebel, J. K., Li, Z., Duati, M., Rampi, M. A., and Whitesides, G. M. *J. Am. Chem. Soc.* **129**, 4336 (2007).

[128] Tran, E., Rampi, M. A., and Whitesides, G. M. *Angew. Chem. Int. Ed.* **43**, 3835 (2004).

[129] Mann, B. and Kuhn, H. *J. Appl. Phys.* **42**, 4398 (1971).

[130] Polymeropoulos, E. and Sagiv, J. *J. Chem. Phys.* **69**, 1836 (1978).

[131] Zhou, C., Deshpande, M. R., Reed, M. A., Jones, L., and Tour, J. M. *J. Appl. Phys. Lett.* **71**, 611 (1997).

[132] Metzger, R. M. *Acc. Chem. Res.* **32**, 950 (1999).

[133] Haick, H. and Cahen, D. *Acc. Chem. Res.* **41**, 359 (2008).

[134] Simmons, J. G. *J. Appl. Phys.* **34**, 1793 (1963).

[135] York, R. L. and Slowinski, K. *J. Electroanal. Chem.* **550**, 327 (2003).

[136] York, R. L., Nguyen, P. T., and Slowinski, K. *J. Am. Chem. Soc.* **125**, 5948 (2003).

[137] Sek, S., Bilewicz, R., and Slowinski, K. *Chem. Commun.* , 404 (2004).

[138] York, R. L., Nacionales, D., and Slowinski, K. *Chem. Phys.* **319**, 235 (2005).

[139] Salomon, A., Cahen, D., Lindsay, S., Tomfohr, J., Engelkes, V. B., and Frisbie, C. D. *Adv. Mater.* **15**, 1881 (2003).

[140] Rampi, M. A. and Whitesides, G. M. *Appl. Phys. Lett.* **72**, 1781 (1998).

[141] Haag, R., Rampi, M. A., Holmlin, R. E., and Whitesides, G. M. *J. Am. Chem. Soc.* **121**, 7895 (1999).

[142] Rampi, M. A. and Whitesides, G. M. *Chem. Phys.* **281**, 373 (2002).

[143] Chabinyc, M. L., Chen, X., Holmlin, R. E., Jacobs, H., Skulason, H., Frisbie, C. D., Mujica, V., Ratner, M. A., Rampi, M. A., and Whitesides, G. M. *J. Am. Chem. Soc.* **124**, 11730 (2002).

[144] Tran, E., Duati, M., Whitesides, G. M., and Rampi, M. A. *Faraday Discuss.* **131**, 197 (2006).

[145] Anariba, F. and McCreery, R. L. *J. Phys. Chem. B* **106**, 10355 (2002).

[146] Ranganathan, S., Steidel, I., Anariba, F., and McCreery, R. L. *NanoLett.* **1**, 491 (2001).

[147] Salomon, A., Boecking, T., Seitz, O., Markus, T., Amy, F., Chan, C., Zhao, W., Cahen, D., and Kahn, A. *Adv. Mater.* **19**, 445 (2007).

[148] Selzer, Y., Salomon, A., and Cahen, D. *J. Phys. Chem. B* **106**, 10432 (2002).

[149] Salomon, A., Boecking, T., Chan, C. K., Amy, F., Girshevitz, O., Cahen, D., and Kahn, A. *Phys. Rev. Lett.* **95**, 266807 (2005).

[150] Wang, B., Luo, J., Wang, X., Wang, H., and Hou, J. G. *Langmuir* **20**, 5007 (2004).

[151] Branden, C. and Tooze, J. *Introduction to Protein Structure.* Garland Publishing, New York, (1991).

[152] Doolittle, R. F. *Annu. Rev. Biochem.* **53**, 195 (1984).

[153] Cacciafesta, P., Humphris, A. D. L., Jandt, K. D., and Miles, M. L. *Langmuir* **16**, 8167 (2000).

[154] Keeton, W. T. and Gould, J. L. *Biological Science.* Norton, New York, (1986).

[155] Danesh, J., R, C., Appleby, P., and Peto, R. *J. Am. Med. Assn.* **279**, 1477 (1998).

[156] Ernst, E. and Resch, K. L. *Ann. Internal Med.* **118**, 956 (1993).

[157] Morrowa, R., McKenziea, D. R., Bileka, M. M. M., MacDonalda, C. L., Stindta, M., Anetsbergera, G., and Martin, A. S. *Physica B* **203**, 203 (2007).

[158] Ostuni, E., Chapman, R. G., Holmlin, R. E., Takayama, S., and Whitesides, G. M. *Langmuir* **17**, 5605 (2001).

[159] Sanders, A. and Jennissen, H. P. *J. Mol. Recognit.* **9**, 503 (1996).

[160] Lin, Y., Wang, J., Wan, L., and Fang, X. *Ultramicroscopy* **105**, 129 (2005).

[161] Castner, D. G. and Ratner, B. D. *Surf. Sci.* **500**, 28 (2002).

[162] Wahlgren, M. and Arnebrant, T. *Trends Biotechnol.* **9**, 201 (1991).

[163] Norde, W. *Adv. Colloid Interfacial Sci.* **25**, 267 (1986).

[164] Yu, Y. and Jin, G. *J. Colloid Interface Sci.* **283**, 477 (2005).

[165] Jackson, D. R., Omanovic, S., and Roscoe, S. G. *Langmuir* **16**, 5449 (2000).

[166] Jordan, C. E. and Corn, R. M. *Anal. Chem.* **69**, 1449 (1997).

[167] Prime, K. L. and Whitesides, G. M. *Science* **252**, 1164 (1991).

[168] Mrksich, M., Sigal, G. B., and Whitesides, G. M. *Langmuir* **11**, 4383 (1995).

[169] Mrksich, M. and Whitesides, G. M. *Annu. Rev. Biophys. Biomol. Struct.* **25**, 55 (1996).

[170] Gettens, R. T. T., Bai, Z., and Gilbert, J. L. *J. Biomed. Mater. Res.* **72**, 246 (2005).

[171] Snopok, B. A. and Kostyukevich, E. V. *Anal. Biochem.* **348**, 222 (2006).

[172] Toscano, A. and Santore, M. M. *Langmuir* **22**, 2588 (2006).

[173] Shao, Z., Mou, J., Czajkowsky, D. M., Yang, J., and Yuan, J. Y. *Adv. Phys.* **45**, 1 (1996).

[174] Wigren, R., Elwing, H., Erlandsson, R., Welin, S., and Lundstrom, I. *FEBS Lett.* **280**, 225 (1991).

[175] Rasmusson, J. R., Erlandsson, R., Salaneck, W. R., Schott, M., Clark, D. T., and Lundstrom, I. *Scanning Microscopy* **8**, 481 (1994).

[176] Ortega-Vinuesa, J. L., Tengvall, P., and Lundstrom, I. *Thin Solid Films* **324**, 257 (1998).

[177] Agnihotri, A. and Siedlecki, C. A. *Langmuir* **20**, 8846 (2004).

[178] Marchin, K. L. and Berrie, C. L. *Langmuir* **19**, 9883 (2003).

[179] van der Veen, M., Stuart, M. C., and Norde, W. *Colloids Surf., B* **54**, 136 (2007).

[180] Ball, V., Bentaleb, A., Hemmerle, J., Voegel, J. C., and Schaaf, P. *Langmuir* **12**, 1621 (1996).

[181] Sarkar, D. and Chattoraj, D. K. *J. Colloid Interface Sci.* **178**, 606 (1996).

[182] Fainerman, V. B., Leser, M. E., Michel, M., Lucassen-Reynders, E. H., and Miller, R. *J. Phys. Chem. B* **109**, 9672 (2005).

[183] Chan, B. M. C. and Brash, J. L. *J. Colloid Interface Sci.* **84**, 263 (1981).

[184] Sheller, N. B., Petrash, S., Foster, M. D., and Tsukruk, V. V. *Langmuir* **14**, 4535 (1998).

[185] Wertz, C. F. and Santore, M. M. *Langmuir* **15**, 8884 (1999).

[186] Giacomelli, C. E., , and Norde, W. *J. Colloid Interface Sci.* **233**, 234 (2001).

[187] Balasubramanian, S., Revzin, A., and Simoniana, A. *Electroanalysis* **18**, 1885 (2006).

[188] Haynes, C. L. and Duyne, R. P. V. *J. Phys. Chem. B* **105**, 5599 (2001).

[189] Shipway, A. N., Katz, E., and Willner, I. *ChemPhysChem* **1**, 18 (2000).

[190] Willets, K. A. and Duyne, R. P. V. *Annu. Rev. Phys. Chem.* **58**, 268 (2007).

[191] Kamat, P. V. *J. Phys. Chem. B* **106**, 7729 (2002).

[192] Kelf, T. A., Sugawara, Y., Baumberg, J. J., Abdelsalam, M., and Bartlett, P. N. *Phys. Rev. Lett.* **95**, 116802 (2005).

[193] Thijssen, M. S., Sprik, R., Wijnhoven, J. E. G. J., Megens, M., Narayanan, T., Lagendijk, A., and Vos, W. L. *Phys. Rev. Lett.* **83**, 2730 (1999).

[194] Braun, P. V. and Wiltziusa, P. *Curr. Opin. Colloid Interface Sci.* **7**, 116 (2002).

[195] Wallraff, G. M. and Hinsberg, W. D. *Chem. Rev.* **99**, 1801 (1999).

[196] Ito, T. and Okazaki, S. *Nature* **406**, 1027 (2000).

[197] Burmeister, F., Schafle, C., Keilhofer, B., Boneberg, C. B. J., and Leiderer, P. *Adv. Mater.* **10**, 495 (1998).

[198] Zakhidov, A. A., Baughman, R. H., IqbaL, Z., Cui, C., KhayrulLin, I., Dantas, S. O., Marti, J., and Ralchenko, V. G. *Science* **282**, 897 (1998).

[199] Bartlett, P. N., Baumberg, J. J., Birkin, P. R., Ghanem, M. A., and Netti, M. C. *Chem. Mater.* **14**, 2199 (2002).

[200] Mahajan, S., Abdelsalam, M., Suguwara, Y., Cintra, S., Russell, A., Baumbergb, J., and Bartlett, P. *Phys. Chem. Chem. Phys.* **9**, 104 (2007).

[201] Abdelsalam, M. E., Bartlett, P. N., Cintra, J. J. B. S., Kelf, T. A., and Russell, A. E. *Electrochem. Commun.* **7**, 740 (2005).

[202] Cintra, S., Abdelsalam, M. E., Bartlett, P. N., Baumberg, J. J., Kelf, T. A., Sugawarab, Y., and Russell, A. E. *Faraday Discuss.* **132**, 191 (2006).

[203] Holland, B. T., Abrams, L., and Stein, A. *J. Am. Chem. Soc.* **121**, 4308 (1999).

[204] Abdelsalam, M. E., Mahajan, S., Bartlett, P. N., Baumberg, J. J., and Russell, A. E. *J. Am. Chem. Soc.* **129**, 7399 (2007).

[205] Bartlett, P. N., Birkin, P. R., and Ghanem, M. A. *Chem. Commun.* , 1671 (2000).

[206] Abdelsalam, M. E., Bartlett, P. N., Baumberg, J. J., and Coyle, S. *Adv. Mater.* **16**, 90 (2004).

[207] Bartlett, P. N., Baumberg, J. J., Coyleb, S., and Abdelsalam, M. E. *Faraday Discuss.* **125**, 117 (2004).

[208] Tessier, P. M., Velev, O. D., Kalambur, A. T., Rabolt, J. F., Lenhoff, A. M., and Kaler, E. W. *J. Am. Chem. Soc.* **122**, 9554 (2000).

[209] Xu, L., Zhou, W. L., Frommen, C., Baughman, R. H., Zakhidov, A. A., Malkinski, L., Wang, J., and Wiley, J. B. *Chem. Commun.* , 997 (2000).

[210] Wijnhoven, J. E. G. J., Zevenhuizen, S. J. M., Hendriks, M. A., Vanmaekelbergh, D., Kelly, J. J., and Vos, W. L. *Adv. Mater.* **12**, 888 (2000).

[211] Cole, R. M., Baumberg, J. J., de Abajo, F. J. G., Mahajan, S., Abdelsalam, M., and Bartlett, P. N. *Nano Lett.* **7**, 2094 (2007).

[212] Coyle, S., Netti, M. C., Baumberg, J. J., Ghanem, M. A., Birkin, P. R., Bartlett, P. N., and Whittaker, D. M. *Phys. Rev. Lett.* **87**, 176801 (2001).

[213] Maliwal, B. P., Malicka, J., Gryczynski, I., Gryczynski, Z., and Lakowicz, J. R. *Biopolymers* **70**, 585 (2003).

[214] Stranik, O., Nooney, R., McDonagh, C., and MacCraith, B. D. *Plasmonics* **2**, 15 (2007).

[215] Brolo, A. G., Kwok, S. C., Moffitt, M. G., Gordon, R., Riordon, J., and Kavanagh, K. L. *J. Am. Chem. Soc.* **127**, 14936 (2005).

[216] Corrigan, T. D., Guo, S., Phaneuf, R. J., and Szmacinski, H. *J. Fluoresc.* **15**, 777 (2005).

[217] Gordon, R., Brolo, A. G., McKinnon, A., Rajora, A., Leathem, B., and Kavanagh, K. L. *Phys. Rev. Lett.* **92**, 037401–1 (2004).

[218] Nicholson, R. S. *Anal. Chem.* **37**, 1351 (1965).

[219] Lakowicz, J. R. *Principles of fluorescence spectroscopy.* Plumen Publisher, New York, (2006).

[220] Palumbo, G. and Pratesi, R. *Lasers and Current Optical Techniques in Biology.* Royal Society of Chemistry, Cambridge, (2004).

[221] Herman, B. *Fluorescence Microscopy.* Bios Scientific Publishers, Oxford, (1998).

[222] Giessibl, F. J. *Rev. Mod. Phys.* **75**, 949 (2003).

[223] Wiesendanger, R. *Scanning Probe Microscopy and Spectroscopy.* Cambridge University Press, Cambridge, (1994).

[224] Bard, A. J., Abruna, H. A., Chidsey, C. E., Faulkner, L. R., Feldberg, S. W., Itaya, K., Majda, M., Melroy, O., Murray, R. W., Porter, M. D., Soriaga, M. P., and White, H. S. *J. Phys. Chem.* **97**, 7147 (1993).

[225] Ferraro, J. R. *Introductory Raman Spectroscopy.* Academic Press, Boston, (1994).

[226] Porter, M. C., Bright, T. B., Allara, D. L., and Chidsey, C. E. D. *J. Am. Chem. Soc.* **109**, 3559 (1987).

[227] Forster, R. J. *Inorg. Chem.* **35**, 3394 (1996).

[228] Stern, D. A., Laguren-Davidson, L., Frank, D. G., Cui, J. Y., Lin, C., Lu, F., Salaita, G. N., Walton, N., Zapien, D. C., and Hubbard, A. T. *J. Am. Chem. Soc.* **111**, 877 (1989).

[229] Boulas, P., Kutner, W., Jones, M. T., and Kadish, K. M. *J. Phys. Chem.* **98**, 1282 (1994).

[230] Jones, M. L., Kurnikov, I. V., and Beratan, D. N. *J. Phys. Chem. A* **106**, 2002 (2002).

[231] Forster, R. J. *Chem. Soc. Rev.* , 289 (1994).

[232] Campagnoli, E. *Immobilisation of redox active molecules as precursors for nanowire self-assembly.* PhD thesis, Dublin City University, (2007).

[233] Trasatti, S. and Petrii, O. A. *Pure Appl. Chem.* **63**, 711 (1991).

[234] Saenger, W. and Steiner, T. *Acta Crystallogr.* **A54**, 798 (1998).

[235] Steiner, T. and Saenger, W. *Acta Crystallogr.* **B54**, 450 (1998).

[236] Ren, B., Huang, Q. J., Cai, W. B., Mao, B. W., Liu, F. M., and Tian, Z. Q. *J. Electroanal. Chem.* **415**, 175 (1996).

[237] Alcock, N. W., Barker, P. R., Haider, J. M., Hannon, M. J., Painting, C. L., Pikramenou, Z., Plummer, E. A., Rissanen, K., and Saarenketo, P. *J. Am. Chem. Soc.* , 1447 (2000).

[238] Pellegrin, Y., Forster, R. J., and Keyes, T. E. *Inorg. Chim. Acta* **361**, 2683 (2008).

[239] Simpson, S. F. and Harris, J. M. *J. Phys. Chem.* **94**, 4649 (1990).

[240] Subramanian, R. and Lakshminarayanan, V. *Electrochim. Acta* **45**, 4501 (2000).

[241] Chailapakul, O. and Crooks, R. M. *Langmuir* **11**, 1329 (1995).

[242] Finklea, H. O., Snider, D. A., Fedyk, J., Sabatani, E., Gafni, Y., and Rubinstein, I. *Langmuir* **9**, 3660 (1993).

[243] Amatore, C., Saveant, J. M., and Tessier, D. *J. Electroanal. Chem.* **147**, 39 (1983).

[244] Haider, J. M., Chavarot, M., Weidner, S., Sadler, I., Williams, R. M., Cola, L. D., and Pikramenou, Z. *Inorg. Chem.* **40**, 3912 (2001).

[245] Atmeh, M., Russell, N. R., Forster, R. J., and Keyes, T. E. *J. Inclusion Phenom. Macrocyclic Chem.* **57**, 607 (2007).

[246] Creager, S. E., Hockett, L. A., and Rowe, G. K. *Langmuir* **8**, 854 (1992).

[247] McNally, A. *Photo and electroactive supramolecular cyclodextrin assemblies.* PhD thesis, Dublin City University, (2005).

[248] McNally, A., Forster, R. J., and Keyes, T. E. *Phys. Chem. Chem. Phys.* **In Print** (2008).

[249] Campagnoli, E., Hjelm, J., Milios, C. J., Sjodin, M., Pikramenou, Z., and Forster, R. J. *Electrochim. Acta* **52**, 6692 (2007).

[250] Mulvaney, P. *Langmuir* **12**, 788 (1996).

[251] Bryant, M. A. and Pemberton, J. E. *J. Am. Chem. Soc.* **113**, 8284 (1991).

[252] Forster, R. J. and Faulkner, L. R. *Langmuir* **11**, 1014 (1995).

[253] Atmeh, M., Russell, N. R., and Keyes, T. E. *Polyhedron* **27**, 1690 (2008).

[254] McCreery, R. L., Viswanathan, U., Kalakodimi, R. P., and Nowak, A. M. *Faraday Discuss.* **131**, 33 (2006).

[255] Kroto, H. W., Allaf, A. W., and Balm, S. P. *Chem. Rev.* **91**, 1213 (1991).

[256] Liu, W., Zhang, Y., and Gao, X. *J. Am. Chem. Soc.* **129**, 4973 (2007).

[257] Zanello, P. *Inorganic electrochemistry: theory, practice and applications.* Royal Society of Chemistry, London, (2003).

[258] Mirkin, C. A. and Caldwell, W. B. *Tetrahedron* **52**, 5113 (1996).

[259] Saffarzadeh, A. *J. Appl. Phys.* **103**, 083705 (2008).

[260] Joachim, C., Gimzewski, J. K., Schlitter, R. R., and Chavy, C. *Phys. Rev. Lett.* **74**, 2102 (1995).

[261] Szejtli, J. *Chem. Rev.* **98**, 1743 (1998).

[262] Strehle, M. A., Rosch, P., Petry, R., Hauck, A., Thull, R., Kieferc, W., and Popp, J. *Phys. Chem. Chem. Phys.* **6**, 5232 (2004).

[263] van Eijk, M. C. P. and Stuart, M. A. C. *Langmuir* **13**, 5447 (1997).

[264] Mottram, L. F., Boonyarattanakalin, S., Kovel, R. E., and Peterson, B. R. *Org. Lett.* **8**, 581 (2006).

[265] Motschmann, H., Stamm, M., and Toprakcioglu, C. *Macromol.* **24**, 3681 (1991).

[266] Marder, V. J., Shulman, N. R., and Carroll, W. R. *J. Biol. Chem.* **244**, 2111 (1969).

[267] Armstrong, F. A. and Wilson, G. S. *Electrochim. Acta* **45**, 2623 (2000).

[268] Armstrong, F. A. *Curr. Opin. Chem. Biol.* **9**, 110 (2005).

[269] Brolo, A. G., Arctander, E., Gordon, R., Leathem, B., and Kavanagh, K. L. *Nano Lett.* **4**, 2015 (2004).

[270] Socrates, G. *Infrared and Raman Characteristic Group Frequencies.* Wiley, Chichester, (2001).

[271] Shipway, A. N. and Willner, I. *Chem. Commun.* , 2035 (2001).

[272] Liu, J., Mendoza, S., Roman, E., Lynn, M. J., Xu, R., and Kaifer, A. E. *J. Am. Chem. Soc.* **121**, 4304 (1999).

[273] Brolo, A. G., Gordon, R., Leathem, B., and Kavanagh, K. L. *Langmuir* **20**, 4813 (2004).